University of Sussex

# Analysis of Low Frequency Plasma Waves in the Turbulent Magnetosheath; Downstream of the Earth's Bow shock

**Nathaniel, Ekong Ufot**

A Thesis Submitted to the Space Science Centre

University of Sussex

In Fulfilment of the Requirements

for the Award of the Doctor of Philosophy Degree

In Space Science of the University of Sussex,

Brighton, UK

September 2010

# Abstract

The knowledge of the dynamics and characteristics of space plasma during solar−terrestrial coupling has been greatly enriched by process that aids the determination of the instantaneous frequencies which support the non−stationary and non−linear nature of signals. Such plasmas are observed in the magnetosheath in the downstream of bow shock. In this thesis a technique was applied which extracts the various contributing oscillatory modes reflecting the waveforms observed in the space by Cluster spacecraft instruments such as FGM, CIS and EFW, and decompose the frequency of each extracted mode using Instantaneous Frequency method that is based on Simple Hilbert Transform (SHT). This is achieved through the use of Empirical Mode Decomposition (EMD). To eliminate the negative frequency of the various extracted modes referred to as intrinsic mode function which appears with Fourier transform, we apply Hilbert transform leading to analytic representation of the signals. This process aids the determination of the instantaneous frequencies of the extracted modes. The combined process of EMD and Hilbert transform is called the Hilbert−Huang transform. The results in this thesis have been based on the improved EMD. To contribute to the understanding of plasma dynamics, the computed instantaneous frequencies are compared with the results obtained from the application of Simple Hilbert Transform. Instantaneous frequencies of overriding waves are easily separated as opposed to the application of just SHT. They offer the advantage of 3−dimensional study of the spatial

characteristics of waves. The understanding of the instantaneous wave number has been achieved through the EMD and SHT combination. This provides the results which give the wave vector for a known frequency at a given instant of time. The instantaneous dispersion relation is determined using the knowledge of the instantaneous frequency and wave vector in the satellite frame, the plasma bulk velocity and the spacecraft velocity (found to be negligible compared with the plasma bulk velocity). This is accomplished using a Doppler shift relation. Wave modes identifications have been carried out by considering the proton temperature anisotropies, plasma beta and plasma bulk velocity and instantaneous phase velocity in the satellite frame. We report Alfvén mode close to the bow shock, spreading out to mirror mode which dominates the middle of magnetosheath. The mirror mode then diminishes towards the magnetopause.

# Benefit of Study

Planet Earth is one of the many planetary objects that have been influenced by the celestial activities. Many events such as space storms accompany ejection of high energetic particles from sun and anomalous cosmic rays. And substorms accompany the most intense space storms as indicated by aurora are capable of disrupting both space missions and ground installations such as astronauts and satellites, communications and navigation systems, computers, electricity sources and transmission lines. These storms produce the most penetrating radiations that also affect aviation industry, cause radio wave disturbance, induce earth currents that affect underground installations, agriculture, and many other areas. The understanding and predicting of space weather is important to describe the environment in which spacecraft and astronauts operate and ensure their safety, monitor these solar activities to help the prescription of suitable technology and best seasons for space exploration and exploitation. It also helps to unravel the advantages of these solar storms, which are found in the shielding it provides to Earth that reduces the intensity of cosmic rays, energetic particles reaching the Earth from the Galaxy.

# Declaration

I hereby declare that this thesis has not been previously submitted to University of Sussex nor any other University in application for a degree or any other qualification. Parts of this thesis have previously appeared in the following publications as:

2010

Instantaneous wave vector of low frequency waves in the turbulent magnetosheath (with Natalia Beloff, Andrew Buckley) in EGU General Assembly Vienna, Austria: Elsevier Volume 12.

Application of Hilbert-Huang Transform (HHT) for the determination of instantaneous low frequency of plasma waves (with Natalia Beloff, Andrew Buckley) in Planetary and Space Science, (Submitted).

2009

Application of Hilbert-Huang Transform for the determination of instantaneous low frequency of Plasma waves (with Natalia Beloff, Andrew Buckley) in 51st Annual Meeting of the APS Division of Plasma Physics, Atlanta, Georgia: APS Volume 54, Number 15.

Application of Hilbert-Huang Transform for the Determination Instantaneous Low Frequency of Plasma Waves (with Natalia Beloff, Andrew Buckley) in Sixth European Space Weather Week, ESWW6, Brugge, Belgium.

# Acknowledgement

I am really grateful to Dr. Natalia Beloff and Dr. Andrew Buckley (my first and second supervisors) for their dedicated supervision throughout the period of this research. I am so thankful to my wife and son (Roseline and Richard) for the cooperation given to me throughout this period.

Thanks are due also to the former Executive Governor of Akwa Ibom State (Nigeria), Obong Victor Attah (Architect) whose vision accorded me the scholarship award that enable me to carry out this research.

I will not forget the following persons and links that enable the success of this research such as: Dr. Peter Smith, Dr. Simon Walker and Dr. Tobia Carozzi for their technical advices. Prof. Huang Norden for the basics of empirical mode decomposition (EMD). Cluster Active Archive (CAA) − ESA, Cluster Science and Data System (CSDS) − ESA and CDAWeb − NASA teams for data used in this thesis. I will also thank Dr. Elizabeth Lucek and Dr. Vassilis Angelopoulos for their supports.

# Acronyms

**3D** −− 3 dimensional

**C1** −− Cluster spacecraft 1

**C2** −− Cluster spacecraft 2

**C3** −− Cluster spacecraft 3

**C4** −− Cluster spacecraft 4

**CAA** −− Cluster Active Archive

**CDAweb** −− Coordinated Data Analysis Web

**CIS** −− Cluster Ion Spectrometry

**CODIF** −− COmposition and DIstribution Function

**CSD** −− Cross Spectral Density

**CSDS** −− Cluster Science and Data System

**CWT** −− Continuous Wavelet Transform

**EFW** −− Electric Field and Wave

**EMD** −− Empirical mode decomposition

**ESA** −− European Space Agency

**FGM** −− Fluxgate magnetometer

**FT** −− Fourier Transform

**HT** −− Hilbert Transform

**HHT** −− Hilbert−Huang Transform

**HIA** −− Hot Ion Analyzer

**IF** −− Instantaneous Frequency

**IFT** −− Inverse Fourier Transform

**ILW** −− Instantaneous Local Wave vector

$imf$ −− intrinsic mode function

**IMF** −− Interplanetary magnetic field

**MCP** −− Micro−Channel Plate

**NASA** −− National Aeronatics and Space Administration

**PSD** −− Power Spectral Density

**R** −− Correlation coefficient

**R (italiced)** −− Reynold number

**RECR** −− Relative Energy Character Rate

**RPA** −− Retarding Potential Analyzer

**Sat** −− satellite

**Sat 13** −− C1 and C3 combination

**Sat 23** −− C2 and C3 combination

**Sat 43** −− C4 and C3 combination

**SD** −− Standard Deviation

**SHT** −− Simple Hilbert Transform

**TOF** −− Time Of Flight

**TV** −− Threshold Value

**UT** −− Universal Time

# Contents

**1 Introduction** **1**

1.1 Introduction . . . . . 1

1.2 Comparison of Fourier analysis (FA), Wavelet analysis (WA) and EMD−HT combination technique . . . . . 3

**2 Background study** **8**

2.1 Overview of Solar-terrestrial coupling . . . . . 8

2.1.1 What is plasma? . . . . . 8

2.1.2 Plasma waves . . . . . 11

2.2 Shocks . . . . . 12

2.2.1 Types of Shocks . . . . . 13

2.2.2 Properties of shock . . . . . 17

2.3 Solar wind and instabilities . . . . . 19

2.3.1 Instabilities associated with magnetosheath; the downstream of terrestrial bow shock . . . . . 19

2.3.2 Ion cyclotron instability . . . . . 21

2.4 Turbulence in Space . . . . . 21

2.4.1 Types of turbulence . . . . . 21

2.5 Summary . . . . . 23

**3 Instrumentations** **24**

3.1 Introduction . . . . . 24

3.2 The Cluster mission instruments . . . . . 24

3.2.1 FGM . . . . . 27

3.2.2 CIS . . . . . 28

3.2.3 EFW . . . . . 31

3.3 Summary . . . . . 32

**4 Determination of Instantaneous frequencies of low frequency plasma waves in the magnetosheath** **33**

4.1 Introduction . . . . . 33

4.1.1 Concept of frequency, instantaneous frequency . . . . . 34

4.1.2 Stationarity . . . . . 35

4.1.3 Variable frequency and non-stationarity . . . . . 36

4.1.4 Instantaneous frequency . . . . . 37

4.2 Empirical mode decomposition (EMD) . . . . . 38

4.2.1 Identified drawbacks of EMD . . . . . 40

4.2.2 Achieved improvement on EMD . . . . . 41

4.3 Simple Hilbert Transform (SHT) . . . . . 42

4.3.1 Filtering and sifting . . . . . 44

4.3.2 Negative Frequency Filtering: Hilbert filter . . . . . 44

4.3.3 Mode separation . . . . . 48

4.3.4 Other non-stationary methods . . . . . 49

4.3.5 $Imfs$, and instantaneous frequency estimation . . . . . 50

4.4 Observations . . . . . 51

4.4.1 Data decomposition and results . . . . . 53

4.4.2 Hilbert Spectra: Instantaneous frequency (IF) for the different $imfs$ . . . . . 69

4.4.3 Spectral analysis . . . . . 74

4.5 Analysis and Discussion . . . . . 86

4.6 Summary . . . . . 90

**5 Local Wave vector analysis** **91**

5.1 Introduction . . . . . 91

5.2 Instantaneous wave vector of low frequency waves in the turbulent magnetosheath . . . . . 93

5.2.1 $Imf$, and instantaneous frequency and wave vector estimation . 93

5.3 Observations and results . . . . . 95

5.4 Minimum Variance Analysis and shock normal . . . . . 101

5.5 Discussion . . . . . 110

5.6 Summary . . . . . 111

**6 Dispersion relations and propagation processes in magnetosheath** **112**

6.1 Introduction . . . . . 112

6.2 Dispersion analysis of downstream plasma waves . . . . . 113

6.3 Determination of instantaneous frequency and phase velocity in the plasma rest frame . . . . . 115

6.4 Dispersion curves . . . . . 121

6.5 Analysis and discussion . . . . . 133

6.6 Summary . . . . . 136

**7 Wave modes identification** **138**

7.1 Introduction . . . . . 138

7.2 Observations . . . . . 141

7.3 Results . . . . . 143

7.4 Analysis and Discussion . . . . . 154

7.4.1 Wave modes identification in zone A close to the magnetopause 154

7.4.2 Wave modes identification in zone B in the middle of magnetosheath 155

7.4.3 Wave modes identification in zone C close to the bow shock . . 157

7.5 Summary . . . . . 158

**8 Conclusion** **159**

8.1 Research summary . . . . . 159

8.2 Major findings . . . . . 161

8.3 Further work . . . . . 163

# List of Figures


2.1 Solar wind coupling with magnetosphere . . . . . 10

2.2 Cluster spacecraft observing solar-terrestrial environment . . . . . 10

2.3 Bow shock . . . . . 14

2.4 Shock foot, ramp and overshoot . . . . . 14

2.5 Perpendicular field lines . . . . . 16

2.6 Parallel field lines . . . . . 16

3.1 Cluster tetrahedral geometry . . . . . 26

3.2 Fluxgate magnetometer . . . . . 28

3.3 Cluster Ion Spectrometer . . . . . 29

3.4 Electric field and waves instrument . . . . . 31

4.1 Negative frequency filtering . . . . . 47

4.2 The plot of a simple periodic wave with frequency of 10 Hz and amplitude of 1 sampled at 1000 Hz. . . . . 54

4.3 Power spectral density for a signal of frequency of 10 Hz and amplitude of 1 sampled at 1000 Hz. . . . . 55

4.4 The plot of scales and frequencies. This plot shows that 81 on the scales axis correspond to 10 Hz on the frequency axis. . . . . 56

4.5 The scalogram for a signal with 10 Hz of frequency and amplitude of 1. 57

4.6 The application of empirical mode decomposition in the extraction of intrinsic mode function (imf) . . . . . 58

4.7 Hilbert spectrum for a signal of frequency of 10 Hz with an amplitude of 1 sampled at 1000Hz. . . . . 59

4.8 Inbound traversal of four Cluster spacecraft from the solar wind to magnetosheath . . . . . 63

4.9 Electric field profile . . . . . 64

4.10 Magnetic field profile . . . . . 65

4.11 Extrema and mean of envelope . . . . . 66

4.12 Extraction of imfs . . . . . 67

4.13 the imf that meets the conditions . . . . . 68

4.14 Hilbert spectra of instantaneous frequencies of the imfs . . . . . 70

4.15 Hilbert spectra of instantaneous frequencies of the imfs . . . . . 71

4.16 Hilbert spectra of instantaneous frequencies of the imfs . . . . . 72

4.17 Hilbert spectra of instantaneous frequencies of the imfs . . . . . 73

4.18 Spectral analysis of 1st imf . . . . . 74

4.19 Spectral analysis of 2nd imf . . . . . 75

4.20 Spectral analysis of 3rd imf . . . . . 75

4.21 Spectral analysis of 4th imf . . . . . 76

4.22 Spectral analysis of all imfs . . . . . 76

4.23 Scalogram of 1st imfs . . . . . 77

4.24 Scalogram of 2nd imfs . . . . . 78

4.25 Scalogram of 3rd imfs . . . . . 79

4.26 Scalogram of 4th imfs . . . . . 80

4.27 Scalogram of the original data . . . . . 81

4.28 Spectral analysis of the original data . . . . . 82

4.29 Hilbert spectra of instantaneous frequencies of 2nd and 3rd imfs . . . . 83

5.1 Magnetic field profile for magnetopause crossing to magnetosheath . . . 96

5.2 Magnetic field profile for observations in magnetosheath . . . . . 97

5.3 Tetrahedral geometry of Cluster at 04 55 30 UT . . . . . 98

5.4 Tetrahedral geometry of Cluster at 05 58 30 UT . . . . . 98

5.5 Tetrahedral geometry of Cluster at 05 37 30 UT . . . . . 98

5.6 Eigen vectors directions during bow shock traversal . . . . . 104

5.7 Side view of the maximum, intermediate and minimum variance . . . . 105

5.8 Instantaneous projection of wave vector along sat13 . . . . . 107

5.9 Instantaneous projection of wave vector along sat23 . . . . . 108

5.10 Instantaneous projection of wave vector along sat43 . . . . . 109

6.1 The average instantaneous frequency . . . . . 114

6.2 Comparison of the ion frequency with electron plasma frequency in solar wind . . . . . 117

6.3 Comparison of the ion frequency with electron plasma frequency in sheath 118

6.4 The f-ksep plot computed from data observed by Cluster FGM instrument in satellite frame . . . . . 124

6.5 The f-ksep plot computed from data observed by Cluster FGM instrument in satellite frame . . . . . 125

6.6 The f-ksep plot computed from data observed by Cluster FGM instrument in satellite frame . . . . . 126

6.7 The f-ksep plot computed from data observed by Cluster FGM instrument in plasma frame . . . . . 127

6.8 The f-ksep plot computed from data observed by Cluster FGM instrument in plasma frame . . . . . 128

6.9 The f-ksep plot computed from data observed by Cluster FGM instrument in plasma frame . . . . . 129

6.10 The dispersion at plasma frame using data from upstream of bow shock 130

6.11 The dispersion at plasma frame using data from upstream of bow shock 131

6.12 Magnetic field profile data observed by Cluster FGM instrument . . . . 132

7.1 Time series plot of magnetic field strength . . . . . 142

7.2 Plot of $(T_p \perp / T_p \parallel) - 1$ and $1/\beta$ in zone A . . . . . 144

7.3 Plot of $(T_p \perp / T_p \parallel) - 1$ and $1/\beta$ in zone B . . . . . 145

7.4 Plot of $(T_p \perp / T_p \parallel) - 1$ and $1/\beta$ in zone C . . . . . 146

7.5 Instantaneous phase velocities in the satellite frame and the plasma bulk velocities within zone A . . . . . 147

7.6 Instantaneous phase velocities in the satellite frame and the plasma bulk velocities within zone B . . . . . 148

7.7 Instantaneous phase velocities in the satellite frame and the plasma bulk velocities within zone C . . . . . 149

7.8 Histogram of the ratio of satellite frame phase velocities and Alfvén velocities in zone A . . . . . 150

7.9 Histogram of the ratio of satellite frame phase velocities and Alfvén velocities in zone B . . . . . 151

7.10 Histogram of the ratio of satellite frame phase velocities and Alfvén velocities in zone B . . . . . 152

7.11 Plasma beta $\beta$ for the three chosen zones A, B and C . . . . . 153

1 Elevation and contour along sat23 . . . . . 181

2 Elevation and contour along sat43 . . . . . 182

3 Elevation and contour along sat13 . . . . . 183

4 Instantaneous projection of wave vector as a function of time . . . . . 184

5 THEMIS probe . . . . . 197

6 THEMIS probe . . . . . 198

7 THEMIS probes in the near and far Earth . . . . . 198

8 Ground stations . . . . . 199

9 Fluxgate magnetometer on THEMIS . . . . . 200

10 THEMIS Probes in the dayside of Earth magnetosphere. . . . . 200

# List of Tables

1.1 Methods comparison summary . . . . . 6

4.1 Correlation coefficients, R between the magnetic and electric field of each Cluster spacecraft. . . . . 52

4.2 Relationship between the ratio of the relative energy character rate of each $imf$ to that of the original data and Power spectral density and continuous wavelet and the mean Hilbert spectra on each $imf$. . . . . 87

4.3 Correlation and coherency on the instantaneous frequencies of second and third $imfs$ extracted from a data of Figure 4.3. The instantaneous frequency space was divided into A, B and C zones. . . . . 89

5.1 Frequency and components of plasma bulk velocity . . . . . 100

5.2 Table of Eigen vectors of the four Cluster spacecraft . . . . . 103

5.3 Direction of maximum, intermediate and minimum variance . . . . . 103

7.1 Wave vector interpolated linearly and the angle of the wave's propagation direction to the magnetic field between 06:16 and 06:19 UT . . . . . 155

1 Angle between the projection of wave vector and separation line of spacecraft . . . . . 185

2 Components of wave vector along the separation of spacecraft . . . . . 186

3 Instantaneous frequency along each component and their error . . . . . 187

4 Instantaneous frequency along each component and their error . . . . . 188

5 The instantaneous ion gyro−frequency, ion frequency, electron gyro−frequency and electron plasma frequency . . . . . 189

6 Instantaneous frequency along each component and their plasma frames frequency . . . . . 190

7 Instantaneous frequency along each and their plasma frames frequency 191

8 Instantaneous wave vectors and wavelength of wave. . . . . 192

9 Instantaneous phase velocity computed from y−component of instantaneous frequency . . . . . 193

10 Instantaneous phase velocity at plasma frame computed from instantaneous frequency of y−component . . . . . 194

11 Angle in degrees between wave vector K and magnetic field B . . . . . 195

12 Angle in degrees between normal n and magnetic field B . . . . . 196

# Chapter 1

# Introduction

## 1.1 Introduction

This thesis deals with the non-linear behaviour of space plasma considered by using the observations of in-situ spacecraft mission in the region in space between the Earth and the Sun. It takes into consideration the techniques suitable for analysis which would give better physical understanding of events and processes taking place as the solar wind makes it's way to the Earth. From the study of the waves arising from the events on the upstream of the bow shock, there is a process of events leading to another regime of waves with turbulent or complex nature in the downstream region otherwise called the magnetosheath. The magnetosheath is a region of thermalized subsonic plasma behind the bow shock. It is an interface between the bow shock and the magnetopause. The plasma in the magnetosheath is denser and hotter than that in the solar wind and the magnetic field strength in the magentosheath is higher than the magnetic field strength in the solar wind. The position of the magnetopause depend on the equilibrium between the overall plasma pressure from the magnetosheath and the magnetic pressure from the

magnetosphere [Baumjohann and Treumann, 1996, Kivelson and Russell, 1995]. The magnetosheath has been a good predictor in the determination and prediction in the responses of the magnetosphere. The magnetosphere responses to the variations in the magnetosheath through reconnection at the magnetopause which aid transport mass, momentum, and energy into the magnetosphere, this changes the dynamics pressure of solar wind according to investigation by Parks *et al.* (1991).

Many analysts have chosen different techniques for the analysis of the resultant waves aimed at understanding these waves. To understand these waves, the knowledge of the frequencies and wave vectors of the waves, and determination of the dispersion relation are essential.

In Physics and other scientific analysis of time series, timescale and the corresponding energy distribution are two most important parameters of a signal. Most plasma analysis in space physics have been carried out with Fourier analysis (FA) or Wavelet analysis (WA). Detailed investigations of the dynamic properties of space plasma have been limited by the use of these standard methods. This limitation is due to the assumptions of linearity and stationary (FA) or linearity and non−stationary (WA) behaviour of the waves.

The truth is that space plasma data are observational data that exhibit unsteady character (non−linear) in oscillations throughout the data. Therefore, the use of the standard spectral methods limits the possibilities of investigating the details of the dynamics of such data.

In order to investigate the details of the dynamics of space plasma, there is need for an approach that is based upon the local characteristic time scale of signal. There is also need for an approach which will help to construct the time evolutions of the signal.

We applied the combination of empirical mode decomposition (EMD) method and Hilbert transform (HT) to investigate the details of space plasma behaviour. This combination helps to analyse both non−linear and non−stationary signals. It also analyses linear and stationary behaviour of the signal.

## 1.2 Comparison of Fourier analysis (FA), Wavelet analysis (WA) and EMD−HT combination technique

Fourier analysis (FA) is a kind of global transform that is most suitable for linear and stationary signals. It provides a general method for examination of the global energy−frequency distributions [Huang et al., 1998]. The stationary assumption of FA is a general one for most of the available data analysis methods. It therefore becomes necessary to look for an approach that will also consider non−stationary signals.

Other than stationary, Huang *et al.*, (1998) has further revealed the dependence of Fourier analysis on linearity. It is true that many natural events can be approximated by linear systems. It is also true that they also have the tendency to be non−linear whenever their variations become finite in amplitude. The imperfection of our probes (or numerical schemes) can lead to non−linear behaviour when there is interaction between the imperfect probes and the linear system.

Observational data are usually of finite duration, non−stationary and from systems that are frequently non−linear either intrinsically or through interactions with the imperfect probes or numerical schemes [Huang et al., 1998]. According to Huang *et al.*, (1998), a lack of alternative method has allowed the application of Fourier

transform to decompose such data. The use of Fourier transforms and the assumptions of linearity and stationarity may give misleading results when applied to space plasma data. Therefore, there is need for approaches that can consider both non−stationary and non−linear behaviours.

Wavelet analysis (WA) is an adjustable window Fourier spectral analysis. WA can supply localised information in time−frequency domain, as it possesses the multi−scale character and mathematical microscope effect that makes it to be capable to detect the sudden component of the signals [Cheng and Yu, 2006]. WA is a better approach than Fourier analysis in the analysis of non−stationary signals.

WA is an approach that involves the scale, a and translation, b parameters. WA is the energy of data of scale, a at time, $t = b$. Because of this basic form of at + b involved in the transformation, WA is also called affine wavelet analysis. Continuous or discrete wavelet analysis is a linear analysis [Huang et al., 1998]. WA is very useful in analysing data with gradual frequency changes.

Since WA is an adjustable window Fourier spectral analysis, the limited window length leads to leakage [Huang et al., 1998]. According to Huang *et al.*, (1998), this makes the quantitative definition of the energy−frequency−time distribution difficult. Such a problem associated with wavelet analysis occurs, for instance, if a change occurring locally is to be defined, it is required that the results are looked for in the high−frequency range. This implies that the higher the frequency, the more localised the basic wavelet will be (see scalogram in Chapter 4). Also for a local event occurring only in the low−frequency range, it is still required that the result be sought for in the high−frequency range.

Although WA remains the best available approach for non−stationary data analysis, it can only give a physically meaningful interpretation to linear events according to

Huang *et al.*, (1998). There is need for approach that will consider the non−linear and non−stationary behaviour of such observational data.

EMD method generates a collection of intrinsic mode functions (imf). The decomposition is based on the direct extraction of the energy associated with various intrinsic timescales. This is the most desirable parameter of the signal. The extracted imfs have well−behaved Hilbert transforms, and therefore the instantaneous frequencies can be computed.

It is possible to localise any event on the time as well as the frequency axis. According to Huang *et al.*, (1998), the decomposition can be viewed as an expansion of the data in terms of the imfs. The imfs can serve as the basis of the expansion which approximates a linear or non−linear behaviour as dictated by the data.

After the extraction of imfs using EMD, the simple Hilbert transform (SHT) approach used in instantaneous local wave vector (ILW) estimation method [Carozzi et al., 2004] can be applied on each imf. The local energy and the instantaneous frequency derived from each imf through Hilbert transform can give a full energy−frequency−time distribution of the data.

See Table 1.1 below for the comparison between empirical mode decomposition (EMD)−Hilbert transform (HT) approach, Fourier and Wavelet analysis. Various qualities have been considered for this comparison between the second and the last rows. This table gives at a glance that the EMD−HT approach is robust for the non−linear and non−stationary signal analysis.

In the analysis of space plasma data collected within the magnetosheath, the existence of some remarkable difference between the upstream and the downstream shows possibilities of more waves generation. This could be due to instabilities arising from

| Method | EMD−HT | Fourier | Wavelet |
|---|---|---|---|
| Basis | Adaptive | Non−adaptive | Non−adaptive |
| Frequency | Differentiation:Local | Convolution:Global | Convolution:Regional |
| Presentation | Energy-time-frequency | Energy-frequency | Energy-time-frequency |
| Non-linearity | Yes | No | No |
| Non -stationarity | Yes | No | Yes |
| Feature Extraction | Yes | No | Discrete: No, Continuous: Yes |
| linearity | yes | yes | yes |
| stationarity | yes | yes | yes |

Table 1.1: Methods comparison summary. This table gives the comparison of the Fourier spectral analysis, Wavelet analysis and EMD−HT analysis at a glance.

upstream of bow shock or within the magnetosheath.

The study of waves and optics in Physics has given the understanding of the effect of many waves coming together to form a wave field or wave packet. The common aspect of such study shows that two or more waves can superimpose constructively or destructively. The sudden high magnetic field data in the magnetosheath displays such possibility of superposition of waves.

In our analysis, we treat each overriding wave as imf. Therefore, we apply EMD-HT to extract the constituent waves (using EMD) and construct the time evolution of the waves (using HT). This is the motivation for the application of this technique in this thesis.

The results we have obtained by applying the combination of EMD and Hilbert spectral analysis have given new insight to the time evolutions of events as dictated by the data. The results such as the dispersion curves of waves are different from the standard pattern obtained using standard spectral analysis methods. Our data for the analysis in this thesis are drawn from observations from Cluster II spacecraft mission.

In the chapters that follow, chapter two deals with the overview of the study in this

thesis, chapter three considers the instrumentations relevant to this thesis, chapter four addresses the analysis of low frequency wave in the magnetosheath based on the HHT technique, chapter five focuses on local wave vector analysis, chapter six discusses the dispersion relations and propagation processes in magnetosheath, chapter seven is aimed at identifying the various wave mode within the magnetosheath, chapter eight sums up all results and summaries in this thesis. This chapter offers the necessary things to be done as extension and improvement to this work.

# Chapter 2

# Background study

## 2.1 Overview of Solar-terrestrial coupling

### 2.1.1 What is plasma?

Plasma is a collection of charged particles, which show some kind of collective behaviour having about the same number of charges with different signs (making plasma to be quasineutral in stationary state) in the same volume element [Parks, 1991, Baumjohann and Treumann, 1996]. But not every collection of charged particles qualifies as a plasma according to Parks (1991). Baumjohann and Treumann further give a statistics of all known visible matter to 99% in plasma state. According to Parks (1991), a more complex plasma system includes neutral atoms and molecules. It is also mentioned that the density of the particles in a plasma is required to be sufficiently low so that the short−range binary collisions are negligible. But long−range electromagnetic forces dominate.

In addition to the quasineutrality of plasma, the collective effect of particles is valid as

a plasma criterion when the number of charge carriers within the sphere of influence called the Debye sphere with radius known as Debye screening length [Baumjohann and Treumann, 1996]. This defines the shielding criterion for a plasma.The macroscopic properties of a plasma (e.g. density) may vary from place to place. The plasma can be divided up into a set of volume elements whose dimensions are small compared to typical length scales, say L, of variations of macroscopic plasma properties (e.g density gradient) but still large compared to particle sizes. It is a good idea to work with fluid volume elements which are each quasineutral, so that we can be sure that the plasma as a whole is quasineutral in steady state. This means that we want a fluid volume element which is big enough so that any charge concentrations that may arise will be safely shielded within the fluid volume element. Quasineutrality criterion for a plasma can be written as: $\lambda_D \ll L$, where $\lambda_D$ is the Debye screening length.

From the quasineutrality condition of plasma and the shielding effect, it is necessary that the sphere contains enough particles. According to Baumjohann *et al.* (1996), the number of particles inside a Debye sphere is $(4\pi/3)n_e\lambda_D^3$. Where the term $n_e\lambda_D^3$ is called plasma parameter. This parameter for plasma is much greater than 1. For collective of particles to be considered as plasma, the electron plasma frequency, which measures plasma oscillations of the electrons, must be large compared to the electron$-$neutral collision frequency that measures frequency of collisions between electrons and neutral particles.

A Plasma is a highly thermalized and ionized gas [Kivelson and Russell, 1995, Parks, 1991, Baumjohann and Treumann, 1996]. This state of high temperature makes atoms dissociate into electrons and ions. The solar wind is a perturbed magnetized plasma flow of ions and electrons. The expansion of the coronal plasma leads to the supersonic flow, which flows across planetary obstacles, moons, comets etc. as solar-wind. Those planetary obstacles with intrinsic magnetic field like the Earth are

enhanced by this magnetic field, which is confined by the solar wind into a region known as magnetosphere. The outer boundary of this magnetosphere, which separates it from the solar-wind is referred to as the magnetopause. The size of this magnetopause depends on the pressure balance involving the planetary magnetic field and solar wind plasma pressure. The solar wind pressure further causes the shape of the magnetosphere to be asymmetric, compressed on the sunward side, and stretched into elongated shape called the magnetotail on the nightside.

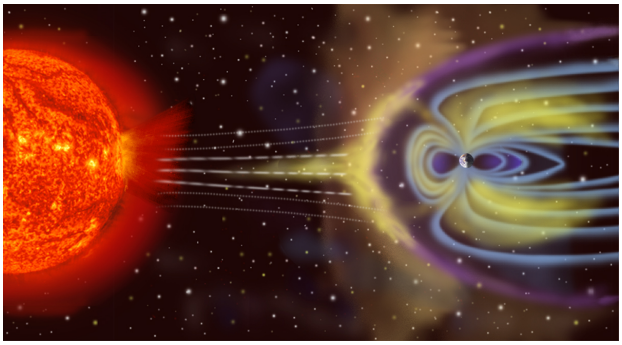

Figure 2.1: Artistic view of Solar-terrestrial coupling showing lines taken by flowing solar wind particles towards and around magnetosphere of planetary object (`http://xeus.esa.int/science-e/www/object/index.cfm?fobjectid=33024&fbodylongid=1116`)

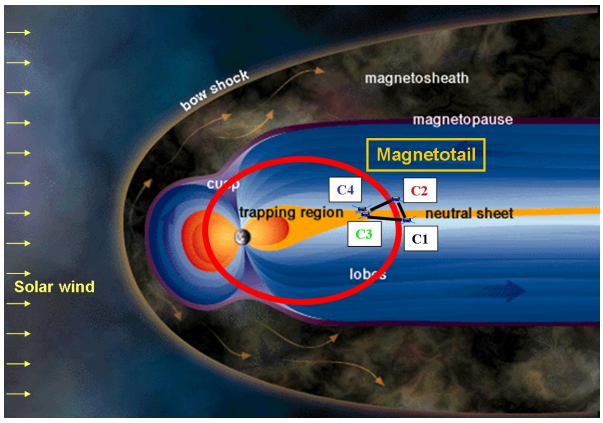


Figure 2.2: Artistic impression of Cluster four spacecraft observing solar-terrestrial environment (`http://clusterlaunch.esa.int/science-e/www/object/index.cfm?fobjectid=36559`)

The solar-terrestrial environment provides us with a natural laboratory for investigating the properties of space plasmas. Spacecraft missions provide us with in situ observations to test theory and enhance our understanding of the terrestrial environment, as well as astrophysical objects elsewhere. Thus, analysis of the data returned from various spacecraft missions data has provided insight into phenomena such as magnetospheric substorms and the aurora, as well as the physical processes underlying them.

### 2.1.2 Plasma waves

Plasma supports a broad variety of waves, which are classified in terms of the frequency and propagation properties of the k-vector with respect to the electric field, E. When the frequency of wave is less than the ion gyro−frequency, then the wave is termed low-frequency wave. Plasma waves are involved in wave-particle interactions. For instance, a zero mean, stationary and homogenous field S($\mathbf{r}$,t) with amplitude A, which is a function of time (t) and space ($\mathbf{r}$) can be approximated by a sine function.

$$S(r,t) = Asin(k\mathbf{r} - wt) \tag{2.1}$$

The time derivative of a phase of a wave is defined as the frequency, $\omega$ of a wave. The frequency, w is

$$\frac{\partial(k.\mathbf{r} - wt)}{\partial t} \tag{2.2}$$

The spatial derivative of a phase of a wave is defined as the wave vector, k. the wave vector, k is

$$\frac{\partial(k.\mathbf{r} - wt)}{\partial \mathbf{r}} \tag{2.3}$$

The total time derivative of the phase, having been set to zero can allow the deduction of the phase velocity.

$$\frac{\partial(k.\mathbf{r} - wt)}{\partial t} = 0; \tag{2.4}$$

$$k.\mathbf{r} - wt = 0, \frac{w}{k} = \frac{\mathbf{r}}{t} = V_{ph} \tag{2.5}$$

Vectorially, $V_{ph}$ is given as

$$V_{ph} = \frac{w}{\mid k \mid^2}\mathbf{k} \tag{2.6}$$

This velocity defines the propagation speed of the wave surface, or the surface of constant phase. When there is a superposition of plane waves [Balikhin and Walker,

2005], each of the contributive waves in the packet may travel at different phase velocities [Kivelson and Russell, 1995, Parks, 1991, Baumjohann and Treumann, 1996]. The characteristics of the downstream plasma flow can be easily determined from upstream plasma flow if the upstream parameters such as Mach number, plasma beta, velocity, temperature, pressure are known. The orientation of the interplanetary magnetic field (IMF) with respect to the bow shock normal (see below for shock normal) plays a role in the plasma density, magnetic field fluctuations and their distribution within the magnetosheath [Shevyrev et al., 2007].

The Plasma beta $\beta$ is the ratio of solar wind thermal pressure, $p_{th}$ to magnetic (field) pressure, $p_m$ .

$$p_m = \frac{B^2}{2\mu_0} \tag{2.7}$$

Where, $B$ is the magnetic field strength, $\mu_0$ is the permeability of free space or magnetic constant.

Therefore,

$$\beta = \frac{p_{th}}{p_m} = \frac{p_{th}}{\frac{B^2}{2\mu_0}} \tag{2.8}$$

For,

$\beta \ll 1$, the plasma is termed low-beta

$\beta \geq 1$,the plasma is termed high-beta

both these types of plasmas are found in space [Parks, 1991].

## 2.2 Shocks

Shocks are formed when supersonic flow interract with obstacles [Kivelson and Russell, 1995].

### 2.2.1 Types of Shocks

There are two major types of shock defined by the means of their generation. There are collisionless and collisional shocks [Parks, 1991, Baumjohann and Treumann, 1996].

1. *Collisionless shocks*:

   Collisionless shocks are shocks formed by the interaction of particles and waves. They are generated during high eruptions on the sun known as solar flares, and also by supernovae, stellar explosions that are believed to be a source of cosmic rays (high energy particles raining down from all directions into the heliosphere onto the earth) [Parks, 1991, Kivelson and Russell, 1995, Baumjohann and Treumann, 1996]. Collisionless shocks enable the acceleration of a small fraction of the particles to very high energies [Russell, 2005] with high temperatures, and eventual decrease in the velocity it hits these obstacles. Collisionless shocks play a very serious role in the processes of space weather, in the control of the dynamics and energisation of the terrestrial magnetosphere, and the energisation of the radiation belts [Russell, 2005] where most spacecraft operate. As the flows temperature is increased due to the heating of the solar-wind plasma, there is an associated increase in the bulk velocity by the shock. The magnetic field strengths are enhanced and these all lead to the wide range of phenomena, such as heating and compression of the plasma [Horbury et al., 2002] and the reference therein), and an increase in the general level of turbulence [Russell, 2005]. The changed properties of flow, can in turn give new properties to the magnetosphere as the magnetic field and plasma are affected (changed). The major processes manifesting in collisionless shocks are the plasma waves [Balikhin and Walker, 2005]. Example of collisionless shock is the bow shock.

- *Bow shock*:

  As the solar-wind gets in contact with obstacle like the Earth, due to the supersonic flow, an analogous process of a supersonic jet travelling through air setting pressure waves due to collisions, takes place due to electromagnetic field then setting a collisionless shock wave ahead of the magnetosphere, which is called the bow shock. This derives its name from bow pattern as caused by the obstacle like the Earth. The bow shock has a thickness of only $100 - 1000km$ [Kivelson and Russell, 1995] that is relatively smaller compared with the mean free path of solar wind plasma. The collisionless refers to the fact that the solar-wind density,$\rho$ is low, about $\rho =$ small value X $10^6/m^3$, where the mean-free path is large, of the order 1AU ($1.5X10^8$km) [Parks, 1991, Kivelson and Russell, 1995].

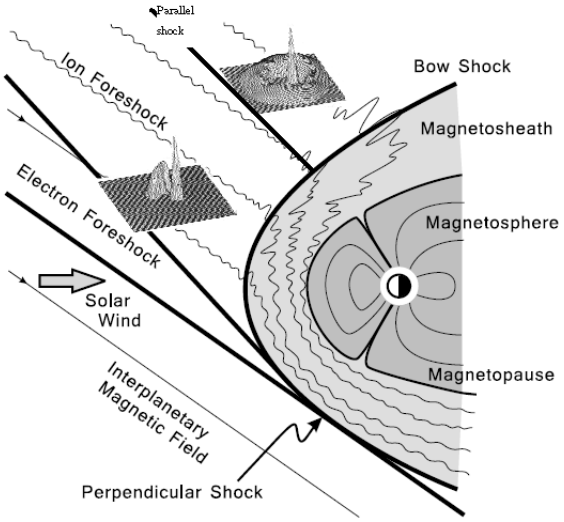


Figure 2.3: A diagram of Planetary object (Earth) environment
[Baumjohann and Treumann, 1996]

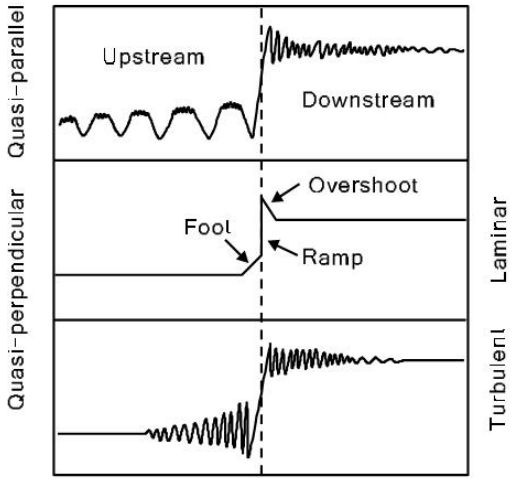


Figure 2.4:
Field line showing the shock foot, ramp and shock overshoot
[Baumjohann and Treumann, 1996]

Upstream of the terrestrial bow shock, the angle the magnetic field makes with the shock normal determines the type of shock. This angle defines the parallel shock, perpendicular shock, quasi- parallel and quasi- perpendicular

shocks. *Perpendicular shock*: The perpendicular shock is formed when the upstream magnetic field forms an angle equals to $90^0$ with the shock normal. This is based on fast magnetosonic upstream waves. Across the shock, magnetic field varies.

*Quasi-perpendicular shock*: This is formed when the magnetic field upstream forms an angle less than $90^0$ but greater than $45^0$ with the shock normal. This shock has a sharp ramp which links the upstream and the downstream of the shock. The quasi-perpendicular shock has a shock foot in front of the shock [Narita et al., 2006]. A shock ramp starts at the shock foot and ends at the shock overshoot, which is a sharp fall of magnetic field downstream of the shock before settling to the average field. The ramp helps in completing the transition from the upstream to the downstream. Frequency of range 1 and over $14Hz$ are associated with the highly coherent waves in the upstream of the ramp of supercritical quasi-perpendicular shocks [Balikhin et al., 1997, Fairfield, 1974].

*Parallel shock*: The parallel shock is formed when the upstream magnetic field is parallel to the shock normal. The angle between the shock normal and the upstream magnetic field is zero. Across the shock, the normal component of magnetic field is constant (unchanged). There is only compression in the plasma but not in the magnetic field [Baumjohann and Treumann, 1996].

*Quasi-parallel shock*: The quasi-parallel shock is formed when the upstream magnetic field forms a small angle with the shock normal. This angle between the shock normal and the upstream magnetic field is less than $45^0$. The quasi-parallel shock is highly fluctuating towards the shock and forms the foreshock. The quasi-parallel shock plays a role in making the reflected ions escape into the foreshock through the field lines from the shock [Baumjohann and Treumann, 1996].

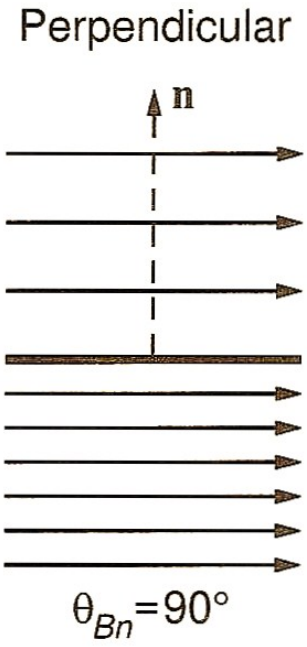


Figure 2.5: Perpendicular field lines and normal
[Baumjohann and Treumann, 1996]

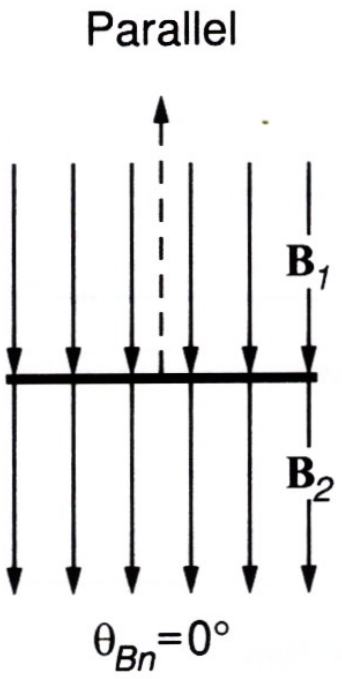


Figure 2.6: Parallel field lines and normal
[Baumjohann and Treumann, 1996]

*Oblique shocks*: These are formed when the upstream magnetic field is between the parallel and perpendicular shocks at angle greater than zero and less than $90^0$ with the shock normal [Baumjohann and Treumann, 1996]. The understanding of the low frequency in the range of 0.5-4.0$Hz$ was investigated [Fairfield, 1974]. Fairfield gave a result of obliquely whistler mode propagation [Balikhin et al., 2003] whose Doppler shifting affected the observed frequency of the waves, their polarization and their spectral densities, and that these waves were generated at the bow shock. These waves have been suggested to be damped in the shock foot and unlikely to reach foreshock where they are observed. These waves are right-handed waves in the plasma rest frame [Fairfield, 1974, Balikhin et al., 2003] and

are generated by cold beam [Narita et al., 2006]. Balikhin (2003) alongside other analysts reported that the early work and result of Fairfield was correct. Upstream whistlers have been observed in other planets like Venus, Mercury, Saturn as well as Earth and its a prominent phenomenon in the collisionless shock. At low frequencies, these right handed whistler waves become the fast magnetosonic wave [Gary, 1986, Narita et al., 2006].

2. *Collisional shocks*:

   Unlike the collisionless shocks, the collisional shocks require particle to particle [Parks, 1991] of collisions. The example of collisional shocks are ordinary gas-dynamic shocks e.g. a supersonic jet in the air. Collisional shocks serve to transfer energy and momentum among particles [Kivelson and Russell, 1995] and the energy and momentum are eventually transformed to sound and heat energies.

### 2.2.2 Properties of shock

For known upstream variables of fluid, the downstream variables can be determined for defined continuity of quantities such as mass, momentum and energy across shocks with assumed adiabatic equation of state. A set of relations between the upstream and downstream variables defining this continuity are called Rankine-Hugoniot relations[Baumjohann and Treumann, 1996, Parks, 1991]. This has been based on shocks from ordinary fluid or collisional gas. But in collisionless plasma, the set of relations defining continuity between the upstream and the downstream as in the collisional gas fail to give particular form for the dependence of the downstream on the upstream since energy conservation offers information about the total pressure only [Kivelson and Russell, 1995]. Therefore, it is important to know the shock properties.

- *Shock strength*: The ratio of the pressure on the downstream, $p_2$ to the pressure on the upstream, $p_1$ measures the strength of the shock.

$$\zeta = \frac{p_2}{p_1} \tag{2.9}$$

- *Compression ratio*: The ratio of the density on the downstream,$\rho_2$ to the density on the upstream, $\rho_1$ defines compression ratio of the shock.

$$\eta = \frac{\rho_2}{\rho_1} \tag{2.10}$$

The compression ratio of shock relates to the flow speed, $u$ in a reverse way,

$$\eta = \frac{u_1}{u_2} \tag{2.11}$$

*Mach number, M*: This is the ratio of the flow speed $u$ to the speed of sound, $c$ on either side of the shock. For the upstream with flow speed $u_1$,

$$M = \frac{u_1}{c_1} \tag{2.12}$$

When the ratio, $M$ is large, shock is strong [Parks, 1991].

For the downstream with flow speed $u_2$,

$$M = \frac{u_2}{c_2} \tag{2.13}$$

When the plasma velocity exceeds the magnetosonic speed, a shock is formed.

## 2.3 Solar wind and instabilities

The ions and electrons have different masses, with the ions moving with a greater mass. This difference in mass allows the ions and electron to flow with different gyro-radius and frequency [Parks, 1991, Kivelson and Russell, 1995, Baumjohann and Treumann, 1996]. The disparity in the gyro-radii makes the depth of penetration of these particles to be different at the shock. Ion with a greater mass makes a deeper penetration than the electrons. An electric field called the charge separation electric field is generated due to this difference in the penetration depth, which reflects a number of ions back to the upstream region, while electrons are attracted and captured. This reflection of the ions plays a vital role due to the mass, momentum and energy it carries, for shock transition process. This reflected ions flow against the incoming upstream flow and sets up ion beam instabilities. These ions beam instabilities set up a large amplitude wave in the upstream flow, which convects the reflected beams together to the shock with a larger upstream flow speed. The eventual shock is as a result of the steepened upstream flow [Schwartz and Burgess, 1991]. Parallel to the magnetic field, the instability has maximum growth rate. Generally, all the ion species in the plasma contribute to their respective cyclotron instability [Narita et al., 2006]. Upstream waves become enhanced at the largest quasi-parallel interplanetary shocks [Kennel et al., 1986] and enhances the rate of acceleration at quasi-parallel shock.

### 2.3.1 Instabilities associated with magnetosheath; the downstream of terrestrial bow shock

In between the magnetopause and the bow shock, where the solar-wind properties are shocked (changed) lies the magnetosheath. Here the plasma is thermalized and

the particles energized. Magnetosheath is a high plasma beta region in space. The properties of the shocked plasma, the magnetosheath is determined by the reflection of the flow due to both quasi-perpendicular and quasi-parallel shocks in the upstream with patchwork of dense warm due to quasi-perpendicular shock and less warm due to quasi-parallel shock [Gosling et al., 1989, Thomsen et al., 1988b, 1990a, Schwartz and Burgess, 1991, Schwartz et al., 1996], and the level of magnetosheath turbulence depends on whether the shock is a quasi parallel or quasi perpendicular. This is a region influenced by instabilities generated at both the bow shock and the magnetopause, and returns a complex and inhomogenous magnetosheath. High turbulent magnetosheath plasma is seen with flows through quasi-parallel shocks than flows through quasi-perpendicular shocks [Narita et al., 2006]. But instabilities arising in the upstream region make the downstream waves more complicated. Low-frequency waves of $0.3Hz$ ion cyclotron frequency ($f_{ci}$) have been identified as kinetic Alfvén waves and range of $(0.3-10)Hz$, a wave between the ion gyro-frequency and lower hybrid frequency reported as dispersive Alfvén waves at the magnetopause [Stasiewicz et al., 2004]. Many sources of the downstream waves have been reported [Chang et al., 2000, Sahraoui et al., 2004, Schafer et al., 2005]. The turbulent nature of the magnetosheath has been associated with a number of sources, such as intrinsic solar wind turbulence processed through bow shock; from foreshock of the quasi-parallel shock, which forms as the ions are reflected back to the incoming upstream flow; which eventually are convected with the solar wind across the shock into the magnetosheath; a possibility of internally generated waves at the bow shock and temperature anisotropy. Temperature anisotropy has been found to affect the growth of the various wave modes encountered in the magnetosheath [Schafer et al., 2005], likewise the different plasma beta $\beta$ values [Denton, 2000]. One of the main causes of temperature anisotropy is linked to the ion beams which are reflected at the quasi-perpendicular bow shock that are convected downstream into the magnetosheath due to the gyration around the magnetic field [Sckopke et al., 1990]. Another cause

of temperature anisotropy is linked to the extension and compression of magnetic field adjacent to the magnetosphere [Crooker and Siscoe, 1977, Schafer et al., 2005].

### 2.3.2 Ion cyclotron instability

This instability is associated with high temperature ($T_\perp$ is large) and low plasma beta ($\beta$ is low), where a transverse electromagnetic ion cyclotron waves at frequencies lower than ion gyro-frequency with left-handed polarization is generated [Gary, 1986, Anderson et al., 1991, Gary et al., 1994a,b, Gary and Lee, 1994c]. This instability is called electromagnetic ion cyclotron instability. The proton and helium are the species responsible for the instabilities in the magnetosheath, called proton and helium instabilities [Gary et al., 1994b]. Behind the bow shock, the magnetosheath plasma exhibits a higher mean density and magnetic field strength as defined by Rankine-Hugoniot relations for a bow shock [Baumjohann and Treumann, 1996, Narita et al., 2006].

## 2.4 Turbulence in Space

A statistical approach is suitable for the treatment of any quantitative analysis since turbulence has a chaotic behaviour [Parks, 1991, Narita et al., 2006]. Turbulence applies in many ways and uses nomenclature according to the environment.

### 2.4.1 Types of turbulence

Two major types of turbulence have been selected for description, namely: *Hydrodynamics turbulence or fluid dynamics turbulence.*

Turbulent flows like waterfalls, smokes exhibit in nature irregular pattern accompanied by eddies on different scales [Parks, 1991, Narita et al., 2006]. Down the turbulent flow, turbulence leads to less fluctuations or Laminar [Parks, 1991]. In fluid dynamics, the dynamics is determined by a parameter called the Reynolds number, $R$ [Parks, 1991, Narita et al., 2006] given as

$$R = \frac{LV}{v} \tag{2.14}$$

$L, V, v$ are the scale length and velocity of flow, and the kinetic velocity respectively. The Reynolds number, $R$ is a control parameter which determines turbulence (high or low) and laminar flow (streamlined flow e.g. viscous flow like honey) [Parks, 1991]. Turbulence is characterized with high R, Laminar with low R.

*Magneto-hydrodynamic turbulence or magnetic field on fluid turbulence.*

Plasma turbulence is approximated by a magnetohydro-dynamic (MHD) model and is a wave observed at the same frequency with different propagation direction [Narita, 2006]. Various analyses from a quasi-parallel to quasi-perpendicular shocks have shown a source of instabilities that characterize the turbulent state of the magnetosheath. Also, the result of many investigations (such as [Hubert, 1994, Schafer et al., 2005]) have shown two major low frequency waves that are reported to originate from the two bounding regions of the magnetosheath; the bow shock and the magnetopause. The general understanding of plasma turbulence settles in the composition of turbulence and statistical analysis from data of linear growth (damping) rate for each observed spatial component (linear), and the estimation of the strength of multi-wave interaction (non-linear) such as three wave process (decay instability), four wave process (modulational instability), and processes in turbulence. According to Narita (2006), material is mostly ionized in space physics and strong turbulence is a widespread phenomenon associated with it. Waves, instabilities, and turbulence are complementary to one another. Turbulent flows or magnetic fields may be regarded as superposed waves,

while instabilities can cause a transition from a smooth flow to turbulent motions.

## 2.5 Summary

In this Chapter, we have reviewed the works done and the assertions made by other analysts in the context of solar-terrestrial interaction. This has been followed by the introduction of the different useful terms related to space plasma and their formula that are applicable in the subsequent chapters. For instance, this review has stated that turbulent flows such as those obtained in the magnetosheath may be regarded as superposed waves. This support our choice of technique that considers signals as aggregates of many component signals with different timescales.

# Chapter 3

# Instrumentations

## 3.1 Introduction

In this Chapter, we have considered the instruments of Cluster II, which have provided observational data for this thesis.

## 3.2 The Cluster mission instruments

Before the advent of Cluster mission, earlier study has been limited to obtaining data at the same temporal scale from one, or at most two spacecraft. The results of analysis of such observations have always given a one-dimensional interpretation. With Cluster mission [Escoubet et al., 2001], however, the view is different as Cluster offers multi-point measurements with high time resolution and identical state-of-the-art instrumentation on all of the satellites. Cluster was launched after a reconstruction by two Soyuz rockets from Russian Cosmodrome in Baikonur through two separate launches on 16 July and 9 August, 2000.

Cluster consists of four spacecraft in tetrahedral formation with inter-spacecraft separation that keep changing as they move around their orbits. It is designed to study small to large scale structures and fluctuations in $3D$ in regions such as the solar wind, the bow shock, the magnetopause, the polar cusps, the magnetotail, and the auroral zones. It has a polar orbit with a perigee about $4R_e$ and an apogee about $20R_e$. Each Cluster spacecraft carries the same set of eleven instruments and each instrument is under the leadership of a principal Investigator (PI). Wave Experiment Consortium is formed from five of the Cluster instruments (DWP, EFW, STAFF, WBD, and WHISPER), which are designed to measure electric and magnetic fields and waves. These instruments are (`http://xeus.esa.int/science-e/www/object/index.cfm?fobjectid=33024&fbodylongid=1116`):

- ASPOC (Spacecraft potential control)
- CIS (Ion composition)
- EDI (Plasma drift velocity)
- FGM (Magnetometer)
- PEACE (Electrons)
- RAPID (High energy electrons and ions)
- DWP (Wave processor)
- EFW (Electric field and waves)
- STAFF (Magnetic and electric fluctuations)
- WBD (Electric field and wave forms.)
- and WHISPER (Electron density and waves)

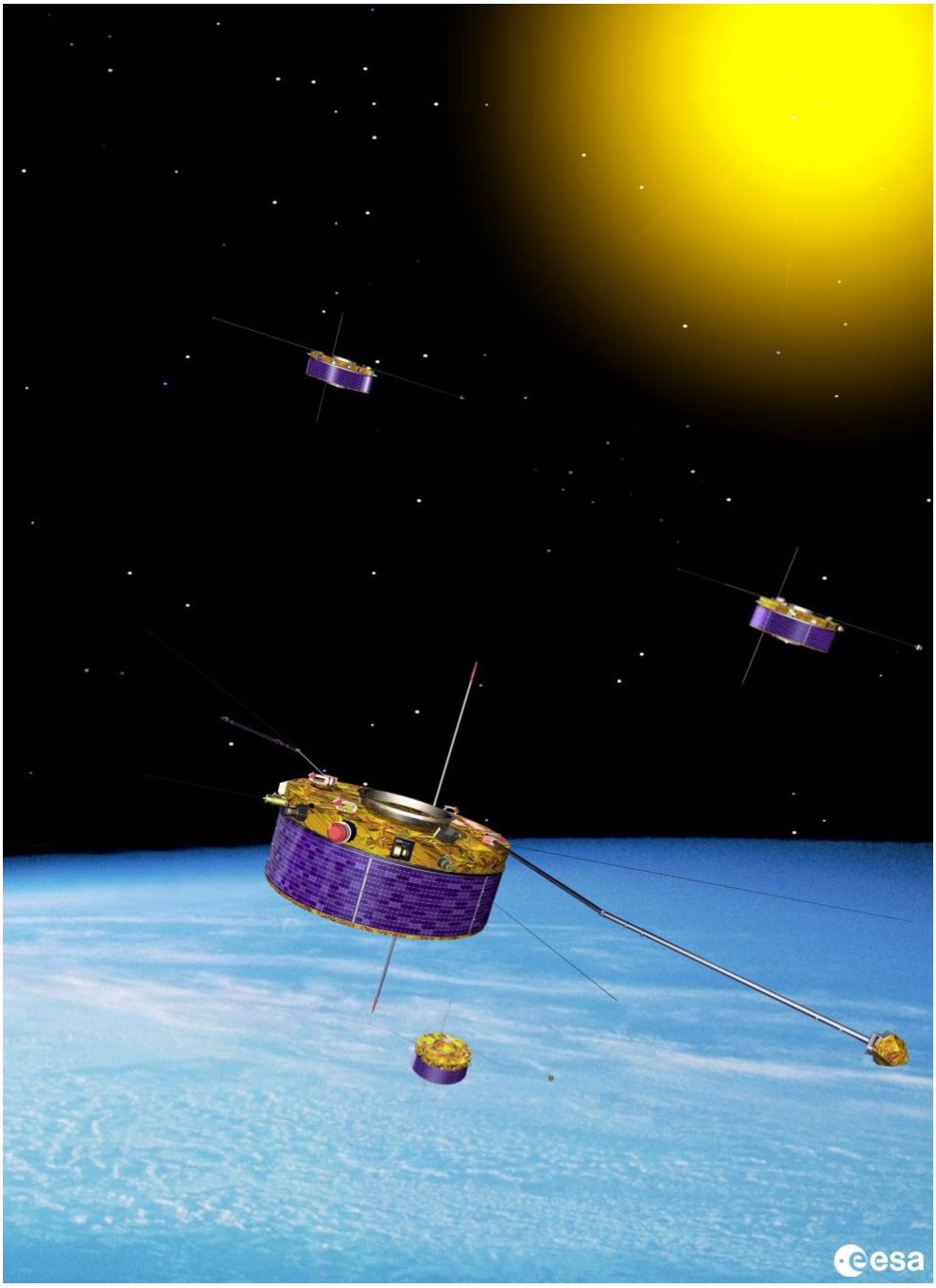


Figure 3.1: A tetrahedron formed by four spacecraft of Cluster (`http://xeus.esa.int/science-e/www/object/index.cfm?fobjectid=33024&fbodylongid=1116`).

.

### 3.2.1 FGM

FGM (Fluxgate Magnetometer) [Balogh et al., 1997, 2001, Narita, 2006, Paschmann and Daly, July 2000] is one kind of magnetic field sensor which combines good sensitivity with relative ease of construction. The basic principle is to compare the drive-coil current needed to saturate the core in one direction as opposed to the opposite direction, and the difference is due to the external magnetic field. The primary winding of the transformer is excited by high-frequency current. The permeability of the core and the strength of the current are chosen so that the core is driven into saturation on each half cycle of excitation. The secondary winding detects a time-varying voltage that is related to the input through the hysteresis curve of the core material. For high-permeability materials, this curve is nonlinear and the output signal is highly distorted, containing harmonics of the input signal. FGM on each Cluster spacecraft consists of two tri-axial fluxgate magnetic field sensors (see figure below) on one of the two radial booms of the spacecraft, and an electronics unit on the main equipment platform. The instrument is designed to be highly failure-tolerant through a full redundancy of all its functions. Either of the two magnetometer sensors can be used as the primary sensor for the main data stream from the instrument. In normal operations the outboard sensor located at the end of the $5m$ radial boom is designated as the primary source of the data. The magnetometers can measure the three components of the field in seven ranges from $64nT$ (smallest) to $65536nT$ (largest). The sampling of vectors from the magnetometer sensor designated as the primary sensor is carried out at the rate of 201.793 vectors/s. This internal sampling rate has been selected to provide an appropriate set of lower rates after filtering for the different telemetry modes and to give the highest frequency response for the short periods of interest. The main operational

modes of the FGM instrument provide the sampling rate from 15.52 vectors/s (normal mode) to 67.25 vectors/s (burst mode). The clock signal used for it is derived from a 223 Hz ($\sim 8MHz$) crystal oscillator internal to the instrument.

Figure 3.2: A picture of a fluxgate magnetometer (`http://xeus.esa.int/science-e/www/object/index.cfm?fobjectid=33024&fbodylongid=1116`
).

### 3.2.2 CIS

The ion data are used for the calculation of the correlations and coherences with the magnetic field fluctuations and plasma bulk velocities, and other investigations. CIS (Cluster Ion Spectrometry) [Réme et al., 2001, Narita, 2006] measures both the cold and hot ions of Maxwellian and non-Maxwellian populations (e.g. beams) from various plasma regimes such as the solar wind, the magnetosheath, the magnetosphere, and the ionosphere. CIS is designed to achieve following features:

- High sensitivity, large dynamic range, and high time resolution
- High angular sampling resolution to detect ion beams and solar wind directions
- Separation of the major ion species from the solar wind to the ionosphere $(H+, He++, He+ and O+)$
- A uniform coverage of ions over the entire steroidal solid angle with good angular resolution
- Wide range of energies up to about $40 keV/e$

. This instrument consists of two different instruments: HIA (Hot Ion Analyzer)

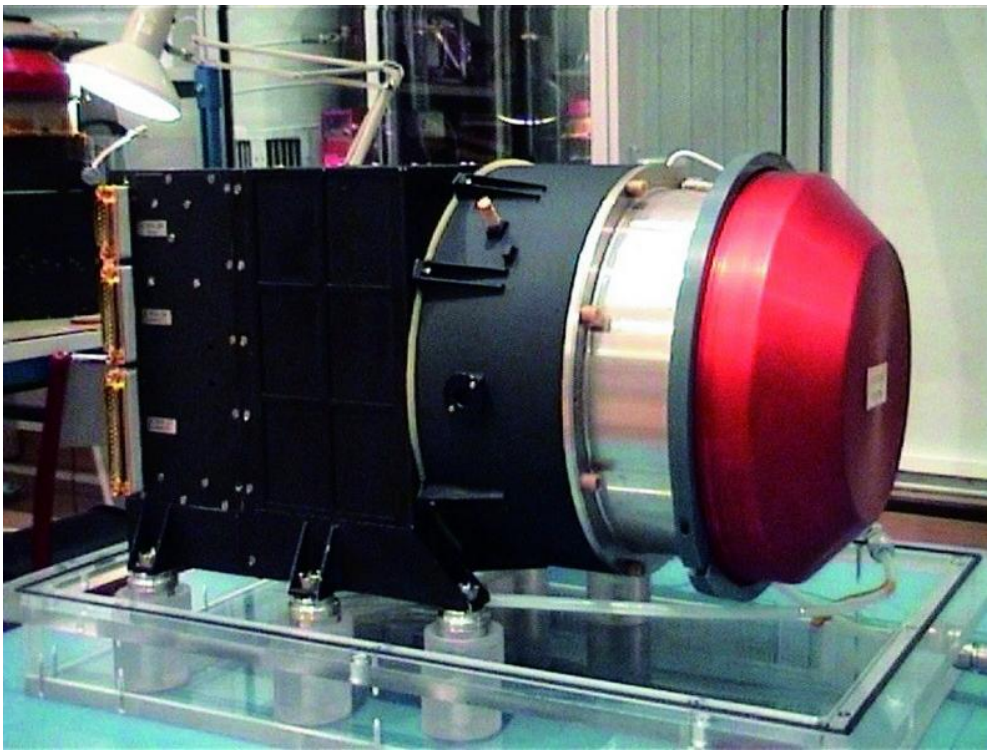

Figure 3.3: A picture of a Cluster Ion Spectrometer (`http://xeus.esa.int/science-e/www/object/index.cfm?fobjectid=33024&fbodylongid=1116`).

sensor and CODIF (time-of-flight ion COmposition and DIstribution Function) sensor. HIA measures ion energy per charge by electrostatic deflection in a symmetrical

quadrispherical analyzer which has a uniform angle-energy response with a fast imaging particle detection system. This particle imaging is based on micro−channel plate (MCP) electron multipliers and position encoding discrete anodes. HIA consists of three concentric spherical elements: an inner hemisphere, an outer hemisphere which contains a circular opening, and a small circular top cap which defines the entrance aperture. In the analyzer an electrostatic potential is applied between the inner and the outer hemisphere, allowing only charged particles with a limited range of energy and initial entrance angle to transmit. The particles are deflected by $90^0$ (quadrispherical) and detected by MCP. The particle exit position is a measure of the incident polar angle which can be resolved by a suitable position-sensitive detector system. A full $4\pi$ steradian scan is completed every spin of the spacecraft (about 4s), giving a full $3D$ distribution of ions in the energy range $5eV/e$ to $32keV/e$.

CODIF is a high sensitivity mass-resolving spectrometer (see figure CIS). It measures complete $3D$ distribution functions of the major ion species ($H+, He++, He+ and O+$) within one spin period of the spacecraft. The sensor primarily covers the energy range between $0.02-38keV/charge$. With an additional Retarding Potential Analyzer (RPA) device in the aperture system of the sensor with pre-acceleration for energies below 25 eV/e. CODIF combines the ion energy per charge with a subsequent velocity measurement (time-of-flight analysis) after acceleration to $15keV/e$. The energy per charge analyzer is a rotationally symmetric toroidal type, which is basically similar to the quadrispheric top hat analyzer used for HIA. RPA allows to extend the energy range below 15 eV/e. The time-of-flight analysis measures the velocity of charged particle through the length of the unit $d$ and the time $\tau$ . After passing the electrostatic analyzer the ions are focused onto a plane close to the entrance foil of time-of-flight (TOF) section, which is held at the potential in order to accelerate the ions. The flight path of the ions is defined by the 3 cm distance between the carbon foil at the entrance and the surface of the stop MCP. The start signal is provided by secondary electrons,

which are emitted from the carbon foil during the passage of the ions. Both HIA and CODIF are able to measure the velocity distribution function of ions $f(v, x, t)$. One can compute the velocity moments of the distribution function in order to obtain the particle number density, bulk velocity, pressure or temperature, and heat-flux [Paschmann and Daly, July 2000, Narita, 2006].

### 3.2.3 EFW

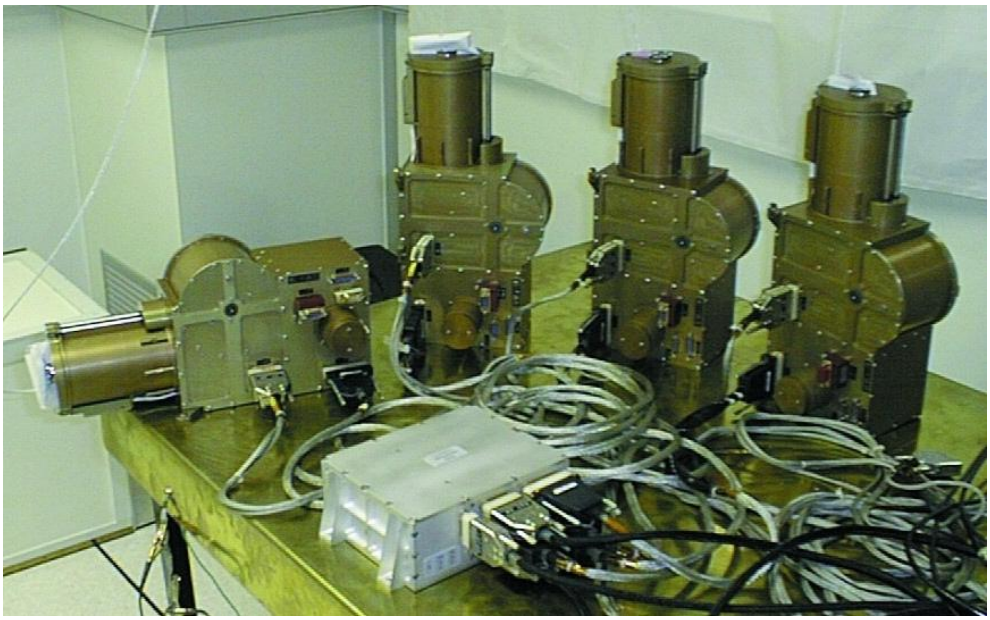

Figure 3.4: A picture of a Electric field and waves instrument (`http://xeus.esa.int/science-e/www/object/index.cfm?fobjectid=33024&fbodylongid=1116`).

The Electric Field and Wave (EFW) [Gustafsson et al., 2001, Narita, 2006] instrument on Cluster is designed with sensors consists of 4 spherical probes, 8 cm in diameter, at the end of a 50 m long wire booms in the spin plane with a separation of 88 m between opposite probes to measure the electric field to study plasma convection and waves. Each sphere can be operated in voltage mode (to obtain the average electric field between the probes in the spin plane) or currents generated in each sensor reveal the density of nearby electrons (current mode to obtain the density). The voltage or

current bias of the probes relative to the spacecraft is programmable and a current-voltage sweep can be made in both current and voltage modes for diagnostic purposes and to obtain the temperature and density of the ambient plasma. It can take up to 36 000 samples per second of the electric field and fluctuations in the plasma density. The converters give a one-bit resolution for the low pass filters of 22 $\mu$V/m, and 0.15 $\mu$V/m for the band pass filter.

## 3.3 Summary

We have given a brief description and functions of the few instruments of Cluster II spacecraft that have provided the observational data used in this thesis. The choice of Cluster instruments is based on the fact that each of the four Cluster spacecraft has eleven instruments that observe events at the same time. This property is added to the four spacecraft plan designed to achieve 3D observations which promises reliable results.

# Chapter 4

# Determination of Instantaneous frequencies of low frequency plasma waves in the magnetosheath

## 4.1 Introduction

The knowledge of the instantaneous frequency can be used to better understand nature's dynamics such as in the solar wind, which exhibits non-stationary and non linear behaviour [Boashash, 1992, Berkant and Loughlin, 1995, Carozzi et al., 2004]. There are many definitions to instantaneous frequency. The basic definitions are considered in two ways, namely;

1. The temporal derivative of phase due to mono-component signal [Boashash, 1992, Cohen and Lee, 1988, Cohen, 1995, Carozzi et al., 2004, Huang et al., 1998]

2. The temporal derivative of phase due to multi-component signal [Berkant and

Loughlin, 1995]. The later definition has been widely considered to provide results that are not meaningful [Boashash, 1992]

But many analysts have also made the data meant to deduce instantaneous frequency lose its physical meaning due to filtering to achieve a mono-component condition that is necessary, and make the instantaneous frequency so determined to be based on either constant amplitude or fixed frequency Fourier expansion. But the application of Hilbert-Huang Transform (HHT) offers results for the instantaneous frequency and amplitude which are functions of time. The instantaneous wave vector deduced from here is also a function of time.

### 4.1.1 Concept of frequency, instantaneous frequency

The understanding of frequency is very important as it is a quantity of essence in the field of oscillatory behaviour [Parks, 1991, Kivelson and Russell, 1995]. In a simple sine wave (sinusoid), the measurement of frequency is obtained by the determination of the time intervals between consecutive zero-crossings. This time interval defines the period, T of the sinusoid. The inverse of this period gives the frequency, $f$.

$$f = \frac{1}{T} \tag{4.1}$$

For non-stationary waves, the definition of frequency becomes hard to determine (e.g. real valued data), where amplitude varies as well as the time intervals (periods) with time. In a classical wave theory, a wave field is considered with an amplitude and phase. Such a wave field is associated with a real data, which is the real part of a complex data function. For instance, given a real wave field $X_r(t)$ as $A_r cos(wt)$

$$X_r = A_r cos(wt) \tag{4.2}$$

A complex function c is given as

$$c = a + ib \tag{4.3}$$

$$i^2 = 1 \tag{4.4}$$

Where a is the real part of c and b is the imaginary part of c. It therefore becomes that in the classical wave field,

$$a = R[a + ib] = X_r \tag{4.5}$$

$$R[a + ib] = A_r cos(wt) \tag{4.6}$$

$R$ is the real value operator, $A$ is the amplitude, $wt$ is the phase. For a good measurement of frequency of a practical real data, the frequency band of the signal has to be extremely narrow [Boashash, 1992]. Since the wave field is a measure of real valued signal and exhibits several extrema between zero-crossings, the frequency content is hard to obtain as opposed to the simple sinusoidal case, and also shows a serious limitation to Fourier transform application.

### 4.1.2 Stationarity

Consider a stationary, zero mean and homogenous wave field $S(x,t)$, which is time dependent, and has spatial dependence also; for simplicity, let one dimensional space (x) be taken. The Fourier transform of $S(x,t)$ is given as the average of harmonic vibrations [Boashash, 1992, Beall et al., 1982]. In order to extract its spectral decomposition, using Fourier transform ($FT$)

$$S(x,t) = \frac{1}{2\pi} \int S(x,w) e^{iwt} dw \tag{4.7}$$

The reconstruction of this wave field in frequency space from equation (4.7) is obtained through inverse Fourier transform ($IFT$)

$$S(x, w) = \int_{-t/2}^{t/2} S(x, t) e^{iwt} dt \tag{4.8}$$

for a period time t.

The spectral equation (4.8) and the analysis equation (4.7) define stationarity for the wave field, which is defined from the time averages of the cosine and sine of the wave field, where its associated frequencies, amplitudes and phases of the cosine and sine are constant.

### 4.1.3 Variable frequency and non-stationarity

Huang *et al.* (1998) has demonstrated variability of frequency of non-linear data using the Duffing equation to show causal effect due to intra-wave modulation, which results in waveform distortion. This distortion in waveform allows for variable frequency, where the use of the Fourier transform to extract the frequency content limits the knowledge of the dynamics of a practical wave form, since the Fourier transform provides the average frequency of the distorted wave.

An observational data like the ones taken by Cluster instrument exhibit a non-stationary behaviour as a function of time. This is the basis of instantaneous frequency, which is the time derivative of phase. The concept of instantaneous frequency has been adopted by many analysts in various field of study such as Communication Engineering, Signal processing, Acoustics, Sonar, Radar, Image processing, Biomedical devices, etc. The application in the analysis of Space Plasma using electric field data [Carozzi et al., 2004] has shown its importance and reliability in results.

Many analysts have also determined instantaneous frequency on the basis of Simple

Hilbert Transform on a filtered data [Boashash, 1992, Cohen and Lee, 1988, Cohen, 1989, Carozzi et al., 2004] since instantaneous frequency can only make meaning for a mono-component signal [Boashash, 1992, Cohen, 1995, Sharpley and Vatchev, 2004, Carozzi et al., 2004, Huang et al., 1998, Huang and Shen, 2005], which does not give the complete physical meaning of the original data.

### 4.1.4 Instantaneous frequency

The determination of the instantaneous frequency of a wave field that has been analytically defined from its real valued data has depended upon the use of Hilbert transform [Gabor, 1946] and a condition of single wave component. The condition of single component of the wave has limited the determination of instantaneous frequency for a practical case [Huang et al., 1998, Huang and Shen, 2005], where the waveform is complicated indicating the presence of many components.

From the many estimation of instantaneous frequency, Fourier transformation has always been used, where the frequency has been defined for the sine or cosine function spanning the whole data length with constant amplitude (approach of Simple Hilbert Transform (SHT)) thus requiring at least one full oscillation of a sine or cosine wave for the definition of the local frequency value.

$$w = \frac{d\theta(t)}{dt} \tag{4.9}$$

where $w$ is the angular frequency, $\theta$ is the phase of wave and $t$ is time.

Space plasma data fall within the non-stationary and non-linear signal which requires a special consideration to accommodate the multi-component signal. The solution to this is given using empirical mode decomposition (EMD) and associated improvements to decompose the real data into many intrinsic mode functions (*imfs*) [Huang et al.,

1998, Rilling and Flandrin, 2006, Huang et al., 2003, Huang and Shen, 2005, Flandrin et al., 2004], and then Hilbert transform [Gabor, 1946] is applied to each of the imfs for the determination of instantaneous frequency [Carozzi et al., 2004, Boashash, 1992]. This is the basis of Hilbert-Huang Transform (HHT) [Huang et al., 1998].

## 4.2 Empirical mode decomposition (EMD)

This is just a step added to help analyse data that are stationary, non-stationary, linear and non-linear where other methods used have lost physical meaning of the data. EMD is the decomposition of a real valued signal into many single components called intrinsic modes functions (*imfs*) characterizing the signal. This method is suitable when combined with SHT in the analysis of observational data having a waveform that is complicated where application of only SHT after filtering has given instantaneous frequency that has lost the physical sense of the data. The EMD method is a local and adaptive method in frequency-time analysis, which enables analysis of stationary and non-stationary signal. The extraction of the imfs from the real value data $S(t)$ is known as sifting [Huang et al., 1998]. The maxima and minima form envelope by using cubic spline line as the upper envelope and another line as the lower envelope of the data. The envelope formed by the two cubic spline lines should extend to cover the entire data. Their mean called the envelope mean $m_1$ is considered as the average of the upper and lower lines, and the difference between the data S(t) and is the first component, $h_1$, *i.e.*

$$S(t) - m_1 = h_1 \tag{4.10}$$

The data $h_1$ is subtracted from the data $S(t)$ to obtain the residue, $r_1$

$$S(t) - h_1 = r_1 \tag{4.11}$$

Where $h_1$ is the first sifted component of $S(t)$ . This process is repeated many times, each time with the residue considered as the data, and a general form for EMD is given for $i$ times of sifting, where $i = 1, 2, ....., n$ as

$$S(t) = \sum_{i=1}^{n} c_i + r_n \tag{4.12}$$

Where $c_i$ are the $imfs$ components that have been extracted, $r_n$ is the residue after the $n$ $imfs$ have been extracted.

$c_1$ is the first $imf$ component extracted and has the finest scale or the shortest period component of $S(t)$, and $r_n$ can be a constant or a mean trend, which may be discarded during the computation of the instantaneous frequency since it has overpowering energy spectrum.

EMD as a dyadic filter is able to extract white noise constituting a signal into $imf$ components having mean periods twice the value of the previous component [Wu and Huang, 2003, Flandrin et al., 2004]. This gives an answer to a question of how to remove noise without damaging the information in the signal. We apply Wu *et al.* (2003) for the separation of the noise. The sifting process of EMD helps to eliminate the overlapping waves and to smooth uneven amplitude. A check to ensure that the *imfs* component maintain enough meaning of both amplitude and frequency modulations is necessary to determine when sifting needs to stop. A typical standard deviation, $SD$ of between 0.2 and 0.3 [Huang et al., 1998] is set to serve as a stopping criterion using two consecutive sifting results.

$$SD = \sum_{t1}^{t_2} [\frac{\mid h_1(t) - h_2(t) \mid^2}{h_1^2(t)}] \tag{4.13}$$

$h_1$ is the first component of the sifting, $h_2$ is the next component and $SD$ is the standard deviation. But Rilling *et al.* (2006) has given a range of $0.05-0.5$ as an improvement to this. Each $imf$, is governed by the following conditions: Extracted $imfs$ have the characteristics of equal number local maximum, local minimum and zero-crossings or

with a difference of one, and the mean value of the upper line forming the upper envelope and the line forming the lower envelope is equal to zero at any point. This makes $imf$ to be symmetric about the mean. And each $imf$ has a unique frequency at the same time. The $imf$ defined here is a mono-component signal.

### 4.2.1 Identified drawbacks of EMD

Though EMD has been seen as an interesting and promising tool for signal analysis, it has been found to be faced with the following drawbacks:

- Lack of mathematical or theoretical framework.

  EMD differs from other adaptive methods of data analysis that treat stationary processes [Huang and Shen, 2005]. Unfortunately, EMD does not have theoretical framework. This generates a lot of questions such as:

  a. how can such a basis be defined?

  b. what are the mathematical properties and problems of the basis functions?

  c. how should the general topic of this type of adaptive method for data analysis be approached?

  EMD is awaiting mathematical foundations like the ones constructed for wavelets.

- The choice of specific interpolation method and sampling.

  One of the operations of EMD requires the identification of upper and lower envelopes over the maxima and minima. The choice of interpolation method is very important here. Best results have been reported with cubic spline while linear and polynomial tend to increase the required number of sifting iterations [Huang and Shen, 2005, Rilling et al., 2003] and over−decompose signals by spreading out

their components over adjacent modes. According to Rilling *et al.* (2003), since the algorithm functions on discrete−time signals, some special attention needs to be paid for proper identification of extrema. This requires over−sampling.

- The existence of border effect.

  Border effect has been a general problem for any known method for data analysis [Huang and Shen, 2005]. The adopted solution is the use of various kinds of windowing such as in Fourier, but HHT by Huang *et al.* (2005) used window frame. This is a way of extending the data beyond its existing range in order to extract some information from all the data.

- The need for effective stopping criteria.

  Extraction of a mode is found as satisfactory when the sifting process is stopped [Huang and Shen, 2005, Rilling et al., 2003]. For this reason EMD requires that the number of extrema and number of zero−crossing must differ at most by 1, and the mean between the upper and lower envelopes must be close to zero according to some criteria. To avoid over−iteration which leads to over−decomposition, care must be given to selection of stopping criteria which must not be too low.

### 4.2.2 Achieved improvement on EMD

In an attempt to improve on the drawbacks of EMD, different experiments have been carried out such as differential equation based formulation [Deléchelle et al., 2005] aimed at providing mathematical framework for EMD, and variations on the EMD algorithms [Rilling and Flandrin, 2006], which minimises error propagation due to finite observation lengths. This involves the addition of extrema by mirror symmetry with respect to the extrema that are closest to the edges for good results. This helps in solving the border problems. Rilling *et al.* (2006) has also identified the need

for effective stopping criteria for sifting, noting that imposing too low threshold for stopping the iteration process also leads to problems. This has been improved by taking care of globally small fluctuations in the mean by introduction of stopping criteria that guarantees this globally small fluctuations in locally large lengths. The choice of cubic spline interpolation has been adopted since other interpolation methods either over−decompose or under−decompose the signal [Rilling and Flandrin, 2006]. These improvements validate EMD as a promising tool for data analysis. Flandrin *et al.* (2004) has added another value to EMD by improving step that identifies and isolates local zones where error remains large, accomplished by introduction of a weighting function, wfn. Therefore, equation (4.10) becomes

$$S(t) - m_1 * wfn = h_1 \tag{4.14}$$

We extracted our $imfs$ based on the algorithms with these improvements.

## 4.3 Simple Hilbert Transform (SHT)

Hilbert transform is applied to each $imf$ component with the assumption that any complicated signal such as a real data is made up of many different oscillatory modes Huang et al. [1998], the $imfs$. For $c_i(t)$ components, the Hilbert spectrum is given for a real valued signal $S(t)$ as

$$H[c_i(t)] = y_i(t) \tag{4.15}$$

where $H$ is the Hilbert transform operator

$$y_i(t) = \frac{1}{\pi} P.V \int_{-\infty}^{\infty} \frac{c_i(\tau)}{t-\tau} d\tau \tag{4.16}$$

where P.V. means the Cauchy principal value of this integral. $c_i(t)$ and $y_i(t)$ form a complex conjugate pair defining an analytic signal $z_i(t)$

$$z_i(t) = c_i(t) + jy_i(t) \tag{4.17}$$

$$c_i(t) + jy_i(t) = a_i(t)e^{j\theta_i(t)} \tag{4.18}$$

where $a_i(t)$ is the instantaneous amplitude defines as

$$a_i(t) = [c_i^2(t) + y_i^2(t)]^{\frac{1}{2}} \tag{4.19}$$

And $\theta$ is the instantaneous phase defined as

$$\theta_i(t) = \tan^{-1}[\frac{y_i(t)}{c_i(t)}] \tag{4.20}$$

Therefore, instantaneous frequency is computed as

$$w_i(t) = \frac{d[\theta_i(t)]}{dt} \tag{4.21}$$

The original data $S(t)$, it can be expressed as

$$S(t) = R\sum_{i=1}^{n} a_i(t)e^{j\int w_i(t)dt} \tag{4.22}$$

Equation (4.22) enables the instantaneous envelopment and the instantaneous frequency to be represented in three dimensions as a function of time. $R$ in equation (4.22) is the real part operator.

### 4.3.1 Filtering and sifting

Filtering as considered in frequency space in most common use, and the filtering of non-stationary and non-linear data appear difficult [Huang et al., 1998]. The use of EMD gives $imfs$ which are sifted into different timescale with preservation of the fundamental modes by not eliminating the harmonics as would happen when using the traditional filtering method in the frequency space. Filtering of non-stationary and non-linear signal becomes only helpful after sifting the signal into its different modes. Sifting process of EMD extracts or filters the signal into timescales that are product of different band filters. High pass filtered result can be seen in the range of signal in equation (4.23) with n-$imf$ components using EMD as

$$S_{ik}(t) = \sum_{i=1}^{k} c_i \tag{4.23}$$

where $i$ and $k$ give a range from starting point to somewhere between $i$ and $n$, while the low pass filtered result is given as

$$S_{kn}(t) = \sum_{k}^{n} c_i \tag{4.24}$$

where $k$ and $n$ give a range from $k$ to $n$. EMD has also been considered as a filter bank [Flandrin et al., 2004].

### 4.3.2 Negative Frequency Filtering: Hilbert filter

For a system considered to be the sum of many sinusoid *e.g.* an $imf$, a Hilbert transform filter is used to shift each contributing sinusoid by a quarter cycle [SmithIII, 2007]. The Hilbert filter has a magnitude of unity at all frequencies with a phase shift of $-90°$ at each positive frequency, and $+90°$ at negative frequency. Every real signal defined with

only its real values can be approximated by a corresponding analytic values [Gabor, 1946] that depend on the sum of the real valued signal and the Hilbert transform (equation 4.15) of the real valued signal. $z_i(t)$ has the characteristic of non-negative frequency, implying that all negative frequencies of $c_i(t)$ have been filtered out with Hilbert transform filter. This is how each of the $imfs$, $c_i$ is handled. $c_i$ could be considered in positive and negative frequency component at a particular frequency $w_0$. Therefore,

$$c_+(t) = e^{jw_0t} \tag{4.25}$$

$$c_-(t) = e^{-jw_0t} \tag{4.26}$$

Hilbert transform filter impresses $\frac{-\pi}{2}$ phase shift on the positive frequency and $\frac{+\pi}{2}$ on the negative-frequency components. On a complex sinusoid, the shift applies to exponent.

$$y_+(t) = e^{-j\frac{\pi}{2}}e^{jw_0t} = -jc_+(t) \tag{4.27}$$

$$y_-(t) = e^{j\frac{\pi}{2}}e^{-jw_0t} = je^{-jw_0t} = jc_-(t) \tag{4.28}$$

Sum both in-phase component and the phase quadrature

$$c_+(t) + y_+(t) = e^{jw_0t} - je^{jw_0t} \tag{4.29}$$

$$c_+(t) - jc_+(t) = e^{jw_0t} - je^{jw_0t} \tag{4.30}$$

Also,

$$c_-(t) + y_-(t) = e^{-jw_0t} + je^{-jw_0t} \tag{4.31}$$

$$c_-(t) + jc_-(t) = e^{-jw_0t} + je^{-jw_0t} \tag{4.32}$$

From equation (4.25) and (4.27),

$$z_+(t) = c_+(t) + jy_+(t) = e^{jw_0t} - j^2e^{jw_0t} = 2e^{jw_0t} \tag{4.33}$$

Also,

$$z_-(t) = c_-(t) + jy_-(t) = e^{-jw_0t} + j^2e^{-jw_0t} = 0 \tag{4.34}$$

Though there is a gain of 2 at the positive frequency, the negative frequency component is filtered out. In the analytic signal representation of

$$z(t) = \frac{1}{2\pi}\int_0^\alpha z(w)e^{jwt} = 2e^{jw_0t} \tag{4.35}$$

$z(w)$ is the complex coefficient (setting the amplitude and phase) of the positive-frequency complex signal $e^{jw_0t}$ at frequency $w$. According to the Bedrosian theorem [Bedrosian, 1963] on the Hilbert transform of signal with more than one frequency, the Hilbert transform will yield a meaning instantaneous frequency if the transformation for the product of two contributing waves such as A(t) and B(t) have the form

$$H[A(t)B(t)] = A(t)H[B(t)] \tag{4.36}$$

Where H is the Hilbert transform operator. This works on conditions that the Fourier spectrum for both A(t) and B(t) are disjoint, and that the frequency range of the spectrum for B(t) is higher than that of A(t). The already extracted $imfs$ have the form of the right hand side of equation (1.18), which forms a system containing amplitude and frequencies. From the Bedrosian (1963) theorem, the Hilbert transform of such $imfs$ becomes,

$$H[a_i(t)\exp j\theta_i(t)] = a_iH[\exp j\theta_i(t)] \tag{4.37}$$

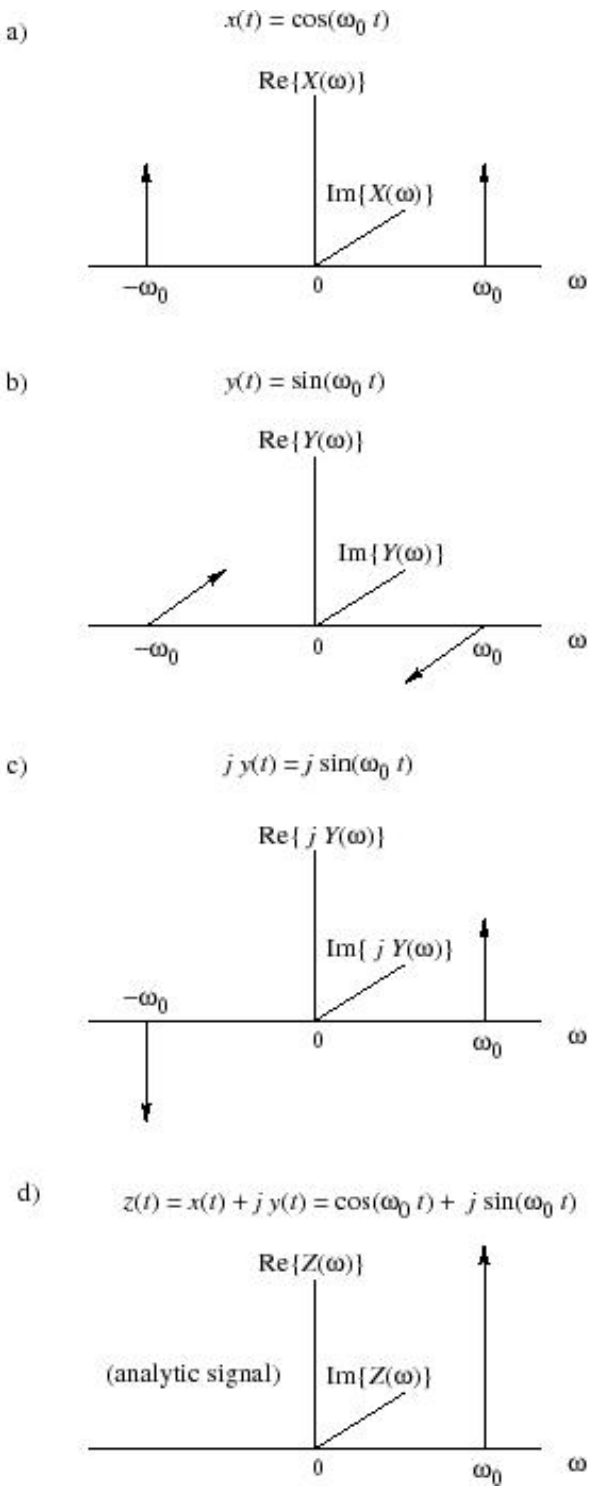


Figure 4.1
Graphical representation of the creation of the analytic signal $z(t)$ from the real signal $c(t)(= x(t))$ and the derived phase quadrature signal $y(t)$. These are viewed from a frequency domain; (a) spectrum of $c$, (b) spectrum of $y$, (c) spectrum of $jy$, and (d) spectrum of $z$ [SmithIII, 2007]

where i=1,2,3,.....,n. As required conditions, $a_i(t)$ has to be a slowly varying amplitude with respect to the frequencies as defined in equation (4.21), and that the frequency spectra for the envelope $a_i(t)$ and the carrier wave are disjoint [Huang and Shen, 2005] and the reference therein. These conditions led to the proposal of normalized $imfs$ Huang et al. [2003]

$$N_{imf} = \frac{imf}{E_t} \tag{4.38}$$

Where $E_t$ is the envelope of the maxima. This normalized $imfs$ are transformed using Hilbert transform.

### 4.3.3 Mode separation

We use these analyses of Fourier transform and wavelet transform to determine the statistical significance of the results obtained from the Hilbert spectrum. To get the information content of the data, fractional Gaussian noise [Flandrin et al., 2004] has been used as a model to compare the behaviour of noise in a data. The characteristics of white noise [Wu and Huang, 2003] has been recommend for the separation of modes with noise from the information carrying modes. We introduce an approach that produces the $imfs$ that are not sensitive to noise and amplitude fluctuations. We define the relative energy character rate [Helong et al., 2007] for the data as the ratio of the difference of the maximum and the minimum instantaneous envelopment to the square root of the integral of the squared instantaneous envelopment over the sampled period.

$$RECR(t) = \frac{maxE(t) - minE(t)}{\sqrt{\int_a^b E^2(t)dt}} \tag{4.39}$$

The ratio of the RECR for $imf$ to RECR for the original data.

$$Qf(t) = \frac{RECRimf}{RECR(data)} \tag{4.40}$$

The information carrying $imfs$ are produced from an appropriately chosen threshold value (TV) for set of Qf(t)s. This selection of TV must be done with care.

### 4.3.4 Other non-stationary methods

The spectrogram is one of the methods used for the analysis of non-stationary signal, but has been classified as a limited time window-width Fourier spectral analysis Huang et al. [1998]. Huang has argued and considered this method to be less reliable for non-stationary data analysis since it depends on simple Fourier spectral analysis through the successive sliding of the window along the time axis and is thus, piecewise stationary.

Wavelet analysis is another method which has been widely used for the analysis of non-stationary signal. A broad review has been carried out by Huang *et al.* (1998) and Helong *et al.* (2007), and interestingly, wavelet analysis has been shown to be an adjustable window Fourier spectral analysis. The wavelet transform of a signal S(t) can be defined as

$$W(a,b;S,\psi) =\mid a \mid^{-\frac{1}{2}} \int_{-\infty}^{+\infty} S(t)\psi^*(\frac{t-b}{a})dt \tag{4.41}$$

where $a$ is the scale parameter and $b$ is the translation of the origin. $\psi^*$ is the basic wavelet function that satisfies certain very general conditions. Time is hidden in $b$ while frequency is found in $\frac{1}{a}$ . $W(a,b;S,\psi)$ is the calculated wavelet coefficients or energy of $S$ of scale $a$ at $t = b$. The equation shows that wavelet analysis is a measure of similarity between the transforming function and the signal. The translation from a to b, $(at + b)$ defines linearity and due to limited length of the basic wavelet function, the Morlet wavelet, which is the widely used wavelet function has been observed to be associated with leakage therefore making quantitative description of energy- frequency time distribution difficult [Huang et al., 1998]. Since the Morlet wavelet is based on the Fourier transform, it is also limited to Fourier spectral analysis, so gives solutions

to linear aspects of the data. However, wavelet analysis has been quite useful for the analysis of space plasma data [Balikhin et al., 1997, Walker et al., 2004] with non-stationary behaviour but with a condition of linearity. Wavelet results spread energy over a much broader frequency space, but with failure for detailed variation in frequency [Huang et al., 1998].

### 4.3.5 $Imfs$, and instantaneous frequency estimation

Now that we have been able to decompose a known data into its different oscillatory modes called the $imf$s, the determination of the numerical estimates of the frequency through instantaneous frequency of the $imf$ is simple using Hilbert transform (see equations 4.15−4.21). In the estimation of the instantaneous local frequency and wave vector, Carozzi *et al.* (2004) has demonstrated with four (4) measurements along worldlines using real valued measurements from observations of four (4) known space-time trajectories as traced by Cluster II mission electric field instruments. We will start our estimation with magnetic field data taken from FGM instrument of Cluster II on the same day and time with that of the one used in the electric field data demonstration, then compare the results obtained by HHT with the electric field data results demonstrated by filtering which has been the basis by which Carozzi and his team−mates made the estimates. Using $\alpha = 1, 2, 3, 4$ Cluster II instruments considered along worldlines Carozzi *et al.* ( 2004), and their trajectories given as

$$r^{(\alpha)}(\sigma) = (t^{(\alpha)}(\sigma), \vec{x}^{(\alpha)}(\sigma)) \tag{4.42}$$

Where $\sigma$ is the sample number in serial mode as the instruments are measuring. The time of the sampled data is measured along the worldlines, given as

$$t^{(1)}(\sigma) = t^{(2)}(\sigma) = t^{(3)}(\sigma) = t^{(4)}(\sigma) \tag{4.43}$$

For these set of instruments, we consider trajectories for which $\vec{x}^{(\alpha)}$ do not all lie in the same plane for any fixed $\sigma$. We will extract data into its different oscillatory modes using EMD as earlier described, then sorts out the modes into their different frequency bands, which will serve as a filter with the advantage that the different oscillating waveforms will be obvious. We assume that $2\pi/k$ is larger than the minimum spacecraft separation. We computed phase differences modulo $2\pi$ since we are not interested in the absolute phase but only its spatial and temporal gradients. From equation (4.15) and (4.17), we treat the measurements analytically [Gabor, 1946]. We express equation (4.21) in discrete form as

$$w_i^{(\alpha)}(\sigma+1) = \frac{[\theta_i^{(\alpha)}(\sigma+1) - \theta_i^{(\alpha)}(\sigma)] mod \pm 2\pi}{t(\sigma+1) - t(\sigma)} \tag{4.44}$$

Equation 4.42 defines the trajectory, equation 4.43 defines the time and equation 4.44 defines the angular frequency.

## 4.4 Observations

FGM instrument data of Cluster II mission for 01 01 2001 at time between 02 00 00 and 02 00 10 $UT$, being the date and period EFW data were selected and used to demonstrate the estimates of instantaneous frequency, is decomposed using EMD into $imf$s and the Hilbert transform (HT) is used to create imaginary components for the real valued data and then the formation of the analytic signal as in equation (4.16).

The magnetic and electric fields for ten (10) mins data selected between 02 00 00 and 02 10 00 UT have profiles that are modulated in both amplitude and frequency. A correlation coefficient shows anti-phase correlation between the two sets of data (see table of coefficient, R below).

| Spacecraft | Correlation coefficient, R |
|---|---|
| 1 | -0.9398 |
| 2 | -0.9085 |
| 3 | -0.9275 |
| 4 | -0.9373 |

Table 4.1: Correlation coefficients, R between the magnetic and electric field of each Cluster spacecraft.

### 4.4.1 Data decomposition and results

Although EMD-HT approach has been used in this thesis for analysis of the observational data collected from Cluster spacecraft, it could also be used in the analysis of data which both Fourier and Wavelet analysis can be applied. We consider a simple case of a stationary and homogenous signal, and a non−linear signal.

**(i) A simple stationary and homogenous signal**

We considered a simple case of a zero mean, stationary and homogenous signal approximated by a sine wave with frequency 10 Hz and amplitude of 1 sampled at 1000 Hz. We used Fourier spectral analysis, Wavelet analysis and EMD-HT combination to recover the frequency of the wave.

**Results:**

Fs = 1000Hz (sample frequency)

f = 10 Hz (signal frequency)

t = 0:1/Fs:1 (time instant)

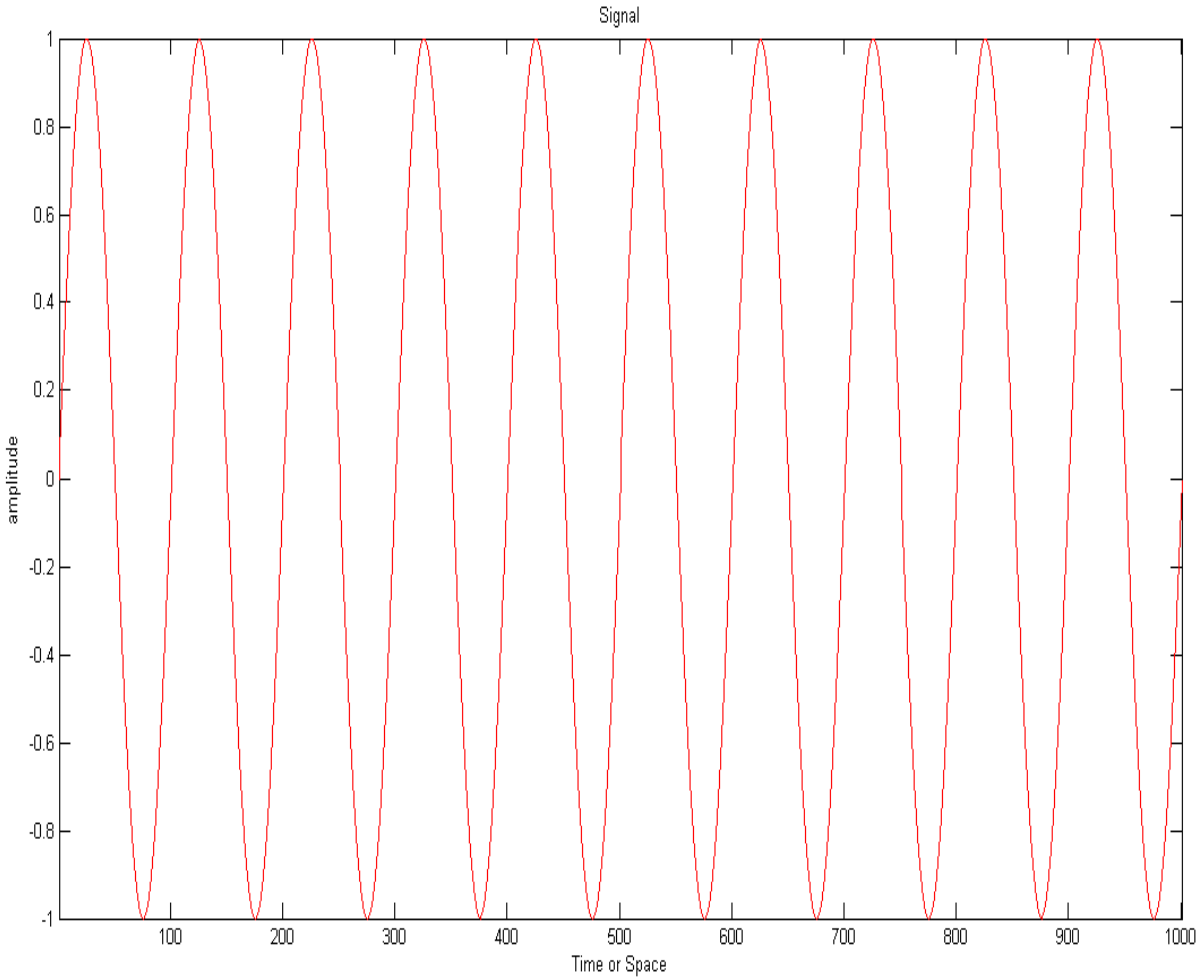


Figure 4.2: The plot of a simple periodic wave with frequency of 10 Hz and amplitude of 1 sampled at 1000 Hz.

*Fourier Spectral analysis*

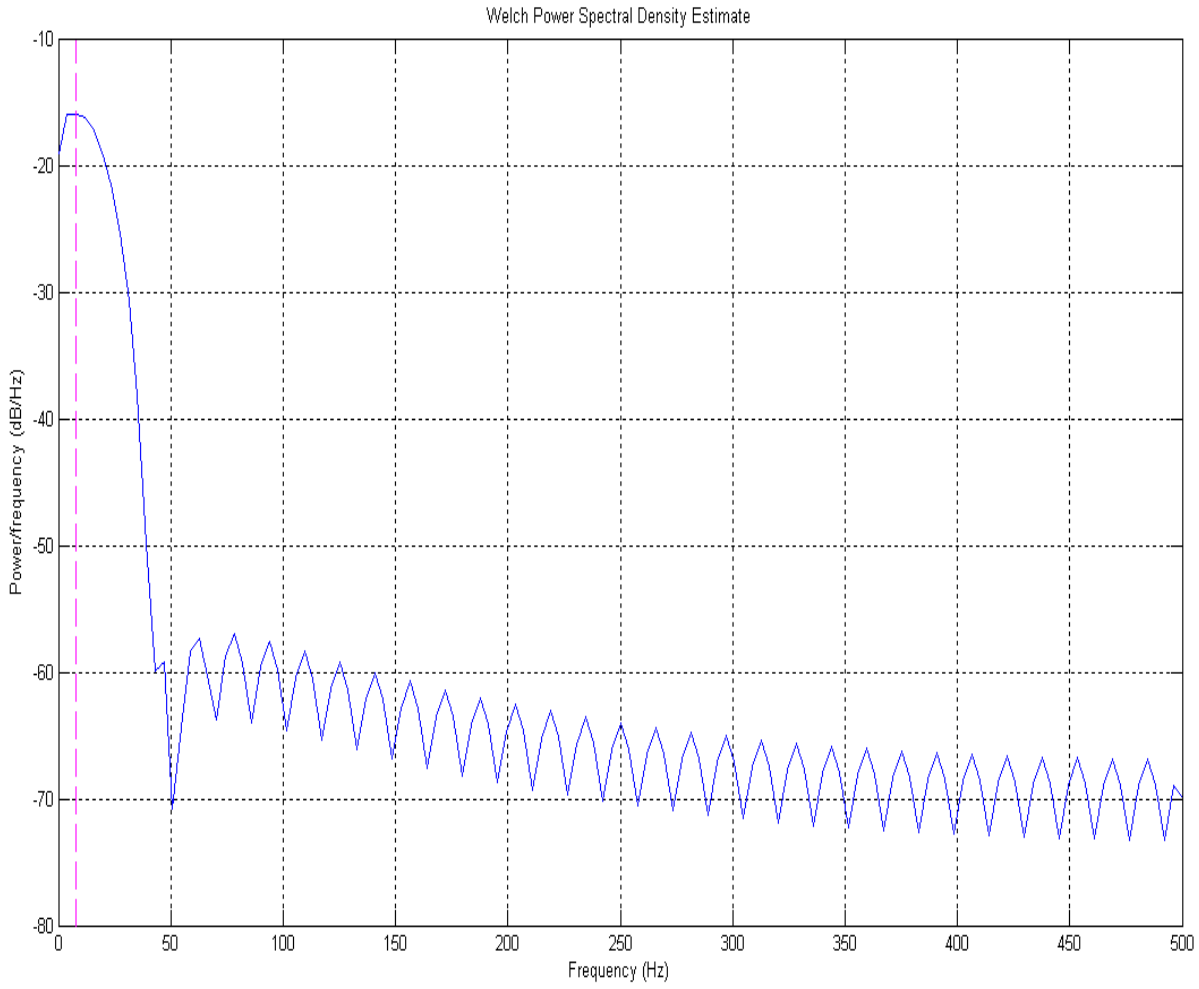


Figure 4.3: Power spectral density for a signal of frequency of 10 Hz and amplitude of 1 sampled at 1000 Hz.

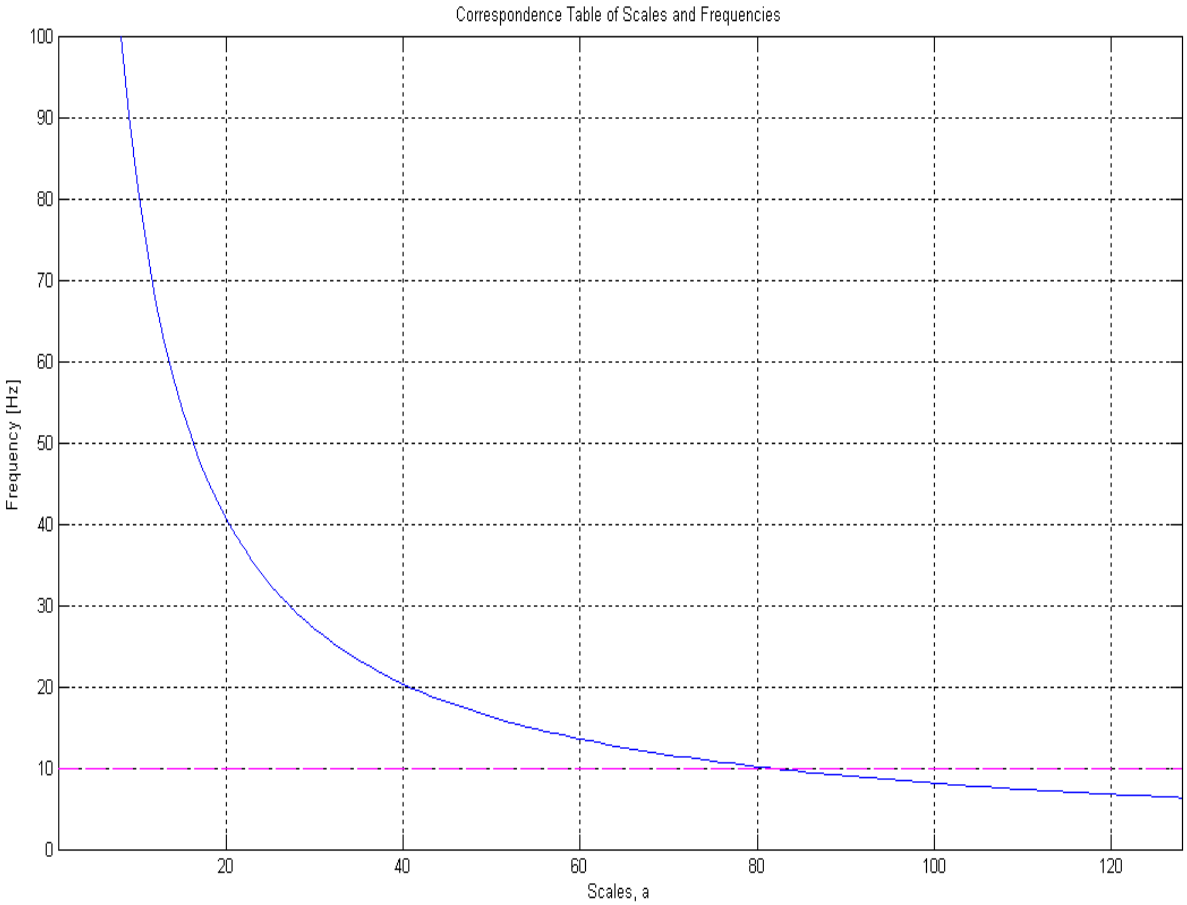


Figure 4.4: The plot of scales and frequencies. This plot shows that 81 on the scales axis correspond to 10 Hz on the frequency axis.

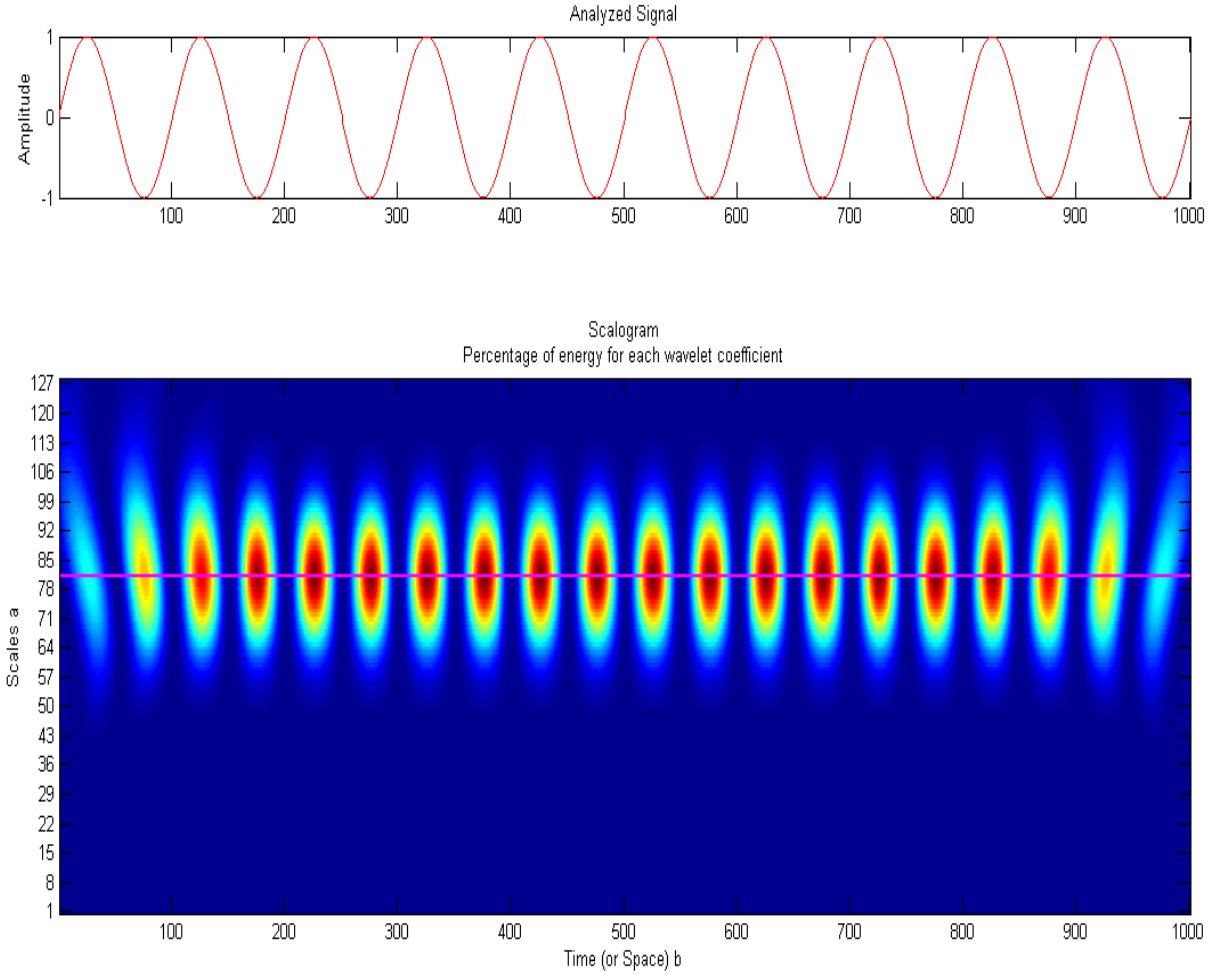


Figure 4.5: The scalogram for a signal with 10 Hz of frequency and amplitude of 1.

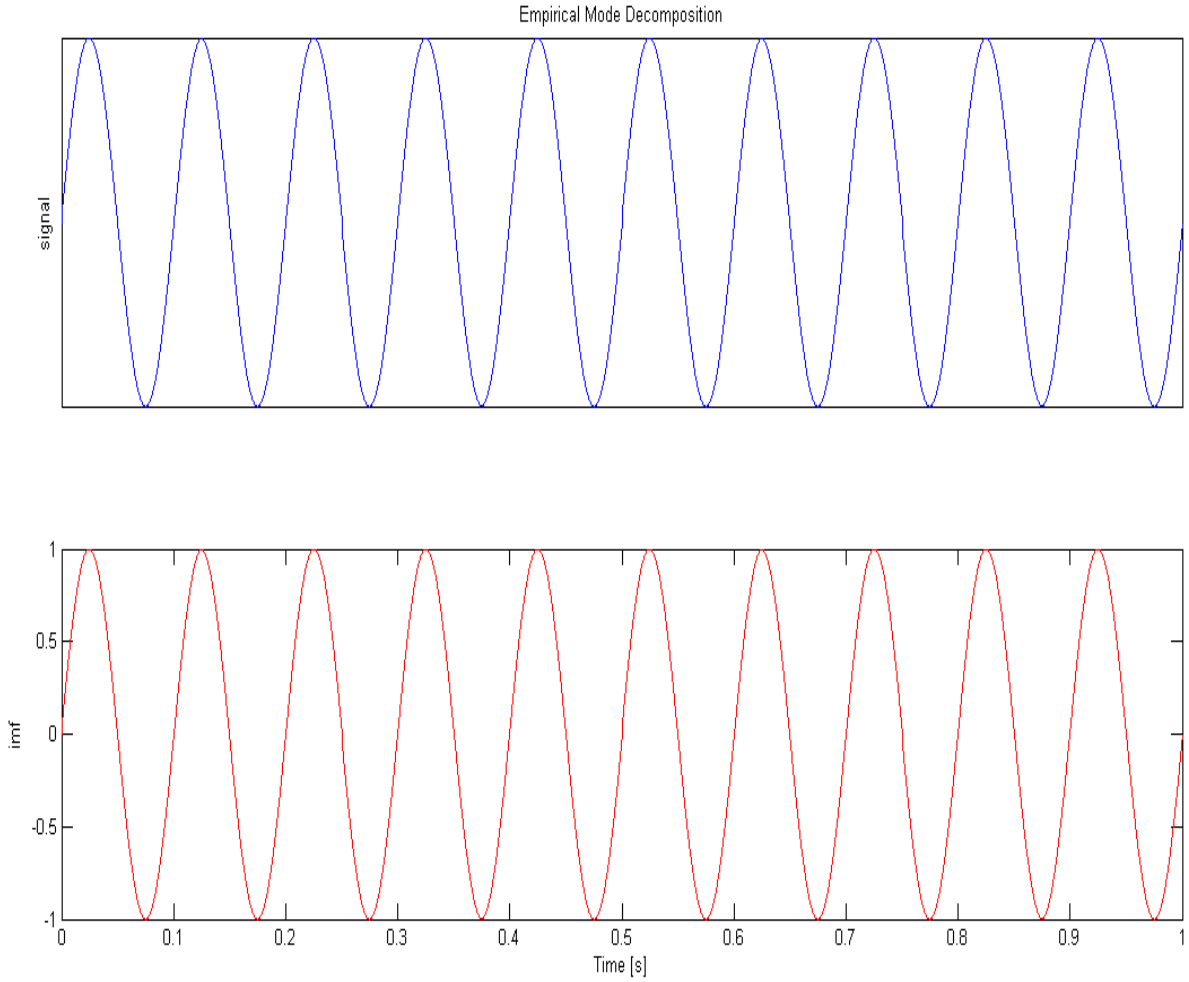


Figure 4.6: The application of empirical mode decomposition in the extraction of intrinsic mode function (imf) in a simple periodic signal with frequency of 10 Hz and amplitude of 1. The top panel is the plot of the signal. The bottom panel is the plot of the imf.

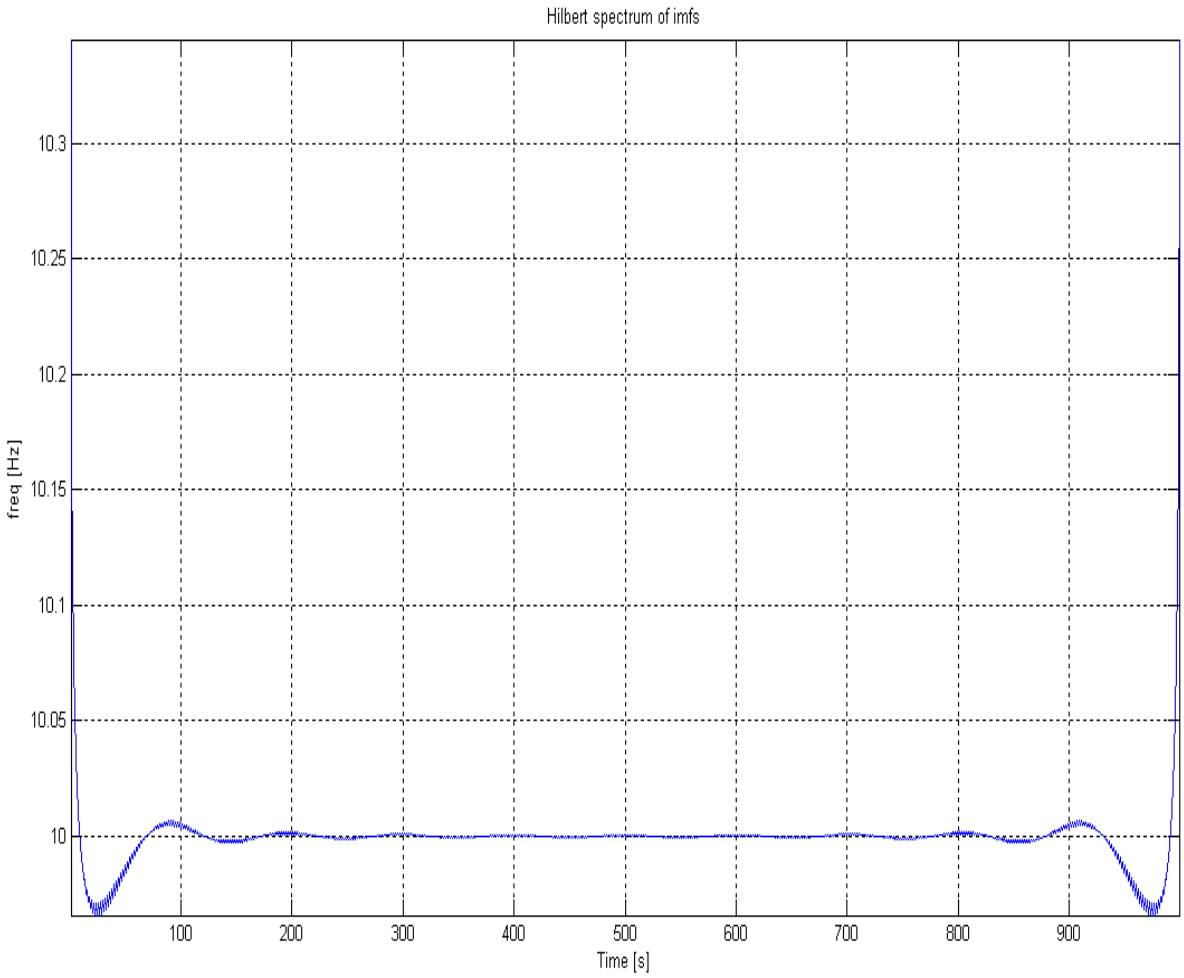


Figure 4.7: Hilbert spectrum for a signal of frequency of 10 Hz with an amplitude of 1 sampled at 1000Hz.

Figure 4.2 is the signal plot for a signal with a frequency of 10Hz and amplitude of 1 sampled at 1000Hz. The plot shows a constant frequency and amplitude. Figure 4.3 is the power spectral density plotted for the signal. Figure 4.4 is the plot for the corresponding scales, a and the frequencies. The curve cuts the 10 Hz mark at 81 mark on the scales axis. Figure 4.5 is the scalogram that shows a plot of scales, a and the translation, b (time). Figures 4.4 and 4.5 are related through the scales, a. The scales help in the determination of the frequency on the scalogram. The top panel of figure 4.5 is the signal plot and the bottom panel is the energy-frequency-time distribution pattern. The 81 mark on scales axis in figure 4.5 correspond to high concentration of energy. This 81 mark indicates that the frequency is 10 Hz. Figure 4.6 is the plot for the signal (top) and the extracted imf (bottom). Figure 4.7 is the Hilbert spectrum for the imf in figure 4.6.

The power spectral density (psd) gives a fundamental frequency of the wave (vertical dashline) and the harmonics. It measures frequency at where the power spectral density shows peak. In figure 4.5, it is observed that the end effect observed in Hilbert transform also affects wavelet transform. This is seen in the faint feature in figure 4.5 between 0 - 130 and 880-1000 seconds on time axis. The scales, which relates the frequency, is read as it runs across the elliptical shape. To be able to read the value on the scales axis (which correspond to the frequency), a line is drawn across the elliptical shape. This is the same way frequency value was determined on power spectral density plot. The line used on the scalogram shows that the 81 mark passes through the centre of the elliptical shape of energy. It is also found that the energy spreads beyond the 81 mark on the scales axis and makes it difficult to read out the exact scales (frequency) of the signal. Like Fourier analysis, the 81 mark is only clearly readable when a line is drawn. But it still gives a very good approximation of the frequency of the signal.

In figure 4.6, the extracted imf is the same as the signal. The use of EMD in this case

does not produce any residue. This shows how good EMD can extract constituents of signal. The extracted imf is similar to the original signal and shows that the there was no other component or external influence on the signal. Figure 4.7 is the Hilbert spectra which gives the time evolution across the entire data. It shows how best to recover the frequency of the signal across the data length. Unlike Fourier and Wavelet analysis, the Hilbert spectra give a better way of reading the frequency at every instant of time. The Hilbert spectrum also shows end effects on the range of 0-100 and 900-1000 seconds on the time axis. This is the similar effect which exists on scalogram in figure 4.5.

The frequency spectrum obtained using EMD-HT shows a better resolution between 100-900 seconds on the time axis than on the scalogram within the same range. This is as opposed to the energy spreading on the scalogram. The 10 Hz mark on the frequency axis is clearly traced across the data. This shows that EMD-HT combination is the better choice for the construction of the time evolution of events when compared with the mentioned standard techniques.

**(ii) Non−linear and non−stationary signal**

The magnetic field profile of 10-mins data is shown in Figure 4.10 featuring a wave form that is modulated in both amplitude and frequency taken from observations of 01 01 2001 between 02 00 00 and 02 00 10 UT . EMD has been used for the extraction of the various constituent signals embedded in the data. This leads to the determination of instantaneous envelopment. This is achieved by forming envelopes on maxima and minima. The envelopes of the maxima and minima alongside their mean are shown in Figure 4.11 determined using cubic spline fitting. The subtraction of the mean from the original data gives the first $imf$ ($imf1$) if the sifting conditions are met. This process continues until the sifting is completed as shown in the Figure 4.12. Using the y-components of the magnetic field of Figure 4.10, the panels in Figure 4.12 looking from top to bottom show the original data (signal), first, second, third, fourth imf and the residue at the bottom. Figure 4.13 shows in the same order the extraction from electric field from panel C1 in Figure 4.9, which also uses y-component. Figure 4.8 shows the magnitude and all components (x,y,z) of the four Cluster spacecraft crossing the bow shock into the magnetosheath. Figure 4.9 is the y−component electric field profile obtained between 02 00 00 and 02 00 10 UT on 01 01 2001 by C1. Figure 4.10 displays the y− component magnetic profile for data obtained between 02 00 00 and 02 00 10 UT. Figure 4.11 shows the instantaneous envelpoment and the mean for data obtained between 02 00 00 and 02 00 10 UT. Figure 4.12 is the plot for original data decomposed with EMD and the extracted $imf$s using magnetic field data obtained by C1. Figure 4.12 is the plot for original data decomposed with EMD and the extracted $imf$s using electric field data obtained by C1.

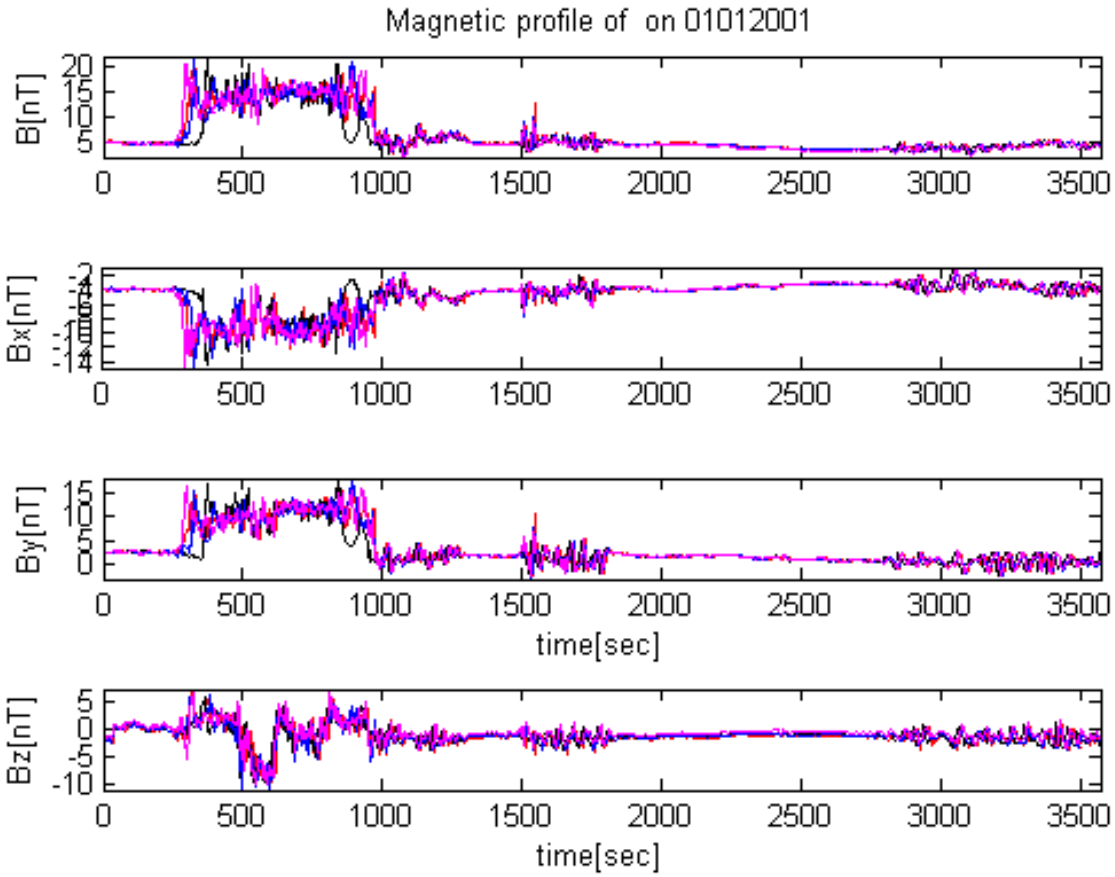


Figure 4.8: Magnetic field profile for the magnitude and all components (x, y, z) of the four Cluster spacecraft crossing the bow shock into the magnetosheath.

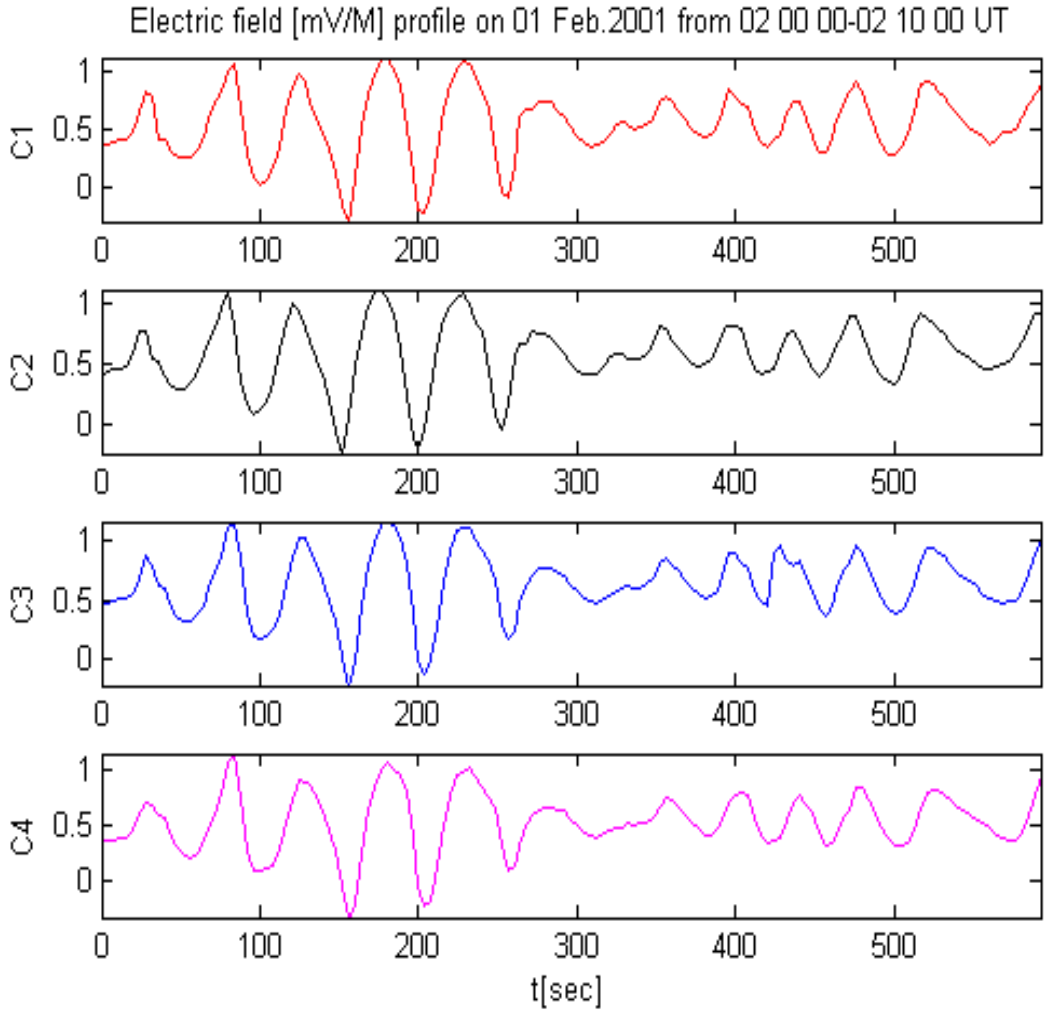


Figure 4.9: The electric field profile on 01 01 2001 between 02 00 00 and 02 10 00 UT showing a wave field that is similar to the magnetic field below.

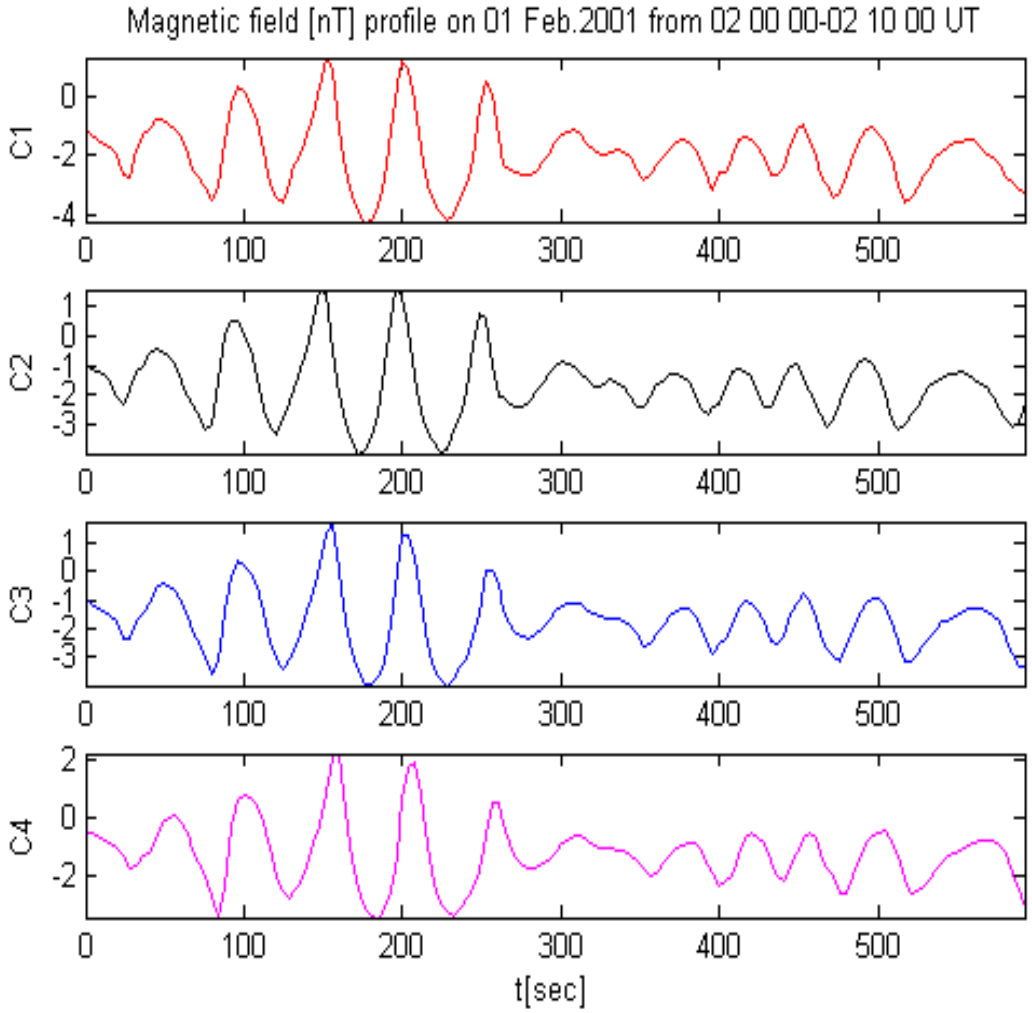


Figure 4.10: The magnetic field profile on 01 01 2001 between 02 00 00 and 02 10 00 UT showing a wave field that is similar to the electric field above.

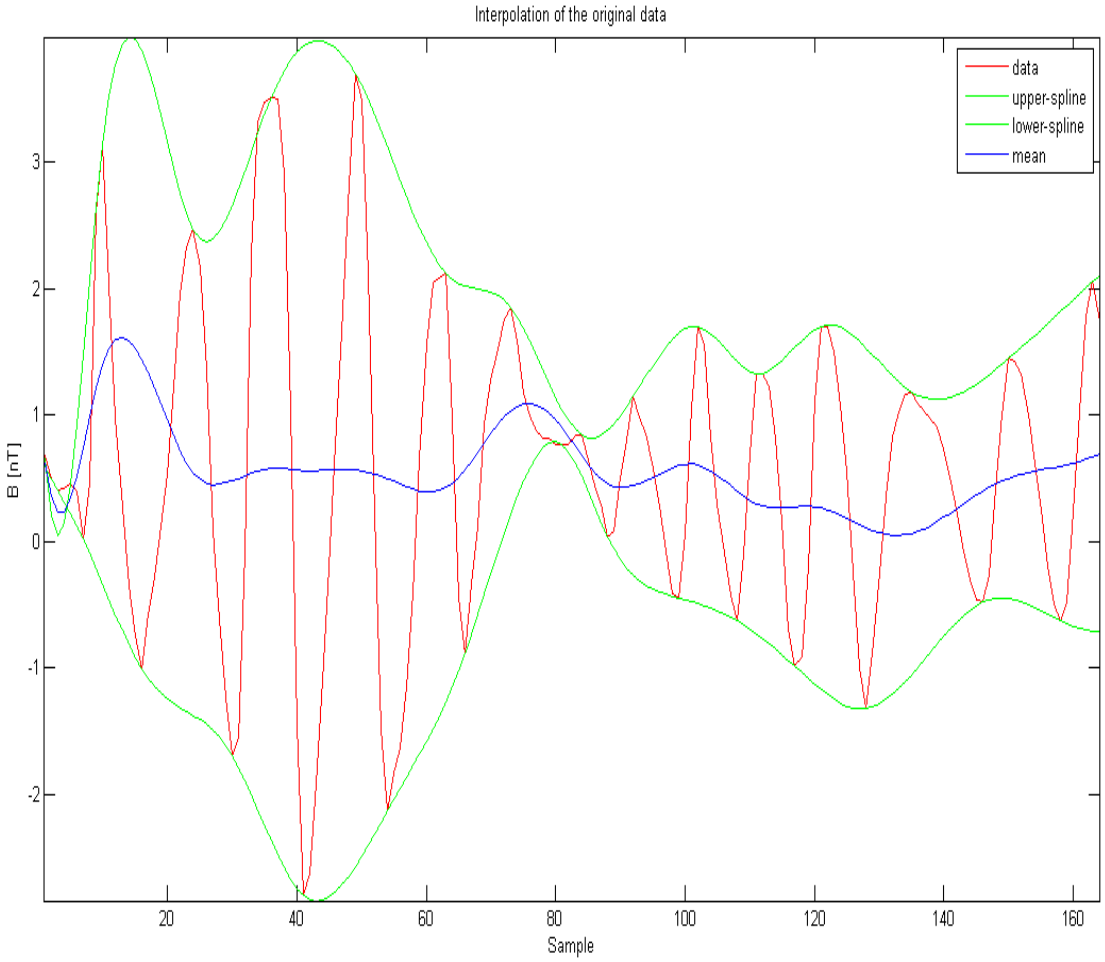


Figure 4.11: The envelopment of the maxima and minima and the mean of the envelope of magnetic field data. The number of sample n, which is an integer and the sampling period T were used for a signals (data) which were discretized for time t=nT.

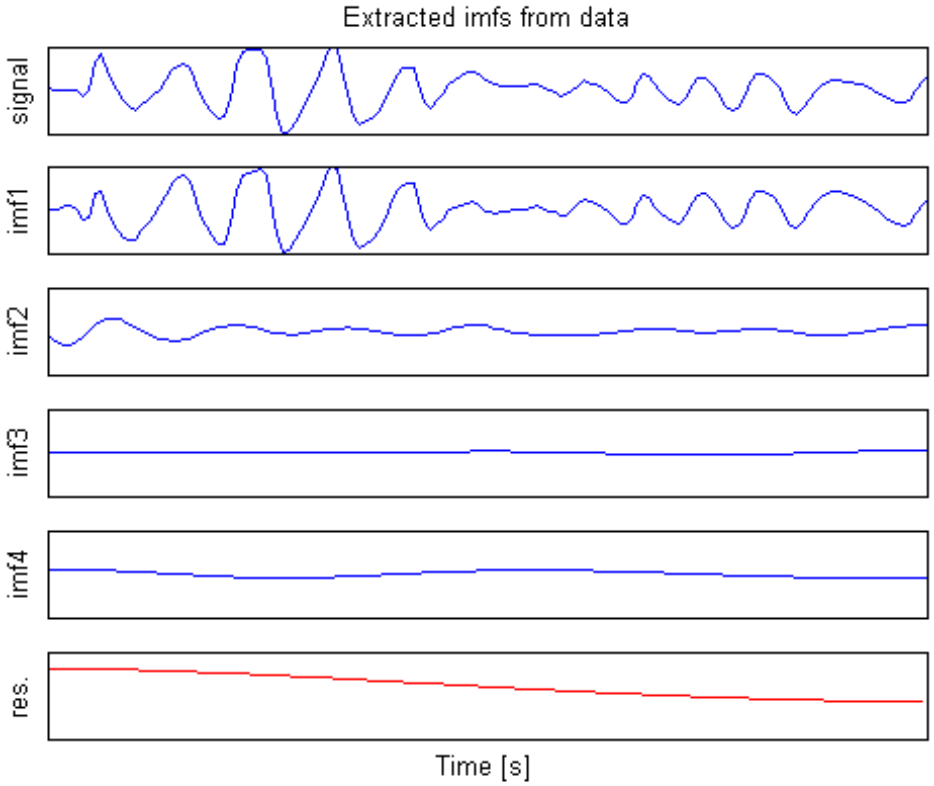


Figure 4.12: The intrinsic mode functions (imfs) for y component of magnetic field data (C1)on 01 01 2001 between 02 00 00 and 02 00 10 UT. From to bottom, panels show original data, 1st, 2nd, 3rd and 4th imfs. The 5th does not meet the conditions earlier stated. The horizontal axis is the time in seconds.

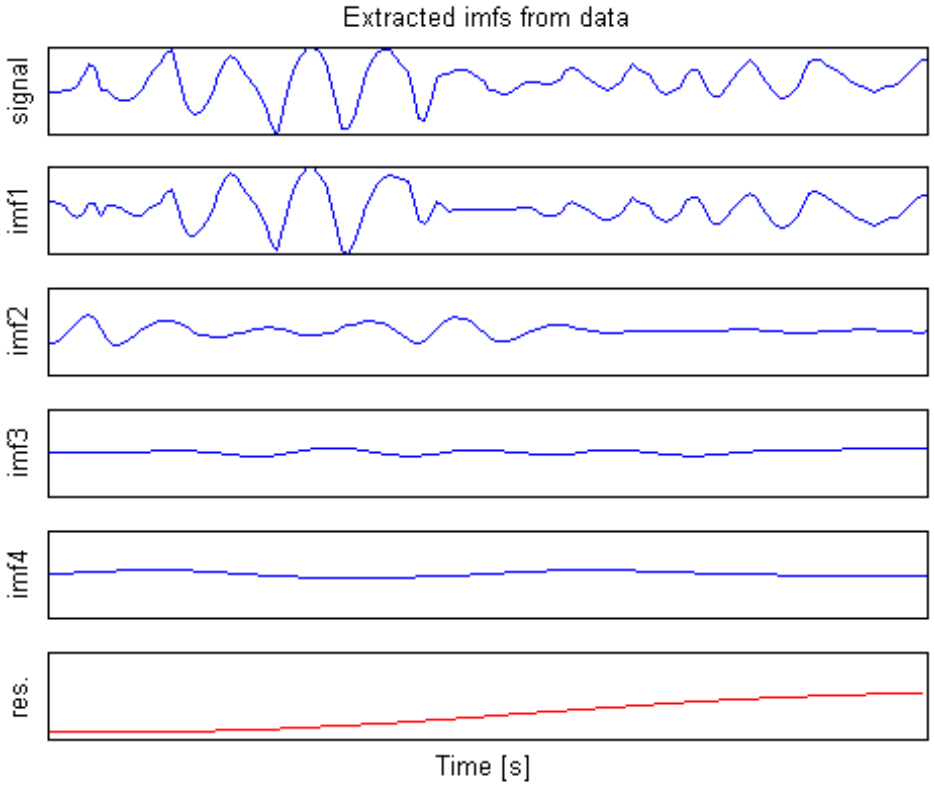


Figure 4.13: The intrinsic mode functions (imfs) for y component of electric field data (C1) on 01 01 2001 between 02 00 00 and 02 00 10 UT. From to bottom, panels show original data, 1st, 2nd, 3rd and 4th imfs , followed by the first imf. The 5th does not meet the sifting conditions.

### 4.4.2 Hilbert Spectra: Instantaneous frequency (IF) for the different $imf$s

The extracted imfs are transformed using a Hilbert transform. The results show instantaneous frequencies of the different imfs extracted from magnetic field data (see Figure 4.14 and 4.15) and electric field (see Figure 4.16 and 4.17). Figure 4.14 shows frequency decomposition using a Hilbert Transform on magnetic field data extracted into $imf$s. Figure 4.15 shows the outline of Figure 4.14. Figure 4.16 shows instantaneous frequency decomposed using a Hilbert Transform on electric field data extracted into $imf$s. Figure 4.17 is the outline of Figure 4.16.

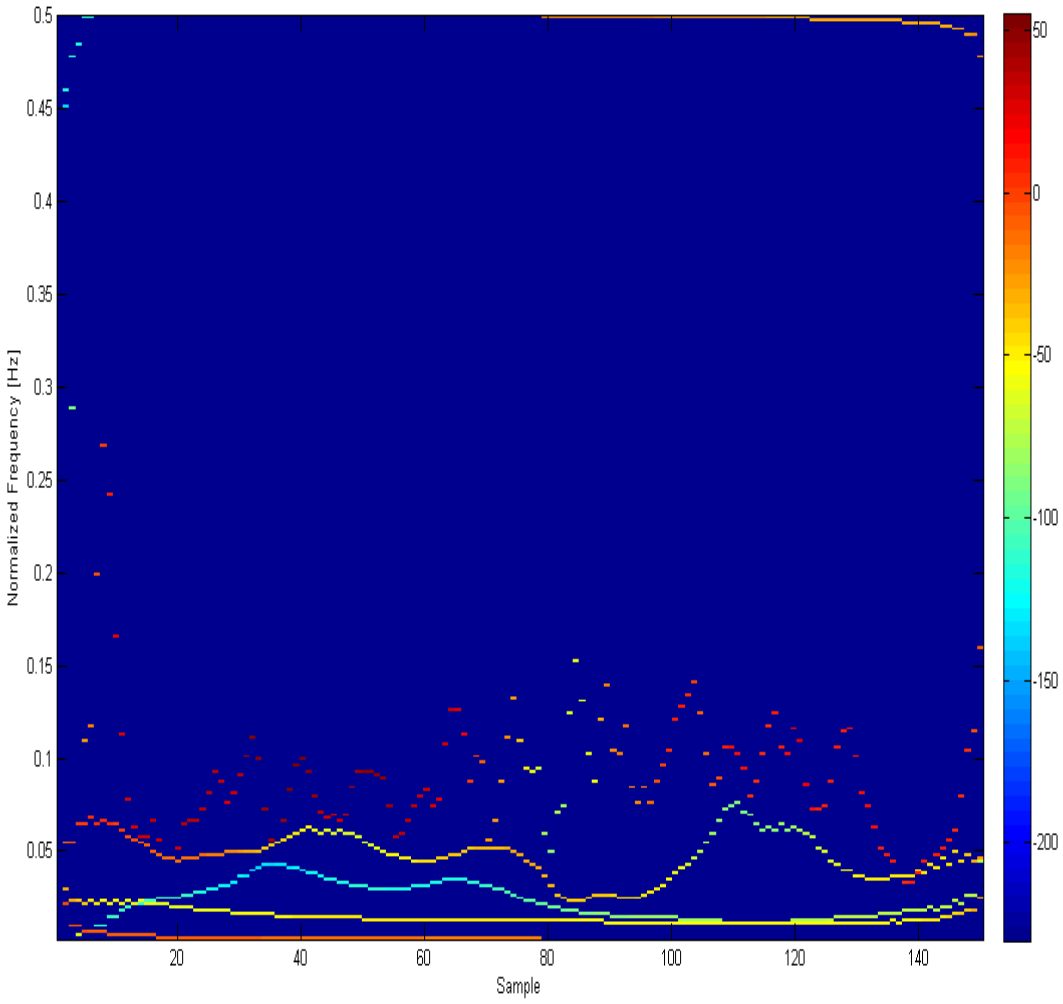


Figure 4.14: The instantaneous frequencies (IF) of all the extracted intrinsic modes from magnetic field data on 01 Feb. 2001 from 02 00 00-02 10 00 UT using Simple Hilbert Transform.

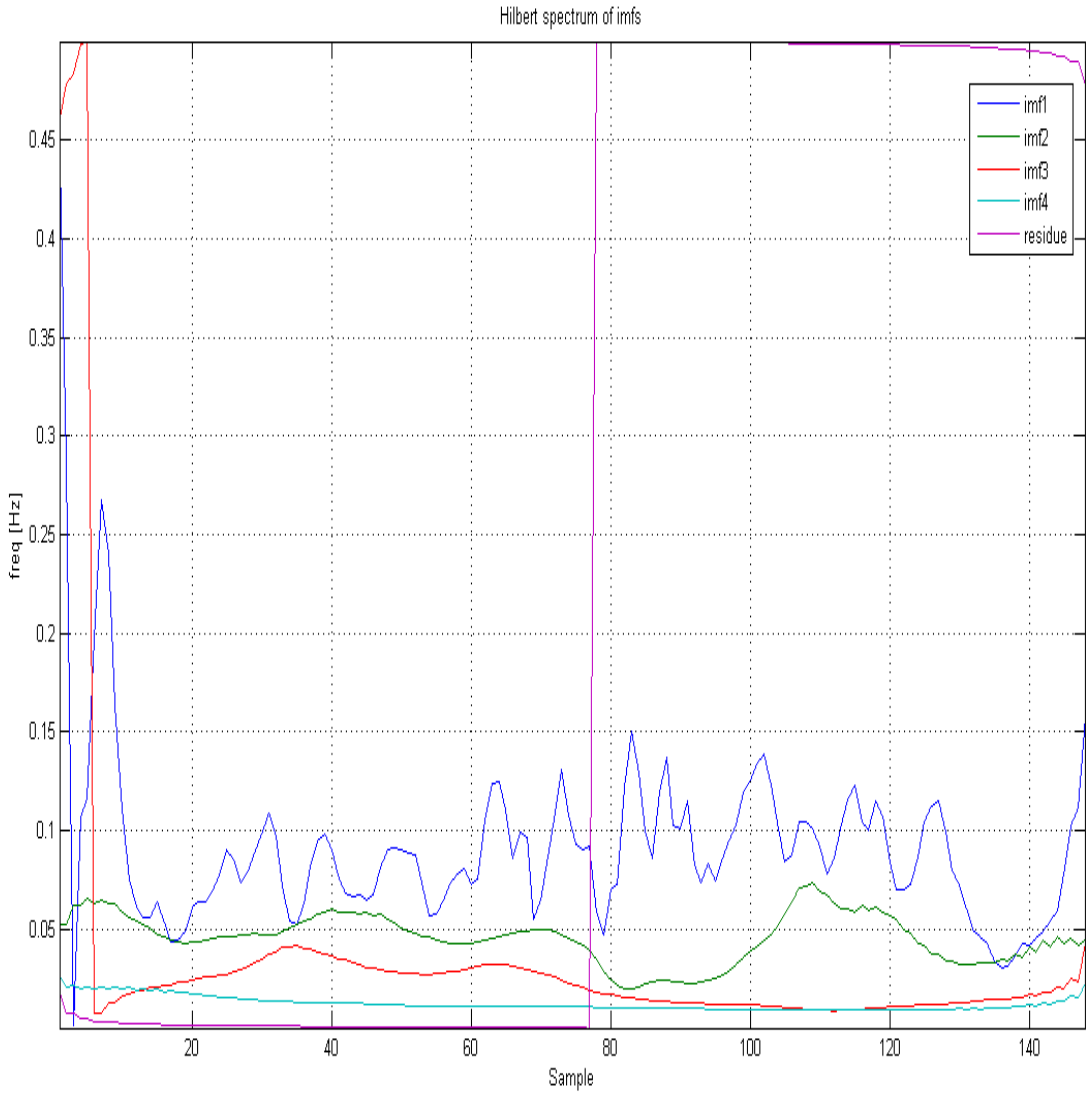


Figure 4.15: The instantaneous frequencies (IF) of all the extracted intrinsic modes from magnetic field data on 01 Feb. 2001 from 02 00 00-02 10 00 UT using Simple Hilbert Transform. This figure shows the outline of figure 4.14. It gives more details of figure 4.14 with legend that labels all the imfs and residue with the associated instantaneous frequencies.

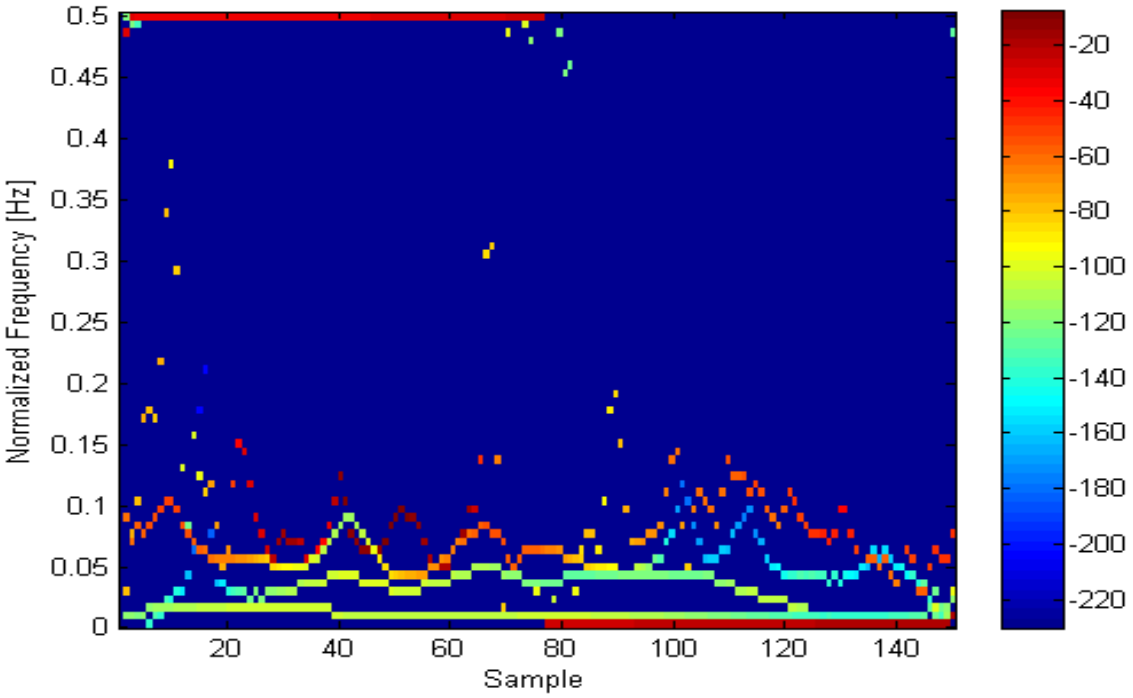


Figure 4.16: The instantaneous frequencies (IF) of all the extracted intrinsic modes from electric field data on 01 Feb. 2001 from 02 00 00-02 10 00 UT using Simple Hilbert Transform.

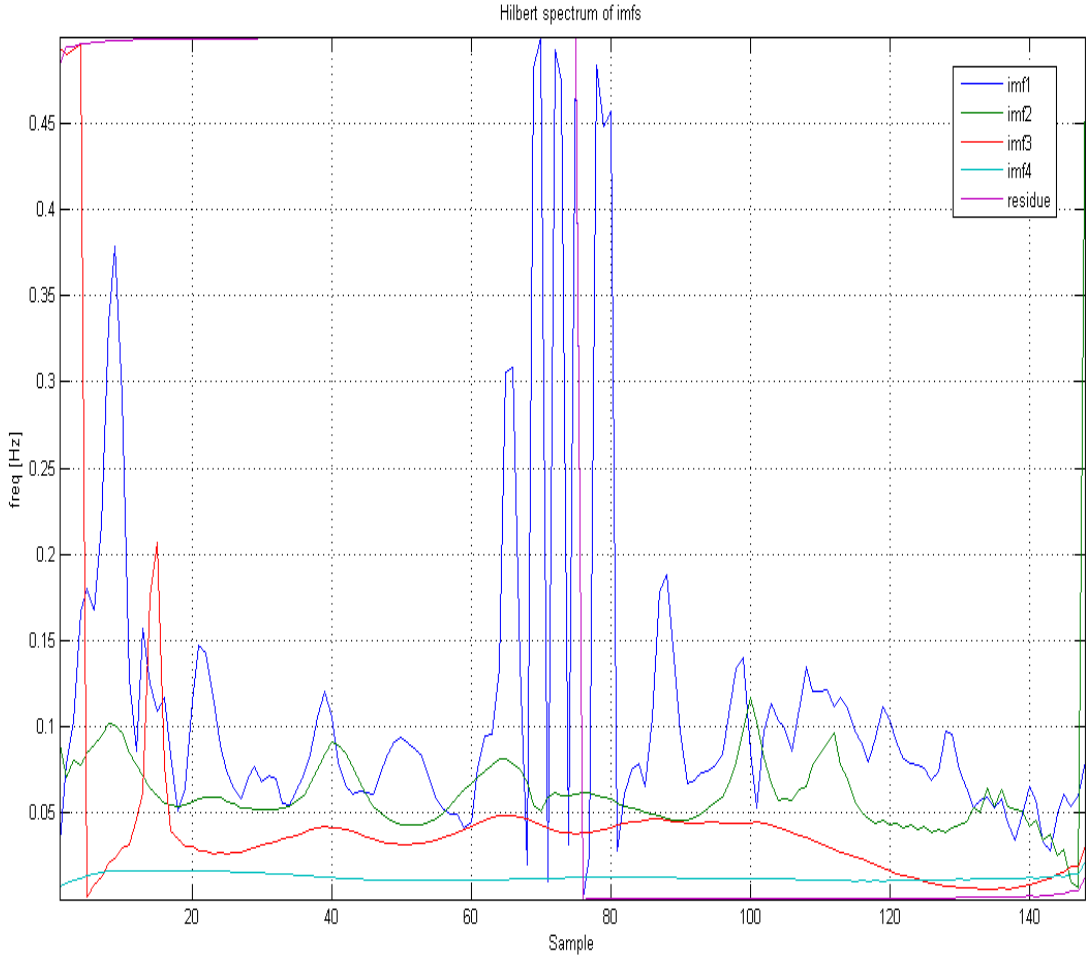


Figure 4.17: The instantaneous frequencies (IF) of all the extracted intrinsic modes from electric field data on 01 Feb. 2001 from 02 00 00-02 10 00 UT using Simple Hilbert Transform. This figure shows the outline of figure 4.16. It gives more details of figure 4.16 with legend that labels all the imfs and residue with the associated instantaneous frequencies.

### 4.4.3 Spectral analysis

We use the spectrogram of the Fourier transform to investigate the average frequency content of each imf, and scalogram of the Wavelet transform to confirm the time instant of the average frequency obtained from the Fourier transform. The results of Fourier transform in the spectrogram of Figures 4.18−4.21 show the power spectral density (psd) of the first, second, third and fourth imfs obtained from y-component data of C1. Figure 4.22 shows the spectrogram of all the imfs plotted together. The vertical dash lines indicate the corresponding average frequency. Another set of results using wavelet (Gaus4) transform in the scalogram of Figures 4.23−4.26 show the continuous wavelet transform of the first, second, third and fourth *imfs*. Thus, determine the instantaneous frequency of the waves, which is the main energy and momentum driver in the considered signal.

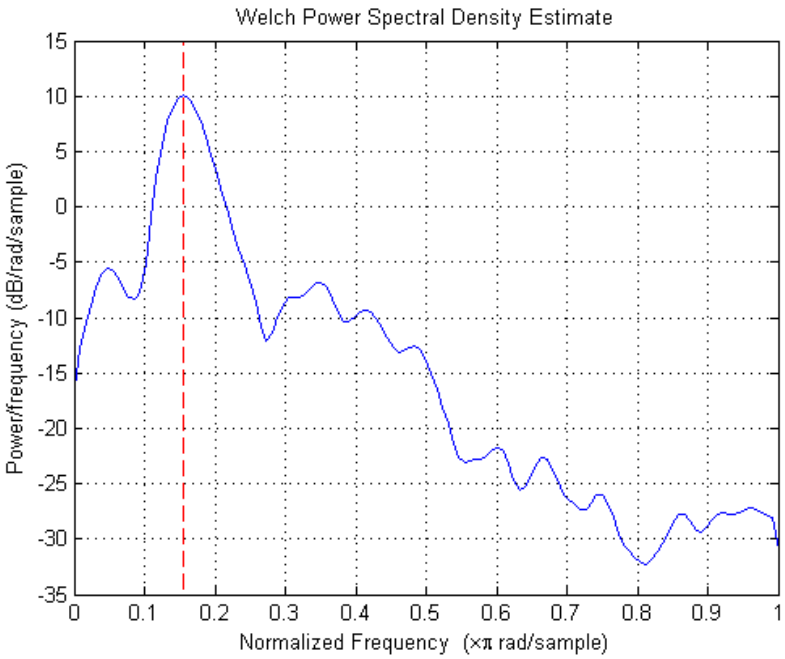


Figure 4.18: Spectral analysis of 1st imf showing average frequency of the that mode. The imf is extracted from a magnetic field data on 01 01 2001 between 02 00 00 and 02 10 00 UT.

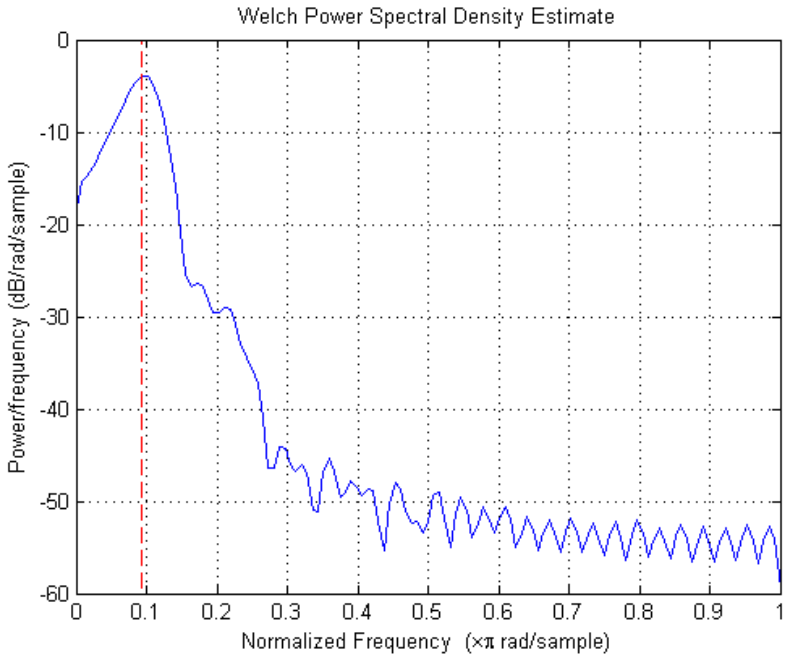


Figure 4.19: Spectral analysis of 2nd imf showing average frequency of the that mode.

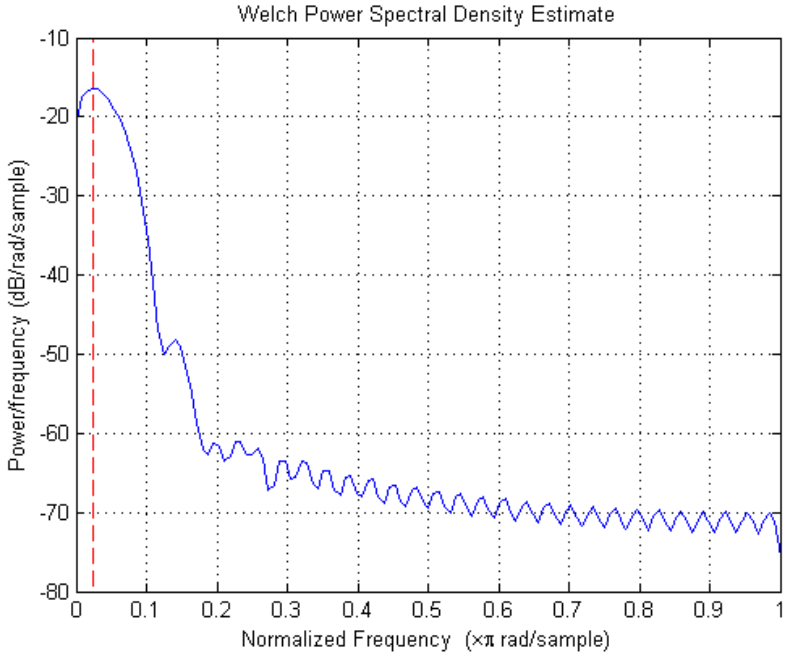


Figure 4.20: Spectral analysis of 3rd imf showing average frequency of the that mode.

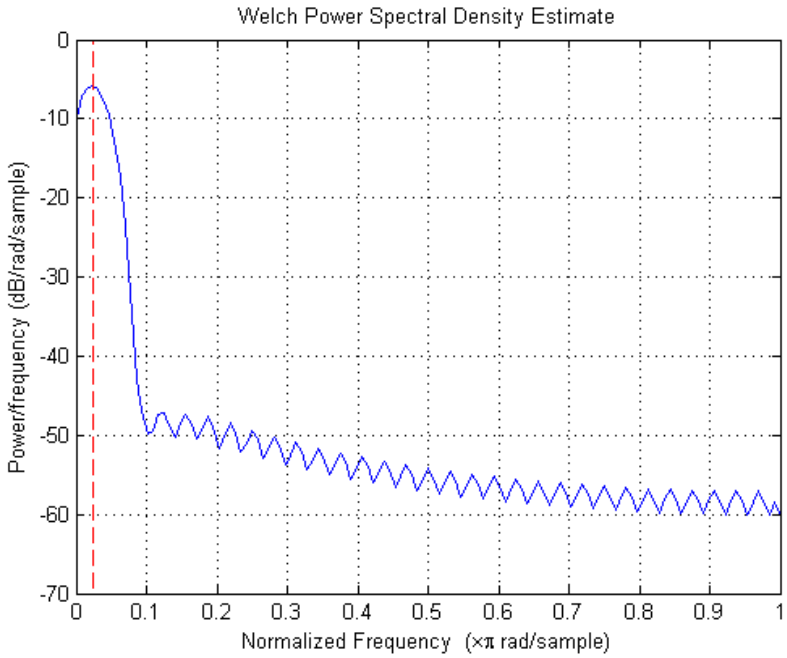


Figure 4.21: Spectral analysis of 4th imf showing average frequency of the that mode.

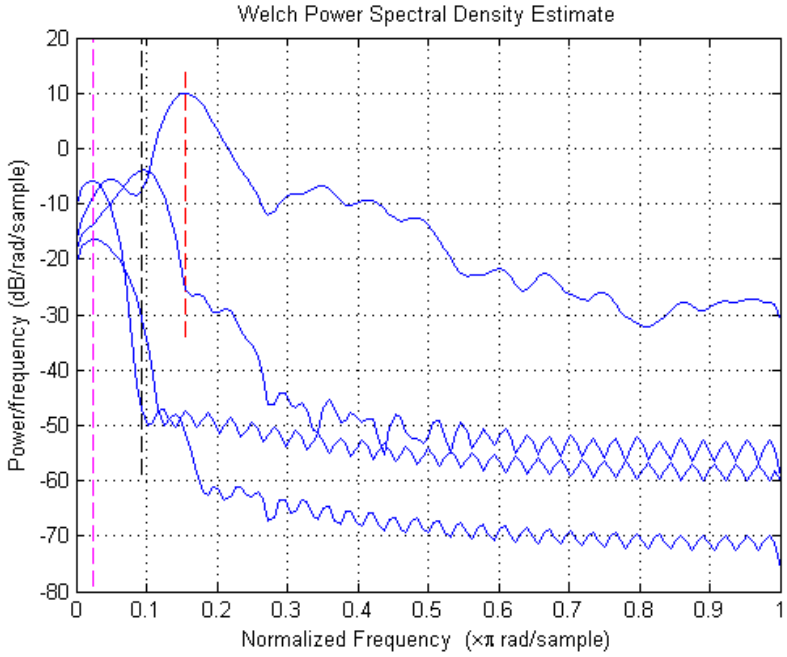


Figure 4.22: Spectral analysis of all imfs showing average frequencies of the modes.

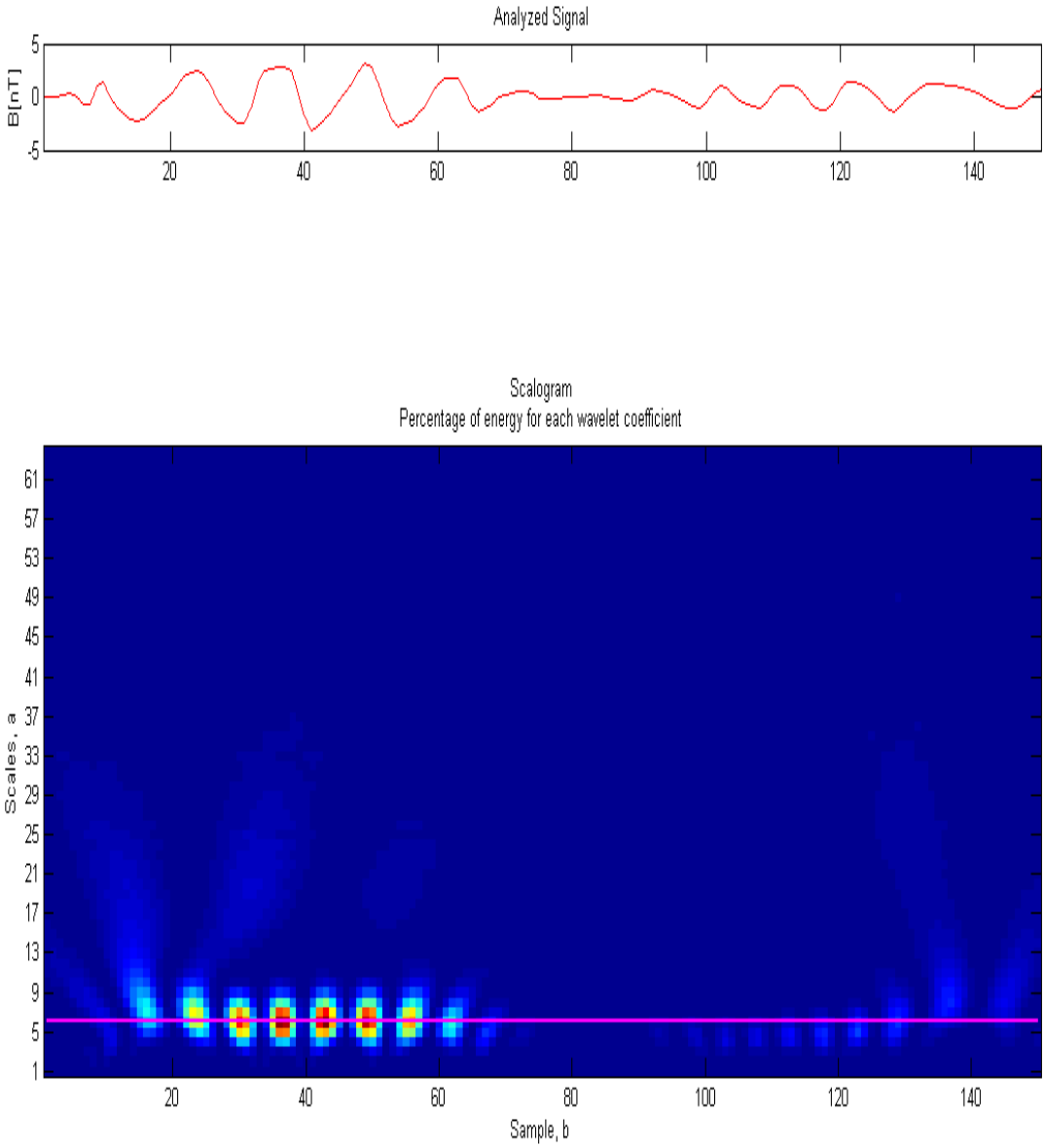


Figure 4.23: Scalogram of 1st imf showing energy associated with the frequency of the mode. Using Gaus4 wavelet in the scalogram, maxima of energy are detected at scale 6, which corresponds to frequency 20.8mHz. This is one method of using wavelet analysis to obtain spectral information. The top panel is the profile for the *imf* being the signal for wavelet transformation. Its y− axis is the amplitude of the signal in [nT] while its x− axis is the number of sample.

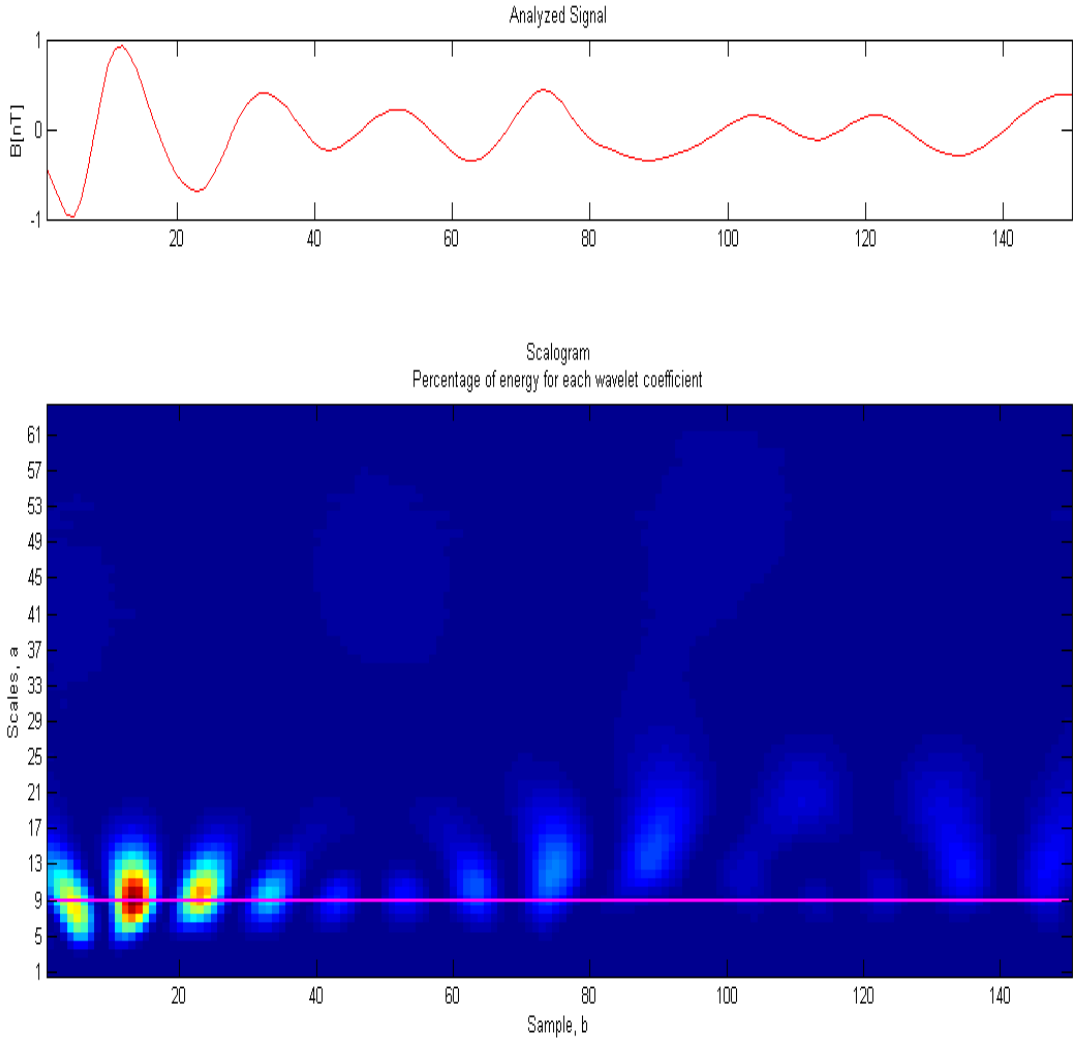


Figure 4.24: Scalogram of 2nd imf showing energy associated with the frequency of the mode. Using Gaus4 wavelet in the scalogram, maxima of energy are detected at scale 9, which corresponds to frequency 13.9mHz. The top panel is the profile for the *imf* being the signal for wavelet transformation. It's y− axis is the amplitude of the signal in [nT] while its x− axis is the number of sample.

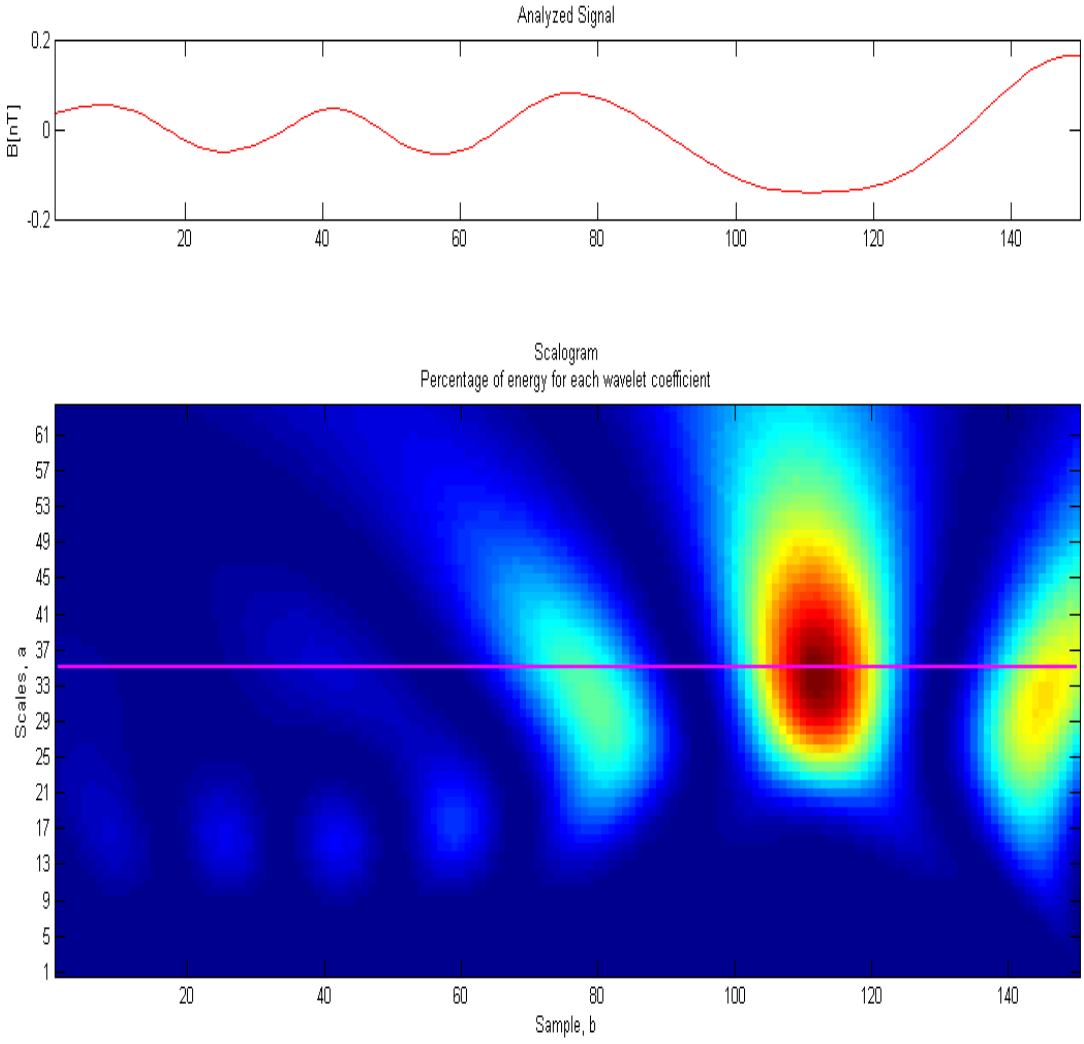


Figure 4.25: Scalogram of 3rd imf showing energy associated with the frequency of the mode. Using Gaus4 wavelet in the scalogram, maxima of energy are detected at scale 35, which corresponds to frequency 3.6mHz. The top panel is the profile for the *imf* being the signal for wavelet transformation. Its y− axis is the amplitude of the signal in [nT] while its x− axis is the number of sample.

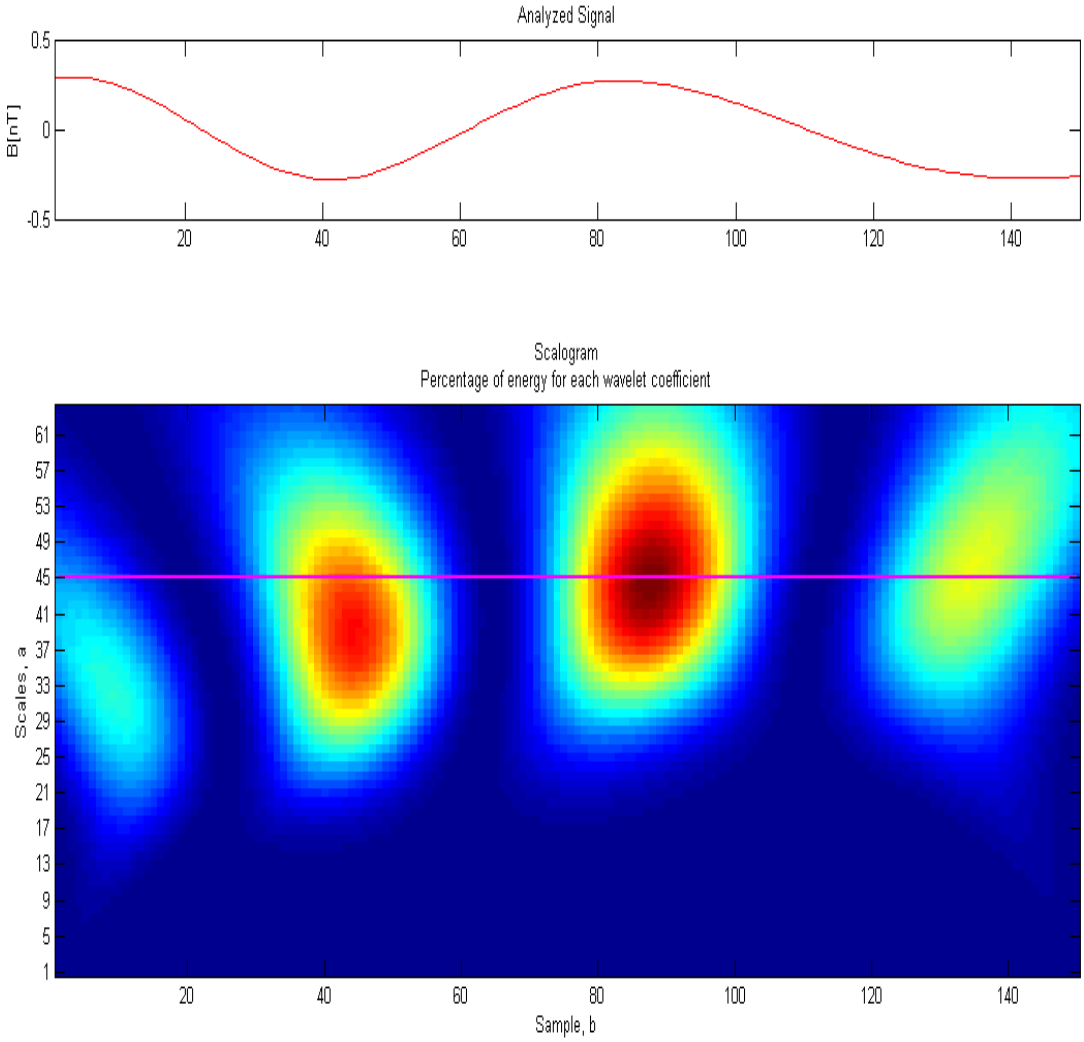


Figure 4.26: Scalogram of 4th imf showing energy associated with the frequency of the mode. Using Gaus4 wavelet in the scalogram, maxima of energy are detected at scale 45, which corresponds to frequency 2.8mHz. The top panel is the profile for the *imf* being the signal for wavelet transformation. Its y− axis is the amplitude of the signal in [nT] while its x− axis is the number of sample.

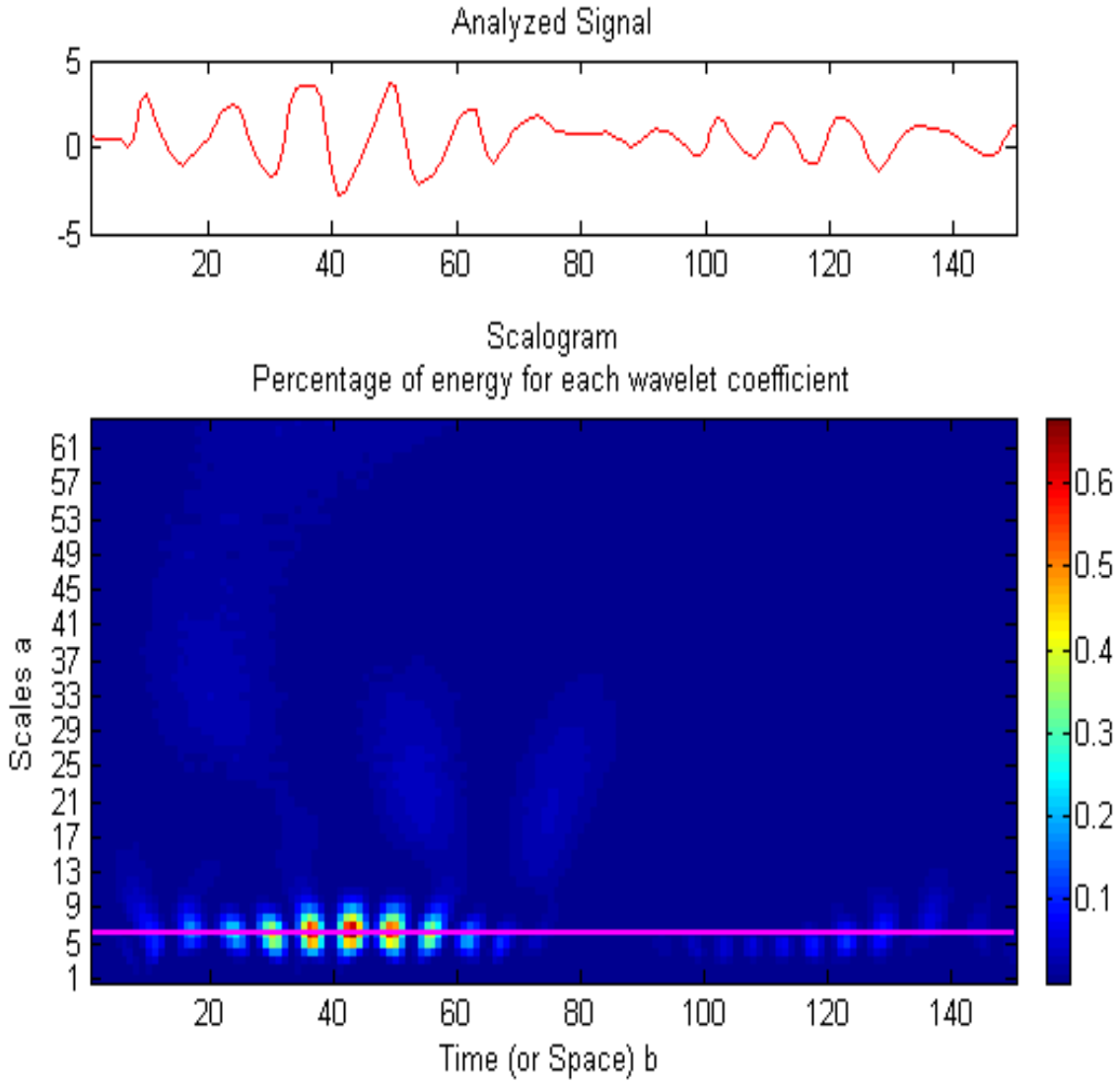


Figure 4.27: Scalogram of the original data showing energy associated with the frequency of the mode. Using Gaus4 wavelet in the scalogram, maxima of energy are detected at scale 6, which corresponds to frequency 20.8mHz. This reveals energy that is high between sample point 20 and 60 for time between 80 and 240 secs. But suddenly reveals very low energy between 240 and 600 sec corresponding to sample point from 60 - 150. The top panel is the profile for the *imf* being the signal for wavelet transformation. Its y− axis is the amplitude of the signal in [nT] while its x− axis is the number of sample.

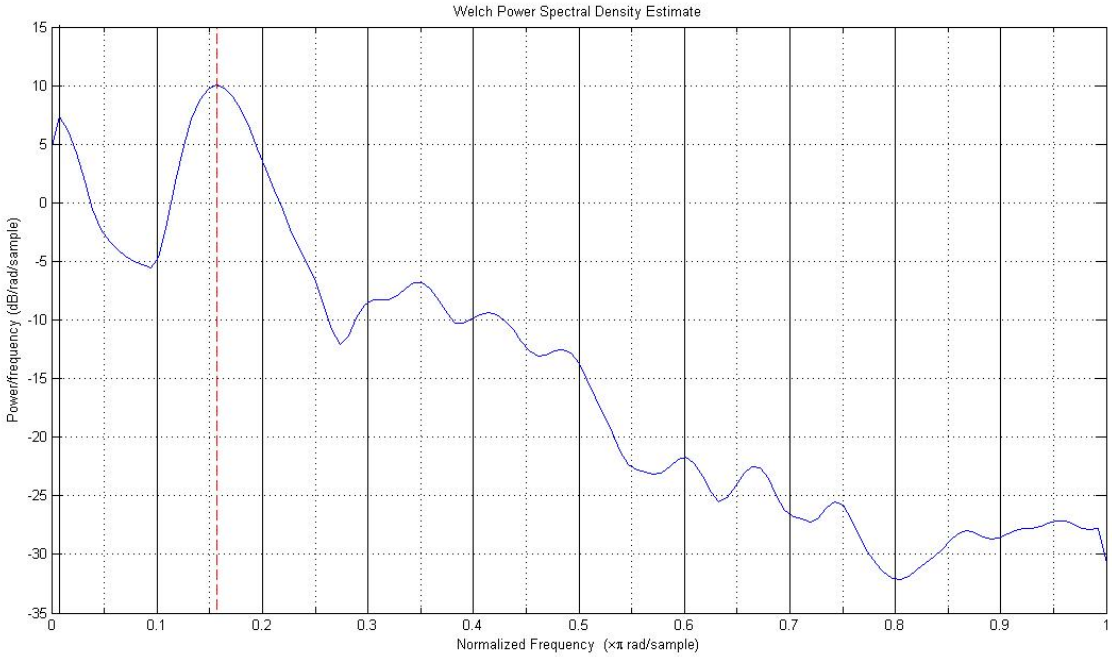


Figure 4.28: Spectral analysis of the original data showing two average frequencies of about 0.01 and 0.16 Hz. The imf is extracted from a magnetic field data on 01 01 2001 between 02 00 00 and 02 10 00 UT.

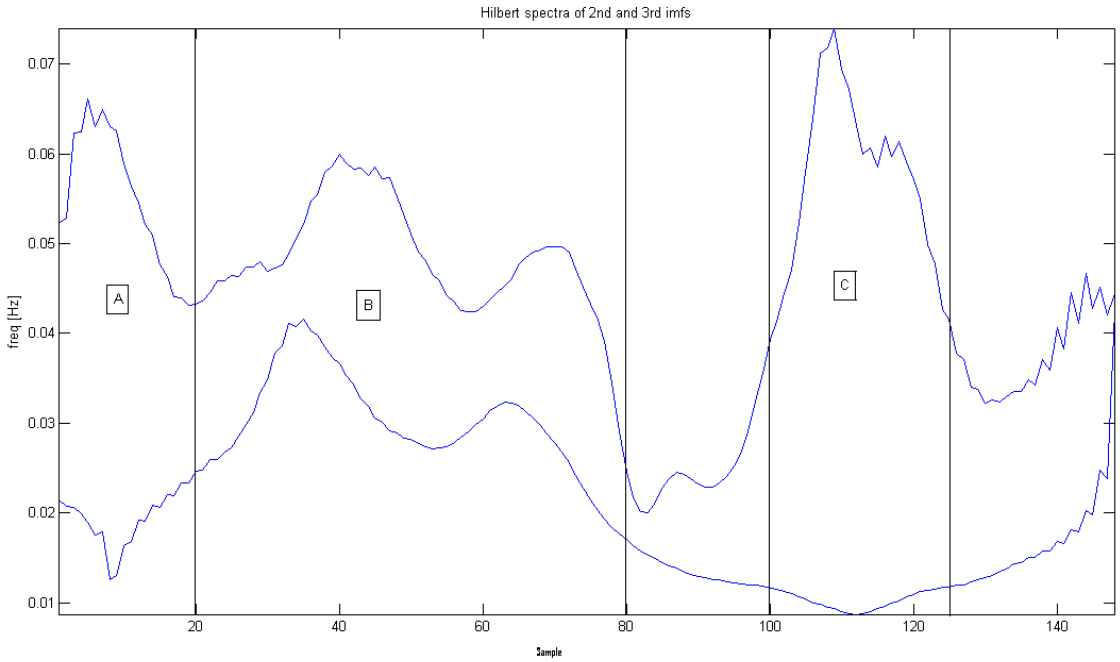


Figure 4.29: The instantaneous frequencies (IF) of 2nd and 3rd imfs of magnetic field data on 01 Feb. 2001 from 02 00 00-02 10 00 UT using Simple Hilbert Transform. The instantaneous frequency of the second $imf$ varies between 0.00 and 0.04 Hz, while the instantaneous frequency of the third $imf$ varies between 0.02 and 0.07 Hz. The plot has been divided into A, B and C portions. Portion A covers $1-20$ samples, B covers $20-80$ samples and C covers $100-125$ samples. Portion A shows anti−phase superposition of two instantaneous frequencies, B shows superposition and C shows another anti−phase superposition.

Wavelet analysis is an adjustable window Fourier spectral analysis that uses scale, a and translation, b parameters. Figure 4.23 is a scalogram of the scale and translation parameters of extracted imf1. This scalogram explains how Wavelet analyses only high amplitude signals. Energy distribution concentrates within $20-60$ samples on scalogram as shown in figure 4.23. But the time series above shows both high and low amplitude fluctuation. This calls for an approach that can analyse both high and low amplitude as dictated by the data. In Wavelet analysis, frequencies and scales relationship is plotted, then this knowledge is used in the plot of scales againt time. This plot quickly gives the insight of what the frequencies are across the data. Figures $4.23-4.27$ show scalograms of the four extracted imfs. These scalograms show the energies distribution of the imfs and the associated frequencies as a function of the scales parameter. Scalogram in figure 4.23 shows concentration of energy between 20 and 60 samples on the imf1. This is the portion where imf1 has high amplitude. It does not give any clear energy for the portion with low amplitude. This characteristics of Wavelet Transform (WT) is found in figures 4.24 and 4.27. This makes WT not suitable for analysis of low amplitude signal.

In figures 4.25 and 4.26, the scalograms show energies that spread out. This makes it difficult to identify the scale, therefore making the determination of frequencies to be difficult. Figures 4.25 and 4.26 have frequencies 3.6 mHz and 2.8 mHz respectively. This shows that at low frequencies Wavelet spectra display energies whose frequencies are difficult to determine. There is similarity in figures 4.23 and 4.27. Figure 4.17 shows the scalogram of imf1 while figure 4.27 shows the scalogram of the original signal. The observed similarity is due to the energy distribution between 20 and 60 samples in imf1 since the energies of low amplitude signals are difficult to detect using wavelet transform.

The choice of Hilbert Transform (HT) for frequency determination has helped to

eliminate these limitations of Wavelet Transform. WT has been the common tool for the analysis of space plasma data due to its ability to analyse linear and non−stationary behaviour of waves.

Our results show that Qf(t)'s (equation 4.40) using first, second, third and fourth imfs extracted from y-component of magnetic field data on 01 02 2001 between 02 00 00 and 02 10 00 UT are 1.0720, 1, 1 and 0.1433. Setting TV=1, allows the second, third and fourth imfs to be selected. The instantaneous frequencies for second and third imfs are given in figure 4.29.

## 4.5 Analysis and Discussion

From Figure 4.15, the Hilbert spectra for the decomposed magnetic field data shows four characteristic instantaneous frequencies. Each representing the instantaneous frequency of each $imf$. Figure 4.17 is the Hilbert spectra of the decomposed electric field data taken from observations on 01 01 2001 between 02 00 00 and 02 10 00 UT. These spectra exhibit the same pattern with similar variation in each instantaneous frequency plot. This behaviour has been further confirmed in the power spectral density. The spectral density for both the magnetic and electric fields decomposed data show similar average frequency (see Figures 4.18−4.21 for magnetic field data, but the electric field figures are not shown.

Continuous wavelet scalogram in Figure 4.23−4.26 reveal characteristics that show that Wavelet can only analyse high frequency signals. The scalogram of figures 4.23 and 4.27 have the same frequency. These figures represent the extracted imf1 and the original data respectively. This characteristics shows that the Wavelet transform has not extracted useful information for the other imfs. It is therefore clear that a wavefield with high and low frequency can not be analysed with Wavelets.

The original data used in all these have been sampled with frequency having a nyquist frequency of about 0.13Hz. This simply informs that the power spectra of the $imf$ above this point will alias. By the introduction of the relative energy character rate, RECR(t), the ratio of this for each $imf$ to the original data gives result with first $imf = 1.0720$, second $imf = 1.0000$, third $imf = 1.0000$ and the fourth $imf = 0.4120$.

Table 4.2 compares Power Spectral Density (PSD), Continuous Wavelet Transform (CWT) and Hilbert Transform (HT) applied on each imf relative to the computed ratio of relative energy character rate (Qf(t)). In the first row from top, we have the imfs

| Imf | 1st (nT) | 2nd (nT) | 3rd (nT) | 4th (nT) |
|---|---|---|---|---|
| Qf(t) | 1.072 | 1.000 | 1.000 | 0.412 |
| PSD | 0.156 Hz | 0.093 Hz | 0.020 Hz | 0.020 Hz |
| Wavelet spectra | 0.021Hz | 0.014 Hz | 0.004 Hz | 0.003 Hz |
| Mean Hilb. spectra | 0.092 Hz | 0.046 Hz | 0.037 Hz | 0.012 Hz |

Table 4.2: Relationship between the ratio of the relative energy character rate of each $imf$ to that of the original data and Power spectral density and continuous wavelet and the mean Hilbert spectra on each $imf$.

with 1st, 2nd, 3rd and 4th extractions in 2nd 3rd, 4th and 5th columns. In the second row, we have the computed Qf(t) of imfs to original signal. The values are in the 2nd, 3rd, 4th and 5th columns. In the third row, the PSD are shown. In the fourth row, the CWT are shown. And in the last row, HT are shown.

In a glance, the frequencies computed with different methods relative to the computed Qf(t) for imfs are clearly seen. By setting the threshold value (TV) to 1, the value of Qf(t) >TV is 1.0720. The PSD for this Qf(t) is 0.156 Hz. The CWT frequency is 0.021 Hz and average HT is 0.092 Hz. But the nyquist frequency is 0.125 Hz while the PSD is 0.156 Hz. This shows that there is a possibility of alias because the the determined PSD is greater than the nyquist frequency. CWT frequency of 0.021 Hz looks good but has only given the frequency of a short portion (between $20-60$ samples) of the data. The average HT frequency of 0.092 Hz also looks good, but the general instanstaneous frequency profile is rapidly changing across the sample. So we discard the imf1 with this value of Qf(t) value.

Considering the value of Qf(t) $\leq$ TV, PSD are 0.093 Hz, 0.020 Hz and 0.020 Hz for 2nd, 3rd and 4th imfs respectively. CWT spectra are 0.014 Hz, 0.004 Hz and 0.003 Hz for 2nd, 3rd and 4th imfs respectively. Average HT spectra are 0.046 Hz, 0.037 Hz and 0.012 Hz for 2nd, 3rd and 4th imfs respectively. Our analysis shows that the instantaneous frequencies using HT give slowly varying frequencies for 2nd, 3rd and

4th imfs. This slow variations shows peak for imf2 at 0.074 Hz which compares well with the PSD value of 0.093 Hz. HT frequency has a mean value at 0.037 Hz which closely compares with PSD of 0.020 Hz for third imf (imf3). HT shows instantaneous frequency that varies slowly with a mean value of 0.012 Hz which closely compares with PSD value of 0.020 Hz for 4th imf. Our analysis also shows that PSD gives values that are better than those of CWT since it is able to give the average frequency of low amplitude and frequency signals. We also found that at very low frequency, PSD gives a contant frequency as in the 4th imf. Since PSD frequency value for the 4th imf is constant, plot of the instantaneous frequencies of 2nd and 3rd imfs gives profile which can be used to understand the dynamics of the waves.

The scalogram of continuous wavelet on the original data reveals energy that is high between sample point 20 and 60 for time between 80 and 240 secs. But suddenly reveals very low energy between 240 and 600 sec corresponding to sample point from 60 - 150 (see Figure 4.27). This scalogram returns the same frequency to that of the first $imf$. Our investigation with PSD on the original data reveals two average frequencies of about 0.01 and 0.16 Hz (see Figure 4.28) . The instantaneous frequency of the second $imf$ varies between 0.00 and 0.04 Hz, while the instantaneous frequency of the third $imf$ varies between 0.02 and 0.07 Hz. We have combined the knowledge of nyquist theorem and the calculated Qf(t) to ascertain the statistical significance of the second and third imfs. We further take into consideration the profile of the original data Figures 4.9 and 4.10, which clearly shows a superposition of waves. In Figure 4.29, we have divided the entire instantaneous frequency space into three portions. The different portions are considered due to the different characteristic behaviours. Portion A covers $1-20$ samples, B covers $20-80$ samples and C covers $100-125$ samples. Portion A shows anti$-$phase superposition of two instantaneous frequencies, B shows superposition and C shows another anti$-$phase superposition. From the table of correlation and coherency

| Zone | A | B | C |
|---|---|---|---|
| Correlation | -0.72 | 0.66 | -0.81 |
| Coherency | 0.75 | 0.67 | 0.84 |

Table 4.3: Correlation and coherency on the instantaneous frequencies of second and third $imfs$ extracted from a data of Figure 4.3. The instantaneous frequency space was divided into A, B and C zones.

between instantaneous frequencies of the second and third $imfs$, we found superposition existing between the two frequency modes. An obvious negative correlation and a strong coherency in zone A explains the attenuated waveform in the original data within that zone due to out of phase superposition. Positive correlation and strong coherency in zone B shows an in-phase superposition which is also found in an enhanced amplitude. Zone C has a high negative correlation and very strong coherency that explain the high attenuation in the waveform of the original data. All of these further confirm the statistical significance of second and third $imfs$ extracted using EMD. Our comparison of the instantaneous frequency obtain in this analysis with the one carried out by Carozzi *et al.* (2004), we found that the instantaneous frequency of the third $imf$ compares well as its PSD at 20 mHz agrees with their range of 20-22 mHz. Between times 0 and 80 secs on Figure 4.9 and 4.10 corresponding to 0 and 20 samples points on Figure 4.29 (zone A) show anti-phase superposition. Between 80 and 320 secs on Figure 4.9 and 4.10 corresponding to 20 and 80 sample points on Figure 4.29 (zone B) show in phase superposition. And between 400 and 600 secs on Figure 4.9 and 4.10 corresponding to 100 and 150 sample points on 4.29 (zone C) show a recovery of anti-phase superposition. This analysis further confirms that the waveform from the original data is as a result of a superposition of two waves.

## 4.6 Summary

The application of Hilbert-Huang transform for the determination of instantaneous low frequency of plasma waves has yielded fruitful results. It offers advantage of revealing more modes embedded in the signal as opposed to the results from the electric field data which was based on simple Hilbert transform. Low frequency is one of the modes defining the dynamics. The use of EMD has clearly shown that the signal which exhibits a non-linear behaviour is made up of two superimposed waves as demonstrated in figures 4.29. The application of HHT, especially when taken into consideration the improvements achieved on EMD, to space plasma could offer results that would represent more informatively the dynamics of the signal. Using HHT shows a low frequency wave and other frequencies waves as opposed to single frequency obtained using SHT, which only computes the low frequency as given by HHT. It is evident in the results of magnetic field data taken at the same period of time as the electric field in Carozzi *et al.* (2004). The above summary confirms that the original data is a superposition of two waves. The electric field results showed one mode with low frequency ranging from $0 - 22mHz$ which is consistent with the third $imf$ with low frequency ranging from $0.00 - 0.04Hz$ showing a peak of 0.04Hz. By comparison, HHT has given more physical meaning to the data which is evident in the realization of superposition of two waves constituting the waveform of figure 4.10. Therefore, the application of HHT for the analysis of space plasma promises meaningful result. The analysed data reveals that the wave−field is made up of superimposed waves. The instantaneous low frequencies of the imfs, which have been separated from high (rapidly varying) frequency imf, show a slowly varying behaviour across the sample. The instantaneous frequencies of the imfs reflect the characteristic beahaviour of the data. Application of HHT will be appreciated as we use it to determine the instantaneous wave vector and study the propagation of plasma waves in the following chapter.

# Chapter 5

# Local Wave vector analysis

## 5.1 Introduction

The instantaneous wave vector analysis depends on complex valued signal [Carozzi et al., 2004] that is analytically treated [Gabor, 1946] for every collected real valued signal. This thesis used Simple Hilbert Transform (SHT) to achieve analytic representation of the real valued signal. The uniqueness in the analysis is based on the combination of empirical mode decomposition (EMD) technique with Simple Hilbert Transform (SHT) to analyse space plasma data. Application of Simple Hilbert Transform [Carozzi et al., 2004] on electric field data yielded a good result but was limited due to its inability to handle multi−component data. The application of EMD has provided solution to this drawback in Instantaneous local wave (ILW) vector estimation. We have found ILW very useful once the data has been extracted to its different wave modes. Four point observations of Cluster provide a unique possibility to determine various characteristics of waves. Wave vectors serves as means by which one can derive wavelengths, propagation directions, phase velocities, dispersion relations,

etc. It was not until the launch of Cluster that it was possible to obtain wave vectors in $3D$ from space plasma observations. The following section introduces how to determine wave properties using both single and multi-point measurements. The analysis of the spatio-temporal behaviour in space has been widely considered with variety of approaches Paschmann et al. [1988]. There is an approach considering the instantaneous local wave vector, which is based on an assumption of mono-component after filtering the signal and use of simple Hilbert analysis [Carozzi et al., 2004]. For good results, wave vector determination requires more than two spacecraft arrangement like Cluster II mission. Other determinations used assumptions of linearity and non-stationary of the signal with use of a phase differencing technique [Balikhin et al., 1997,b, Walker et al., 2004] or linearity and non-stationary assumptions with K-filtering method [Pincòn and Lefeuvre, 1991, Glassmeier et al., 2001] to determine the three dimensional structure of plasma dynamics. It is true that the basic step to study waves is to identify characteristic time variations of field oscillations of interest. It is of course also possible to directly count the period of waves in the time series representation, but generally it is difficult to do because waves are not quasi-monochromatic in many cases. Instead, one computes the cross spectral density ($CSD$) as a function of frequency by Fourier transforming magnetic field data and identied wave power at various frequencies to see which frequencies are contributing in the fluctuation [Jenkins and Watts, 1968., Bendat and Piersol, 1980]. To enable the elimination of the assumption of stationarity and linearity, which limit reliable result on the analysis of practical signal such as space plasma, we introduced empirical mode decomposition ($EMD$) technique [Huang et al., 1998] and the improvements that follow have been applied to the data [Flandrin et al., 2004, Huang and Shen, 2005, Rilling and Flandrin, 2006]. This allows the extraction of different wave modes constituting the signal (see Chapter 4). The use of EMD makes the convolution to be local and not global as in other analyses [Huang et al., 1998, Rilling and Flandrin, 2006].

The frequency decomposition of the signals is done using simple Hilbert transform ($SHT$), which is based on the analytic representation Gabor [1946] (see chapter 4) of each extracted wave mode called intrinsic mode function ($imf$). The resultant frequency is instantaneous [Boashash, 1992, Carozzi et al., 2004]. The benefit of the improved EMD and SHT (simply termed Hilbert-Huang transform, $HHT$) is found in the better frequency resolution at low frequencies required and the instantaneous frequency spectra that make available statistics based on the phase differences at each instant of phase. The EMD used here has been improved [Rilling et al., 2003, Flandrin et al., 2004, Huang and Shen, 2005].

## 5.2 Instantaneous wave vector of low frequency waves in the turbulent magnetosheath

### 5.2.1 $Imf$, and instantaneous frequency and wave vector estimation

After the decomposition of a chosen signal (known data) into its different oscillatory modes called the $imfs$ (see chapter 4), the determination of the numerical estimates of the frequency through instantaneous frequency, and the instantaneous spatial gradient of phase of the *imf* is straightforward. The estimation of the frequency content is easily obtained using single or more spacecraft data but the determination of the wave vector requires more than one spacecraft, and provides best results for multi-spacecraft data. The estimation of the instantaneous local frequency and wave vector [Carozzi et al., 2004] has been demonstrated with measurements along worldlines using real valued measurements of four (4) known space-time trajectories as traced by Cluster

II mission electric field instruments. We will start our estimation with magnetic field data similar to the one used in the electric field data demonstration, then compare the results obtained by HHT with the electric field data results demonstrated by filtering which has been the basis by which Carozzi *et al.* 2004 made the estimates. Our average values will be compared with the results of Walker *et al.* (2004).

Using equation 4.42 - 4.44 (see chapter 4), the instantaneous frequencies are determined. The instantaneous wave vector expressed as the spatial gradient of the phase with time is given for two fixed probes [Beall et al., 1982] and multi-probes [Carozzi et al., 2004] and reference therein), the case of multi-probes is given as,

$$\mathbf{k}_i(\sigma) = -\frac{d_x^{(\alpha,1)}\theta_i^{(\alpha)}(\sigma)}{d_x^{(\alpha,1)}\mathbf{x}^{(\alpha)}(\sigma)} \tag{5.1}$$

In x,y,z,

$$\mathbf{k}_i = \begin{pmatrix} k_x \\ k_y \\ k_z \end{pmatrix} \tag{5.2}$$

Using $C_3$ as a reference spacecraft,

$d_x^{(\alpha,1)}\mathbf{x}^{(\alpha)}(\sigma) \equiv$

$$\begin{pmatrix} x^{(1)-(3)} & y^{(1)-(3)} & z^{(1)-(3)} \\ x^{(2)-(3)} & y^{(2)-(3)} & z^{(2)-(3)} \\ x^{(4)-(3)} & y^{(4)-(3)} & z^{(4)-(3)} \end{pmatrix} \tag{5.3}$$

$d_x^{(\alpha,1)}\theta_i^{(\alpha)}(\sigma) \equiv$

$$\begin{pmatrix} \theta_i^{(1)} - \theta_i^{(3)} \\ \theta_i^{(2)} - \theta_i^{(3)} \\ \theta_i^{(4)} - \theta_i^{(3)} \end{pmatrix} \tag{5.4}$$

where $i = 1, 2, 3, ...., n$, is an integer on the $imf$.

Balikhin et al., 2003 has treated the transformation from the projection coordinates

which are non-orthogonal to physical coordinates (GSM, GSE, etc.). In this thesis, we treat $\hat{A}$ for every sample which gives a $3X3$ matrix from the satellite pair separations which are linearly independent. As given in Balikhin *et al.* (2003), $\hat{A}$ is also a transformation matrix computed from the magnitude of the satellite pair separation distances to form non-orthogonal basis vectors . Instantaneous wave vector k is computed using the calculated projection of wave vector along satellite separation (see Table 5.4) .

$$\hat{A}\vec{k} = \check{k} \tag{5.5}$$

where

$$\vec{k} = [\hat{A}]^{-1}\check{k} \tag{5.6}$$

$$\check{k} = [k_1, k_2, k_3] \tag{5.7}$$

where 1, 2 and 3 are the sat13, sat 23 and sat43 pairs. The computed $\vec{k}$ is the instantaneous wave vector, while $\check{k}$ is the instantaneous wave vector projection along satellite pair separations.

## 5.3 Observations and results

The data used in this analysis was obtained from the FGM instrument of Cluster mission [Balogh et al., 1997]. The magnetic field was decomposed using improved empirical mode decomposition (EMD) technique [Rilling and Flandrin, 2006, Huang et al., 2003, Huang and Shen, 2005, Flandrin et al., 2004]. This was done with aim of extracting the different oscillatory modes called intrinsic mode functions ($imf$) constituting the data and removal of the noise contribution in the data that requires great attention. The average frequency content in the different extracted modes was viewed using spectrogram and the time instant of the average frequency viewed with

scalogram. This choice was set as a confirmatory step, which offers an idea to what the instantaneous frequency will look like. The process of noise removal using EMD [Huang et al., 2003, Flandrin et al., 2004], has confirmed EMD as a dyadic filter.

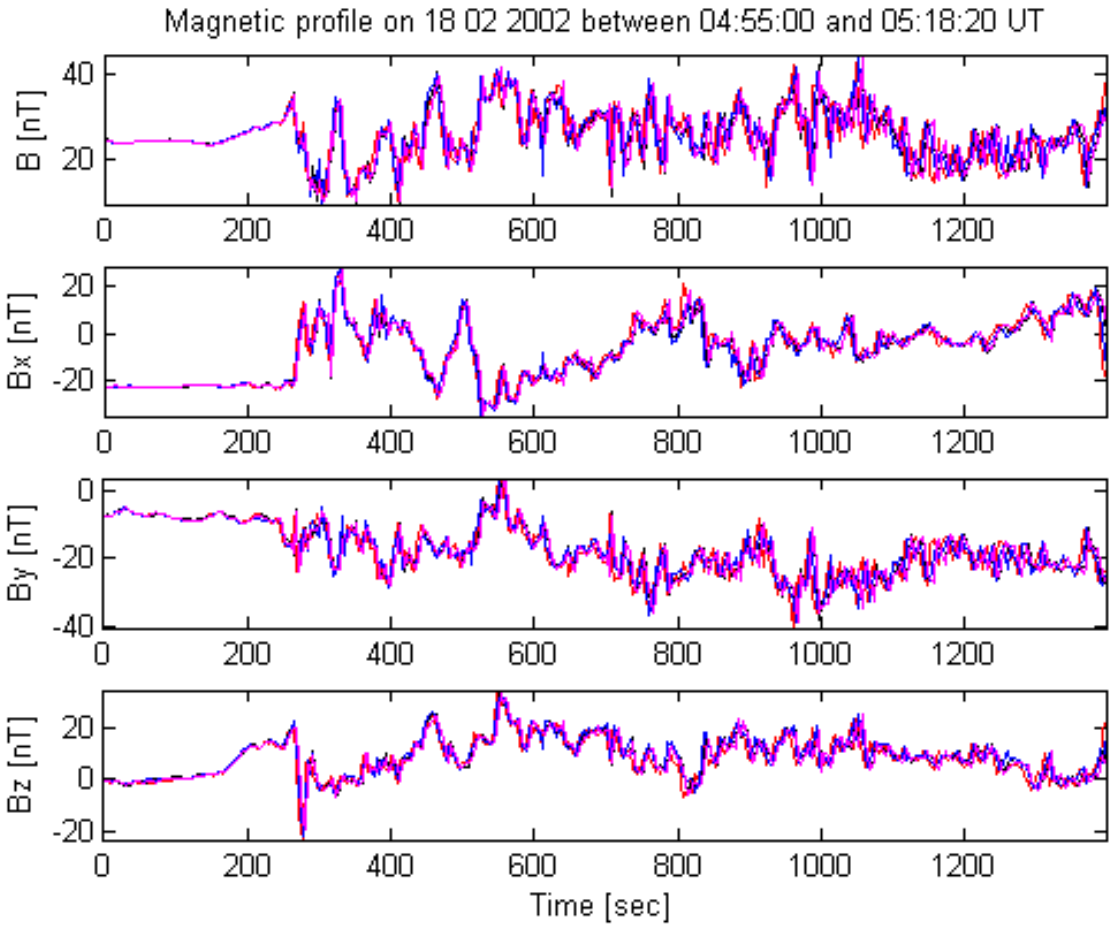


Figure 5.1: Magnetic field profile as spacecraft are outbound towards magnetosheath from Magnetopause. These were collected from the observations of four FGM instrument of Cluster (C1, C2, C3 and C4) spacecraft. The different colours represent data from C1 (red), C2 (black), C3 (blue) and C4 (magenta). From top to bottom, panels show magnetic field magnitude, X, Y, and Z components of magnetic field in GSE coordinates.

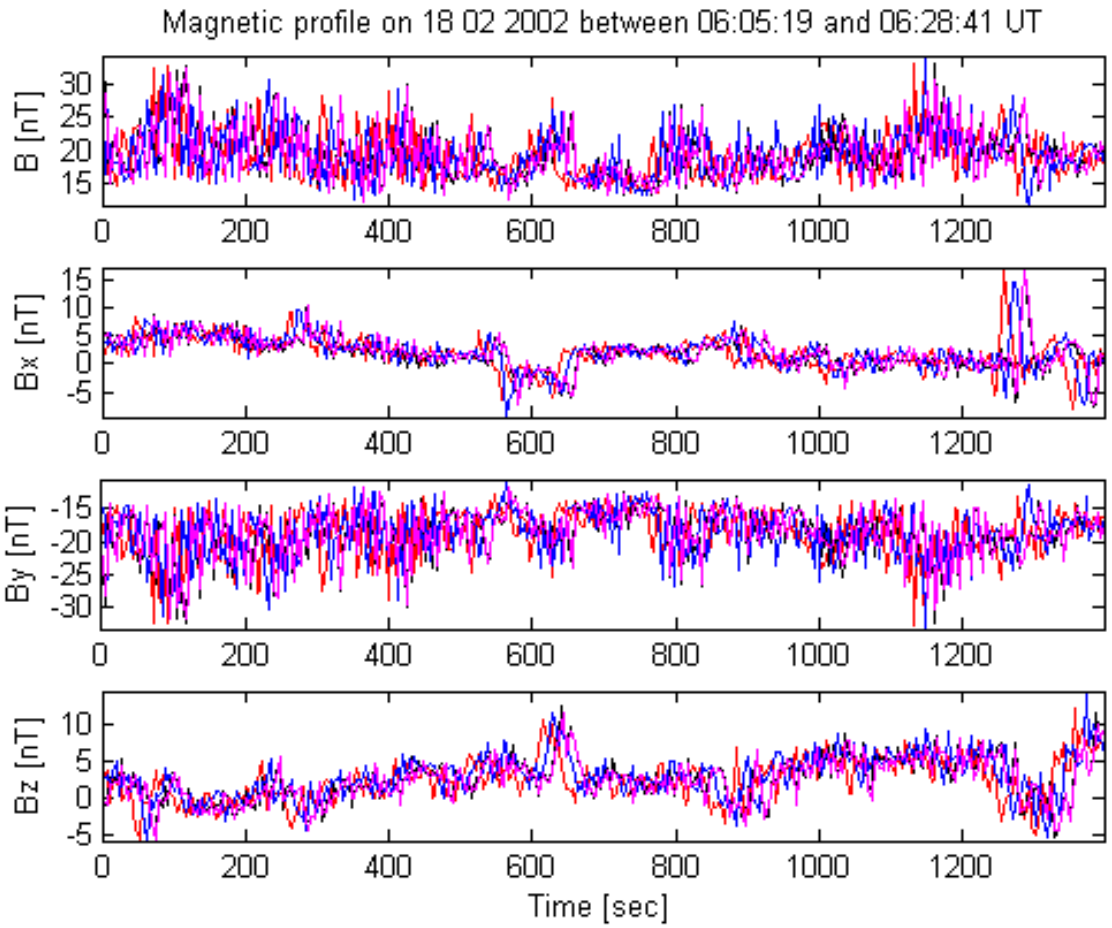


Figure 5.2: Magnetic profile for the magnetosheath data taken close to the bow shock, used for the determination of shock normal. It was collected from the observations of four FGM instrument of Cluster (C1, C2, C3 and C4 spacecraft. The different colours represent data from C1 (red), C2 (black), C3 (blue) and C4 (magenta). From top to bottom, panels show magnetic field magnitude, X, Y and Z components of magnetic field in GSE coordinates.

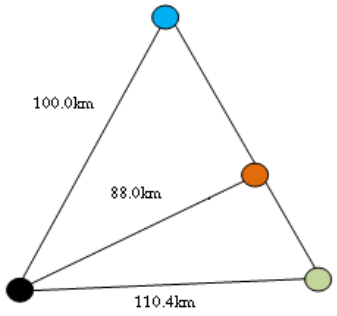


Figure 5.3: A diagram of tetrahedral geometry of the four Cluster spacecraft on 18 02 2002 at 04:55:30 UT. C1 =blue, C2=red, C3=black and C4=green. E=0.18 and P=0.13.

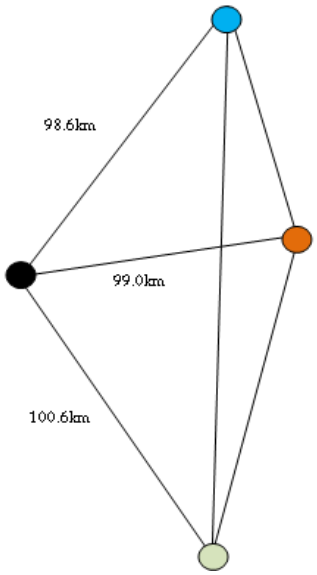


Figure 5.4: A diagram of tetrahedral geometry of the four Cluster spacecraft on 18 02 2002 at 05:58:30 UT. E=0.020 and P=0.003.

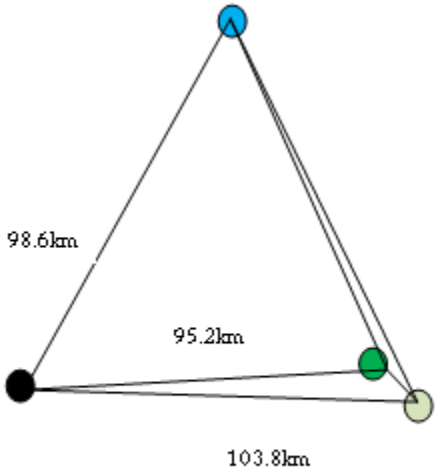


Figure 5.5: A diagram of tetrahedral geometry of the four Cluster spacecraft on 18 02 2002 at 05:27:30 UT. E=0.070 and P=0.040. This is the model we are working with. Scale: 20km=1cm.

The data was taken within the period selected by Walker *et al.* (2004) in their analysis to identify the main wave mode. This analysis compares its results which are based on waveform reflecting non-linear and non-stationary behaviour with that of Walker et al, 2004 using assumption of linear and non−stationary behaviour. The latitude of the spin axis of all four spacecraft is $-84^0$ (in the GSE coordinate). This axis gives a similar of the GSE frame spinning around the X-axis by $180^0$ [Walker et al., 2004]. This analysis is aimed at determining the instantaneous wave vector within the magnetosheath. Downstream data close to bow shock were used to determine the direction of the magnetic field normal [Sonnerup and Cahill., 1967] to bow shock. The data for the determination of shock normal was taken between 06:05:19 and 06:28:41 UT on 18 Feb. 2002. Figure 5.1 is the magnetic field profile as the spacecraft are outbound towards the magnetosheath from the magnetosphere for data collected between 04:55:00 and 05:18:20 UT. The magnetopause was crossed at about 04:59 :00 UT. These were collected from the observations of four FGM instrument of Cluster (C1, C2, C3 and C4) spacecraft. The different colours represent data from C1 (red), C2 (black), C3 (blue) and C4 (magenta). From top to bottom, panels show magnetic field magnitude, X, Y, and Z components of magnetic field in GSE coordinates. And figure 5.2 is the magnetic field profile for magnetosheath data selected for the determination of shock normal. Minimum variance method was used for the determination of the shock normal, which shall be mentioned later. The data was collected from the observations of four FGM instrument of Cluster (C1, C2, C3 and C4 spacecraft. The different colours represent data from C1 (red), C2 (black), C3 (blue) and C4 (magenta). From top to bottom, panels show magnetic field magnitude, X, Y and Z components of magnetic field in GSE coordinates. We collected data in the downstream (magnetosheath) of the bow shock between 05:15:00 and 05:35:00 UT to determine instantaneous wavevector ($\mathbf{k}$). The average minimum and maximum spacecraft separation were 88 and 108 km respectively. The two major parameters of the spacecraft tetrahedral geometry,

| t [h:m:s] | f1 [Hz] | f2[Hz] | Vx[$kms^{-1}$] | Vy[$kms^{-1}$] | Vz [$kms^{-1}$] | \| V \| [$kms^{-1}$] |
|---|---|---|---|---|---|---|
| 05:15:30 | 0.051 | 0.049 | -210 | 56 | 124 | 250 |
| 05:16:30 | 0.051 | 0.065 | -191 | 32 | 116 | 226 |
| 05:17:30 | 0.061 | 0.069 | -161 | 34 | 111 | 199 |
| 05:18:30 | 0.062 | 0.052 | -215 | 116 | 120 | 272 |
| 05:19:30 | 0.062 | 0.043 | -269 | 140 | 155 | 340 |
| 05:21:30 | 0.058 | 0.035 | -211 | 43 | 126 | 249 |
| 05:22:30 | 0.057 | 0.033 | -195 | 28 | 102 | 222 |
| 05:23:30 | 0.059 | 0.035 | -188 | 42 | 120 | 227 |
| 05:24:30 | 0.064 | 0.039 | -185 | 35 | 125 | 226 |
| 05:25:30 | 0.070 | 0.044 | -179 | 43 | 120 | 219 |
| 05:26:30 | 0.076 | 0.056 | -171 | 39 | 115 | 209 |
| 05:27:30 | 0.072 | 0.055 | -198 | 35 | 132 | 240 |
| 05:28:30 | 0.065 | 0.053 | -174 | 33 | 122 | 215 |
| 05:29:30 | 0.057 | 0.045 | -165 | 40 | 126 | 211 |
| 05:30:30 | 0.048 | 0.037 | -159 | 36 | 133 | 211 |
| 05:31:30 | 0.040 | 0.029 | -174 | 33 | 117 | 212 |
| 05:32:30 | 0.047 | 0.021 | -187 | 38 | 137 | 235 |
| 05:33:30 | 0.043 | 0.021 | -176 | 36 | 125 | 219 |
| 05:34:30 | 0.043 | 0.021 | -181 | 39 | 128 | 225 |
| 05:35:30 | 0.044 | 0.021 | -184 | 33 | 125 | 225 |

Table 5.1: Frequency and, plasma bulk velocity components and magnitude between 05:15:30 and 05:35:30 UT on 18-02-2002. The mean and standard errors on the frequencies f1 and f2 are 0.057 ± 0.002 Hz and 0.041 ± 0.003 Hz respectively for x− component of the data.

the tetrahedron elongation E and the planarity P were considered for effective 3-D determination of instantaneous wavevector. Their average values were $E = 0.076 \pm 0.006$ and $P = 0.053 \pm 0.004$ [Robert et al., 1998]. These values are small enough to guarantee good results of $3-D$ measurement since the values of E and P for a regular tetrahedron are close to zero. Figure 5.3 to 5.5 show the various tetrahedral geometries that have been selected to compare with our choices which guarantees our data. Figure 5.3 shows a tetrahedral pattern for data collected at $04:55:30$ UT with $E = 0.180$ and $P = 0.130$ for a scale of $20.000km : 1.000cm$. Where C1=blue, C2=red, C3=black and C4=green. Figure 5.4 is a pattern that supports $E = 0.020$ and $P = 0.003$ for data collected at $05:58:30$ UT. Also, Figure 5.5 shows a pattern that supports

$E = 0.070$ and $P = 0.040$ for data collected at 05 : 27 : 30 UT. We are using the models of Figures 5.4 and 5.5 since both E and P are very small and are close to zero as mentioned above. During this selected period, plasma bulk velocity has the average value of $[-175, 52, 112] kms^{-1}$. In Table 5.1, the instantaneous frequencies are determined from the x− component of the selected data. We observed two waves with instantaneous frequencies f1 and f2 [Hz]. We also observed two set of instantaneous frequencies with z− components. But we observed that the y− component has one wave. The selected period in the magnetosheath exhibits turbulent behaviour which requires special attention in the choice of analysis technique. The period covers the early arrival of waves near bow shock and the region close to the magnetopause. The velocities in Table 5.1 show an anti-sunward flow in the x− direction. The magnitude indicates a wave packet with a non−stationary behaviour that can easily be attributed to superposition of many waves.

## 5.4 Minimum Variance Analysis and shock normal

The Table 5.2 below shows the direction of shock normal using minimum variance technique for waves propagating in towards the bow shock as observed by Cluster instruments $C1$, $C2$, $C3$ and $C4$. The first column of this table shows the four Cluster spacecraft, the second column shows the eigenvectors for the four spacecraft in the first column, third column shows the smallest eigenvalues corresponding to the eigenvectors in the second column and fourth column shows the standard deviation on the magnetic field component along the estimated normal computed from the eigenvalues in the third column. The computed minimum variance results are close to the magnitude of the unit vector in the direction of normal that is given as unity. The eigenvectors in the table are the estimators for the vector normal to the bow shock as the four Cluster

spacecraft crossed the bow shock. And the eigenvalue in the table gives the variance of the magnetic field component along the estimated normal. It is clear from the table that the normal field component for this event fluctuates with average standard deviation of $1.271nT$ about the estimated normal as observed by C1, $1.319nT$ by C2, $1.354nT$ by C3 and $1.395nT$ by C4. The variance analysis is based on Sonnerup and Cahill (1967). Table 5.3 shows the direction of the maximum, intermediate and minimum variance for observation made by C1. The first column is the number of rows for both the eigenvectors and eigenvalues computed from the covariance matrix of the data. The second column is the eigenvalue. The third, fourth and fifth columns are the eigenvectors corresponding to the X, Y and Z − components in Cartesian coordinate system. The sixth column is the product of the mean magnetic field and the eigenvectors. The smallest value in the second column indicates the row with eigenvectors suitable as the direction of normal, which in this case is 1.616. The ratios of the eigenvalues for C1, C2, C3 and C4 have been computed (Table 5.2). Since there is difference between the intermediate and minimum eigenvalues as seen in the ratios of the eigenvalues, it implies that the minimum variance direction is well defined. Figure 5.6 shows the orthogonality of the maximum, intermediate and minimum variance. The direction of the minimum variance corresponds to the normal magnetic field Bn, the direction of the maximum and intermediate variances are $90^0$ apart, and are tangential to the plane of the normal which is referred in the figure as bow shock normal. The data was selected between 06:05:31 and 06:28:41 UT from C1 satellite. Figure 5.7 is the side view of Figure 5.6.

| Instrum.: FGM | Eig.vector $[nT]$ X, Y, Z | Eig.value $[nT]^2$ | Std. dev. | $\lambda_{min} : \lambda_{int} : \lambda_{max}$ |
|---|---|---|---|---|
| C1 | 0.889, 0.458, -0.014 | 1.616 | 1.271 | 1:6:11 |
| C2 | 0.859, 0.510, -0.036 | 1.741 | 1.319 | 1:6:14 |
| C3 | 0.896, 0.443, 0.023 | 1.834 | 1.354 | 1:6:11 |
| C4 | 0.905, 0.425, 0.040 | 1.946 | 1.395 | 1:6:10 |

Table 5.2: Table for the Eigen vectors of minimum variance for all the spacecraft used. The first column shows the four spacecraft. The next column shows the eigenvector of the covariance matrix of the magnetic field data used. The following column shows the eigenvalues associated with the eigenvectors. The next column shows the standard deviation of the calculated eigenvalues. The last column is the ratios of the eigenvalues for C1−C4.

| i | Eig.val $[nT]^2$ | Eig.vec x1X $[nT]$ | Eig.vec x2Y $[nT]$ | Eig.vec x3Z $[nT]$ | $<B>$xi $[nT]$ |
|---|---|---|---|---|---|
| 1 | 1.616 | 0.889 | 0.458 | -0.014 | 8.474 |
| 2 | 10.144 | -0.232 | 0.425 | -0.875 | 4.364 |
| 3 | 17.227 | -0.395 | 0.781 | 0.484 | -0.132 |

Table 5.3: Showing Direction of maximum, intermediate and minimum variance using Cluster C1. The first column is the number of rows for both the eigenvectors and eigenvalues computed from the covariance matrix of the data. The second column is the eigenvalue. The third, fourth and fifth columns are the eigenvectors corresponding to the X, Y and Z − components in Cartesian coordinate system. The sixth column is the product of the mean magnetic field and the eigenvectors. The <>denotes an expectation value operator. The ith row with the smallest eigenvalue indicates the row of eigenvector defining the normal and tangential components of the field, which in this case is the first row with eigenvalue of 1.6158.

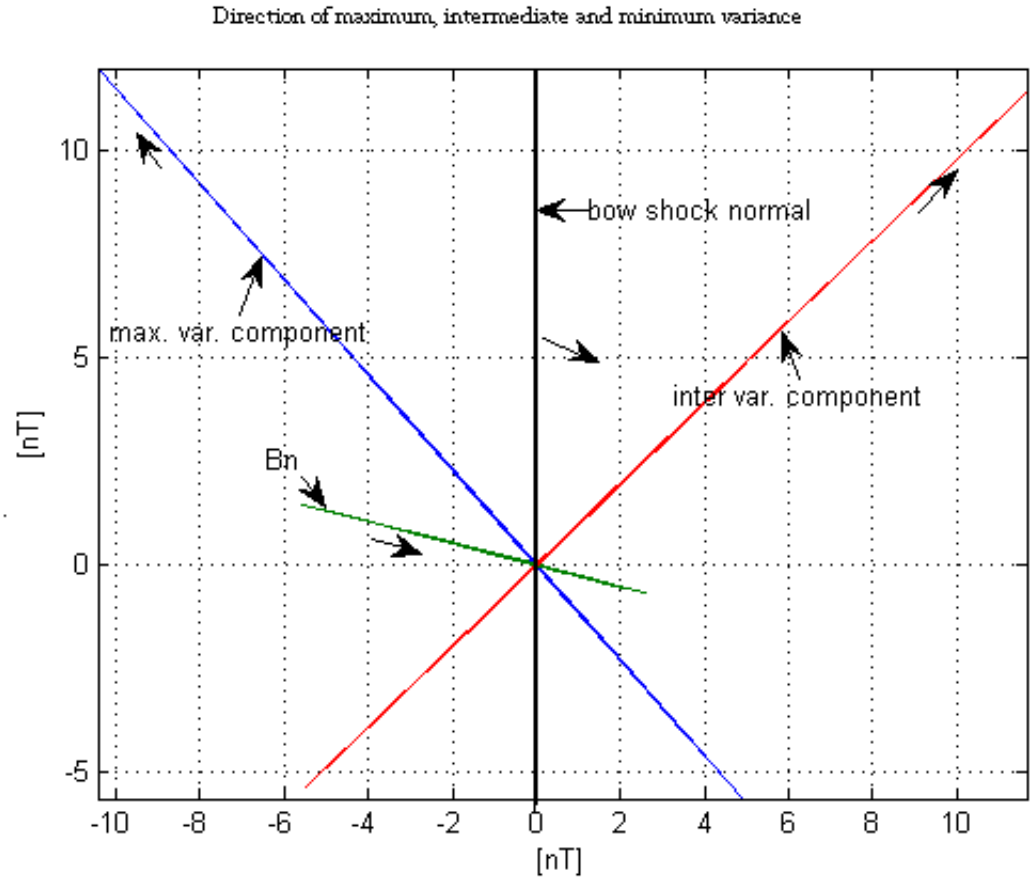


Figure 5.6: Eigen vectors showing the maximum variance, intermediate and minimum directions of the magnetic at the bow shock normal. It also shows orthogonality of the three components, which has two tangential and one normal components during traversal of bow shock by Cluster spacecraft C1 on 18 Feb. 2002, 06:05:31 to 06:28:41 UT.

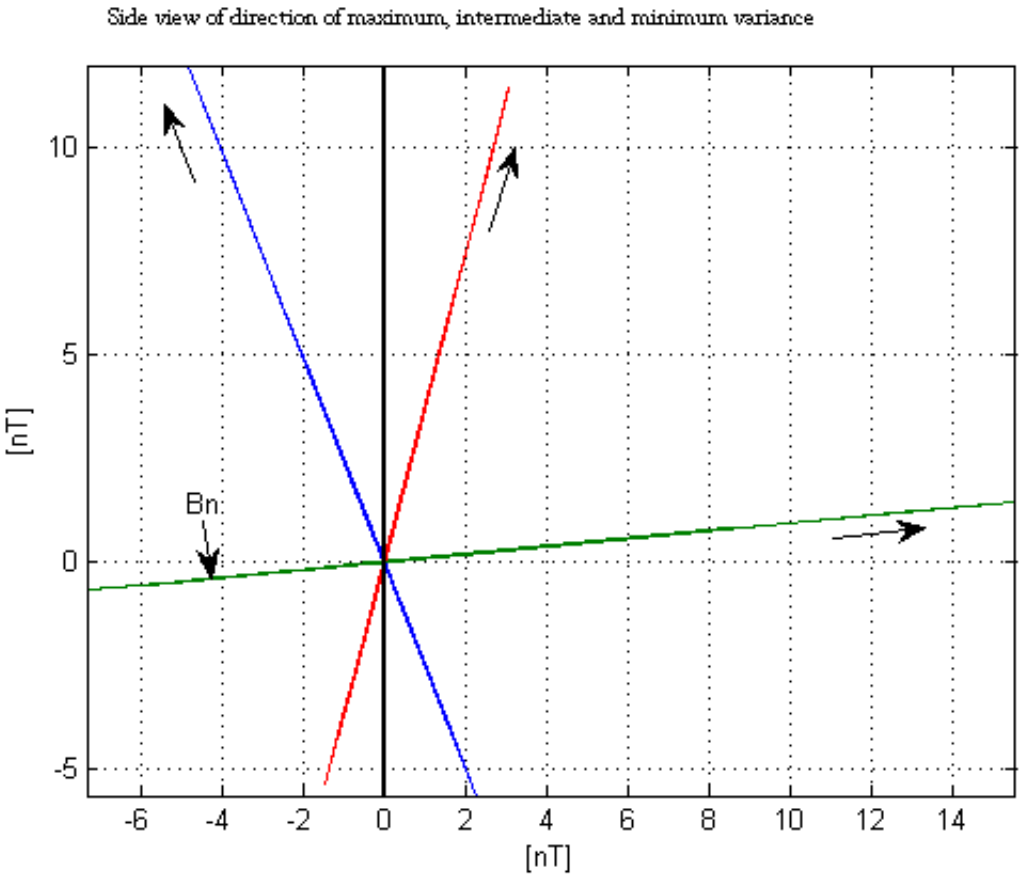


Figure 5.7: Side view of the maximum, intermediate and minimum variance of the Eigen vectors.

We used the y−component of magnetic field for frequency decomposition and have plotted the instantaneous wave vector projection along the separation between two spacecraft as in Figures 5.8−5.10. We have chosen to denote satellite pairs (which could also be called spacecraft or instrument pair) as sat13 being the combination of Cluster C1 and C3, sat23 being combination of C2 and C3 and sat43 being combination of C4 and C3. Where satellite pair 13, 23 and 43 are also valid combination conveying the same meaning. We use spacecraft C3 as the reference spacecraft. We looked at the elevation and contour of these wave vectors projections (see Figures 1−3 in Appendix A, Part A). The plots reveal that satellite pairs 23 and 43 have paths that enable sat2 and sat4 to have observed the same events. Figures 5.9 and 5.10 are correlated. These figures 1 and 2 in Part A of Appendix A are similar but different from figure 3. By comparing figure 5.8 and figure 1 of this Appendix A, it confirmed that satellite pair 13 recorded event differently from the other two pairs. Table 1 in Appendix A, Part A shows the angle between the projection of wave vector and separation line of spacecraft for data collected from 05:15:30 to 05:35:30 UT. From first column to the last: sat13x to sat43z are the angles formed between the components of the projection of wave vector along spacecraft separation and the spacecraft separation line. The first three columns are the angles between the projection of wave vector and the separation line between sat C1 and C3. These angles are in the X, Y and Z GSE coordinate system. The results show values that may suggest that the projection of the wave vector is perpendicular to the separation line of C1 and C3. Columns 4, 5, 6 and 7, 8 & 9 further confirms our early statement that sat pairs 23 and 43 have paths that enable them to observe the same events. These angles for sat23 and sat43 show propagation direction that is parallel/quasi parallel to these spacecraft separation lines.

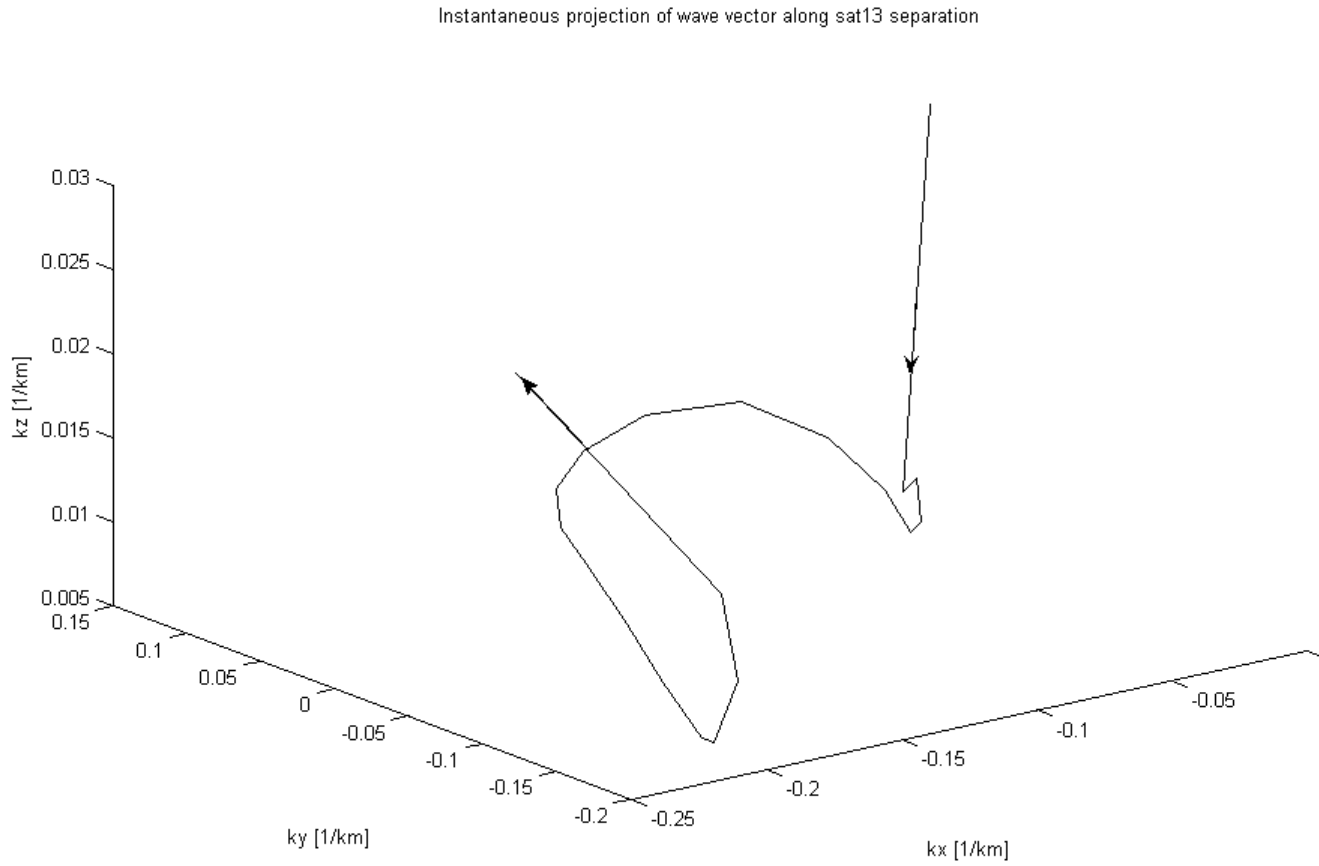


Figure 5.8: Instantaneous projection showing evolution of wave vector components along sat13 separation. The mean spacecraft separation along this satellite pair is $(34.8, 15.9, 91.1)km$. The arrow shows the direction of propagation.

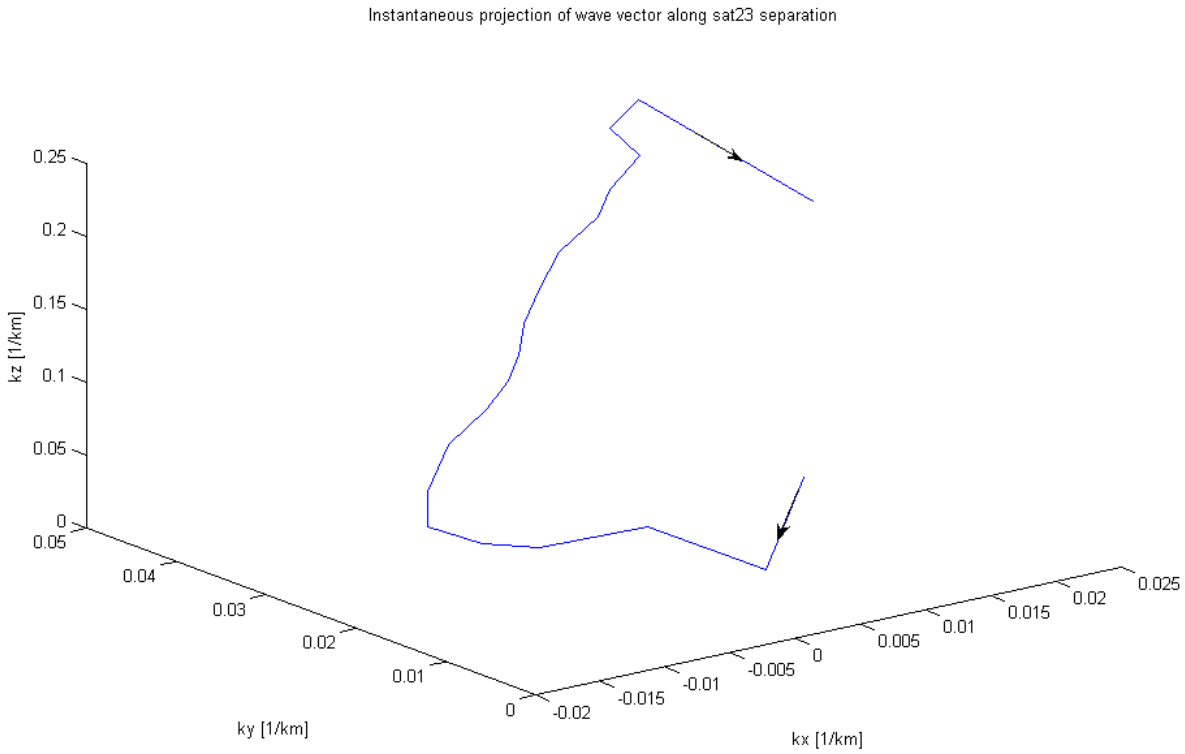


Figure 5.9: Instantaneous projection showing evolution of wave vector components along sat23 separation. The mean spacecraft separation along this satellite pair is $(64.1, -55.3, 38.8)km$. The arrow shows the direction of propagation.

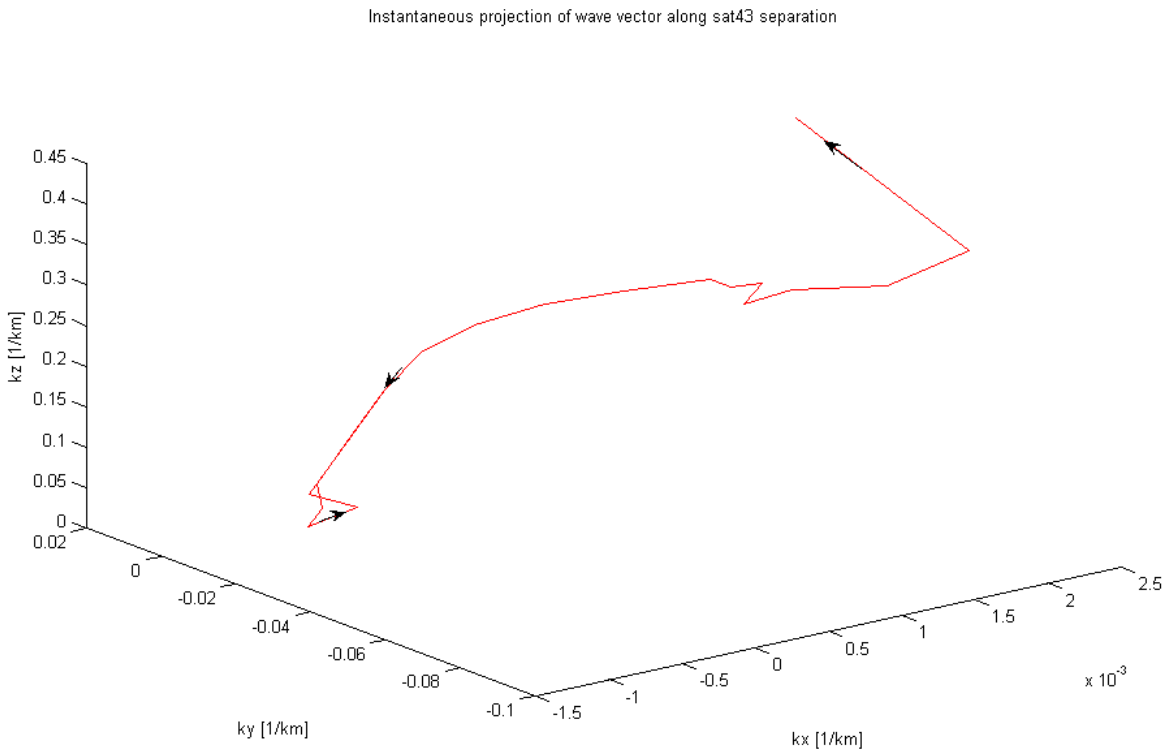


Figure 5.10: Instantaneous projection showing evolution of wave vector components along sat43 separation. The mean spacecraft separation along this satellite pair is $(99.2, 29.1, 21.8)km$. The arrow shows the direction of propagation.

Figure 4 in Appendix A, Part A is the plot of the instantaneous wave number and time. This once again shows the similarity in the combination of sat 23 (green) and sat43 (red) in figure 5.13. Table 2 in Appendix A, Part A shows the components of wave vector along the separation of pairs of spacecraft. The reference spacecraft is C3. A 20 mins data were collected from 05:15:30 to 05:35:30 UT. The results in the table are computed using equation 5.1. Table 8 in Appendix A, Part A is the instantaneous wave vector for wave propagation with a mean frequency of 78 mHz computed using equation 5.6. The wavelengths of the wave are computed. The minimum wavelength is larger than the minimum separation between spacecraft.

## 5.5 Discussion

The determination of instantaneous wave vector reveals that the separation line between spacecraft C1 and C3 lies in a perpendicular direction to the projection of the wave vector. The angle between the projection of each component of the wave vector and the separation line of sat13 pair is in the range of $87 - 91^o$ (Table 1 of Appendix A, Part A). This suggests that the locations of C1 and C3 are in the dawn−dusk direction. The study of the angle between the projection of each component of wave vector of sat23 pair and sat43 pair reveals that the projection of the x- and z- components are parallel to the separation line. This also suggest that C2 and C4 are located in the sunward direction. It also shows that the y-component of the projection of the wave vector for both sat23 pair and sat43 pair is perpendicular to the separation line (dawn−dusk direction). The elevation and contour of Figures 1 and 2 in Appendix A, Part A further shows that sat23 pair and sat43 pair lie in the direction which allow them to observed the same events with difference in position. But those of sat13 pair are different. This similarity in the sat23 and sat43 pairs could be seen in the values of projection of wave vector in Table

1, Figures 2−3 and 4 (in the Appendix A, Part A). It therefore implies that sat13 pair and the separation line is in the dawn-dusk or west-east direction. It also implies that sat24 pair has its separation line in the north-south or sunward direction of the solar wind coordinate system. Figure 5.8 to 5.10 are the characteristics exhibited by sat13 pair, sat23 and sat43 pairs, which shows similarity in sat23 and sat43 combinations.

## 5.6 Summary

This analysis has considered spacecraft geometry that does not have the spacecraft in the same plane (see Figures 5.3 - 5.5). Figure 5.5 is the model of the geometry we are considering in this analysis since its tetrahedral elongation, E and planarity, P values are small enough to allow a $3D$ analysis. Plasma-ion data availability has provided data for magnetic field, plasma bulk speed and satellite separation data. The determination of instantaneous wave vector along satellite separation was carried out. This gave three dimensional results along each satellite pair separation. The angles these components made with the satellite separation line further allowed the knowledge of the position of the satellite in the tetrahedral geometry relative to the sunward direction using solar wind coordinate system [Narita, 2006].

In the next chapter we will treat the dispersion relation as the relation of instantaneous frequency and wave vector for data collected in the magnetosheath.

# Chapter 6

# Dispersion relations and propagation processes in magnetosheath

## 6.1 Introduction

The dispersion relations ($f - k/2\pi$) determined from the computed instantaneous frequency, f and instantaneous wave vector, k leads to the instantaneous dispersion relations. Using data from FGM instrument of Cluster II mission on 18-02-2002 selected from 05:15:30-05:35:30 UT, the dispersion relations considered at instantaneous frequency, f at plasma frame depend on instantaneous wave vector, k plasma bulk velocity [Balikhin et al., 1997]

$$\omega_{rest(i)} = \omega sat(i) - \mathbf{k(i)}.V_{flow(i)} \tag{6.1}$$

Where $i = 1, 2, 3, ...., n$. n is the total number of extraction from original data. Where $\omega_{sat}$ is the angular frequency in the satellite frame (see Chapter 4), $\omega rest$ is the angular frequency in the plasma rest frame, $\mathbf{k}$ is the wave vector and $V_{flow}$ is the plasma flow speed. The spacecraft motion is about $3kms^{-1}$ compared to that flow speed in the solar wind and the magnetosheath. The plasma flow speed in the solar wind is between 300 and $380kms^{-1}$ and in the magnetosheath between 100 and $200kms^{-1}$. Combination of the known instantaneous angular frequency (see Chapter 4) and instantaneous wave vector (see Chapter 5) is used to calculate instantaneous phase velocities in the satellite and plasma frames. The instantaneous wavelength was calculated from the known instantaneous wave vector using $\lambda_i = k_i/2\pi$.

## 6.2 Dispersion analysis of downstream plasma waves

Instantaneous wave frequencies in a unsteady streaming medium such as space plasmas are modulated due to Doppler shift. We take into account the plasma flow speed and spacecraft speed, wave vectors and the frequencies in the spacecraft frame to determine the plasma frame frequencies. From the data we used, well defined low frequencies were observed downstream of the bow shock for the selected period from 05:15:30 - 05:35:30 UT. We observed two frequency modes. One of the modes was found in all three components (x, y and z) considered. The second mode was observed only along x and z components of C1 and C3 respectively. C2 and C4 have similarity which was also found in the computed instantaneous frequencies of their components. We computed the instantaneous frequency for all the components with the associated standard errors (see Table 3 and 4 in Appendix A Part A). Figure 6.1 is the profile for the instantaneous frequencies for all the four satellites C1, C2, C3 and C4. In figure 6.1, C2 (green) and

C4 (magenta) are correlated with a phase shift. The y-component of magnetic field data was considered here. Also C1 (blue) and C3 (red) are anti−correlated as in figure 6.1.

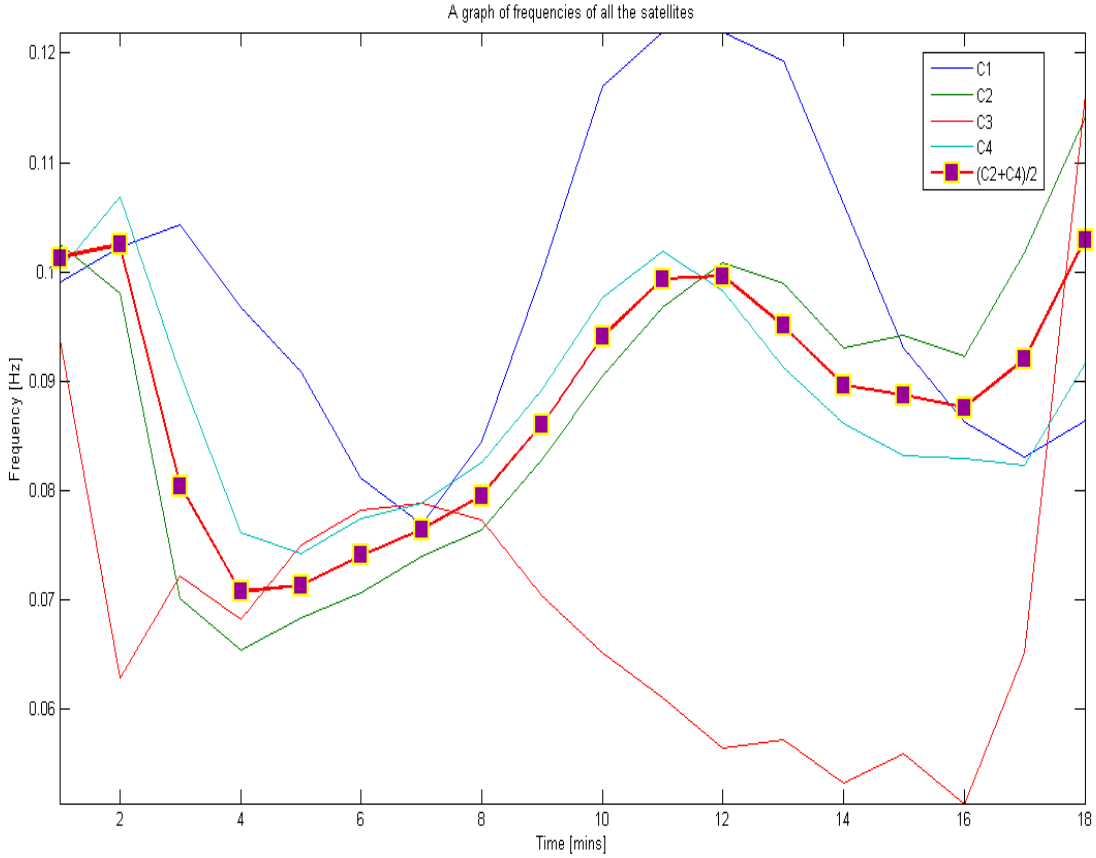


Figure 6.1: The instantaneous frequencies for all the four satellites C1, C2, C3 and C4. The line with squares is the mean taken from the instantaneous frequencies of C2 and C4.

## 6.3 Determination of instantaneous frequency and phase velocity in the plasma rest frame

We computed the instantaneous frequencies for both the satellite and plasma frames for data selected from 05:15:30 − 05:35:30 UT. The results are presented in the Tables 6 and 7 below in Appendix A part A. Column 1 is the instantaneous frequencies at satellite frame averaged over 4 spacecraft along x−component and column 2 is the instantaneous frequency at the plasma frame. $f_{plas1x}$, $f_{plasy}$ and $f_{plas1z}$ are the plasma frame from C1 and C3. While $f_{plas2x}$, $f_{plasy}$ and $f_{plas2z}$ are from C2 and C4. The plasma frame instantaneous frequencies were observed to posses a negative sign. This is an indication that the plasma frame wave is moving in the opposite direction to that at satellite frame. The average value for the ratio of the downstream ion density to the upstream ion density (equation 2.10) is 3.14 for data taken between 09:17:34 and 09:42:40 UT on 18 02 2002. This ratio defines the compression in the downstream region as the solar wind gets to the Earth magnetosheath. It is also defined [Parks, 1991] as the ratio of the upstream bulk speed to the downstream bulk speed. Taking the ratio of the downstream to upstream bulk velocity (equation 2.11), the value is 0.32. This implies that the downstream is heated up while the medium is compressed and the flow slowed down by a maximum factor of the upstream values (3.14). The average value for ratio of the downstream pressure to the upstream pressure (equation 2.9) is 11.36. Table 5 in the Appendix A, Part A shows the ion gyro−frequency (column 1), ion frequency (column 2), electron gyro−frequency (column 3) and electron (electron frequency) computed from data taken in the solar wind. The comparison of the ion frequency and electron frequency shows that the electron motion was almost uniform while that of the ion was non − uniform by as in Figures 6.2 and 6.3 . Mean plasma beta $\beta$ (equation 2.8) is 0.958 ($\approx 1$) for data taken in the solar wind region as in Table 9 in Appendix A, Part

A column 6. The ion and electron frequency responses in the solar wind from 09:17:34 − 09:42:40 UT on 18 02 2002 and magnetosheath from 05:15:30 − 05:35:30 UT have been plotted for comparison. Figures 6.2 and 6.3 show the responses in solar wind and magnetosheath respectively for data sampled at 60 secs interval using the results in Table 5 as its data. There is a major variation in the ion frequency from the solar wind to the magnetosheath, while the electron frequency remain fairly steady in both regions. The average ion gyro−frequency and the uncertainty are $2.5290 \pm 0.0140[rads^{-1}]$, average ion frequency and the uncertainty are $0.4020 \pm 0.0020$ [Hz], average electron gyro−frequency and the uncertainty are $0.1390 \pm 0.0010[rads^{-1}]$,average electron frequency and the uncertainty are $0.0220 \pm 0.0001$ [Hz] for data collected from 09:17:34 − 09:42:40 UT. Right side: The instantaneous ion gyro−frequency, ion frequency, electron gyro−frequency and electron frequency. The average ion gyro−frequency and the uncertainty are $-6.6140 \pm 0.2110[rads^{-1}]$, average ion frequency and the uncertainty are $-1.0520 \pm 0.0340$ [Hz], average electron gyro−frequency and the uncertainty are $-0.364 \pm 0.012$ [Hz], average electron frequency and the uncertainty are $-0.0580 \pm 0.0020$ [Hz] for data collected from 05:15:30 − 05:35:30 UT. The average value of the plasma beta $\beta$ here presents a value that could draw a quick conclusion that the magnetic and dynamic pressures are almost the same. But we found out that it varies as in last column of Table 9, Appendix A. The mean flow velocity in the solar wind is (-359, 37, 3) $kms^{-1}$ while the mean flow velocity in the magnetosheath is (-116, 60, 92) $kms^{-1}$.

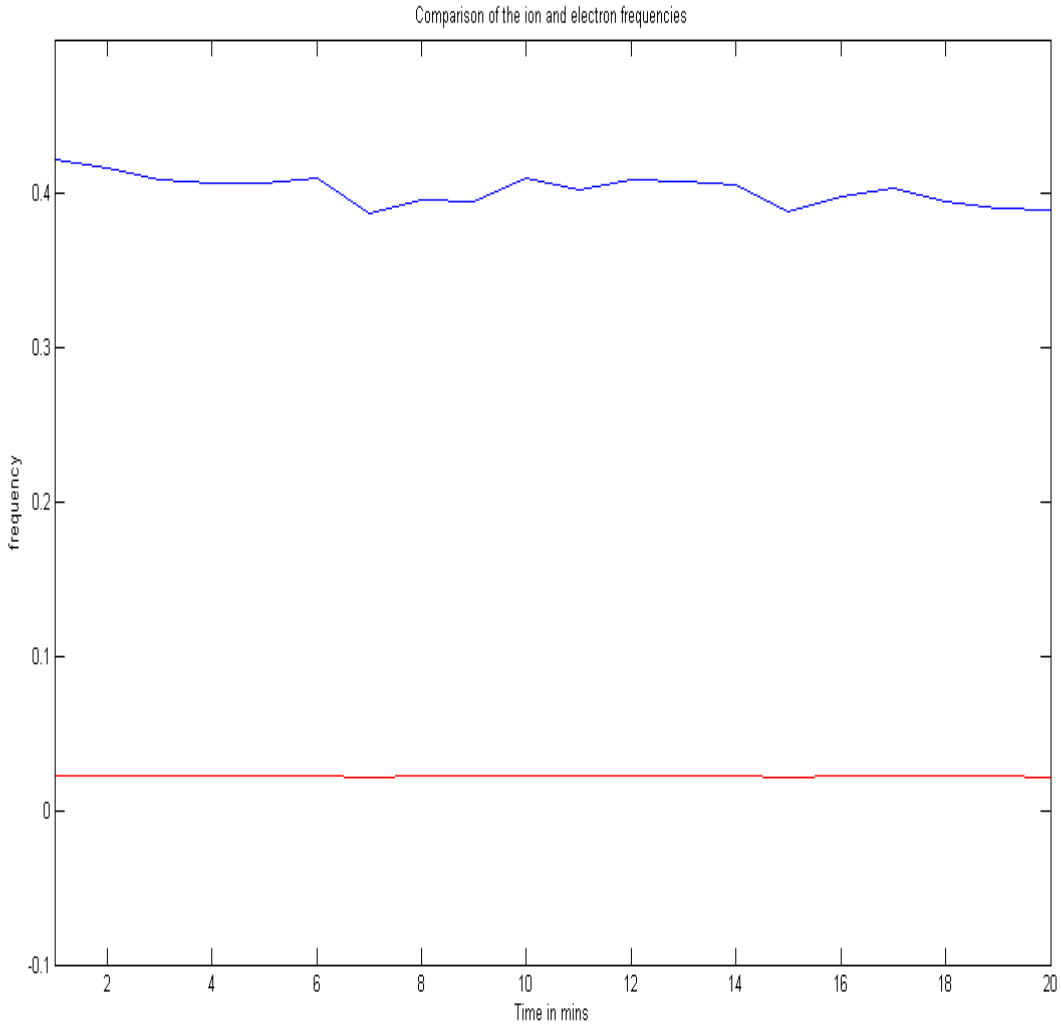


Figure 6.2: Comparison of the ion frequency with electron plasma frequency for data collected in the solar wind. Ion frequency is in blue, while electron frequency is in red almost buried in the baseline showing how small the variation is.

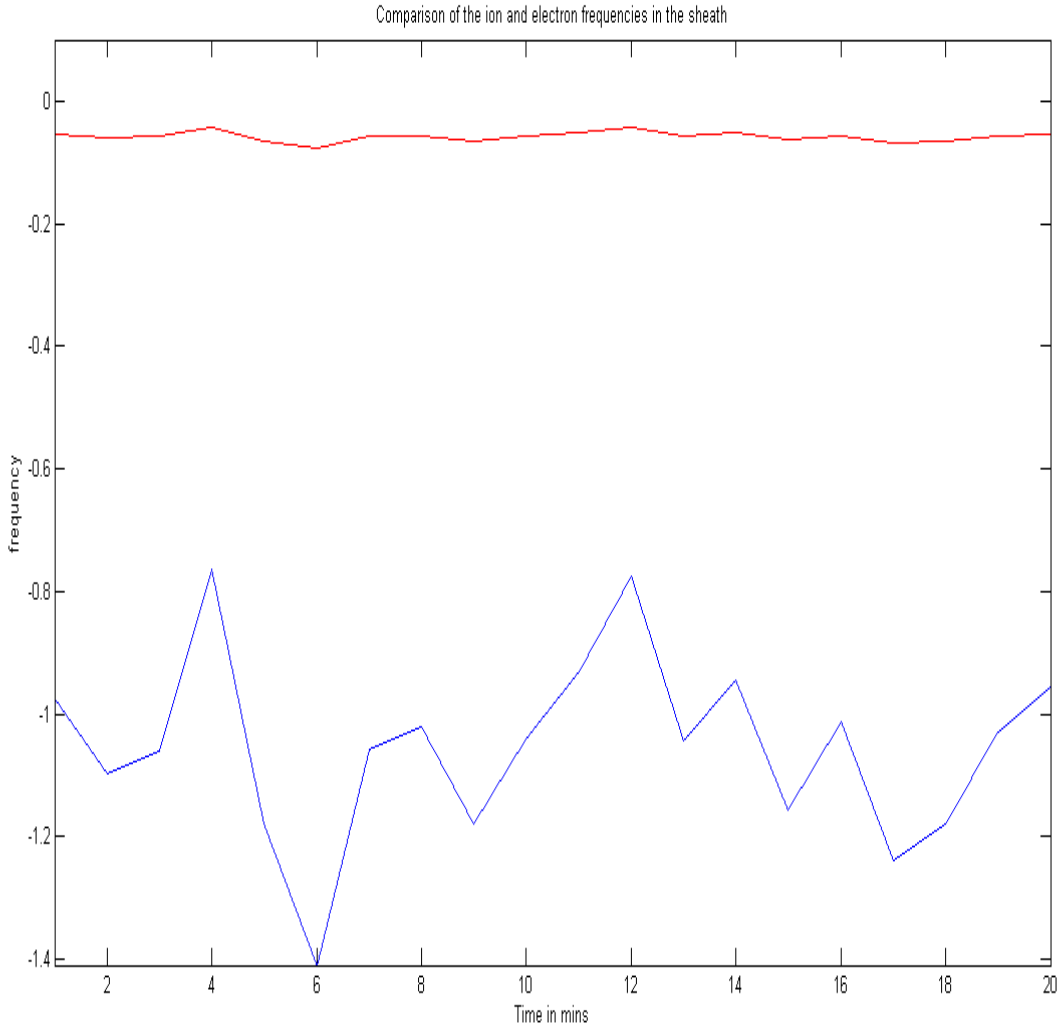


Figure 6.3: Comparison of the ion frequency with electron plasma frequency for data collected in the magnetosheath. Ion frequency is in blue, while electron plasma frequency is in red.

The computed instantaneous wavelength $\lambda$ in Table 8 in Appendix A, Part A has a minimum value that is larger than the minimum value of the spacecraft separation [Carozzi et al., 2004]. This indicates that the right branch which corresponds to the principal branch in the arctan function has been chosen. The instantaneous phase velocity as in Tables 9 in Appendix A $V_{ph(i)}$ computed from $V_{ph(i)} = \omega(i)/k(i)$ which can also be represented Vectorially as $V_{ph(i)} = \omega(i)\mathbf{k}(\mathbf{i})/\mid k(i) \mid^2$ for wave observed at the spacecraft frame. Instantaneous phase velocities $V_{ph(obs)}$components and its magnitudes at satellite frame are given in the Table 9 columns $1 - 4$. Column 5 shows the Alfvén velocity for data collected in the solar wind region between 09:17:34 and 09:42:40 UT. Column 6 shows the plasma beta $\beta$ in the selected solar wind data. Column 7 shows the Alfvén velocity in the magnetosheath collected from 05:15:30−05:35:30 UT. Column 8 shows the plasma beta within the region for the selected period obtained from the PEACE Cluster instrument. Instantaneous phase velocities in the plasma frame computed from the stable mode of instantaneous frequency decomposed from y−component of data collected on 18 02 2002 from 05:15:30−05:35:30 UT are shown in Table 10 (Appendix A Part A). Columns 1−4 show the velocity components and the magnitude. Where $i = 1, 2, 3, ..., n$. Where n is the total number of sample used.

The minimum separation is $[33.181, 14.870, 90.542]km$. It is therefore clear that the minimum wavelength (Table 8 of Appendix A, Part A) of the wave is larger than the minimum satellite separation. Table 11 (Appendix A, Part A) shows the angle in degrees between wave vector K and magnetic field B for data collected from 05:15:30 − 05:35:30 UT on 18 02 2002. The mean and standard error are 87.585 ± 0.100 for C1; 87.658 ± 0.109 for C2; 87.567 ± 0.104 for C3; 87.647 ± 0.112 for C4. The fifth column shows angle in degrees between normal n and wave vector k for data collected from 05:15:30 - 05:35:30 UT on 18 02 2002. The mean and standard error are 114.824 ± 9.756. And Table 6.11 shows angle in degrees between normal n and magnetic field B

for data collected from 05:15:30 − 05:35:30 UT on 18 02 2002. The mean and standard error are 68.202 ± 6.942 for C1; 69.365 ± 7.719 for C2; 71.567 ± 6.768 for C3; 75.212 ± 8.247 for C4. These angles define a quasi perpendicular shock regime.

## 6.4 Dispersion curves

The instantaneous angular frequency and wave vector distributions that define the dispersion relations of wave are studied here using dispersion curves. Figure 6.4 displays a curve that defines the instantaneous phase velocity properties of the wave for sat13. The distribution shows the time evolutions of the velocity of the wave. The wave starts at point marked x, follows the arrow sign and stops at the black dot. This $f$-$k_{sep}$ distribution is computed from data observed by Cluster FGM instrument for satellites combination 13 using instantaneous frequencies decomposed from y−component of data collected on 18 02 02002 from 05:15:30 − 05:35:30 UT. $k_{sep}$ is the wave vector projection along the satellite pair separation line. Figure 6.5 displays the distribution for sat23, and Figure 6.6 displays the distribution for sat43. Figures 6.7 − 6.9 are the plasma frame dispersion relations. These figures display opposite features to the dispersionin the satellite frame. Figure 6.7 displays prominently a negative gradient, which implies that waves are propagating from the first C1 to the C3 in the satellite pair. The phase velocities at different instants of time shows decreasing velocity in the sunward direction (at 4th, 8th, 11th and 16th minute) computed from data collected on 18 02 2002 from 05:15:30 − 05:35:30 UT.. The negative sign on the frequency axis indicate opposite propagation in the plasma frame. The opposite propagation implies that the waves is propagated with phase velocity in the direction opposite to the waves at the satellite frame.

The phase velocity along the separation of sat23 has negative sign for the few selected time instant. The low values of the phase velocity suggest the wave is slow along this separation. But there is a considerable increase in the phase velocity along sat43 separation. The phase velocities along this separation has positive values with a mean value of 202 km/s. This suggest that the wave is propagating in the anti−sun direction.

The average angle formed here in this case is $90^0$ (Chapter 5) that lead to a suggestion of both satellite being located in dawn − dusk direction.

The phase velocity in the plasma frame for the selected time instant show a slow wave with an average of approximately 3 km/s along the separation of sat13 with positive sign. This velocity increases steadily along sat23 separation with positive values. This implies that the wave was propagating in the sunward direction. The phase velocity along sat43 separation has average value of approximately 300 km/s. The positive values show that the wave propagated in the sunward direction. From the positive part of the gradient defining the phase velocity on Figures 6.5 and 6.6, the dispersion shows that waves are propagating from the second satellite to the first in the combination pair. This agrees with the waveform in Figure 6.12 and the satellite arrangement of the order of wave propagation across sat1, 3, 4 and 2. There are other relationships that exist between C1 and C3, such as the instantaneous frequency profile (Figure 6.1). This property shows anti − phase superposition between C1 and C3. But this figure shows in − phase correlation between C4 and C2.

Figures 6.10 and 6.11 display the dispersion relations computed with plasma frame frequencies '*' using magnetosheath magnetic field data, ion frequencies 'o' with data from the solar wind in the upstream region of the Earth bow shock and electron frequencies 'x' using upstream data (Figure 6.11), and dispersion relations computed with plasma frame frequencies, ion and electron frequencies using magnetosheath data (Figure 6.11). These Figures (6.10 and 6.11) are dispersions curves from the computed instantaneous wave vector magnitude with the instantaneous frequency decomposed from y−component of the data. The dispersion curves in Figures 6.10 reveals a range of frequencies between 38−48 mHz for the plasma frame frequency, frequencies of 0.37 and 0.45 Hz for ion frequency specified by 'o' for data taken from the upstream of bow shock and a frequencies range of 20 and 25 mHz for electron frequencies specified

by 'x' and wave vectors of range 4.6x10$^{-3}$ and 6.2x10$^{-3}$ $km^{-1}$. Figure 6.11 reveals a frequency range of 0.24 and 0.45 Hz for the ion frequency and 13 and 25 mHz for the electron frequency. Both Figures 6.10 and 6.11 display dispersions which implies that the wave propagation is strongly driven by electron density crossing the bow shock to the magnetosheath. Figure 6.12 displays the magnetic profile for data sampled at four (4) secs interval observed by Cluster (C1, C2, C3, and C4) FGM instruments between 05:15:30 and 05:35:30 UT on 18 02 2002. C1 is coloured black, C2 is coloured red, C3 is coloured magenta and C4 is coloured blue. From top to bottom: the first panel is the magnitude, second, third and fourth panels are the x, y and z components of the magnetic field.

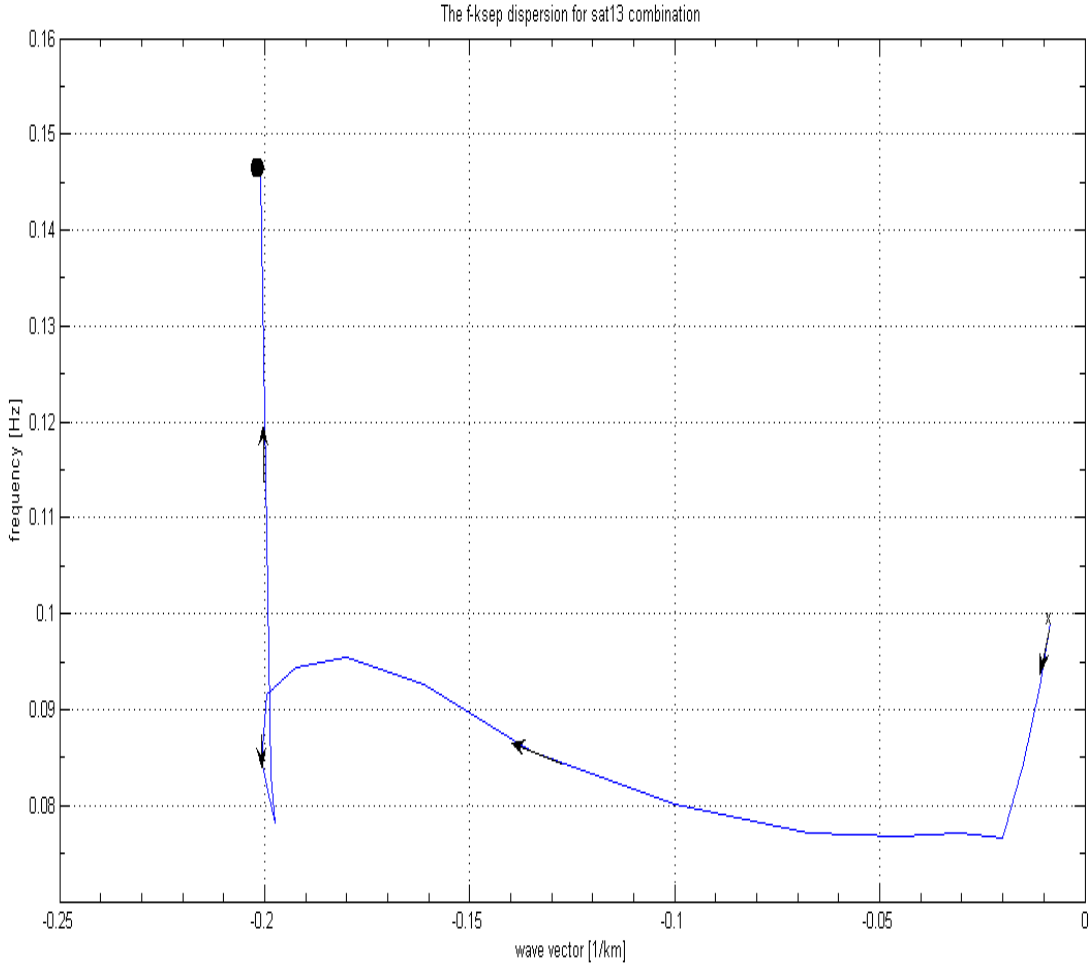


Figure 6.4: The time evolution of f-ksep plot computed from data observed by Cluster FGM instrument for satellite combination C1 and C3 using frequencies decomposed from the y−component of data collected between 05:15:30 and 05:35:30 UT on 18 02 2002 in the satellite frame.

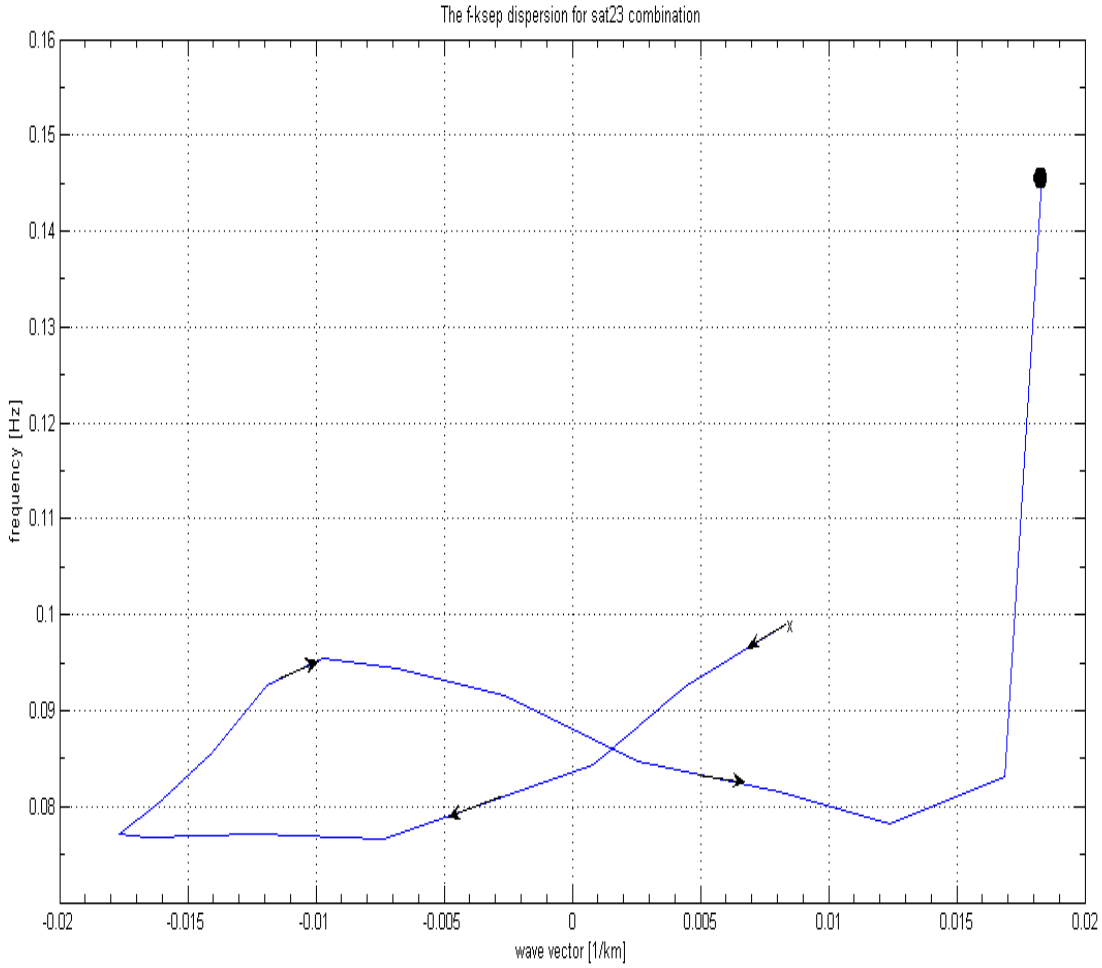


Figure 6.5: The time evolution of f-ksep plot computed from data observed by Cluster FGM instrument for satellite combination C2 and C3 using frequencies decomposed from the y−component of data collected between 05:15:30 and 05:35:30 UT on 18 02 2002 in the satellite frame.

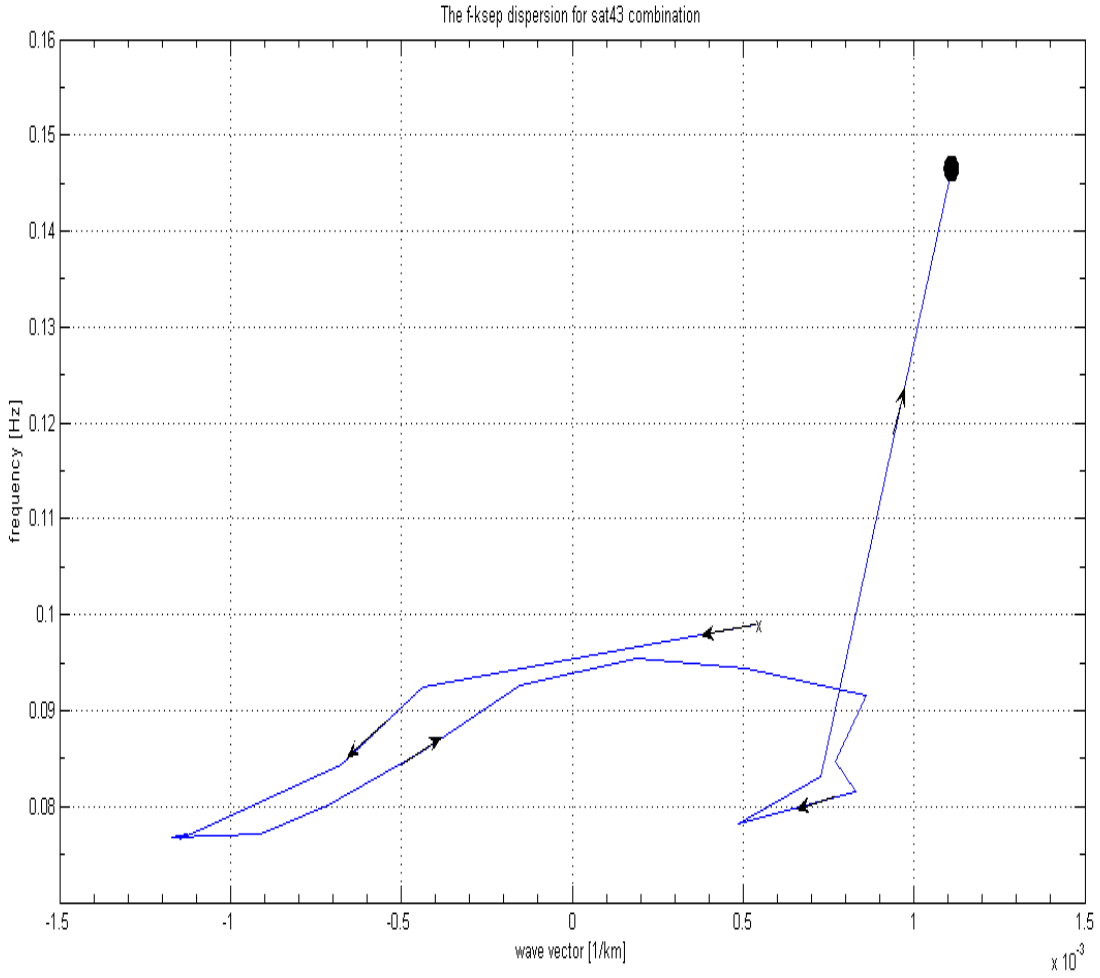


Figure 6.6: The time evolution of f-ksep plot computed from data observed by Cluster FGM instrument for satellite combination C4 and C3 using frequencies decomposed from the y−component of data collected between 05:15:30 and 05:35:30 UT on 18 02 2002 in the satellite frame.

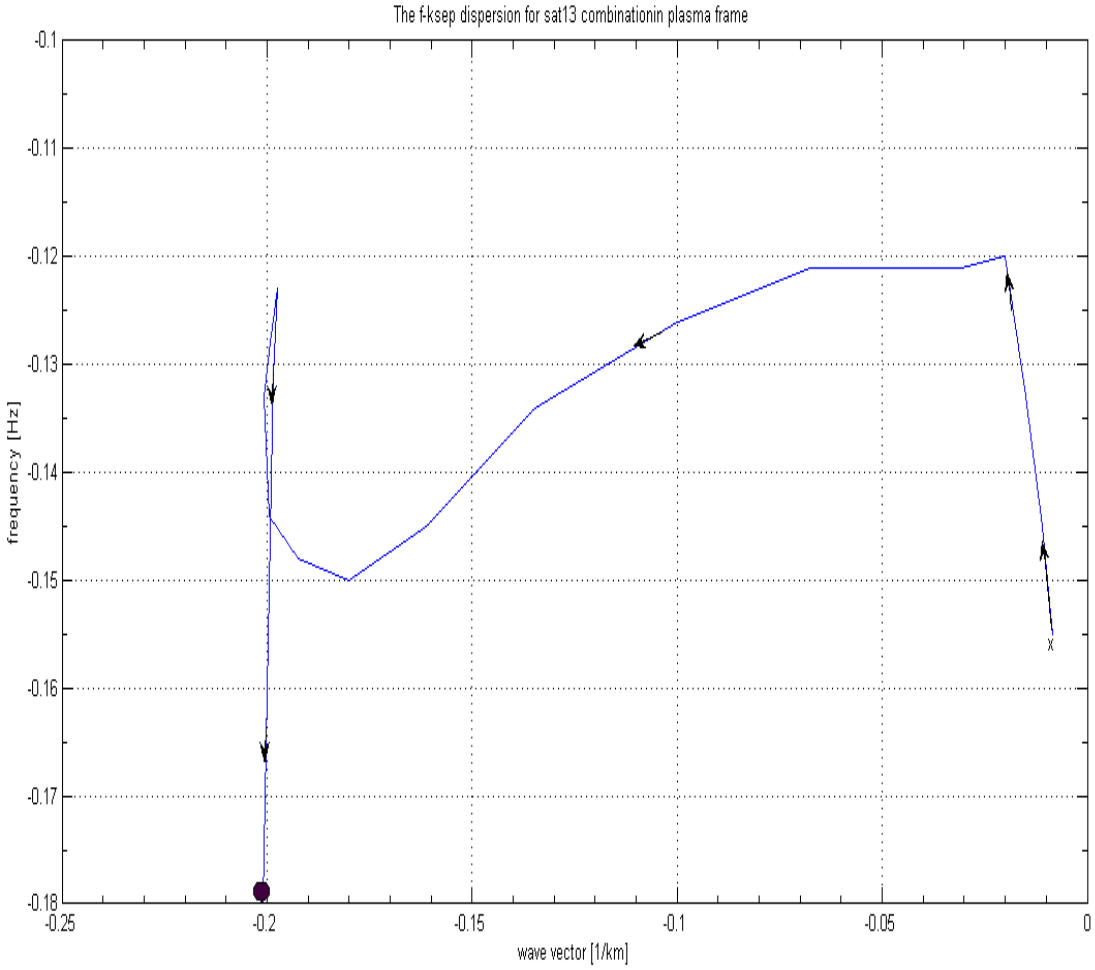


Figure 6.7: The time evolution of f-ksep plot computed from data observed by Cluster FGM instrument for satellite combination C1 and C3 using frequencies decomposed from the y−component of data collected between 05:15:30 and 05:35:30 UT on 18 02 2002 in the plasma frame.

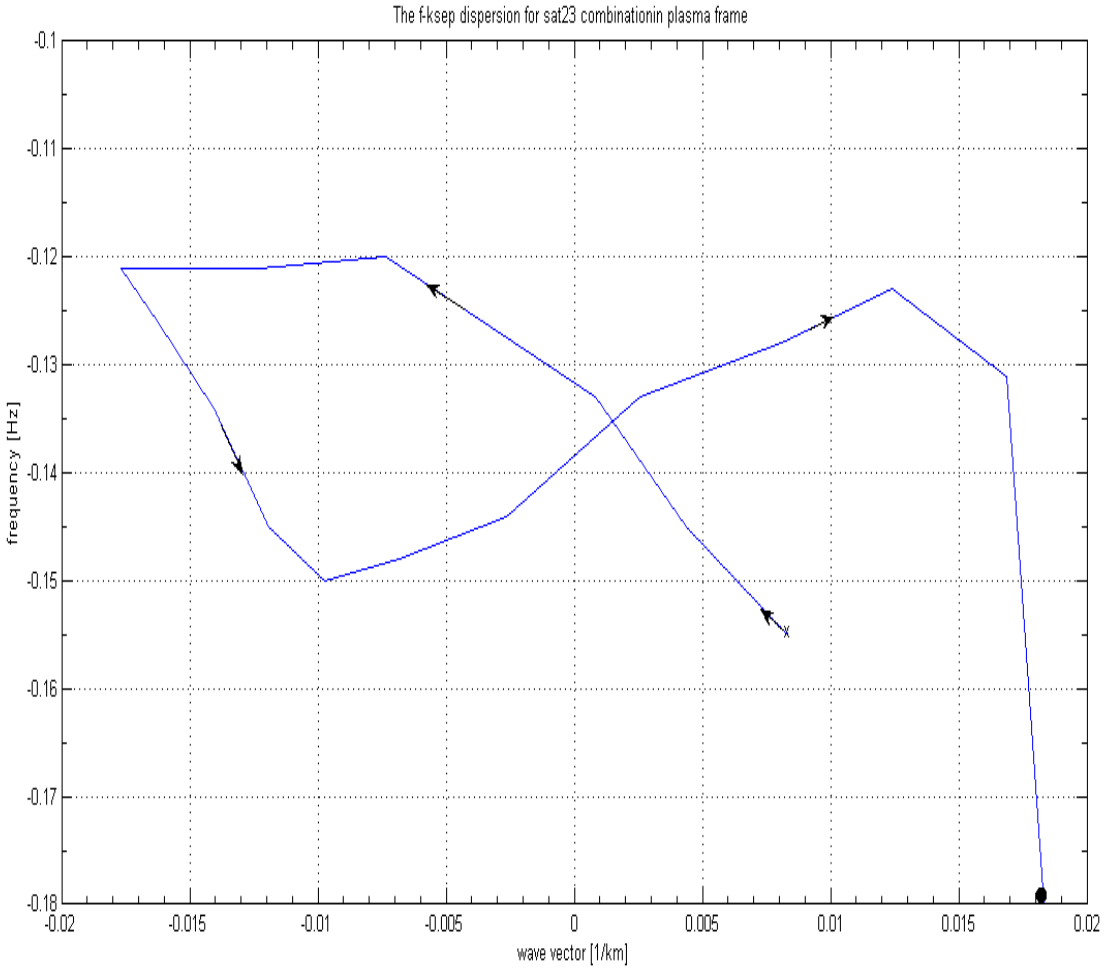


Figure 6.8: The time evolution of f-ksep plot computed from data observed by Cluster FGM instrument for satellite combination C2 and C3 using frequencies decomposed from the y−component of data collected between 05:15:30 and 05:35:30 UT on 18 02 2002 in the plasma frame.

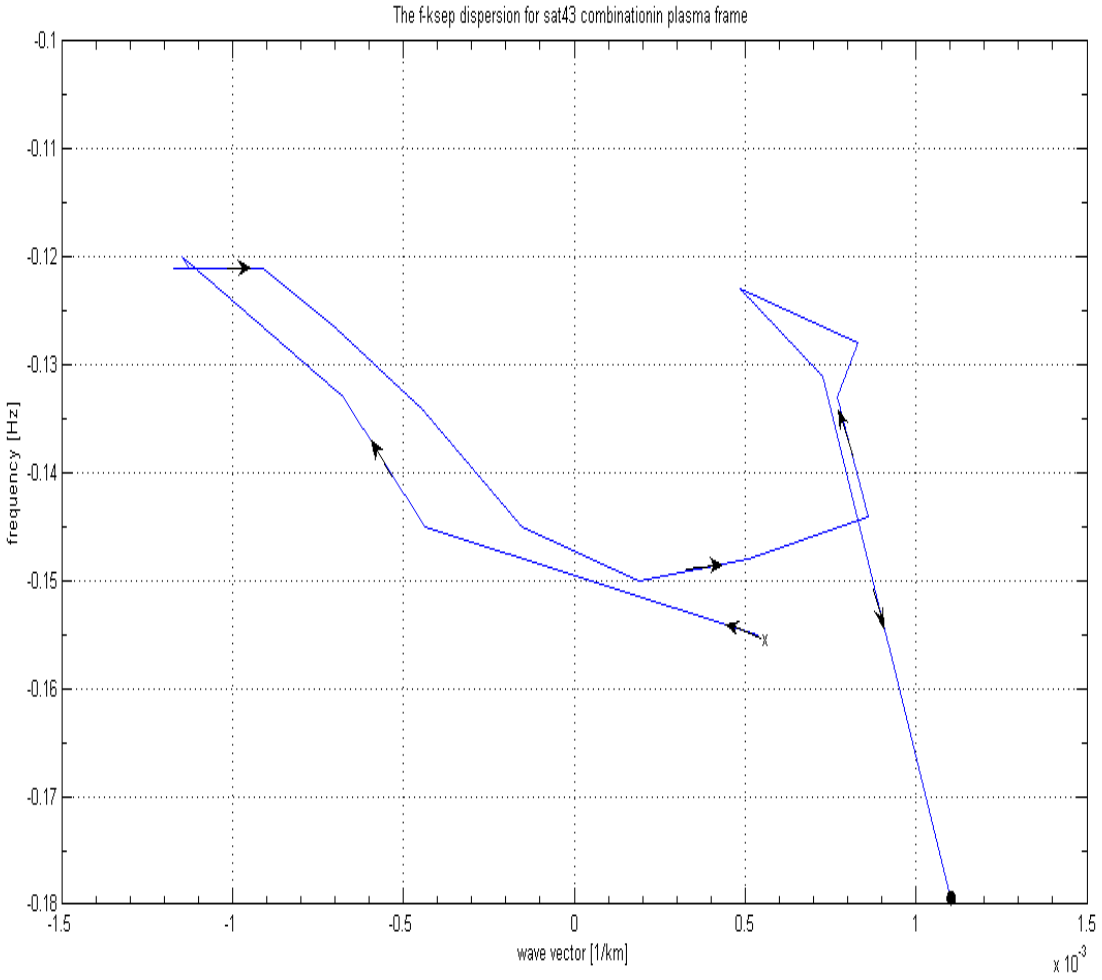


Figure 6.9: The time evolution of f-ksep plot computed from data observed by Cluster FGM instrument for satellite combination C4 and C3 using frequencies decomposed from the y−component of data collected between 05:15:30 and 05:35:30 UT on 18 02 2002 in the plasma frame.

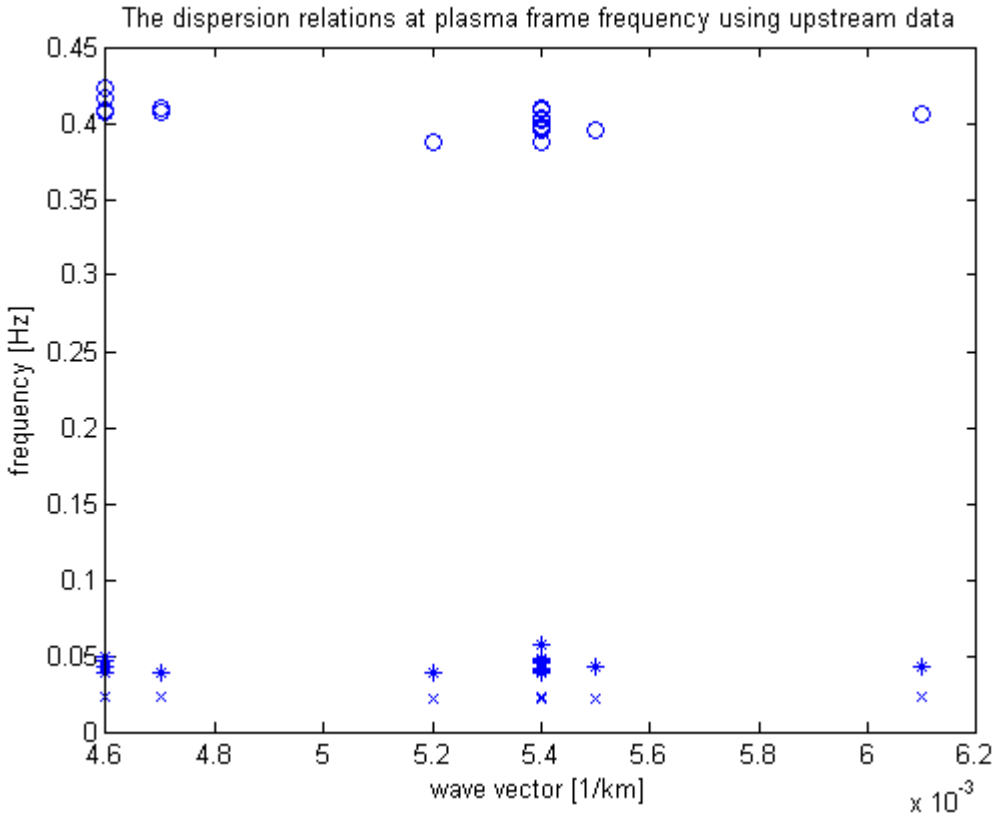


Figure 6.10: The dispersion at plasma frame using data from upstream of bow shock. The '*' represents the dispersion relations using plasma frame frequencies for the wave observed from 05:15:30 − 05:35:30 UT in the magnetosheath, 'o' represents the dispersion relations using ion frequencies and 'x' represents dispersion relations using electron frequencies for data taken in the solar wind in the upstream region.

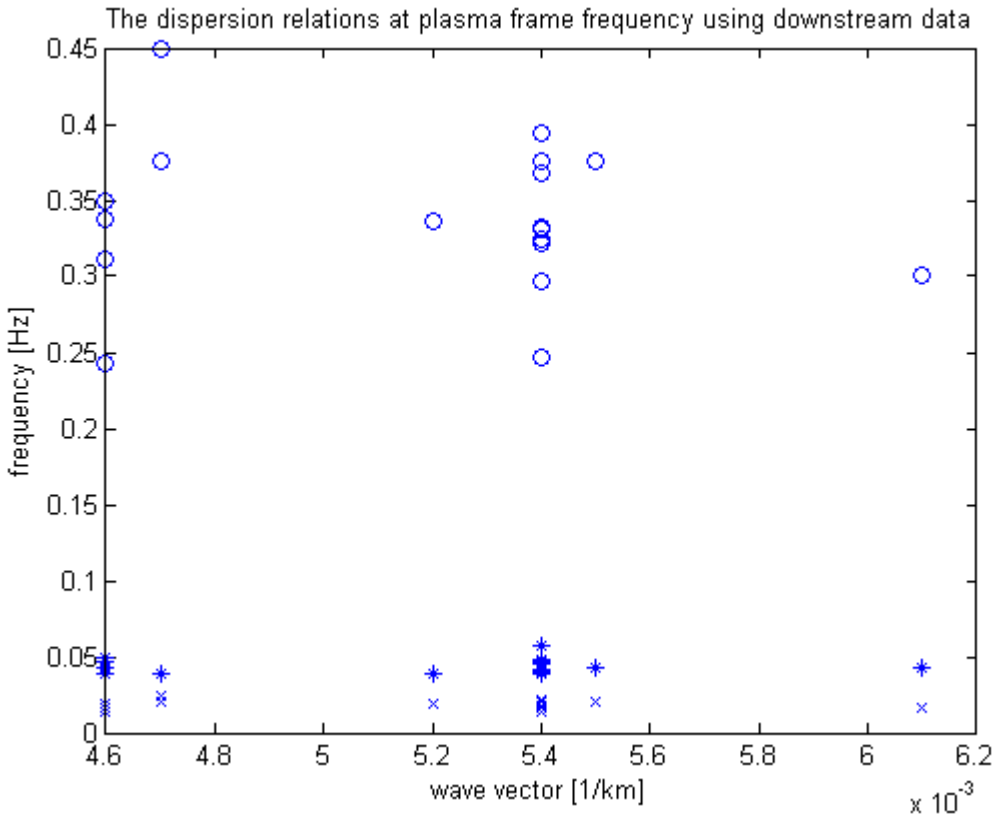


Figure 6.11: The dispersion at plasma frame using data from upstream of bow shock. The '*' represents the dispersion relations using plasma frame frequencies for the wave observed from 05:15:30 − 05:35:30 UT in the magnetosheath, 'o' represents the dispersion relations using ion frequencies and 'x' represents dispersion relations using electron frequencies for data taken in the solar wind in the downstream region.

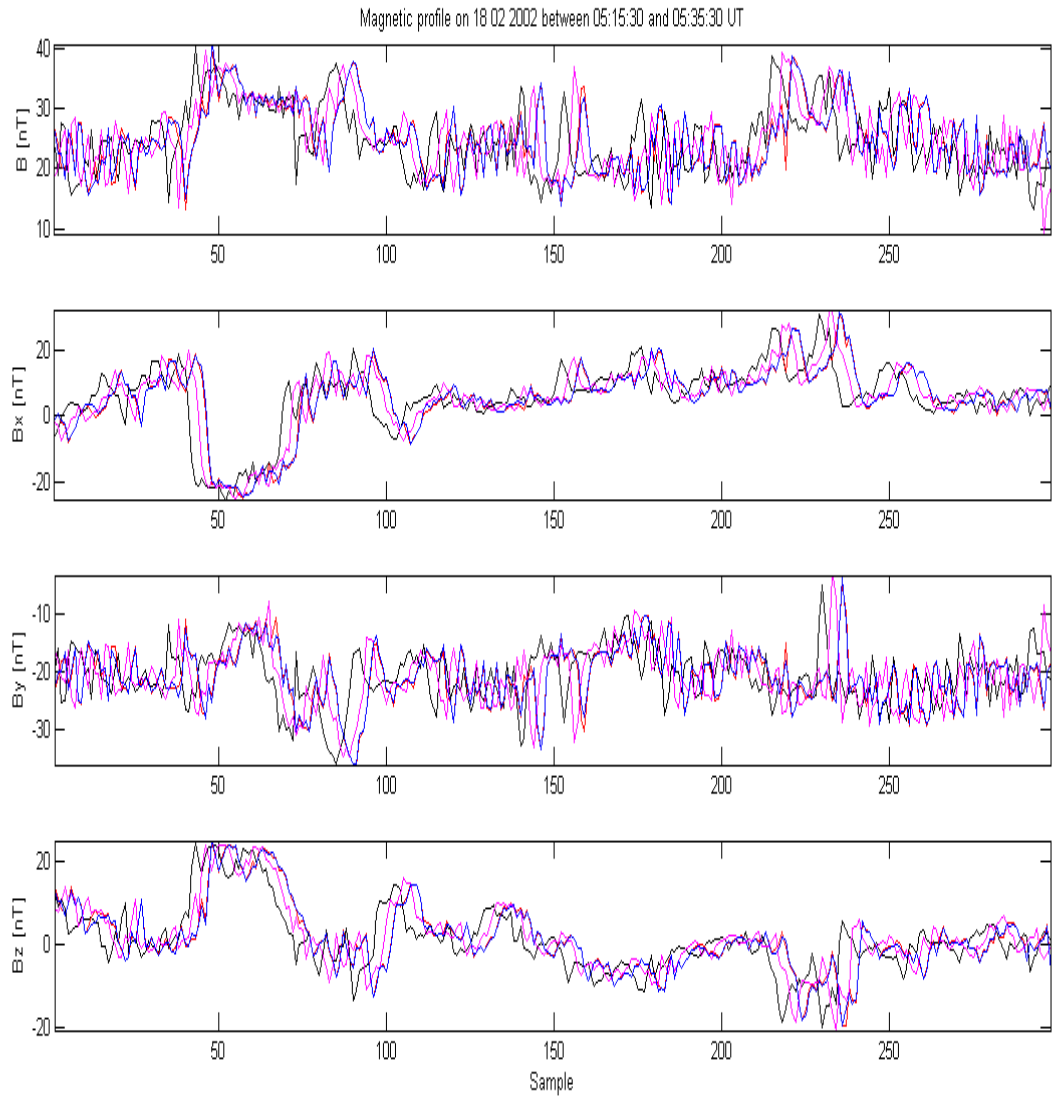


Figure 6.12: The magnetic field profile for data sampled at four (4) secs interval observed by Cluster (C1, C2, C3, and C4) FGM instruments between 05:15:30 and 05:35:30 UT on 18 02 2002. C1 is coloured black, C2 is coloured red, C3 is coloured magenta and C4 is coloured blue. From top to bottom: the first panel is the magnitude, second, third and fourth panels are the x, y and z components of the magnetic field.

## 6.5 Analysis and discussion

We consider here the dispersion relations of waves in the plasma frame that are easily determined with the knowledge of the instantaneous wave vector k (see Chapter 5). This was accomplished with the knowledge of the plasma bulk velocities which were obtained from CIS measurements. We used the Doppler shift equation to obtain the plasma frame instantaneous frequencies and phase velocities. These properties are built into the waves and are not influenced by convection arising from the background plasma flow. The average magnitude of the phase velocity is calculated to be $161.716 kms^{-1}$. This is about five (5) error bars from the mean value of $181.250 kms^{-1}$ of the projection of the plasma bulk velocity in the direction of the wave vector. The angle of propagation with respect to the magnetic field with average value of about $88^0$. The error in the determination of wave vector's projection along sat13 pair is $\pm 12.0\text{x}10^{-3} Km^{-1}$, $\pm 2.7\text{x}10^{-3} Km^{-1}$ along sat23 pair, and $\pm 6.0\text{x}10^{-3} Km^{-1}$ along sat43 pair. The error on the overall wave vector k is $\pm 0.098\text{x}10^{-3} km^{-1}$. The computed plasma frame instantaneous frequencies have negative sign. The physical sense of the negative instantaneous frequencies can be understood by close examination of the reversal in instantaneous phase velocity values at satellite frame (Table 5.1) and Table 10 of Appendix A, Part A. At the spacecraft frame in Table 5.1, the $x-$ component of the instantaneous phase velocities indicate that the wave propagates in the opposite or anti$-$sun direction. This is opposite in the case of the plasma frame instantaneous phase velocities in Table 6.10 (Appendix A), where this indicates a wave propagating in sunward direction.

The essence of using Hilbert filter for frequency decomposition was just to avoid negative frequencies, but the plasma frame instantaneous frequencies still have negative values. To solve this, it is believed that the change of the sign on $\omega$ and $\mathbf{k}$ will not lose generality [Narita and Glassmeier, 2006] and will keep the phase velocities unchanged

but with a change in the representation of the sense of the polarization from right-hand to left-hand orientation and vice versa. This change of sign is accompanied by a change in the angle between the wave vector k and the magnetic field. This resulted in the average value of about $90^0$ at the spacecraft frame. We first of all use the knowledge of the instantaneous frequencies and wave vectors and plot frequency against the wave vector for the identified waves using satellite pairs 13, 23 and 43 as observed at satellites frame. These satellite combinations enable the determination of dispersion relations along the projections of wave vectors on the separation lines between satellites. The uncertainty calculations used are: for instantaneous plasma frame frequency $\omega_{pl}$, $\Delta\omega_{pl} = [(\Delta\omega_{obs}/\omega_{obs})^2 - ((\Delta k/k)^2 + (\Delta V/V)^2)]^{1/2}\omega_{pl}$.Where $\omega_{pl}$ is the angular frequency in the plasma frame, $\omega_{obs}$ is the angular frequency in the satellite frame, **k** is the wave vector, V is the plasma bulk velocity and $\Delta$ signifies uncertainty. This is computed from the earlier equation for the plasma frame frequency obtained using Doppler shift. Plasma frame instantaneous phase velocity $V_{ph}$ has uncertainty calculated as: $\Delta V_{Ph} = [(\Delta\omega_{pl}/\omega_{pl})^2 + (\Delta k/k)^2]^{1/2}V_{ph}$. This is computed from the earlier calculated plasma frame instantaneous phase velocity. The error on the plasma frame instantaneous frequency is given in appendix A part in table A.1. The errors on the instantaneous frequency in plasma frame range between 3.00 and 5.00 %. The magnitude of errors on instantaneous frequencies and phase velocities in plasma frame is smaller than those of Narita *et al.* (2006). That of the instantaneous phase velocity in plasma frame is between 3.60 and 4.55 %. The resulting instantaneous frequencies in the plasma frame are averaged as $9.40f_{ci}$ and $0.52f_{ce}$. Where $f_{ci}$ and $f_{ce}$ are the ion cyclotron frequency and electron cyclotron frequency respectively.

The instantaneous frequencies in plasma frame is consistent with the order of the results obtained by Narita *et al.* (2006). The order of the error in the determination of the wave vector is $0.1\text{x}10^{-3}$. The average errors in the determination of the wave vector along

the satellite separation lines above are of the same order with the result of Walker *et al.* (2004). The angle of propagation with respect to the magnetic field in table 6.10 has an average of about $88^0$ which is similar to the value obtained by Walker *et al.* (2004). The order of the plasma frame instantaneous phase velocity in Table 10, Appendix A were averaged to be $167.476 \pm 5.219\ kms^{-1}$ and a standard deviation of $22.144\ kms^{-1}$. The average phase velocity seems to be less than the value obtained by Walker *et al.* (2004) whose data were collected between 05:34 and 05:35 UT. But our result varies and is of the order of $212.778 \pm 5.219\ kms^{-1}$ at 05:32:30 UT. This indicates that the result $212.778 - 5.219\ kms^{-1}$ compares well with the value obtained by Walker *et al.* (2004) two minutes after with order of one error bar.

The computed average instantaneous phase velocity ($167.476 \pm 5.219\ kms^{-1}$) in Table 10, Appendix A is similar to the average of the magnitude of instantaneous Alfvén velocity ($175.064 \pm 7.172\ kms^{-1}$) in Column 7, Table 9, Appendix A. A closer comparison goes with $175.064 - 7.172\ kms^{-1}$ leading to $167.900\ kms^{-1}$. This confirms that the waves propagate with Alfvénic speed since the computed phase velocity approximates the computed Aifvén velocity. The average values of our results have been consistent with the results obtained by Schafer *et al.* (2005) which studied the phase propagation and dispersion analysis of low frequency waves in the magnetosheath from 05:50 − 06:24 UT on 18 02 2002. Their results show a wavelength above 200 $km$ and the results in this analysis have an average of $1286.30km$. Their frequency decomposition reveals low frequency and associated error that compares well with our results. Our wave vector magnitude is of the range $0.0046 - 0.0054\ km^{-1}$ agrees with their wave vector magnitude of $0.005\ km^{-1}$. Instantaneous phase velocity at spacecraft frame computed has given an average value of $166\ kms^{-1}$ which agree with the value of 166 km/s obtained by Schafer *et al.* (2005). Comparison of the plasma beta $\beta$ in the upstream and downstream shows a regime from low (upstream) $\beta$ to high

(downstream) $\beta$ . This confirms magnetosheath to be a high $\beta$ region [Parks, 1991, Kivelson and Russell, 1995, Baumjohann and Treumann, 1996]. The angles between the wave vectors and the magnetic field are prominently in a quasi-perpendicular direction. Many characteristics found in C1 are similar to those on C3. While characteristics on C2 are common on C4. A typical case is found on the instantaneous angle between the magnetic field and the shock normal computed using minimum variance technique. These characteristics display a magnetic field that flow from a quasi-perpendicular direction to a quasi-parallel direction. This is a characteristics that shows that the wave field is non-homogeneous. The computed instantaneous wavelength reveals that the wave field exhibits a non-stationary behaviour. The minimum wavelength computed is larger than the minimum separation between satellite in the combination. This is consistent with the assumption as stated in Carozzi *et al.* (2004).

## 6.6 Summary

In this chapter, the instantaneous dispersion relations of waves have been studied using the knowledge of the instantaneous frequencies in the plasma frame and the instantaneous wave vector. The dispersion curves have been used to find the order of which the waves propagate across the spacecraft. This study reveals that the waves propagate first from sat1 then sat3, then sat4 and sat2. The dispersion relations display a characteristic behaviour with change in the phase velocities at both satellite and plasma frames. The wave in the plasma frame exhibits an opposite propagating direction to that in the satellite frame. The instantaneous analysis reveals the analysed plasma data does not have an homogenous and stationary pattern. The account of the non-homogenous nature of the waves have been analysed. The non-stationarity has been accounted for. The average instantaneous values of some of the studied properties

agree well with the results obtained on the assumption of non−stationarity and linearity. This study has revealed that magnetosheath is a turbulent region with high plasma beta $\beta$. The average values of the computed quantities show results that are comparable to those obtained from Walker *et al.* (2004) whose analysis was based on assumption of non−stationarity and lineariity. The results of this study are consistent with the assumptions of instantaneous local wave vector estimation. Our computed average values show departure from average values obtained by techniques that are based on Fourier transform due variations in the instantaneous frequency and wave vector which conform to the non-linear and non-stationary nature of the waves that are studied here. The average values of our results have been consistent with the results obtained by Schafer *et al.* (2005) which studied the phase propagation and dispersion analysis of low frequency waves in the magnetosheath from 05:50 − 06:24 UT on 18 02 2002. Their results show a wavelength with average value above 200 $km$. Our results give a wavelength (with average of $\approx$ 1287 km) in this analysis that is larger than the minimum spacecraft separation. Their frequency decomposition reveals low frequency and associated error that compares well with our results. Our wave vector magnitude is of the range $0.0046 - 0.0054\ km^{-1}$ that agrees with their wave vector magnitude of $0.005\ km^{-1}$. Instantaneous phase velocity at spacecraft frame computed has given an average value of 166 $kms^{-1}$ which agree with the value of 166 km/s obtained by Schafer *et al.* (2005). We therefore conclude that the analysis has provided lower errors, thereby offering reliable results. In the following chapter, the identification of the wave mode will be carried out since the various properties of the waves have now been determined.

# Chapter 7

# Wave modes identification

## 7.1 Introduction

The region of magnetosheath close to the bow shock has been dominated by Alfvén Ion Cyclotron (AIC), while the middle region is characterised by mixed Alfvén ion cyclotron and mirror modes [Hubert, 1994]. Alfvén ion cyclotron waves are left-hand polarized and propagate parallel to the magnetic field direction [Schafer et al., 2005]. The data used here for the study of the magnetosheath were taken using Cluster II mission instrument for observations made on 18 02 2002 for a period 05:15:30 and 07:35:30 UT. The period is divided into six subdivision. Three time zones A, B and C of twenty (20) minutes each have been chosen for this analysis representing the region of magnetosheath close to the magnetopause, the middle magnetosheath and region of magnetosheath close to the bow shock respectively. The magnetic field profile and its associated intrinsic mode functions, and their instantaneous frequencies for the different chosen regions are computed in both spacecraft and plasma frames. The instantaneous wave vectors, phase velocity and wavelength in the plasma frame are determined. We

considered it necessary to compute proton temperature anisotropy ($T_p \perp / T_p \parallel$) and plasma beta ($\beta$). Polarization has been used by previous analysts in the identification of waves modes [Hubert, 1994, Narita and Glassmeier, 2006]. It has been proposed that the dayside magnetosheath displays turbulence at frequencies lower than the local proton frequency [Hubert, 1994]. The analysis of the magnetic field and ion data in the magnetosheath of a quasi-perpendicular bow shock revealed an anti-phase correlation between the magnetic field and the ion data. Frequency decomposition reveals frequency lower than $0.1Hz$ [Shevyrev, 2005]. From the analysis carried out which reveals different waves modes in the different regions of the magnetosheath, it becomes obvious that the magnetosheath is non-uniform. This means that the plasma state differs across magnetosheath from the bow shock to the magnetopause. Shevyrev (2005) suggests that the magnetosheath is non-uniform in the transverse (perpendicular) direction. The angle ($\theta_{Bn}$) between the magnetic field and normal determines the mutual orientation of the bow shock and the interplanetary magnetic field (IMF) direction. This according to Shevyrev (2005), has influence on waves of frequency between 0.02-$1Hz$. It was also mentioned that as angle $\theta_{Bn}$ decreases, it sets highly turbulent waves across a quasi-parallel shock. And that this variation is twice that set by a quasi-perpendicular shock. But at frequency lower than $0.1Hz$ [Shevyrev, 2005], the magnetic field magnitude is rather intense in some events for a quasi-perpendicular shock.

$(T_p \perp / T_p \parallel) - 1 \geq 1/\beta$ [Shevyrev, 2005] has been considered an instability criterion for mirror mode waves which are identified with compression waves showing anti$-$correlation in ion flux density and magnetic field magnitude with linear polarization and zero phase velocity in the plasma frame [Hubert, 1994],([Shevyrev, 2005] and the references therein). It has been shown that the electron cyclotron frequency is steady across the shock from the upstream to downstream (see Chapter 6), so the choice of ion flux since it exhibits high fluctuation in the downstream than in the upstream. Parallel and perpendicular to the average magnetic field direction,

the behaviour of the amplitudes of variation exhibit a double strength for the parallel component, and this grows to over seven times close to the magnetopause. This implies that compression waves dominate according Shevyrev (2005), which are the properties of both the slow and mirror mode waves. These modes are distinguished by their characteristics. Slow modes waves are identifiable with its non-zero phase velocity in the plasma frame while the mirror modes have zero phase velocities. The mirror mode is characterised with an anti-phase correlation in the magnetic field and density fluctuations. Mirror modes are linearly polarized and are non-propagating wave or standing structures in the plasma frame.

In this chapter, the determination of the ratios of the perpendicular to parallel components of proton temperature are made. This ratio defines the temperature anisotropy. The plasma beta $\beta$ has been computed and the instantaneous phase velocities in the satellite frame are computed. This allow for easy comparison with the plasma bulk velocities. We also computed the ratio of the phase velocities in the satellite frame to that of the Alfvén velocities. We used these computations with the various modes identification criteria to identify the modes in the magnetosheath.

## 7.2 Observations

We have chosen a period between 05:15 − 07:35 UT on 18 02 2002 for this study. We have divided the period into six equal subdivisions and have chosen three periods (Figure 7.1) of these subdivisions, viz: 05:15 − 05:35, 06:15 − 06:35 and 07:15 − 07:35 UT. The chosen periods were when the Cluster spacecraft were in the magnetosheath outbound from the magnetosphere towards the Earth's bow shock. The period 05:15 − 05:35 is marked as zone A chosen close to the magnetopause, the period 06:15 − 06:35 is marked as zone B chosen in the middle of the magnetosheath and the period 07:15 − 07:35 is marked as zone C chosen close to the bow shock . The magnetopause was crossed at about 04:59 UT. The magnetic field data used have been averaged over 1 minute. The shock regime as these Cluster spacecraft traverse the magnetosheath has an average value for the angle between the magnetic field data and the normal of $\approx 18^0$ computed using magnetic coplanarity theorem [Paschmann and Daly, July 2000]. This angle indicates a quasi-parallel shock regime. Figure 7.1 is the magnetic profile for the field strength collected on 18 Feb. 2002 from 04:00 − 10:00 UT. Figures 7.2 − 7.4 are the plots comparing the $(T_p \perp / T_p \parallel) - 1$ and $1/\beta$. Figure 7.2 is the computed result for zone A, Figure 7.3 is the result for zone B and Figure 7.4 is the result for zone C. $T_p \perp$ and $T_p \parallel$ are temperature components perpendicular and parallel to the background magnetic field **B**. Figures 7.8 − 7.10 show the instantaneous phase velocities in the satellite frame and the plasma bulk velocities. Figure 7.8 shows the satellite frame and plasma bulk velocities computed from data from zone A, Figure 7.9 shows the satellite frame and bulk velocities computed from zone B and Figure 7.10 shows the velocities computed from data from zone C. The average value of the phase velocity and bulk velocity in Figure 7.8 are $\approx 106 km/s$ and $\approx 232 km/s$ respectively. The average value of the phase velocity and bulk velocity in Figure 7.9 are $\approx 156 km/s$ and $\approx 212 km/s$ respectively. The average value of the phase velocity and bulk velocity in Figure 7.10

are $\approx 176km/s$ and $\approx 224km/s$ respectively. $V_{ph}$ denotes satellite frame velocity and $V_{pb}$ denotes plasma bulk velocity.

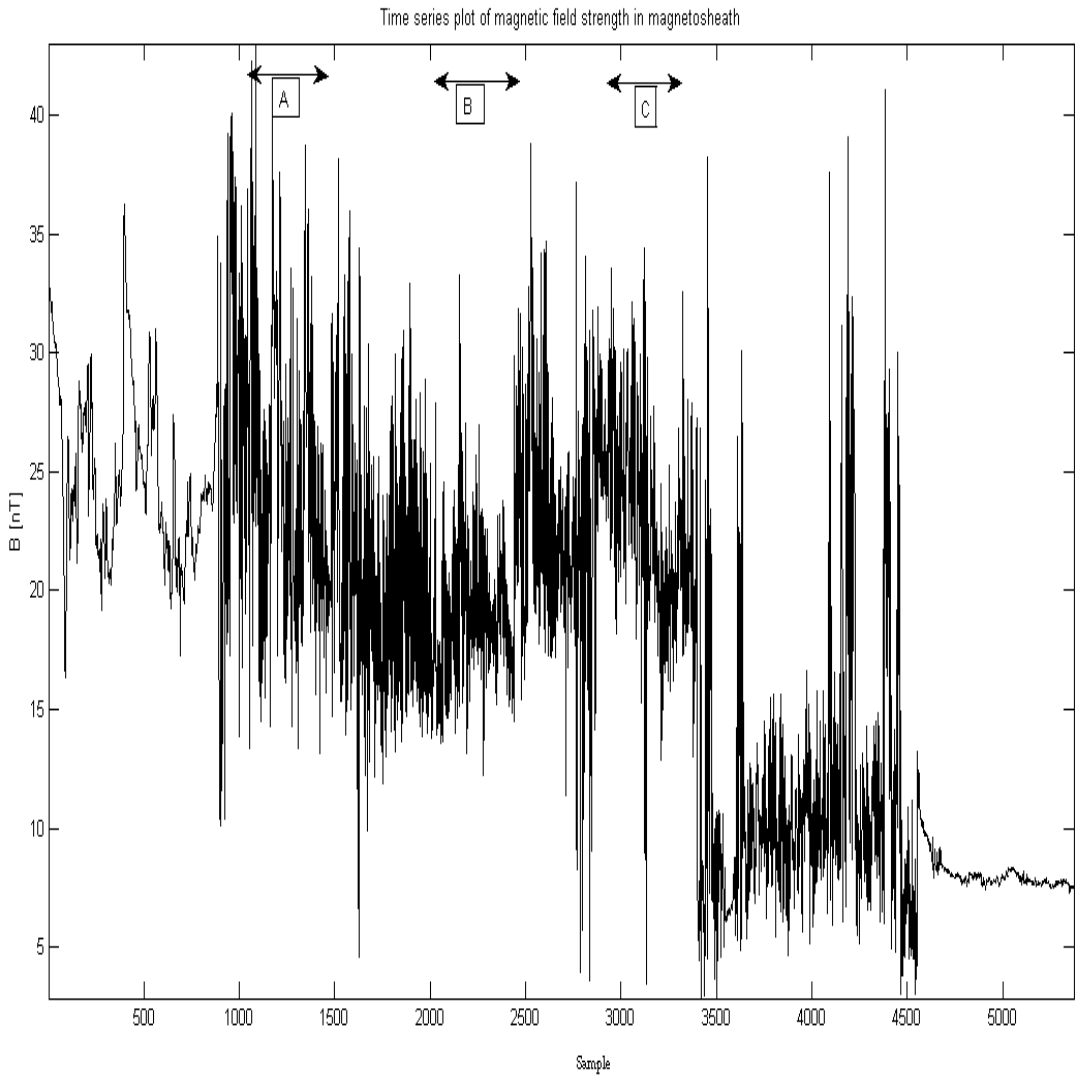


Figure 7.1: Time series plot of magnetic field strength collected between 04:00 and 10:00 UT on 18 02 2002. A, B and C are the chosen zones for analysis.

## 7.3 Results

Using the parallel and perpendicular proton temperatures observed by CIS instrument of Cluster [Réme et al., 2001], we have computed temperature anisotropies (Figures 7.2−7.4) in the three selected zones to characterise the wave modes using the ratio of $T_{p(\perp)}$ and $T_{p(\parallel)}$. Where $T_{p(\perp)}$ and $T_{p(\parallel)}$ are the perpendicular and parallel proton temperatures to the background magnetic field. The computed results for plasma beta $\beta$ (Figure 7.14) show high plasma beta that vary within the three chosen zones. Figures 7.5 − 7.7 also displays comparisons of the satellite frame phase velocities with the plasma bulk velocities. The average value in the phase velocity is $\approx 106 km/s$ while average value for plasma bulk velocity is $\approx 232 km/s$. $V_{ph}$ denotes satellite frame velocity and $V_{pb}$ denotes plasma bulk velocity. Blue represents Phase velocity and red represents plasma bulk velocity. Figures 7.8−7.10 are the histograms of the ratio of the phase velocities in the satellite frame to the Alfĕn velocities. Computed results of the ratio of the satellite frame phase velocities give mean value within the range of 0.60−0.69 in the zone A, within the range of 1.40−1.69 in zone B and within the range of 1.00−1.29 in zone C. Between figures 7.2−7.14, some mixed mode properties exist.

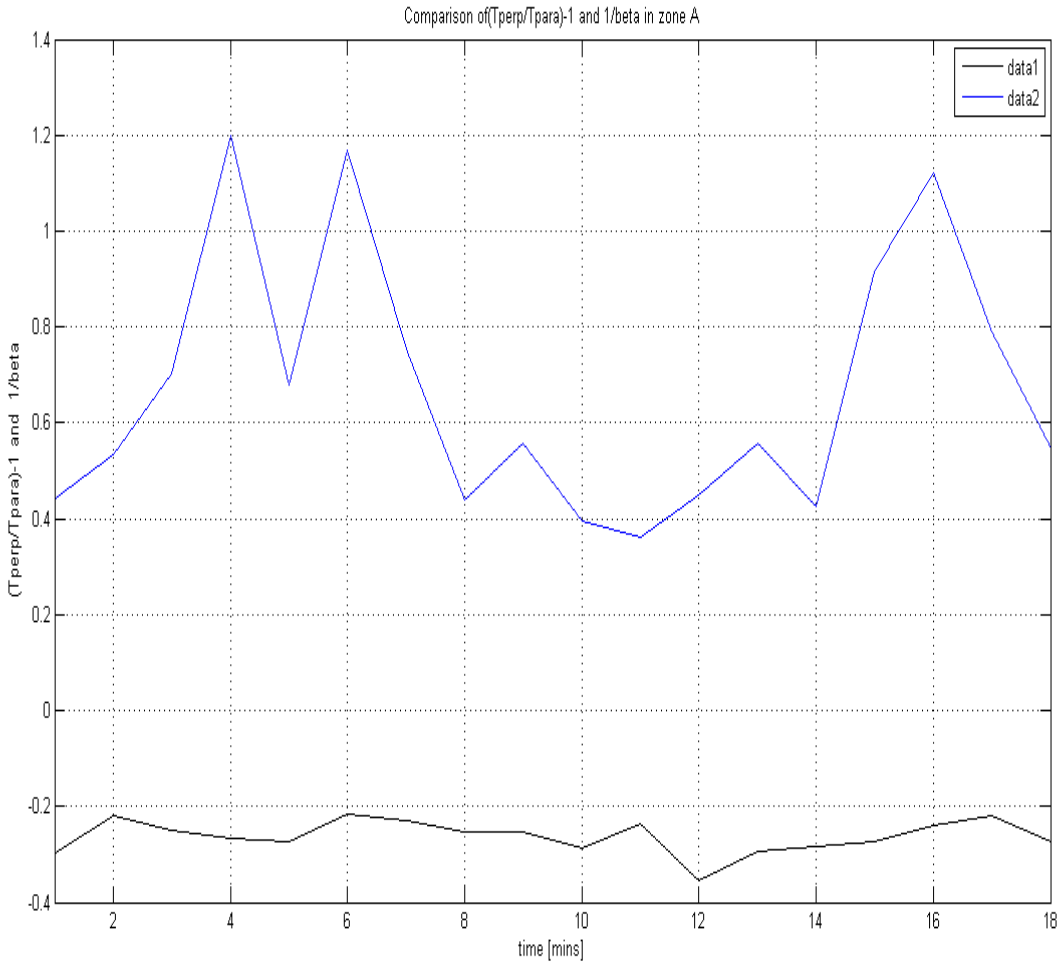


Figure 7.2: Plot of $(T_p \perp / T_p \parallel) - 1$ and $1/\beta$ in zone A. Data1 is $(T_p \perp / T_p \parallel) - 1$ (black) while data2 is $1/\beta$ (blue).

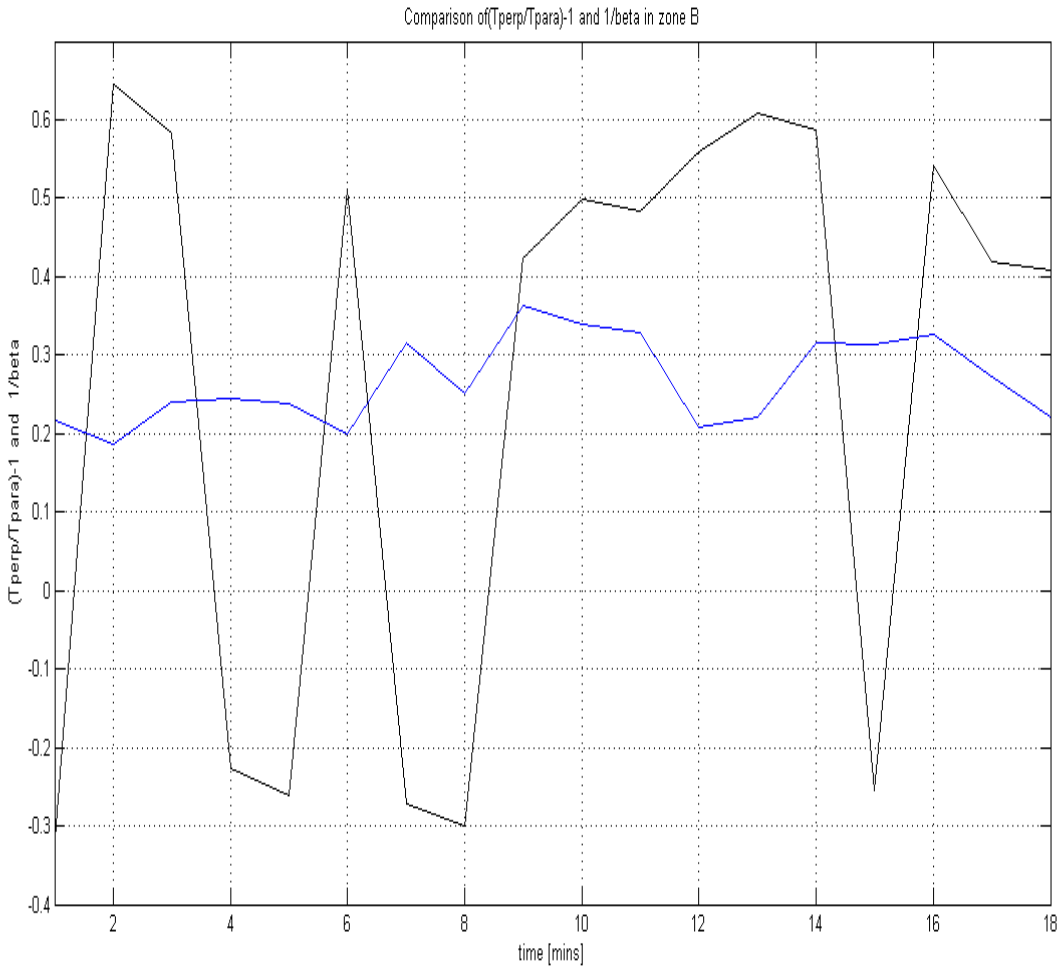


Figure 7.3: Plot of $(T_p \perp / T_p \parallel) - 1$ and $1/\beta$ in zone B. Data1 is $(T_p \perp / T_p \parallel) - 1$ (black) while data2 is $1/\beta$ (blue).

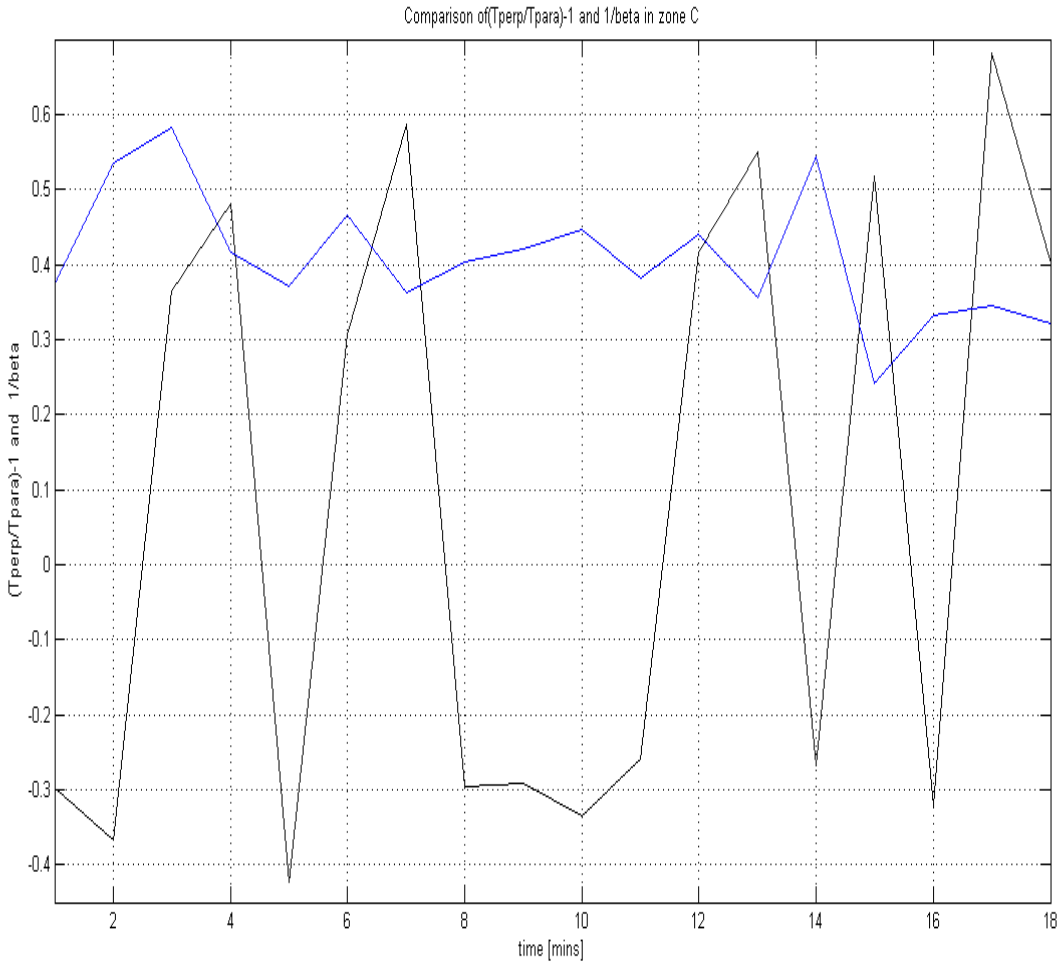


Figure 7.4: Plot of $(T_p \perp / T_p \parallel) - 1$ and $1/\beta$ in zone C. Data1 is $(T_p \perp / T_p \parallel) - 1$ (black) while data2 is $1/\beta$ (blue).

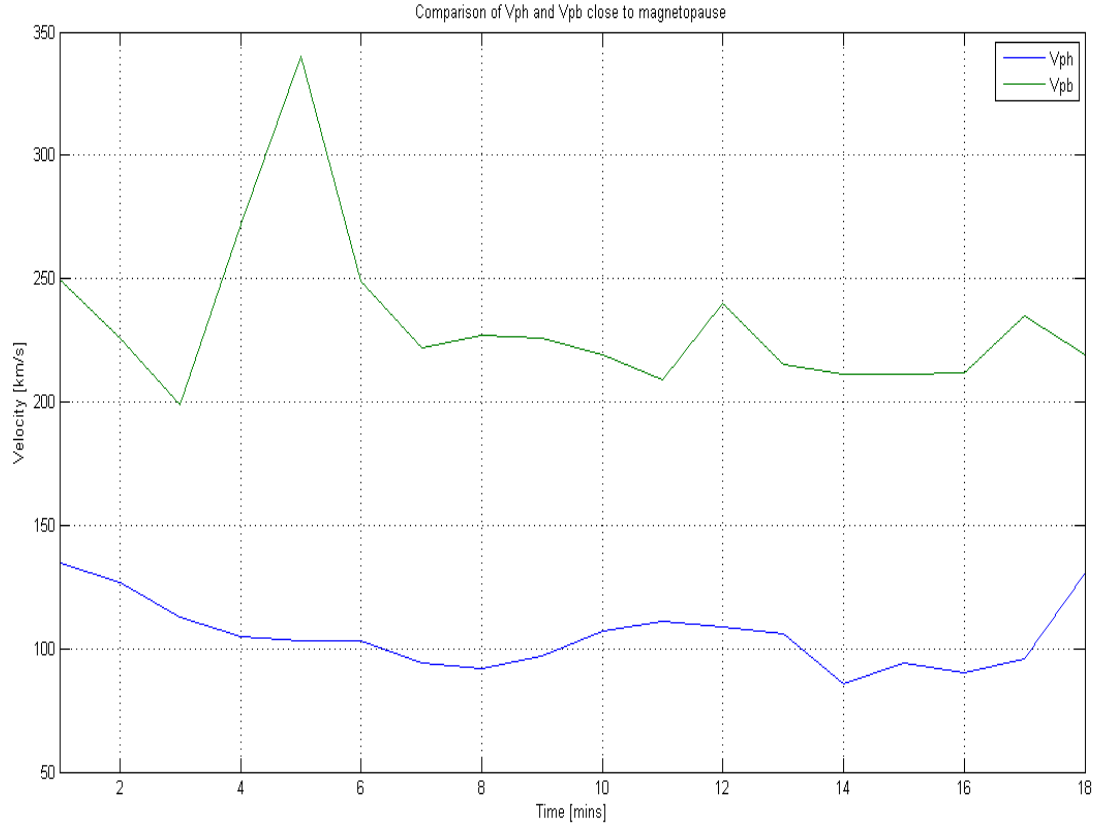


Figure 7.5: Instantaneous phase velocities in the satellite frame and the plasma bulk velocities within zone A. The average value in the phase velocity is $\approx 106km/s$ while average value for plasma bulk velocity is $\approx 232km/s$. $V_{ph}$ denotes satellite frame velocity and $V_{pb}$ denotes plasma bulk velocity. Blue represents Phase velocity and red represents plasma bulk velocity.

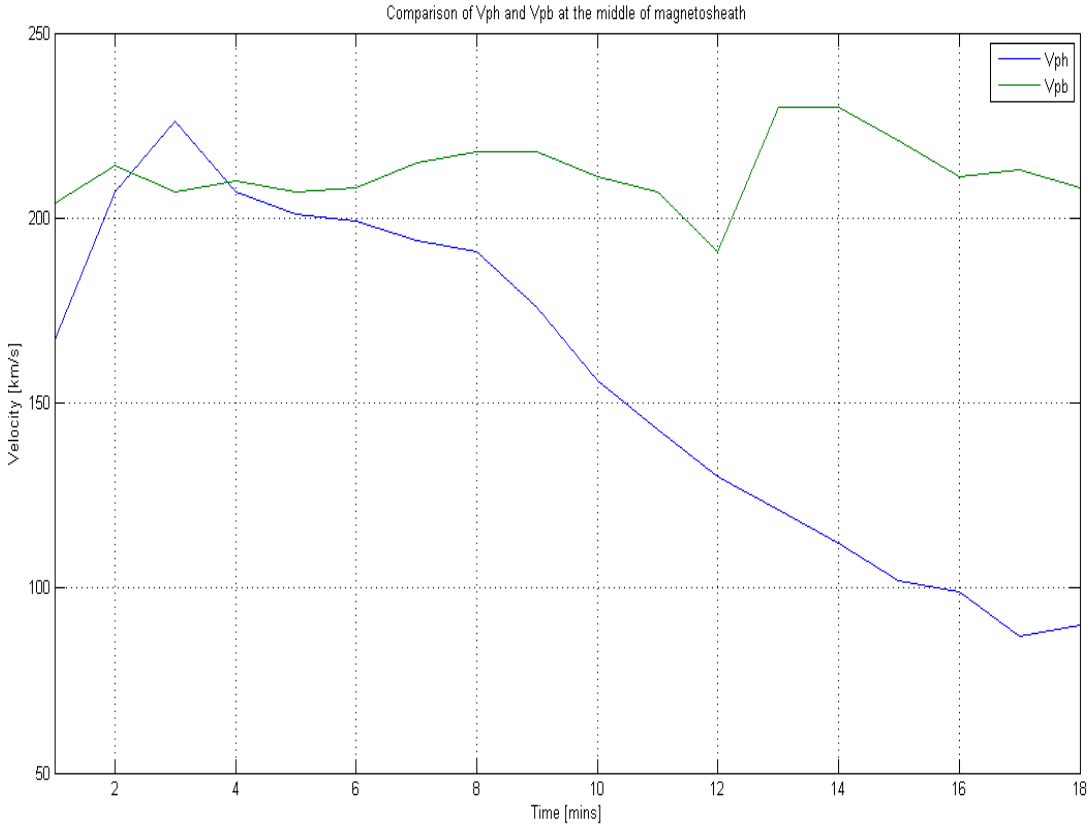


Figure 7.6: Instantaneous phase velocities (blue) in the satellite frame and the plasma bulk velocities (red) within zone B. The average value in the phase velocity is $\approx 156 km/s$ while plasma bulk velocity is $\approx 212 km/s$.

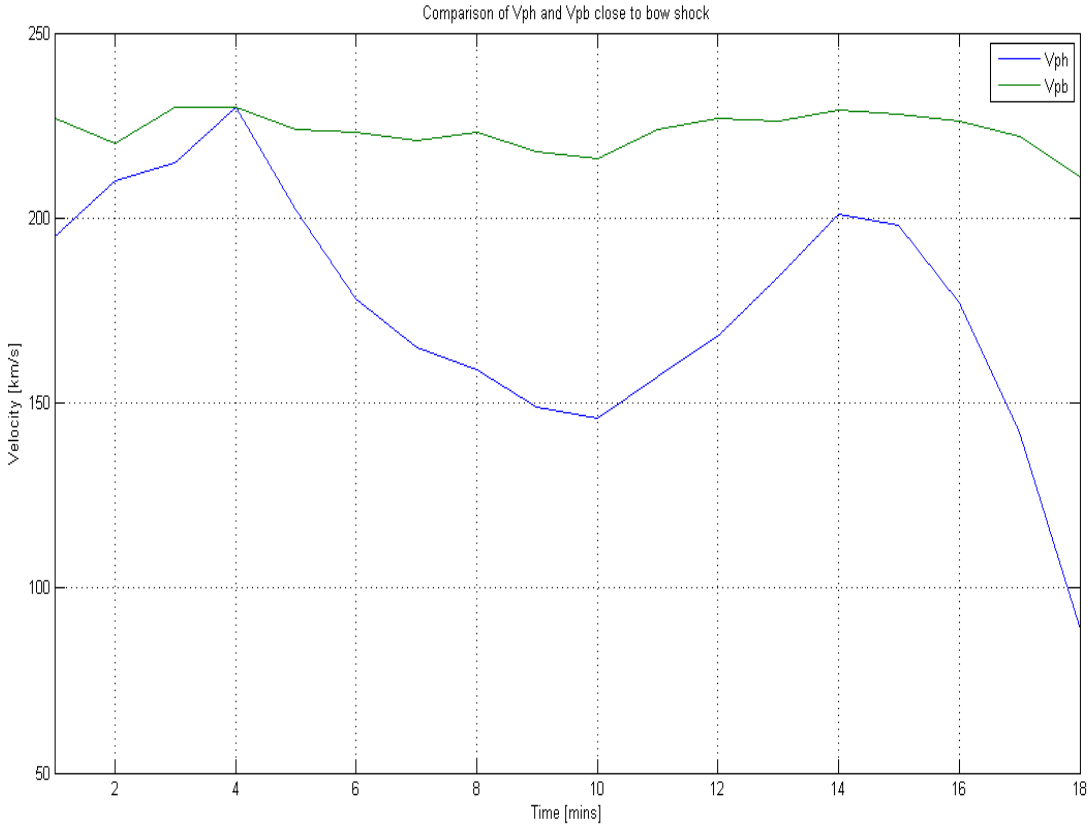


Figure 7.7: Instantaneous phase velocities in the satellite frame and the plasma bulk velocities within zone C. The average value in the phase velocity is $\approx 176 km/s$ and plasma bulk velocity is $\approx 224 km/s$.

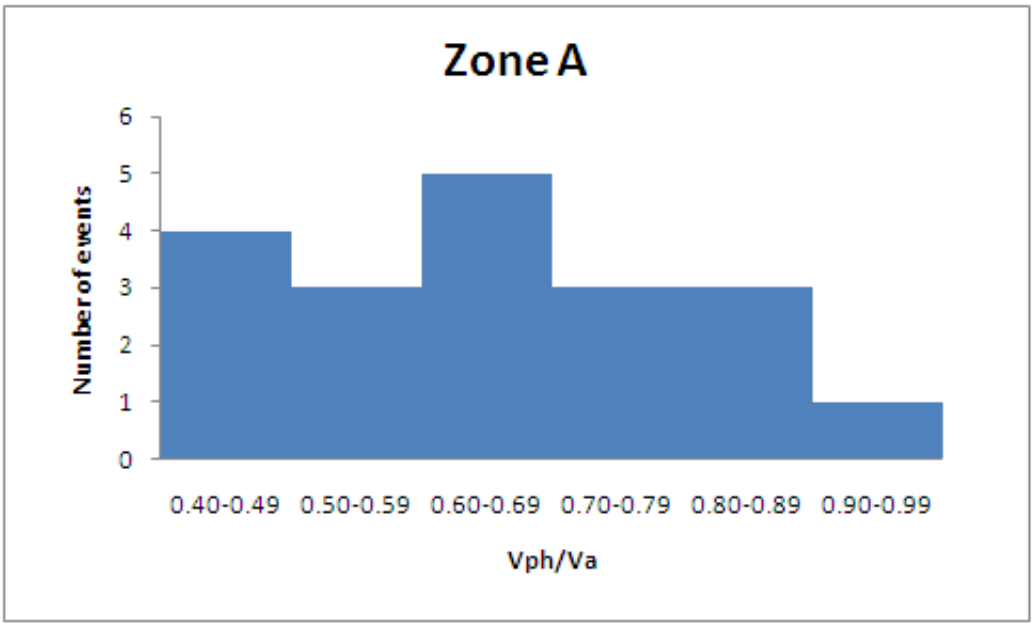


Figure 7.8: Histogram of the ratio of satellite frame phase velocities and Alfvén velocities across the magnetosheath for selected zones A.

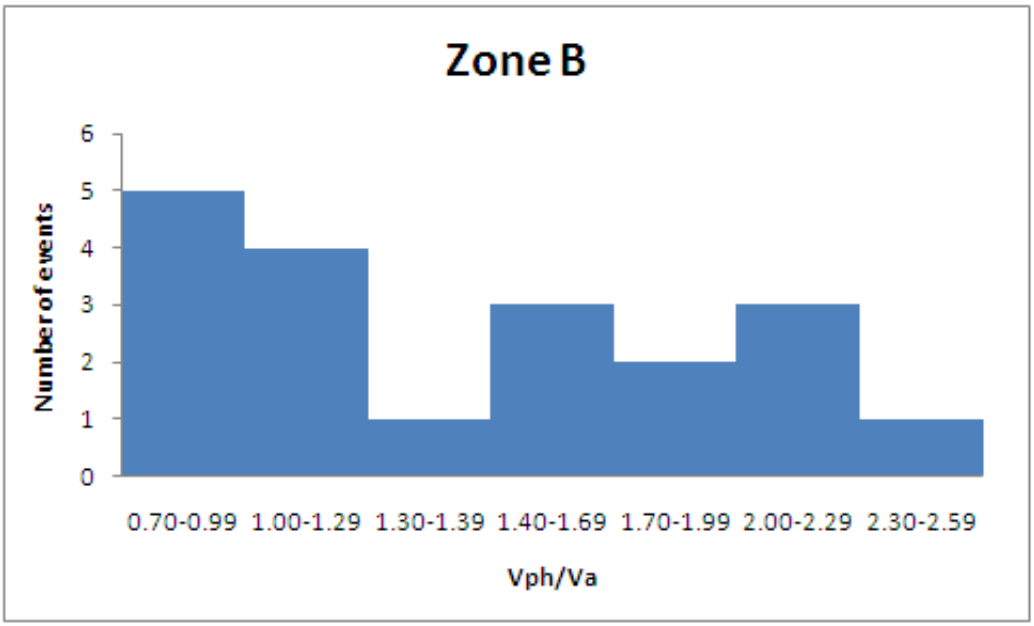


Figure 7.9: Histogram of the ratio of satellite frame phase velocities and Alfvén velocities across the magnetosheath for selected zones B.

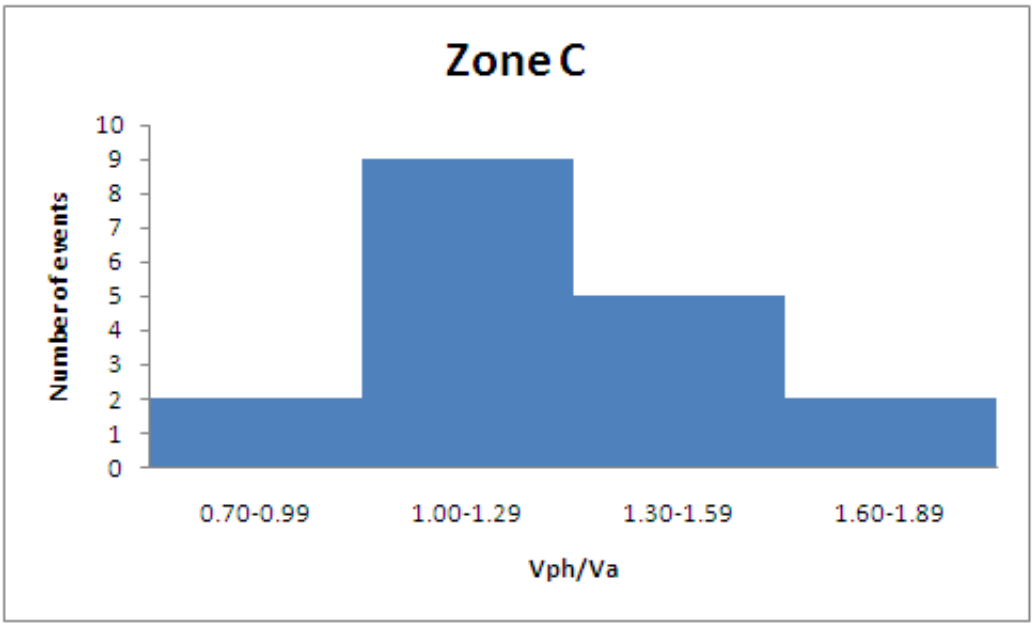


Figure 7.10: Histogram of the ratio of satellite frame phase velocities and Alfvén velocities across the magnetosheath for selected zones C.

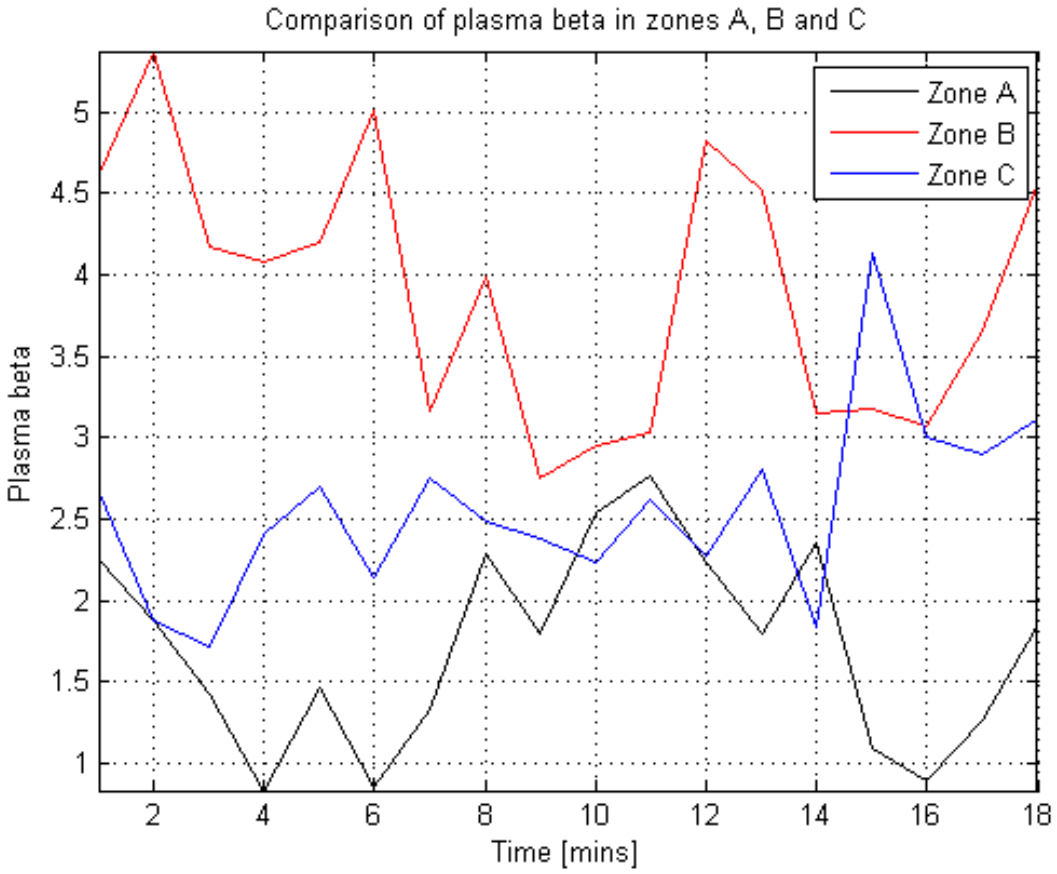


Figure 7.11: Plasma beta $\beta$ for the three chosen zones A, B and C. Blue represents zone A, red represents zone B and green represents zone C.

## 7.4 Analysis and Discussion

### 7.4.1 Wave modes identification in zone A close to the magnetopause

Between 05:15 and 05:35 UT referred to as zone A (Figure 7.1), the wave properties computed using magnetic field, proton, temperature and velocity data are displayed in Figures 7.2, 7.5 and 7.8. The plot of $(T_p \perp / T_p \parallel) - 1$ and $1/\beta$ in Figure 7.2 shows that $(T_p \perp / T_p \parallel) - 1 < 1/\beta$. This shows that the mirror mode criterion is not met in this zone. Figure 7.5 shows satellite frame phase velocity with average value of 106 km/s and plasma bulk velocity of mean value of $\approx$ 232 km/s. The histogram in figure 7.8 shows that the ratio of phase velocity to the Alfvén velocity in this zone is dominated by low values in the range of $0.4-0.89$. These values indicate that this zone has a phase velocity lower than the proton cyclotron velocity or Alfvén velocity. It also indicates that close to the magnetopause, waves with phase velocities lower than Alfvén proton cyclotron velocity dominate. This lower velocity decreases as the wave approaches the magnetopause. As earlier mentioned, wave phase velocities lower than the intermediate or Alfvén velocities are identified as slow mode waves. Our results show that the plasma beta $\beta$ in this zone are greater than unity but less than those in zone B and C (Figure 7.11). The comparison of the instantaneous phase velocities and the plasma bulk velocities in this zone shows phase velocities (in blue) that are lower than the plasma bulk velocities (in red) as shown in Figure 7.5. And it has phase velocities in the satellite frame which are lower than the plasma bulk velocities and Alfvén velocities. We can say that slow mode dominates in this zone.

### 7.4.2 Wave modes identification in zone B in the middle of magnetosheath

Between the period 06:15 and 06:35 UT referred to as zone B, the estimated instantaneous phase velocities fluctuate in the satellite frame as does the plasma bulk velocity as shown in Figure 7.6. This figure plots velocities on the vertical axis and time in minutes on the horizontal axis. In the first two minutes, the phase velocity (blue) increases as does the plasma bulk velocity. Within the next two minutes, $V_{ph} \geq V_p b$. The figure further shows that the values of the phase velocities decrease as the satellite is moving and approaching the bow shock. The average values in both instantaneous phase and bulk velocities are $\approx$ 210 km/s and 209.5 km/s respectively. According to Balikhin *et al.* (2003), the coincidence in the two velocities or closeness could only be possible if the wave phase velocity in the plasma frame is zero. The wave vector interpolated linearly and the angle of the wave's propagation direction to the magnetic field between 06:16 and 06:19 UT are given in Table 7.1. The angles between the wave vectors and the magnetic field are large with an average of $\approx$ 77 degrees within the period 06:16 and 06:19 UT. The wave vectors give average wavelength in anti−sun (x) direction as $2828km$, $14923km$ in dawn−dusk (y) direction and $5593km$ in the upward (z) direction. This implies that the wave propagated fastest in the anti−sun direction. It propagated slowest in the dawn−dusk direction. Between 06:27 and 06:33

| $k_x[km^{-1}]$ | $k_y[km^{-1}]$ | $k_z[km^{-1}]$ | $\theta_{kb}$ |
|---|---|---|---|
| 0.0021 | 0.0004 | 0.0011 | 77 |
| 0.0022 | 0.0004 | 0.0011 | 82 |
| 0.0023 | 0.0004 | 0.0011 | 79 |
| 0.0023 | 0.0005 | 0.0012 | 71 |

Table 7.1: Wave vector interpolated linearly and the angle of the wave's propagation direction to the magnetic field between 06:16 and 06:19 UT.

UT, the average value of the computed instantaneous phase velocities in the satellite frame decreases to about 106 km/s with a bulk velocity of $\approx$ 214 km/s. This is close to the computed average value of the Alfvén velocity of $\approx$ 110 km/s in this zone. This indicates that this region of the zone is dominated by Alfvén ion cyclotron mode waves. This conclusion is also found in the histogram (Figure 7.9) of the instantaneous phase velocity normalised to Alfvén velocity within the range of $1.00-1.29$.The range of $0.70 - 0.99$ (i.e. sub$-$Alfvén) corresponds to the range mentioned in zone A (Figure 7.8). This indicates a mode with phase velocity which is not alfvénic but a mode with velocity smaller than the Alfvén velocity. We conclude that this is a slow mode wave. The computed results of instantaneous phase velocity normalized to Alfvén velocity also give a super$-$Alfvén range of $1.39 - 2.59$ (Figure 7.9), which indicates that the computed instantaneous phase velocities are larger than the values of the Alfvén velocity. This is further asserted with the results obtained by comparing the instantaneous phase velocities with the plasma bulk velocities in this zone, which has been mentioned above to show a mirror mode towards the middle of the magnetosheath as the waves are crossing the bow shock. This indicates that this region is dominated by mirror waves. The Plasma beta $\beta$ is largest in this zone as in Figure 7.11 (red). We also combined the computed results of the proton temperature anisotropy to define the criterion for mirror mode (Figure 7.3). The plot in this figure shows that $(T_p \perp / T_p \parallel) - 1 \geq 1/\beta$ (where the graph with black line crosses the graph with blue line). We link this result to mirror mode. We have seen such overlap in zone A that may suggest a possibility of mixed wave mode in this zone (B).

### 7.4.3 Wave modes identification in zone C close to the bow shock

Between 07:15 and 07:35 UT (zone C), the computed phase velocity is higher than the Alfvén velocity but close to the plasma bulk velocity with average values of $\approx 229$ km/s (see 4 mins. mark on figure 7.7) for phase velocity in the satellite frame and 225 km/s for the plasma bulk velocity as shown in figure 7.7. The closeness in the values conforms to the earlier cases found for a mirror mode in zone B. We can conclude that this region in zone C is mirror mode. Beyond this region between 07:20 and 07:31, the average value for the computed instantaneous phase velocity is $\approx 168$ km/s and the average value for the plasma bulk velocity is $\approx 222$ km/s. The average value for the computed Alfvén velocity is $\approx 167$ km/s. This value coincides with the computed satellite frame phase velocity. This confirms that this region of this zone is Alfvén wave mode. The histogram of the phase velocity normalized to Alfvén velocity (figure 7.10) shows a peak in the range $1.00 - 1.29$. This implies that the phase velocity is approximately equal to the Alfvén velocity. This suggests an Alfvén wave mode. The zone has high plasma beta in regions identified as Alfvénic (as in Figure 7.11 (blue)) lower than those in region B (red) and larger than those in region identified as slow mode (black). We further combine the plasma beta and proton temperature anisotropy to analyse if this zone has met mirror mode criterion $((T_p \perp / T_p \parallel) - 1 \geq 1/\beta)$. Our results show that this criterion is met with values of $(T_p \perp / T_p \parallel) - 1$ being less than $1/\beta$ in most cases. The few cases when $(T_p \perp / T_p \parallel) - 1 \geq 1/\beta$ such as periods $6-8$, $12-14$, $14-16$ and $16-18$ (on time axis) are dominated by condition where $(T_p \perp / T_p \parallel) - 1 < 1/\beta$. We therefore conclude Alfvén mode waves. We conclude that part of this zone is mixed mode of Alfvénic and mirror wave modes .

## 7.5 Summary

The study of the wave modes in the magnetosheath for the three chosen zones A, B and C has confirmed earlier results which stated existence of Alfvén ion cyclotron, mirror and slow modes. The presence of these modes have been linked to the activities in the upstream foreshock according to [Constantinescu et al., 2007], and Narita (2006). The presence of these modes have also been linked to proton temperature anisotropies according to Hubert (1994), Schafer *et al.* (2005) and [Denton, 2000]. We have used satellite frame phase velocity normalized to the Alfvén velocity in each zone to identify the wave modes. We have also used proton temperature anisotropies combined with plasma beta to define the criterion for mirror wave mode, using the instantaneous relation of phase velocities and plasma bulk velocities to support our results. Our results show that zone A which is near the magnetopause is characterised with slow mode wave. This zone is also found to have mirror mode, which diminishes towards the magnetopause. We have also found that the ratio of the thermal pressure to the magnetic pressure is high with dominant thermal pressure within the magnetosheath. This thermal pressure is greatest within the middle magnetosheath found in zone B. Mirror mode growth is stable as the proton temperature anisotropy shows larger parallel proton temperature. The mirror instabilities grow when $(T_p \perp / T_p \parallel) - 1 \geq 1/\beta$. The computed results show that zone B is dominantly mirror mode. The inner magnetosheath which zone C form part is close to the bow shock, and has been identified with Alfvén mode waves based on the computed satellite frame instantaneous phase velocity. Histogram of the phase velocity normalized to Alfvén velocity show peak in the range $1.00 - 1.29$ implying that the wave mode is dominantly alfvénic. The histogram also shows higher values implying that this zone is also mixed with mirror mode.

# Chapter 8

# Conclusion

## 8.1 Research summary

This chapter condenses the main results presented in this thesis, which considers the analysis of space plasma in the magnetosheath without any limitations to non−stationary and non−linear behaviour using measurements and observations taken by the four Cluster spacecraft. The magnetosheath is the medium in between the bow shock and the magnetopause. The properties of the magnetosheath are influenced by the solar wind bulk speed, which sets up a bow shock that regulates the flow of solar wind particles around the magnetopause. The position of the magnetopause depends on the equilibrium between the overall plasma pressure from the magnetosheath and the magnetic pressure from the magnetosphere (Parks *et al.* (1991), Baumjohann (1996), Kivelson *et al.* (1991). The study of the magnetosheath has been used successfully in the determination and prediction of the responses of the magnetosphere.

We have studied this downstream of the Earth bow shock with the aim of unravelling the significant importance of the bow shock and the physical processes within the

magnetosheath. We began by presenting the background of the solar−terrestrial coupling with the reviews of the basics of magnetic field and particles measurements in Chapter 2. The types and functions of Cluster instruments related to this thesis are presented in Chapter 3.

The applicability of Hilbert−EMD otherwise called Hilbert−Haung Transform, for the extraction of the various contributing signals, referred to as intrinsic mode functions ($imf$s), in data and the determination of the instantaneous frequencies of the various $imf$s is presented in Chapter 4. This chapter presented results indicating superposition of waves for observations collected within the period previously analysed using SHT was carried out. The results presented are based on both the analysis found with EMD and SHT. The superposition of wave presented gave a representation of the time series of the original data without a loss of sense and reliable physical meaning as shown in Figure 4.29.

Chapter 5 has presented the local wave vector analysis. The instantaneous wave vectors are determined for corresponding instantaneous frequencies. The instantaneous wave vector $\mathbf{k}$ is computed from the projection of wave vectors computed along satellite separations. The results in this chapter were computed for every instantaneous value of frequency decomposed using Hilbert transform for each $imf$ extracted. The results show instantaneous wave number that varies with the instantaneous frequency.

Chapter 6 outlined the instantaneous dispersion relations in the magnetosheath. This chapter combines the knowledge of the instantaneous frequency and wave vectors. The results revealed the instantaneous properties of the wave. The results in this chapter for one of the $imf$s show that the instantaneous wavelength were consistent with previous analysis using Instantaneous Local Wave (ILW) vector estimation technique that is based on SHT and assumption that the wavelength of the wave must be larger than

the smallest separation between spacecraft.

Chapter 7 presented results of wave mode identification in the magnetosheath. This showed that downstream of the Earth's bow shock the physical processes change as shown by the change in the various properties of the waves in the magnetosheath. The dispersion curves were investigated as the spacecraft traversed the magnetosheath. The results show transitions from Alfvén ion cyclotron to mirror and to slow modes characteristics. Alfvén ion cyclotron mode characteristics were dominantly detected close to the bow shock. This mode was found to be mixed with mirror mode as the spacecraft moved away from the bow shock. Further away from the bow shock into the middle of the magnetosheath, mirror mode characteristics were often detected with finite propagation velocities. Close to the magnetopause, slow mode characteristics were detected, but were also mixed with mirror mode as the spacecraft fleet moved away from the middle towards the magnetopause. The mixture of modes revealed that space plasmas in the region were non−stationary and inhomogeneous. The general characteristics in the magnetosheath show a stronger dependence on perpendicular propagation of waves relative to the background magnetic field.

## 8.2 Major findings

This thesis has given contributions that attempt to give answers to the questions on space plasmas and waves analysis, and has created opportunity for improvements that will give clearer understanding of different space plasma analysis. The results presented in this thesis could be improved if the following drawbacks are improved. These are:

- The criteria for separation of tones. To avoid analysing frequencies with no relevant physical information about the data, there is need for better criteria

for separating the noise frequencies from the information carriers (see subsection 4.3.3).

- Improvements have been made on EMD for providing greater detail, but more improvements are still needed to be done (see subsection 4.2.2).

This thesis is aimed at investigating the physical processes within the magnetosheath. The following conclusions are that in this thesis:

1. A technique has been developed (section 4.2 and 4.3) that does not assume stationary and homogeneity. This technique allows for the determination of wave properties instantaneously, being able to extract the constituent signals in data and treats each signal as mono−component signal. It therefore attempts to answer question on multi−component waves.

2. Results are presented which show that the physical processes downstream of the Earth's bow shock are different from those obtained upstream (section 7.3), which makes the bow shock to be considered as a regulator of solar−wind plasma interactions. These results confirmed other investigations which concluded that ion reflection is the cause of the different physical processes accompanying different excitation of waves in the upstream and the downstream of the bow shock (section 7.3).

3. Alfvén ion cyclotron wave with larger growth rate for temperature anisotropy instabilities was identified from the observational data. This observation of larger growth rate is seen mixed with constant temperature anisotropy instabilities. Our results (section 7.3) are consistent with other analysis confirming larger plasma beta for regions of dominantly mirror mode than regions with Alfvén and slow modes properties.

4. The attempt is given to answer the question of complex behaviour of magnetosheath otherwise known as turbulence (section 7.3).

## 8.3 Further work

The understanding of the sudden change in the solar wind properties within the magnetosheath requires a mission such as the THEMIS mission, which has a set of five spacecraft that allows to probe across the magnetosheath simultaneously on different scales. The analysis of THEMIS observations by other investigators consider stationary condition which offers less relevance to practical condition of the plasma which is non-stationary. The use of EMD and SHT combination has been tested with Cluster spacecraft observations without any exclusion of non−stationary and non−linear conditions. This combination of EMD and Hilbert transform implies that the parameters of plasma are analysed at every instant along the path of the spacecraft, and the dispersion in plasma frame computed using Doppler shift. The aims of THEMIS mission can be achieved especially with the availability of both space and ground instruments observing the time series of events. A correlation analysis could be carried for both the space and ground instantaneous frequencies and wave vectors which may allow better understanding of wave propagation that will aid the easy study of substorms.

We shall particularly look into application of the technique considered in this thesis in the context of observational data from THEMIS instruments. We intend to exploit the linear array of these instrument across the magnetosheath. This will be targeted at high solar activity seasons. A brief instrument plan for THEMIS and brief discription are given in Appendix A. The technique used in this thesis is not limited to the understanding of the space physics in the Earth's environment alone but could also be

used in the analysis of instantaneous frequency and wave vector for better understanding of space physics for observations obtained in other planetary environments and other space environments.

# Bibliography

*http://themis.ssl.berkeley.edu/instruments.shtml. Accessed on 12th July 2010.*

*http://xeus.esa.int/science-e/www/object/index.cfm?fobjectid=33024&fbodylongid=1116. Accessed on 18th February 2010.*

*http://cdaweb.gsfc.nasa.gov/cgi-bin/eval2.cgi. Accessed on 23rd March 2010.*

*http://clusterlaunch.esa.int/science-e/www/object/index.cfm?fobjectid=36559. Accessed on 14th July 2010.*

*http://www.ens-lyon.fr/ flandrin/software.html. Accessed on 24th March 2010.*

B. J. Anderson, S. A. Fuselier, and D. Murr. Electromagnetic ion cyclotron waves observed in the depletion layer. *Geophysical Research Letter*, 18:1955–1958, 1991. 21

B. J. Anderson, S. A. Fuselier, S. P. Gary, and R. E. Denton. Magnetic spectral signatures in the earth's magnetosheath and plasma depletion layer. *J. Geophysical Research Letter*, 99:5877–5891, 1994.

V. Angelopoulos. Overview of the themis mission. In *Overview of the THEMIS mission*, 2002. 197

M. A. Balikhin and S. N. Walker. Methods of plasma turbulence analysis: Application to shock studies. *American Institute of Physics*, 731:123–128, 2005. 11, 13

M. A. Balikhin, T. Dudok de Wit, H. St. C. K. Alleyne, V. Krasnoselśkikh, W. A. C. Mier-Jedrzejeowicz, and W. Baunmjohann. Experimental determination of the dispersion of waves observed upstream of quasi-perpendicular shock. *Geophysical Research Letter*, 24, NO. 7:787–790, 1997. 15, 50, 92, 112

M. A. Balikhin, L. J. C. Woolliscroft, H. St. C. Alleyne, M. Dunlop, and M. A. Gedalin. Determination of the dispersion of low-frequency waves downstream of quasi-perpendicular shock. *Ann. Geophysicae*, 15:143–151, 1997b. 92

M. A. Balikhin, O. A. Pokhotelov, S. N. Walker, and M. André. Identification of low frequency waves in the vicinity of the terrestrial bow shock. *Planetary and Space Science*, 51:693–702, 2003. 16

A. Balogh, M. W. Dunlop, S. W. H. Cowley, D. J. Southwood, J. G. Thomlinson, K. H. Glassmeier, G. Musmann, H. Luhr, S. Buchert, M. H. Acuńa, D. H. Fairfield, J. A. Slavin, W. Riedler, K. Schwingenschuh, and M. G. Kivelson. The cluster magnetic field investigation. *Space Sci. Rev.*, 79:65 – 92, 1997. 27, 95

A Balogh, C. M. Carr, M. H. Acuna, M. W. Dunlop, T. J. Beek, P. Brown, K.-H. Fornacon, E. Georgescu, K.-H. Glassmeier, J. Harris, G. Musmann, T. Oddy, and K. Schwingenschuh. The cluster magnetic field investigation: Overview of in-flight performance and initial results. *Ann. Geophysicae*, 19:1207–1217, 2001. 27

I. Bates, M. A. Balikhin, H. St. C. K. Alleyne, and M. André. Minimum-variance free determination of magnetosheath wave propagation vectors. *Sheffield Space Plasma Meeting: Multipoint Measurements versus Theory, Les Woolliscroft Memorial Conference held 24-26 April, 2001 in Sheffield, UK. Eurpoean Space Agency*, page 133, 2001.

W. Baumjohann and R. A. Treumann. *Basic Space Plasma Physics*. Imperial College Press, London, 1996. 2, 8, 9, 12, 13, 14, 15, 16, 17, 19, 21, 136

J. M. Beall, Y. C. Kim, and E. J. Powers. Estimation of wavenumber and frequency spectra using fixed probe pairs. *J. Appl. Physics*, 53:3933–3940, 1982. 35, 94

E. Bedrosian. A product theorem for hilbert transform. *Proc. IEEE*, 51:868–869, 1963. 46

J. S. Bendat and A. G. Piersol. *Engineering applications of correlation and spectral analysis, pp. 54-56.* John Wiley & Sons, Inc., New York, 1980. 92

T. Berkant and P. J. Loughlin. Instantaneous frequency and time-distributions. *Proc. IEEE*, pages 1013–1016, 1995. 33

D. Biskamp and H. Welter. Ion heating in the high-mach-number, oblique, collisionless shock waves. *Phys. Rev. Letter*, 28:410–413, 1972.

B. Boashash. Estimating and interpreting the instantaneous frequency of a signal- part 1: Fundamentals. *Proc. IEEE*, 80, No. 4:520–538, 1992. 33, 34, 35, 37, 38, 93

R. Bruno, V. Carbone, B. Bavassano, and L. Sorriso-Valvo. Observations of magnetohydrodynamic turbulence in the 3d heliosphere. *Advances in Space Research*, 35:939–950, 2005.

T. D. Carozzi, A. M. Buckley, and M. P. Gough. Instantaneous wave vector estimation from multi-spacecraft measurements using few spatial points. *Annales Geophysicae*, 22:2633–2641, 2004. 5, 33, 36, 37, 38, 91, 92, 93, 94, 119

S. W. Chang, J. D. Scudder, J. F. Fennell, R. Friedel, and R. P. Lepping. Energetic magnetosheath ions connected to the earth's bow shock: Possible source of cusp energetic ions. *Journal of Geophysical Research*, 105, No. A3:5471–5488, 2000. 20

Y. Da Cheng, J. and Y. Yu. Research on the intrinsic mode function (imf) criterion in emd method. *Mechanical Systems and Signal Processing*, 20:817–824, 2006. 4

L. Cohen. Time-frequency distributions. *A review. Proc. IEEE*, 77, No. 7:941– 981, 1989. 37

L. Cohen. *Time-frequency analysis*. Prentice Hall PTR, 1995. 33, 37

L. Cohen and Lee. Instantaneous frequency, its standard deviation and multicomponent signals. *SPIE Advanced Algs. Archs. Sig. Proc. III*, 975:186–208, 1988. 33, 37

O. D. Constantinescu, K.-H. Glassmeier, R. A. Treumann, and K.-H. Fornacon. Magnetic mirror structures observed by cluster in the magnetosheath. *Geophys. Res. Lett*, 30, 2003.

O. D. Constantinescu, K.-H. Glassmeier, P. M. E. Décŕeau, M. Franz, and K.-H. Fornacon. Low frequency wave sources in the outer magnetosphere, magnetosheath, and near earth solar wind. *Ann. Geophysicae*, 25,:2217–2228, 2007. 158

N. U. Crooker and G. L. Siscoe. A mechanism for pressure anisotropy and mirror instability in the dayside magnetosheath. *J. Geophys. Res. Lett*, 82:185 – 186, 1977. 21

N. U. Crooker, T. E. Eastman, and G. S Stiles. Observations of plasma depletion in the magnetosheath of the dayside magnetopause. *J. Geophysical Research Letter*, 84: 869–874, 1979.

E. Deléchelle, J. Lemoine, and O. Niang. Empirical mode decomposition: An analytical approach for sifting process. *IEEE Signal Processing Letters*, 12, NO. 11:764–767, 2005. 41

R. E. Denton. Ulf waves in the magnetosheath. *Inter. J. Geomagn.*, 2:1 – 14, 2000. 20, 158

R. E. Denton, S. P. Gary, X. Li, B. J. Anderson, J. W. LaBelle, and M. Lessard. Low-frequency fluctuations in the magnetosheath near the magnetopause. *J. Geophysical Research Letter*, 100:5665–5679, 1995.

M. E. Dieckmann, B. Eliasson, P. K .Shukla, N. J. Sircombe, and R. O. Dendy. Two-stream instability in collisionless shocks and foreshock. *Plasma Phys. Control. Fusion*, 48:B303–B311, 2006.

M. W. Dunlop, A. Balogh, P. Cargill, R. C. Elphic, K.-H. Fornacon, E. Georgescu, F. Sedgemore-Schulthess, and the FGM team. Cluster observes the earth's magnetopause: Co-ordinated four-point measurements. *Ann. Geophysicae*, 2001.

G. Erdos and A. Balogh. Statistical properties of minor mode structures observed by ulysses in the magnetosheath of jupiter. *J. Geophys. Res. lett.*, 101:1–12, 1996.

G. M. Erickson, G. L. Siscoe, D. R. Weimer, K. D. Siebert, M. A. Heinemann, B. U. O. Sonnerup, N. C. Maynard, and W. W. White. Prediction of alfvénic turbulence near the magnetospheric sash. *Planetary and Space Science*, 50:627– 632, 2002.

C. P. Escoubet, M. Fehringer, and M. Goldstein. The cluster mission. *Ann. Geophysicae,*, 19:1197–1200, 2001. 24

D. H. Fairfield. Whistler waves observed upstream from collisionless shocks. *J. Geophysical Research Letter*, 79:1368–1378, 1974. 15, 16

M. H. Farris, S. M. Petrinec, and C. T. Russell. The thickness of the magnetosheath: constraints on the polytropic index. *J. Geophys. Res. lett.*, 18:1821, 1991.

C. J. Farrugia, R. P. Rijnbeek, M. A. Saunders, D. J. Southwood, D. J. Rodgers, M. F. Smith, C. P. Chaloner, D. S. Hall, P. J. Christiansen, and L. J. C. Woolliscroft. A multi-instrument study of flux-transfer event structure. *J. Geophysical Research Letter*, 93:144–165, 1988.

A. N. Fazakerley and D. J. Southwood. Mirror instability in the magnetosheath. *Adv. Space Res.*, 14, No. 7:65–68, 1994a.

A. N. Fazakerley and D. J. Southwood. Theory and observation of magnetosheath waves, in solar wind sources of magnetospheric ulf waves. *Geophysical Monogr. Ser.*, 81:147–158, 1994b.

P. Flandrin, G. Rilling, and P. Goncalves. Empirical mode decomposition as a filter bank. *IEEE Signal Process. Lett.*, 11, no. 2:112–114, 2004. 38, 39, 44, 48, 92, 93, 95, 96

V. Formisano. Orientation and shape of the earth's bow shock in the three dimensions. *Planet Space Science Reviews*, 27:1151–1161, 1979.

D. Gabor. Theory of communication. *Jour. IEE*, 93, Part III, No. 26:429–457, 1946. 37, 38, 45, 51, 91, 93

S. P. Gary. Low-frequency waves in a high-beta collisionless plasma: Polarization, compressibility and helicity. *J. Plasma Phys.*, 35:431–447, 1986. 17, 21

S. P. Gary and M. A. Lee. The ion cyclotron anisotropy instability and the inverse correlation between proton anisotropy and proton beta. *J. Geophysical Research Letter*, 99:11,297–11,301, 1994c. 21

S. P. Gary, P. D. Convery, R. E. Denton, S. A. Fuselier, and B. J. Anderson. Protons and helium cyclotron anisotropy instability thresholds in the magnetosheath. *J. Geophysical Research Letter*, 99:5915–5921, 1994a. 21

S. P. Gary, M. E. Mckean, D. Winske, B.J. Anderson, R. E. Denton, and S. A. Fuselier. The proton cyclotron instability anisotropy and the anisotropy / $\beta$ inverse correlation. *J. Geophysical Research Letter*, 99:5903–5914, 1994b. 21

M. Gedalin, M. A. Balikhin, R. J. Strangeway, and C. T. Russell. Long −wavelength mirror modes in multispecies plasmas with arbitrary distributions. *J. Geophys. Res. Lett.*, 106, 2002.

B. Gérard, F. Sahraoui, and L. Rezeau. Measuring and understanding space turbulence. *Advances in Space Research*, 37:1503–1515, 2006.

K.-H. Glassmeier, U. Motschmann, M. Dunlop, A. Balogh, M. H. Acuńa, C. Carr, G. Musmann, K.-H. Fornacon, K. Schweda, J. Vogt, E. Georgescu, and S. Buchert. Cluster as a wave telescope- first results from the fluxgate magnetometer. *Ann. Geophysicae*, 19:1439–1447, 2001. 92

D. G. Gleaves and D. J. Southwood. Magnetohydrodynamic fluctuations in the earths magnetosheath at 15:00 lt-isee 1 and isee 2. *J. Geophys. Res.*, 96:129–142, 1991.

J. T. Gosling, M. F. Thomsen, S. J. Bame, and C. T. Russell. Ion reflection and downstream thermalization at the quasi-parallel bow shock. *J. Geophysical Research Letter*, 94:10027–10037, 1989. 20

G. Gustafsson, M. André, T. Carozzi, A. I. Eriksson, C. G. Fälthammar, R. Grard, G. Holmgren, J. A. Holtet, N. Ivchenko, T. Karlsson, Y. Khotyaintsev, S. Klimov, H. Laakso, P.-A. Lindqvist, B. Lybekk, G. Marklund, F. Mozer, K. Mursula, A. Pedersen, B. Popielawska, S. Savin, K. Stasiewicz, P. Tanskanen, A. Vaivads, and J-E.Wahlund. First results of electric field and density observations by cluster $efw$ based on initial months of operation. *Annales Geophysicae*, 19:1219–1240, 2001. 31

A. Hasegawa. Plasma instabilities and non-linear effects. *Springer Verlag*, 1975.

P. Hellinger, P. Trávnícek, A. Mangeney, and R. Grappin. Hybrid simulations of the magnetosheath compression: Marginal satability path. *J. Geophys. Res. Lett*, 30: 1959–1963, 2003.

L. Helong, Xiaoyan Deng, and Hongliang Dai. Structural damage detection using the combination method of emd and wavelet analysis. *Mechanical Systems and Signal Processing*, 21:298–306, 2007. 48

T. S. Horbury, P. J. Cargill, E. A. Lucek, J. Eastwood, A. Balogh, M. W. Dunlop, K. H. Fornacon, and E. Georgescu. Four spacecraft measurements of the quasi-perpendicular terrestrial bow shock: Orientation and motion. *Journal Geophysical Research*, 107, No. A8, 2002. 13

N. E. Huang and S. S. Shen. *Hilbert−Huang Transform and its applications*. World Scientific Publishing Co. Pte Ltd., Singapore., 2005. 37, 38, 40, 41, 48, 92, 93, 95

N. E. Huang, Z. Shen, S. R. Long, M. C. Wu, H. H. Shih, Q. Zheng, N. Yen, C. C. Tung, and H. H. Liu. The empirical mode decomposition and the hilbert spectrum for nonlinear and non-stationary time series analysis. *Proc. R. Soc. Lond. A*, 454: 903–995, 1998. 3, 4, 33, 37, 38, 39, 42, 44, 49, 50, 92

N. E. Huang, M. Wu, W. Qu, S. R. Long, and S. S. P. Shen. Applications of hilberthuang transform to non-stationary financial time series analysis. *Appl. Stochastic Models Bus. Ind.*, 19:245–268, 2003. 38, 48, 95, 96

D. Hubert. Nature and origin of wave modes in the dayside earth magnetosheath. *Adv. Space Res.*, 14, No. 7:55–64, 1994. 22, 138, 139

D. Hubert, C. Lacombe, C. C. Harvey, M. Moncuquet, C. T. Russell, and M. F. Thomsen. Nature, properties, and origin of low-frequency waves from an oblique shock to the inner magnetosheath. *JGR-Space*, 103 , No. A11:26,783, 1998.

G. M. Jenkins and D. G. Watts. Spectral analysis and its applications. *Holden-Day, San Francisco*, pages 313–317, 1968. 92

R. Kallenbach, K. Bamert, M. Hilchenbach, and C. W. Smith. Observations of turbulence near interplanetary travelling shocks. *American Institute of Physics*, 781: 129–134, 2005.

C. F. Kennel, F. W. Coroniti, F. L. Scarf, W. A. Livesey, C.T. Russell, and E. J. Smith. A test of lee's quasi-linear theory of ion acceleration by interplanetary traveling shocks. *J. Geophys. Res. lett.*, 91:11917–11928, 1986. 19

M. G. Kivelson and C. T. Russell, editors. *Introduction to space physics*. Cambridge University Press, 1995. 2, 9, 12, 13, 14, 17, 19, 34, 136

N. A. Krall. What do we know about the collisionless shock? *Adv. Space Res.*, 20: 715–724, 1997.

J. A. Krommes. Fundamental statistical descriptions of plasma turbulence in magnetic fields. *Physics Reports*, 360:1352, 2002.

C. Lacombe and G. Belmont. Waves in the earth's magnetosheath: Observations and interpretations. *Adv. Space Research*, 15. No. 84:329–340, 1995.

M. A. Lee. Generation of turbulence at shocks. *American Institute of Physics*, 781: 240–245, 2005.

E. A. Lucek, M. W. Dunlop, A. Balogh, P. Cargill, W. Baumjohann, E. Georgescu, G. Haerendel, and K.-H. Fornacon. Identification of magnetosheath mirror modes in equator-s magnetic field data. *Ann. Geophysicae*, 17:1560–1573, 1999.

E. A. Lucek, M. W. Dunlop, T. S. Horbury, A. Balogh, P. Brown, P. Cargill, C. Carr, K. H. Fornacon, E. Georgescu, and T. Oddy. Cluster magnetic field observation in the magnetosheath: four-point measurements of mirror structures. *Ann. Geophysicae*, 19: 1421–1428, 2001.

J. G. Luhmann, C.T. Russell, and R. Elphic. Spatial distributions of magnetic field fluctuations in the dayside magnetosheath. *J. Geophys. Res. lett.*, 91:1711, 1986.

S. Matsukiyo and M. Scholer. Modified two-stream instability in the foot of high mach number quasi-perpendicular shocks. *J. Geophysical Research Letter*, 108:19, 2003.

Y. Narita. *Low-frequency wave upstream and downstream of the terrestrial bow shock*. PhD thesis, Universities of Braunschweig and Gottingen, 2006. 22, 27, 28, 31, 111

Y. Narita and K.-H. Glassmeier. Propagation pattern of low frequency waves in the terrestrial magnetosheath. *Annales Geophysicae*, Vol. 24:2441–2444, 2006. 133, 139

Y. Narita, K. H. Glassmeier, and R. A. Treumann. Wave-number spectra and intermittency in the terrestrial foreshock region. *Physical Review Letters*, 97:191101–4, 2006. 15, 17, 19, 20, 21, 22

G. K. Parks. *Physics of Space Plasmas: An Intrduction*. Addison-Wesley Publishing Company, The Advanced Book Program, 350 Bridge Parkway, Redwood City, CA 94065, 1991. 8, 9, 12, 13, 14, 17, 18, 19, 21, 22, 34, 115, 136

G. Paschmann and P. W. Daly. Analysis methods for multi-spacecraft data. July 2000. 27, 31, 141

G. Paschmann, N. Sckopke, S. J. Bame, and J. T. Gosling. Observations of gyrating ions in the foot of the nearly-perpendicular bow shock. *J. Geophysical Research Letter*, 9: 881–884, 1982.

G. Paschmann, G. Haerendel, N. Sckopke, E. Mobius, H. Luhr, and C. W. Carlson. Three-dimensional plasma structure with anomalous flow directions near the earth's bow shock. *J. Geophysical Research Letter*, 93:11279–11294, 1988. 92

M. Peredo, J. A. Slavin, E. Mazur, and S. A. Curtis. Three-dimensional position and shape of the bow shock and their variation with alfvenic , sonic and magnetosonic

mach numbers and interplanetary magneticfield orientation. *Journal Geophysical Research*, 100, No. A5:7907–7916, 1995.

T. D. Phan, G. Paschmann, W. Baumjohann, N. Sckopke, and H. Luhr. The magnetosheath region adjacent to the dayside magnetopause- ampte/irm observations. *J. Geophysical Research Letter*, 99:121–141, 1994.

J. L. Pincòn and F. Lefeuvre. Local characterisation of homogeneous turbulence in a space plasma from simultaneous measurements of field components at several points in space. *J. Geophys. Res. lett.*, 96:1789, 1991. 92

C. P. Price, D. W. Swift, and L. C. Lee. Numerical simulation of non−oscillatory mirror waves at the earth's magnetosheath. *J. Geophys. Res. lett.*, 91:101–112, 1986.

L. Qinghuan and D. Melrose. Alfvén turbulence in collisionless plasmas. *Planetary and Space Science*, 55:2281–2285, 2007.

H. Réme, C. Aoustin, J. M. Bosqued, I. Dandouras, B. Lavraud, J. A. Sauvaud, A. Barthe, J. Bouyssou, Th. Camus, O. Coeur-Joly, A. Cros, J. Cuvilo, F. Ducay, Y. Garbarowitz, J. L. Medale, E. Penou, H. Perrier, D. Romefort, J. Rouzaud, C. Vallat, D. Alcaydé, C.Jacquey, C. Mazelle, C. DÚston, E. Mobius, L. M. Kistler, K. Crocker, M. Granoff, C.Mouikis, M. Popecki, M. Vosbury, B. Klecker, D. Hovestadt, H. Kucharek, E. Kuenneth, G. G. Paschmann, M. Scholer, N. Sckopke, E. Seidenschwang, C. W. Carlson, D. W. Curtis, C. Ingraham, R. P. Lin, J. P. McFadden, G. K. Parks, T. Phan, V. Formisano, E. Amata, M. B. Bavassano-Cattaneo, P. Baldetti, R. Bruno, G. Chionchio, A. di Lellis, M. F. Marcucci, G. Pallocchia, A. Korth, P. W. Daly, B. Graeve, H. Rosenbauer, V. Vasyliunas, M. McCarthy, M. Wilber, L. Eliasson, R. Lundin, S. Olsen, E. G. Shelley, S. Fuselier, A. G. Ghielmetti, W. Lennartsson, C. P. Escoubet, H. Balsiger, R. Friedel, J.-B. Cao, R. A. Kovrazhkin, I. Papamastorakis, R. Pellat, J. Scudder, and B. Sonnerup.

First multispacecraft ion measurements in and near the earths magnetosphere with the identical cluster ion spectrometry (cis) experiment. *Ann. Geophysicae*, 19:1303–1354, 2001. 28, 143

G. Rilling and P. Flandrin. On the influence of sampling on the empirical mode decomposition. *IEEE*, page 4, 2006. 38, 41, 42, 92, 95

G. Rilling, P.Flandrin, and P. Goncalvès. On empirical mode decomposition and its algorithms. *in Proc. IEEE EURASIP Workshop Nonlinear Signal Image Processing, Grado, Italy*, 1:1–5, 2003. 40, 41, 93

P. Robert, A. Roux, C. C. Harvey, M. W. Dunlop, P. W. Daly, and K. H. Glassmeier. Analysis methods for multi-spacecraft data (tetrahedron geometric factors). *Int. Space Sci. Inst., Bern, Switzerland*, pages 323–348, 1998. 100

C. T. Russell. An introduction to the physics of collisionless shocks. *American Institute of Physics*, 781:3–14, 2005. 13

C. T. Russell and R. C. Elphic. Initial isee magnetometer results: magnetopause observations. *Space Science Reviews*, 22:681, 1978.

F. Sahraoui, G. Belmont, J. L. Pincon, L. Rezeau, A. Balogh, P. Robert, , and N. Cornilleau-Wehrlin. Magnetic turbulence spectra in the manetosheath: new insights. *Ann. Geophysicae*, 22:2283–2288, 2004. 20

S. Schafer, K.-H Glassmeier, Y. Narita, K. H Fornacon, I. Dandouras, and M. Franz. Statistical phase propagation and dispersion of low frequency waves in the magnetosheath. *Annales Geophysicae*, 23:3339–3349, 2005. 20, 21, 22, 138

S. J Schwartz and D. Burgess. Quasi-parallel shocks - a patchwork, of three-dimensional structures. *J. Geophysical Research Letter*, 18:373–376, 1991. 19, 20

S. J. Schwartz, R. L. Kessel, C. C. Brown, L. J. C. Woolliscroft, Malcolm W. Dunlop, and C. J. Farrugia. Active current sheets near the earth's bow shock. *J. Geophysical Research Letter*, 93:11295–11310, 1988.

S. J. Schwartz, D. Burgess, and J. J. Moses. Low-frequency waves in the earth's magnetosheath: present status. *Ann. Geophysicae*, 14:1134–1150, 1996. 20

N. Sckopke, G. Paschmann, A. L. Brinca, C. W. Carlson, and H. Luhr. Ion thermalization in quasi-perpendicular shocks involving reflected ions. *J. Geophys. Res. Lett*, 95:6337–6352, 1990. 20

R. C. Sharpley and V. Vatchev. Analysis of the intrinsic mode functions. Technical report, Department of Mathematics, University of South Carolina, 2004. 37

N. N. Shevyrev. Mirror mode waves in the earth's magnetosheath observed by the interball-1. *Cosmic Research*, 43:291–298, 2005. 139

N. N. Shevyrev and G. N. Zastenker. Some features of the plasma flow in the magnetosheath behind quasi-parallel and quasi-perpendicular bow shocks. *Planet Space Science Reviews*, 53:95–102, 2005.

N. N. Shevyrev, G. N. Zastenker, M. N. Nozdrachev, Z. Nèmeček, J. Safrànkovà, and J. D. Richardson. High and low frequency large amplitude variation s of plasma and magnetic field in the magnetosheath: radial profile and some features. *Adv. Space Res.*, 31, No. 5:1389, 1994.

N. N. Shevyrev, G. N. Zastenker, and J. Du. Statistics of low-frequency variations in solar wind, foreshock and magnetosheath: Interball-1 and cluster data. *Planetary and Space Science*, 55:2330–2335, 2007. 12

G. L. Siscoe, N. U. Crooker, G. M. Erickson, B. U. O . Sonnerup, N. C. Maynard, J. A.

Schoendorf, K. D. Siebert, D. R. Weimer, W. W. White, and G. R. Wilson. Mhd properties of magnetosheath flow. *Planetary and Space Science*, 50:461–471, 2002.

J. O. SmithIII. *Mathematics of the Discrete Fourier Transform (DFT)*. W3K Publishing (Second Edition), 2007. 44, 47

P. Song. Isee observations of the dayside magnetosheath. *Adv. Space Res.*, 14:71–80, 1994.

P. Song, C.T. Russell, and M. F. Thomsen. Waves in the inner magnetosheath: A case study. *J. Geophysical Research Letter*, 19:2191–2194, 1992b.

B. U. O Sonnerup and L. J. Cahill. Magnetopause structure and attitude from explorer 12 observations. *J. Geophys. Res. lett.*, 72, No. 1:171–183, 1967. 99

K. Stasiewicz, Y. Khotyaintsev, and M. Grzesiak. Dispersive alfven wave observed by cluster at the magnetopause. *Adv. Space Res.*, 107:171–175, 2003.

K. Stasiewicz, M. Longmore, S. Buchert, P. K. Shukla, B. Lavraud, and J. Pickett. Properties of fast magnetosonic shocklets at the bow shock. *Geophysical Research Letters*, 30:2241, 2004. 20

M. Tatrallyay and G. Erdos. *Mirror mode fluctuations in the terrestrial magnetosheath, in: The Solar Wind-Magnetosphere system−3*. Verlag der Osterreichischen Akademie der Wissenschchaften, 2000.

M. F. Thomsen, J. T. Gosling, and C.T Russell. Isee studies of the quasi-parallel bow shock. *Adv. Space Res.*, Vol. 8:pp. (9)175–(9)178, 1988b. 20

M. F. Thomsen, J. T. Gosling, S. J. Bame, T. G. Onsager, and C. T. Russell. Two-state ion heating at quasi-parallel shocks. *j. Geophysical Research Letter*, 95:6363–6374, 1990a. 20

A. J. Tylka. The role of quasi-perpendicular shocks in solar energetic particle events. *American Institute of Physics*, 781:185–190, 2005.

S. N. Walker, F. Sahraoui, M. A. Balikhin, G. Belmont, J. L. Pincon, L. Rezeau, H. Alleyne, N. Cornilleau-Wehrlin, and M. André. A comparison of wave mode identification techniques. *Anales Geophysicae*, 22:3021–3032, 2004. 50, 92, 99

C. S. Wu, D. Winske, Y. M. Zhou, S. T. Tsai, P. Rodriguez, M. Tanaka, K. Papadopoulos, K. Akimoto, C. S. Lin, M. M. Leroy, and C. C. Goodrich. Microinstabilities associated with a high mach number, perpendicular shock. *Space Science Reviews*, 37:63–109, 1984.

Z. Wu and N. E. Huang. A study of the characteristics of white noise using the empirical mode decomposition method. *Proc. R. Soc. Lond. A*, 460:1597–1611, 2003. 39, 48

G. P. Zank and J. A. le Roux V. Florinski X. Ao and. W. K. M. Rice G. Li, G. M. Webb. Acceleration at collisionless shocks: An overview. *American Institute of Physics*, 781: 170–179, 2005.

# Appendix A

# Part A

## Positions of satellites and wave vectors

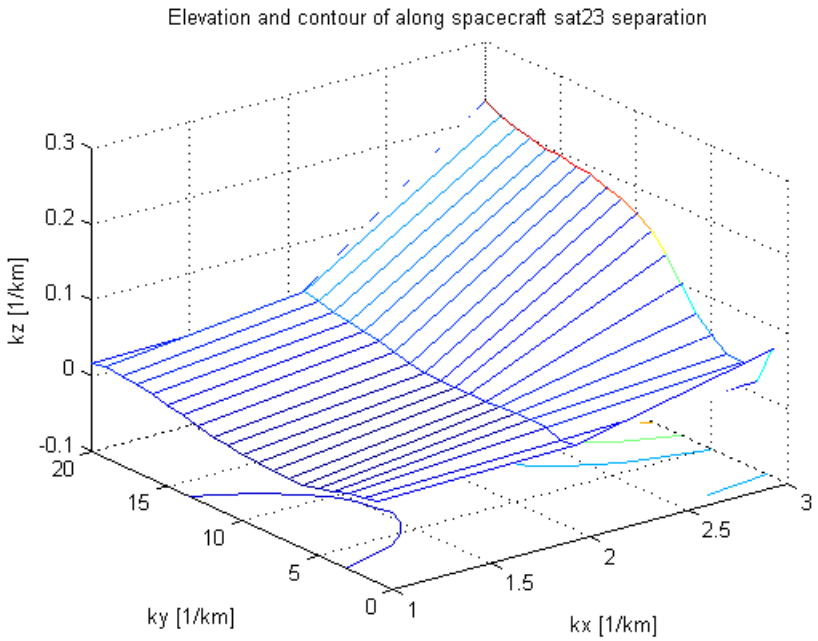


Figure 1: Elevation and contour of projection of wave vector along sat23 separation.

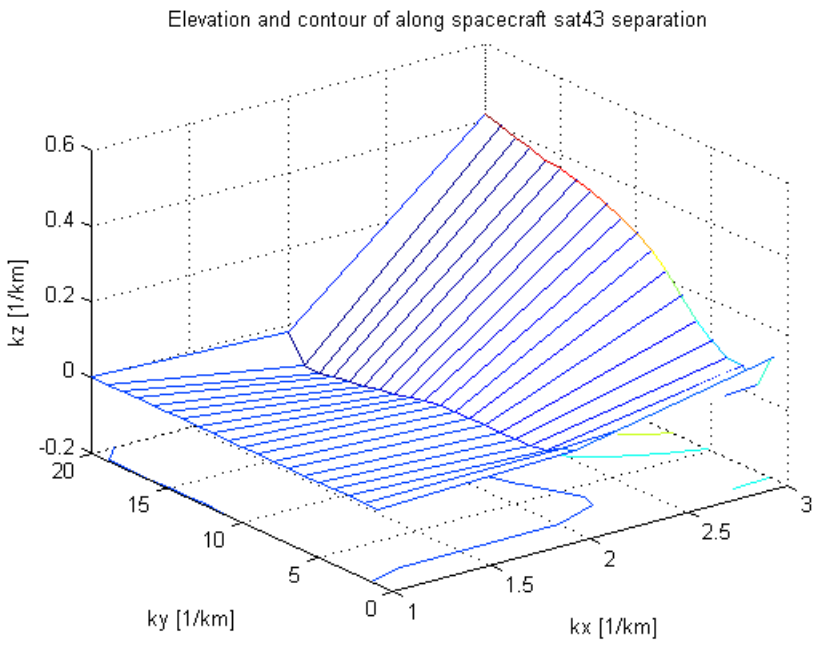


Figure 2: Elevation and contour of projection of wave vector along sat43 separation.

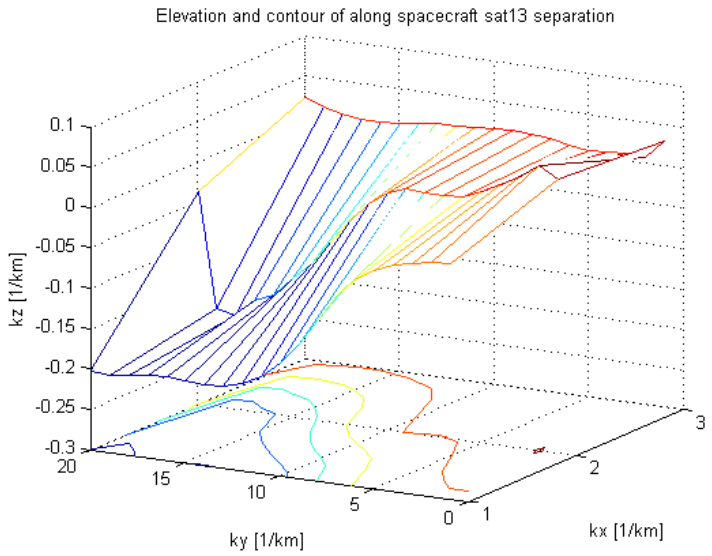


Figure 3: Elevation and contour of projection of wave vector along sat13 separation.

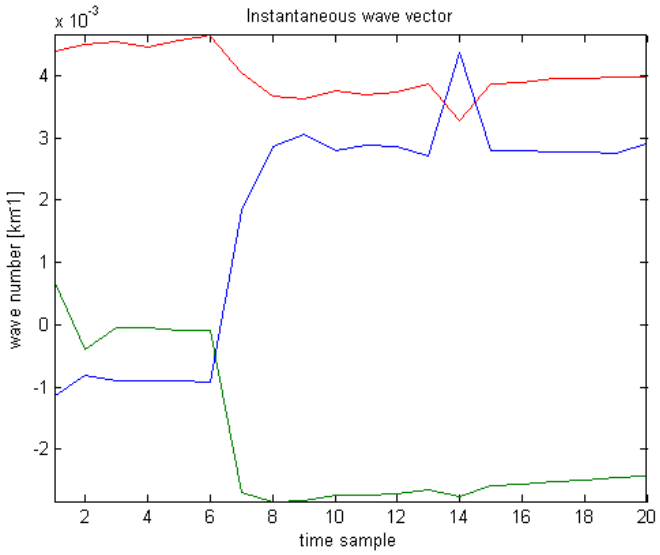


Figure 4: Instantaneous projection of wave number as a function of time.

| sat13x | sat13y | sat13z | sat23x | sat23y | sat23z | sat43x | sat43y | sat43z |
|---|---|---|---|---|---|---|---|---|
| 91.0196 | 89.9995 | 91.1059 | 180 | 129.2835 | 0 | 180 | 96.493 | 0 |
| 88.4406 | 89.7072 | 89.4589 | 0 | 84.6861 | 180 | 0 | 82.169 | 180 |
| 87.744 | 90.3734 | 88.4307 | 0 | 93.4974 | 0 | 0 | 95.4253 | 0 |
| 87.5319 | 90.3073 | 88.3491 | 0 | 137.5643 | 0 | 0 | 111.0154 | 0 |
| 87.9396 | 89.4614 | 88.5356 | 0 | 70.777 0 | 0 | 0 | 69.3972 | 0 |
| 90.6963 | 89.7455 | 92.3431 | 0 | 55.6499 | 0 | 0.4231 | 72.1716 | 180 |
| 89.7298 | 90.3748 | 88.9727 | 0.9572 | 90.7195 | 0.7554 | 0.9156 | 90.6354 | 0.8758 |
| 90.1759 | 89.8234 | 90.4087 | 0.8956 | 90.0073 | 0.8693 | 0.9042 | 89.8491 | 0.8924 |
| 90.1656 | 89.9042 | 89.0386 | 0.8971 | 89.7027 | 0.9101 | 0.8997 | 89.8909 | 0.8961 |
| 89.4871 | 89.8981 | 88.8205 | 0.8936 | 89.267 | 0.8668 | 0.8959 | 89.6956 | 0.8861 |
| 89.3064 | 90.46 | 88.9975 | 0.8808 | 91.1998 | 0.8659 | 0.8894 | 90.5848 | 0.8834 |
| 89.7205 | 89.9964 | 88.5129 | 0.8977 | 90.4093 | 0.8826 | 0.8989 | 90.1433 | 0.8864 |
| 90.6764 | 90.0316 | 93.6282 | 0.9059 | 89.9652 | 0.8581 | 0.9063 | 90.0517 | 0.946 |
| 89.3357 | 89.9646 | 88.0846 | 0.8955 | 89.9787 | 0.9515 | 0.8962 | 89.9522 | 0.8844 |
| 89.4179 | 89.9397 | 88.5015 | 0.8736 | 89.8535 | 0.8475 | 0.8884 | 89.8837 | 0.8747 |
| 89.4422 | 90.0793 | 89.3962 | 0.8807 | 90.3029 | 0.8575 | 0.8902 | 90.204 | 0.8799 |
| 89.541 | 89.6709 | 89.4208 | 0.9125 | 89.1076 | 0.9097 | 0.9034 | 89.4838 | 0.9046 |
| 90.5621 | 90.0322 | 89.5058 | 0.8839 | 90.1258 | 0.8858 | 0.8964 | 89.996 | 0.8913 |
| 89.9286 | 90.0582 | 90.5294 | 0.9062 | 89.9535 | 0.8945 | 0.9012 | 90.1576 | 0.904 |

Table 1: Angle between the projection of wave vector and separation line of spacecraft for data were collected from 05:15:30 to 05:35:30 UT. From first column to the last: sat13x to sat43z are the angles formed between the components of the projection of wave vector along spacecraft separation and the spacecraft separation line.

| t [h:m:s] | k13x | k13y | k13z | k23x | k23y | k23z | k43x | k43y | k43z |
|---|---|---|---|---|---|---|---|---|---|
| 05:15:30 | 0.0208 | -0.3664 | 0.0013 | -0.0001 | 0.0005 | 0.0006 | 0.001 | -0.0003 | 0.0032 |
| 05:16:30 | -0.0201 | -0.3713 | 0.0181 | 0.0032 | 0.0004 | -0.0068 | 0.0017 | -0.0003 | -0.0066 |
| 05:17:30 | -0.0072 | -0.3791 | -0.0024 | 0.002 | -0.0003 | 0.0044 | 0.0015 | 0.0009 | 0.0084 |
| 05:18:30 | -0.0043 | -0.3722 | -0.0021 | 0.0025 | 0.0008 | 0.0037 | 0.0019 | -0.0011 | 0.0073 |
| 05:19:30 | -0.0043 | -0.3804 | -0.0026 | 0.0035 | 0.0005 | 0.0037 | 0.0024 | -0.0015 | 0.0069 |
| 05:20:30 | -0.0067 | -0.3874 | -0.0018 | 0.0039 | -0.0018 | 0.0034 | 0.0025 | 0.0027 | 0.0057 |
| 05:21:30 | 0.0215 | -0.387 | -0.0077 | -0.0016 | -0.0006 | -0.114 | -0.001 | 0.0007 | -0.192 |
| 05:22:30 | 0.0006 | -0.3881 | -0.0058 | 0.0061 | 0.0011 | -0.1597 | 0.0022 | -0.0023 | -0.283 |
| 05:23:30 | -0.0023 | -0.3932 | 0.0016 | 0.0009 | -0.0004 | -0.1697 | 0.0002 | 0.0009 | -0.3019 |
| 05:24:30 | 0.0014 | -0.3962 | -0.0032 | -0.0001 | 0 | -0.1565 | -0.0005 | -0.0003 | -0.2796 |
| 05:25:30 | -0.0026 | -0.3934 | -0.0041 | 0.0006 | 0.0005 | -0.1595 | 0.0002 | -0.0013 | -0.2857 |
| 05:26:30 | 0 | -0.3959 | -0.002 | 0.0016 | 0.0005 | -0.1594 | 0.0012 | -0.0004 | -0.2853 |
| 05:27:30 | -0.0038 | -0.4036 | -0.0053 | 0.0016 | -0.0001 | -0.1524 | 0.001 | 0.0001 | -0.2741 |
| 05:28:30 | 0.0006 | -0.4067 | -0.003 | -0.0011 | 0.0005 | -0.2381 | -0.0007 | -0.0011 | -0.4236 |
| 05:29:30 | -0.0045 | -0.4087 | -0.0045 | 0.0008 | 0 | -0.1555 | 0.0005 | 0.0001 | -0.2837 |
| 05:30:30 | 0.0011 | -0.4104 | -0.0017 | -0.0003 | -0.0004 | -0.1559 | -0.0002 | 0.001 | -0.2841 |
| 05:31:30 | 0.0045 | -0.4166 | 0.0051 | -0.0001 | 0.0001 | -0.1566 | 0.0001 | -0.0004 | -0.2853 |
| 05:32:30 | -0.0105 | -0.4174 | -0.0021 | 0.0022 | -0.0006 | -0.1561 | 0.0014 | 0.0013 | -0.2864 |
| 05:33:30 | 0.0072 | -0.4186 | -0.001 | -0.0014 | -0.0012 | -0.1536 | -0.001 | 0.0024 | -0.2834 |
| 05:34:30 | 0.0037 | -0.4243 | 0.0009 | 0.0001 | 0.0004 | -0.162 | 0.0006 | -0.0009 | -0.2992 |

Table 2: Components of wave vector along the separation of spacecraft. The reference spacecraft is C3. A 20 mins data were collected from 05:15:30 to 05:35:30 UT.

## Instantaneous frequencies for data collected on 18 02 2002

Tables 1 and 2 are the instantaneous frequencies along each component and their standard errors. Column 1 and 2 are the instantaneous frequency for the first mode (M1x) computed using the x − component of the selected magnetic field from 05:15:30 − 05:35:30 UT on 18 02 2002. M2x is the second mode observed using this same data. M1x and M2x are the first and second modes along x which were found from C1 and C3 data only. My is the instantaneous frequency computed using y − component. M1z and M2z are the instantaneous frequency for the first and second modes computed using z − component, which were observed on C1 and C3. M is used here to represent mode.

| M1x [Hz] | std error [Hz] | M2x [Hz] | std error [Hz] | My [Hz] | std error [Hz] |
|---|---|---|---|---|---|
| 0.051 | 0.012 | 0.049 | 0.012 | 0.099 | 0.023 |
| 0.051 | 0.012 | 0.065 | 0.015 | 0.093 | 0.022 |
| 0.061 | 0.014 | 0.069 | 0.016 | 0.084 | 0.020 |
| 0.062 | 0.015 | 0.052 | 0.012 | 0.077 | 0.018 |
| 0.062 | 0.015 | 0.043 | 0.010 | 0.077 | 0.018 |
| 0.058 | 0.014 | 0.035 | 0.008 | 0.077 | 0.018 |
| 0.057 | 0.013 | 0.033 | 0.008 | 0.077 | 0.018 |
| 0.059 | 0.014 | 0.035 | 0.008 | 0.080 | 0.019 |
| 0.064 | 0.015 | 0.039 | 0.009 | 0.086 | 0.020 |
| 0.070 | 0.016 | 0.044 | 0.010 | 0.093 | 0.022 |
| 0.076 | 0.018 | 0.049 | 0.012 | 0.095 | 0.022 |
| 0.077 | 0.018 | 0.056 | 0.013 | 0.094 | 0.022 |
| 0.072 | 0.017 | 0.055 | 0.013 | 0.092 | 0.022 |
| 0.065 | 0.015 | 0.053 | 0.012 | 0.085 | 0.020 |
| 0.057 | 0.014 | 0.045 | 0.011 | 0.082 | 0.019 |
| 0.048 | 0.011 | 0.037 | 0.009 | 0.078 | 0.018 |
| 0.040 | 0.009 | 0.029 | 0.007 | 0.083 | 0.020 |
| 0.017 | 0.004 | 0.021 | 0.005 | 0.146 | 0.034 |

Table 3: Instantaneous frequency along each component and their standard errors. M1x and M2x are the first and second modes along x. My is the component along y. M1z and M2z are the first and second modes along z axis. M1x, My and M1z are instantaneous frequencies of first mode. While M2x, My and M2z are instantaneous frequencies of second mode.

| M1z [Hz] | std error [Hz] | M2z [Hz] | std error [Hz] |
|---|---|---|---|
| 0.068 | 0.016 | 0.067 | 0.016 |
| 0.067 | 0.016 | 0.069 | 0.016 |
| 0.068 | 0.016 | 0.070 | 0.017 |
| 0.076 | 0.018 | 0.067 | 0.016 |
| 0.077 | 0.018 | 0.065 | 0.015 |
| 0.074 | 0.017 | 0.061 | 0.014 |
| 0.075 | 0.018 | 0.061 | 0.014 |
| 0.078 | 0.018 | 0.063 | 0.015 |
| 0.083 | 0.020 | 0.068 | 0.016 |
| 0.082 | 0.019 | 0.072 | 0.017 |
| 0.080 | 0.019 | 0.075 | 0.018 |
| 0.079 | 0.019 | 0.077 | 0.018 |
| 0.076 | 0.018 | 0.074 | 0.017 |
| 0.075 | 0.018 | 0.069 | 0.016 |
| 0.065 | 0.015 | 0.062 | 0.015 |
| 0.061 | 0.014 | 0.056 | 0.013 |
| 0.046 | 0.011 | 0.049 | 0.012 |
| 0.051 | 0.012 | 0.059 | 0.014 |

Table 4: Contd.: Instantaneous frequency along each component and their standard errors. M1x and M2x are the first and second modes along x. My is the component along y. M1z and M2z are the first and second modes along z axis. M1x, My and M1z are instantaneous frequencies of first mode. While M2x, My and M2z are instantaneous frequencies of second mode.

## Instantaneous ion gyro−frequency, ion frequency, electron gyro−frequency and electron plasma frequency

| $\omega_{i(u)}$ [Hz] | $f_{i(u)}$ [Hz] | $\omega_{e(u)}$ [Hz] | $f_{e(u)}$[Hz] | $\omega_{i(sh)}$ [Hz] | $f_{i(sh)}$ [Hz] | $\omega_{e(sh)}$ [Hz] | $f_{e(sh)}$ [Hz] |
|---|---|---|---|---|---|---|---|
| 2.654 | 0.422 | 0.146 | 0.023 | -6.136 | -0.976 | -0.338 | -0.054 |
| 2.618 | 0.417 | 0.144 | 0.023 | -6.902 | -1.098 | -0.380 | -0.061 |
| 2.567 | 0.409 | 0.141 | 0.023 | -6.668 | -1.061 | -0.367 | -0.058 |
| 2.558 | 0.407 | 0.141 | 0.022 | -4.798 | -0.764 | -0.264 | -0.042 |
| 2.560 | 0.407 | 0.141 | 0.022 | -7.409 | -1.179 | -0.408 | -0.065 |
| 2.579 | 0.410 | 0.142 | 0.023 | -8.862 | -1.410 | -0.488 | -0.078 |
| 2.432 | 0.387 | 0.134 | 0.021 | -6.640 | -1.057 | -0.366 | -0.058 |
| 2.490 | 0.396 | 0.137 | 0.022 | -6.407 | -1.020 | -0.353 | -0.056 |
| 2.481 | 0.395 | 0.137 | 0.022 | -7.409 | -1.179 | -0.408 | -0.065 |
| 2.578 | 0.410 | 0.142 | 0.023 | -6.536 | -1.040 | -0.360 | -0.057 |
| 2.523 | 0.402 | 0.139 | 0.022 | -5.849 | -0.931 | -0.322 | -0.051 |
| 2.569 | 0.409 | 0.141 | 0.023 | -4.873 | -0.775 | -0.268 | -0.043 |
| 2.564 | 0.408 | 0.141 | 0.023 | -6.555 | -1.043 | -0.361 | -0.057 |
| 2.552 | 0.406 | 0.141 | 0.022 | -5.937 | -0.945 | -0.327 | -0.052 |
| 2.437 | 0.388 | 0.134 | 0.021 | -7.266 | -1.156 | -0.400 | -0.064 |
| 2.503 | 0.398 | 0.138 | 0.022 | -6.360 | -1.012 | -0.350 | -0.056 |
| 2.536 | 0.404 | 0.140 | 0.022 | -7.788 | -1.239 | -0.429 | -0.068 |
| 2.483 | 0.395 | 0.137 | 0.022 | -7.409 | -1.179 | -0.408 | -0.065 |
| 2.458 | 0.391 | 0.135 | 0.022 | -6.477 | -1.031 | -0.357 | -0.057 |
| 2.444 | 0.389 | 0.135 | 0.021 | -5.999 | -0.955 | -0.330 | -0.053 |

Table 5: The instantaneous ion gyro−frequency, ion frequency, electron gyro−frequency and electron plasma frequency. The average ion gyro−frequency and the uncertainty are $2.529 \pm 0.014[rads^{-1}]$, average ion frequency and the uncertainty are $0.402 \pm 0.002$ [Hz], average electron gyro−frequency and the uncertainty are $0.139 \pm 0.001[rads^{-1}]$, average electron frequency and the uncertainty are $0.022 \pm 0.000$ [Hz] for data collected from 09:17:34 − 09:42:40 UT. Right side: The instantaneous ion gyro−frequency, ion frequency, electron gyro−frequency and electron frequency. The average ion gyro−frequency and the uncertainty are $-6.614 \pm 0.211[rads^{-1}]$, average ion frequency and the uncertainty are $-1.052 \pm 0.034$ [Hz], average electron gyro−frequency and the uncertainty are $-0.364 \pm 0.012[rads^{-1}]$, average electron frequency and the uncertainty are $-0.058 \pm 0.002$ [Hz] for data collected from 05:15:30 − 05:35:30 UT.

## Instantaneous frequencies computed along each component with their plasma frames frequency

| M1x [Hz] | $f_{plas1x}$ [Hz] | M2x [Hz] | $f_{plas2x}$ [Hz] | My [Hz] | $f_{plasy}$ [Hz] |
|---|---|---|---|---|---|
| 0.051 | -0.079 | 0.049 | -0.077 | 0.099 | -0.155 |
| 0.051 | -0.081 | 0.065 | -0.102 | 0.093 | -0.145 |
| 0.061 | -0.095 | 0.069 | -0.108 | 0.084 | -0.133 |
| 0.062 | -0.098 | 0.052 | -0.081 | 0.077 | -0.120 |
| 0.062 | -0.098 | 0.043 | -0.067 | 0.077 | -0.121 |
| 0.058 | -0.090 | 0.035 | -0.055 | 0.077 | -0.121 |
| 0.057 | -0.090 | 0.033 | -0.052 | 0.077 | -0.121 |
| 0.059 | -0.093 | 0.035 | -0.054 | 0.080 | -0.126 |
| 0.064 | -0.101 | 0.039 | -0.061 | 0.086 | -0.134 |
| 0.070 | -0.110 | 0.044 | -0.070 | 0.093 | -0.145 |
| 0.076 | -0.119 | 0.049 | -0.077 | 0.095 | -0.150 |
| 0.077 | -0.122 | 0.056 | -0.088 | 0.094 | -0.148 |
| 0.072 | -0.113 | 0.055 | -0.087 | 0.092 | -0.144 |
| 0.065 | -0.103 | 0.053 | -0.083 | 0.085 | -0.133 |
| 0.057 | -0.090 | 0.045 | -0.071 | 0.082 | -0.128 |
| 0.048 | -0.075 | 0.037 | -0.058 | 0.078 | -0.123 |
| 0.040 | -0.063 | 0.029 | -0.046 | 0.083 | -0.131 |
| 0.017 | -0.027 | 0.021 | -0.033 | 0.115 | -0.180 |

Table 6: Instantaneous frequencies computed along each component with their plasma frames frequency. $f_{plas1x}$, $f_{plasy}$ and $f_{plas1z}$ are the plasma frame for the unstable mode. While $f_{plas2x}$, $f_{plasy}$ and $f_{plas2z}$ are the stable mode.

| M1z [Hz] | $f_{plas1z}$ [Hz] | M2z [Hz] | $f_{plas2z}$ [Hz] |
|---|---|---|---|
| 0.068 | -0.108 | 0.067 | -0.105 |
| 0.067 | -0.105 | 0.069 | -0.108 |
| 0.068 | -0.106 | 0.070 | -0.110 |
| 0.076 | -0.119 | 0.067 | -0.105 |
| 0.077 | -0.121 | 0.065 | -0.102 |
| 0.074 | -0.117 | 0.061 | -0.09 |
| 0.075 | -0.118 | 0.061 | -0.095 |
| 0.078 | -0.122 | 0.063 | -0.099 |
| 0.083 | -0.131 | 0.068 | -0.107 |
| 0.082 | -0.129 | 0.072 | -0.114 |
| 0.080 | -0.125 | 0.075 | -0.118 |
| 0.079 | -0.124 | 0.077 | -0.120 |
| 0.076 | -0.119 | 0.074 | -0.116 |
| 0.075 | -0.117 | 0.069 | -0.109 |
| 0.065 | -0.103 | 0.062 | -0.098 |
| 0.061 | -0.096 | 0.056 | -0.088 |
| 0.046 | -0.072 | 0.049 | -0.078 |
| 0.051 | -0.081 | 0.059 | -0.092 |

Table 7: Contd.: Instantaneous frequency along each component and their plasma frames frequency. $f_{plas1x}$, $f_{plasy}$ and $f_{plas1z}$ are the plasma frame for the unstable mode. While $f_{plas2x}$, $f_{plasy}$ and $f_{plas2z}$ are the stable mode.

## Instantaneous wave vector computed from data collected on the 18 02 2002 by Cluster spacecraft

| t[h:m:s] | $K_x[1/km]$ | $K_y[1/km]$ | $K_z[1/km]$ | $K[1/km]$ | $\lambda[km]$ |
|---|---|---|---|---|---|
| 05:15:30 | -0.0011 | 0.0007 | 0.0044 | 0.0046 | 1365.91 |
| 05:16:30 | -0.0008 | -0.0004 | 0.0045 | 0.0046 | 1365.91 |
| 05:17:30 | -0.0009 | 0.0000 | 0.0046 | 0.0046 | 1365.91 |
| 05:18:30 | -0.0009 | 0.0000 | 0.0045 | 0.0046 | 1365.91 |
| 05:19:30 | -0.0009 | -0.0001 | 0.0046 | 0.0047 | 1336.85 |
| 05:20:30 | -0.0009 | -0.0001 | 0.0046 | 0.0047 | 1336.85 |
| 05:21:30 | 0.0018 | -0.0027 | 0.004 | 0.0052 | 1208.31 |
| 05:22:30 | 0.003 | -0.0028 | 0.0037 | 0.0054 | 1163.55 |
| 05:23:30 | 0.0031 | -0.0028 | 0.0036 | 0.0055 | 1142.4 |
| 05:24:30 | 0.0028 | -0.0027 | 0.0038 | 0.0054 | 1163.55 |
| 05:25:30 | 0.0029 | -0.0027 | 0.0037 | 0.0054 | 1163.55 |
| 05:26:30 | 0.0029 | -0.0027 | 0.0037 | 0.0054 | 1163.55 |
| 05:27:30 | 0.0027 | -0.0026 | 0.0039 | 0.0054 | 1163.55 |
| 05:28:30 | 0.0044 | -0.0028 | -0.0033 | 0.0061 | 1030.03 |
| 05:29:30 | 0.0028 | -0.0026 | 0.0039 | 0.0054 | 1163.55 |
| 05:30:30 | 0.0028 | -0.0026 | 0.0039 | 0.0054 | 1163.55 |
| 05:31:30 | 0.0028 | -0.0025 | 0.0039 | 0.0054 | 1163.55 |
| 05:32:30 | 0.0028 | -0.0025 | 0.004 | 0.0054 | 1163.55 |
| 05:33:30 | 0.0027 | -0.0025 | 0.004 | 0.0054 | 1163.55 |

Table 8: Instantaneous wave vectors and wavelengths for wave propagation with a mean frequency of 78 mHz. The reference spacecraft is C3. A 20 minutes data were collected from 05:15:30 to 05:35:30 UT on 18 02 2002. The last column is the wavelength. The first column is the wavelength along sat13 separation, second column is the wavelength along sat23 separation and third column is the wavelength along sat43 separation.

## Instantaneous phase velocity computed from instantaneous frequency of y−component of magnetic field

| $V_{phx}[km/s]$ | $V_{phy}[km/s]$ | $V_{phz}[km/s]$ | $V_{mag}[km/s]$ | $V_{a(up)}[km/s]$ | $\beta_{up}$ | $V_{a(sheath)}[km/s]$ | $\beta_{sheath}$ |
|---|---|---|---|---|---|---|---|
| -32.312 | 20.562 | 135.123 | 140.446 | 167.633 | 0.558 | -157.496 | 1.219 |
| -21.979 | -10.990 | 126.381 | 128.748 | 166.222 | 1.005 | -176.944 | 0.984 |
| -22.535 | 0.000 | 115.180 | 117.364 | 154.325 | 0.516 | -168.431 | 1.084 |
| -20.476 | 0.000 | 104.663 | 106.647 | 145.847 | 1.797 | -155.867 | 1.752 |
| -19.7434 | -2.194 | 103.104 | 105.001 | 150.293 | 3.262 | -226.230 | 1.054 |
| -19.673 | -2.186 | 102.737 | 104.626 | 163.340 | 1.713 | -240.035 | 0.587 |
| 32.269 | -48.403 | 93.221 | 109.883 | 151.911 | 3.075 | -202.925 | 0.684 |
| 50.115 | -48.387 | 93.317 | 116.451 | 159.702 | 0.807 | -147.749 | 1.287 |
| 55.085 | -49.755 | 97.732 | 122.725 | 160.546 | 0.527 | -193.792 | 0.818 |
| 55.853 | -53.858 | 107.716 | 132.751 | 169.270 | 0.482 | -166.419 | 1.175 |
| 59.613 | -55.501 | 111.003 | 137.680 | 163.714 | 0.570 | -141.961 | 1.567 |
| 58.988 | -54.920 | 109.839 | 136.237 | 164.772 | 0.553 | -123.224 | 1.849 |
| 53.319 | -51.345 | 106.640 | 129.813 | 163.192 | 0.525 | -154.676 | 1.221 |
| 62.893 | -40.023 | 87.192 | 114.716 | 167.855 | 0.488 | -157.785 | 1.158 |
| 49.231 | -45.715 | 94.946 | 116.311 | 160.170 | 0.588 | -175.437 | 1.054 |
| 47.195 | -43.824 | 91.019 | 111.500 | 164.631 | 0.512 | -158.365 | 1.165 |
| 50.106 | -44.738 | 96.633 | 117.686 | 160.830 | 0.524 | -199.658 | 0.731 |
| 87.844 | -78.432 | 169.413 | 206.323 | 160.667 | 0.458 | -204.156 | 0.742 |

Table 9: Instantaneous phase velocity at spacecraft frame computed from the instantaneous frequency decomposed from y−component of data collected on 18 02 2002 from 05:15:30−05:35:30 UT. Column 5 is the Alfvén velocity computed with the selected magnetic field data and ion density data between 09:17:34 and 09:42:40 UT. Columns 6, 7 and 8 are the plasma beta in the solar wind, Alfvén velocity in the magnetosheath and the plasma beta in the magnetosheath for data collected from 05:15:30−05:35:30 UT.

| $V_{phx}$ $[kms^{-1}]$ | $V_{phy}$ $[kms^{-1}]$ | $V_{phz}$ $[kms^{-1}]$ | $V_{mag}$ $[kms^{-1}]$ | error on mag. |
|---|---|---|---|---|
| 50.776 | -32.312 | -203.103 | 211.833 | 8.454 |
| 34.539 | 17.269 | -194.281 | 198.081 | 8.119 |
| 35.413 | 0.000 | -180.997 | 184.429 | 7.795 |
| 32.179 | 0.000 | -160.895 | 164.081 | 7.333 |
| 31.025 | 3.447 | -158.574 | 161.617 | 7.204 |
| 30.915 | 3.435 | -158.008 | 161.041 | 7.192 |
| -50.708 | 76.062 | -112.684 | 145.101 | 6.594 |
| -78.751 | 76.036 | -100.476 | 148.589 | 6.560 |
| -86.563 | 78.186 | -100.524 | 153.984 | 6.602 |
| -87.768 | 84.634 | -119.114 | 170.453 | 6.930 |
| -93.677 | 87.216 | -119.519 | 175.120 | 7.013 |
| -92.695 | 86.302 | -118.266 | 173.284 | 6.980 |
| -83.788 | 80.685 | -121.027 | 167.863 | 6.884 |
| -98.831 | 62.893 | -74.123 | 138.627 | 6.165 |
| -77.363 | 71.837 | -107.756 | 150.854 | 6.597 |
| -74.163 | 68.866 | -103.299 | 144.615 | 6.496 |
| -78.738 | 70.302 | -109.671 | 152.216 | 6.619 |
| -108.612 | 96.975 | -155.160 | 212.780 | 7.722 |

Table 10: Instantaneous phase velocity at plasma frame computed from the instantaneous frequency decomposed from y−component of data collected on 18 02 2002 from 05:15:30−05:35:30 UT. The fifth column is the error on the magnitude of the instantaneous phase velocity. The error is of the range of 3.60 and 4.55 %.

## Angle in degrees between wave vector K and magnetic field B

| $\psi_{kB}C1$ | $\psi_{kB}C2$ | $\psi_{kB}C3$ | $\psi_{kB}C4$ | $\eta_{nk}$ |
|---|---|---|---|---|
| 87.636 | 87.862 | 86.941 | 87.855 | 150.648 |
| 87.658 | 87.295 | 86.648 | 87.230 | 135.994 |
| 87.924 | 87.639 | 87.533 | 87.673 | 142.128 |
| 88.403 | 87.985 | 88.547 | 88.009 | 141.671 |
| 88.162 | 87.987 | 88.185 | 88.014 | 140.163 |
| 87.783 | 88.218 | 87.486 | 88.175 | 140.163 |
| 87.821 | 88.463 | 88.189 | 88.463 | 127.003 |
| 86.764 | 87.678 | 87.959 | 87.598 | 133.986 |
| 87.498 | 87.557 | 87.155 | 87.657 | 135.009 |
| 87.109 | 87.456 | 87.628 | 87.419 | 135.824 |
| 87.350 | 86.816 | 87.102 | 86.778 | 43.996 |
| 87.353 | 87.036 | 87.130 | 86.971 | 43.996 |
| 86.892 | 88.044 | 87.522 | 88.083 | 137.687 |
| 86.947 | 87.139 | 87.838 | 87.209 | 37.444 |
| 88.037 | 87.057 | 87.544 | 86.959 | 41.329 |
| 87.803 | 88.183 | 87.965 | 88.229 | 41.328 |
| 87.591 | 88.010 | 87.676 | 87.986 | 140.888 |
| 88.145 | 88.128 | 87.546 | 88.070 | 141.616 |
| 87.495 | 87.702 | 87.605 | 87.670 | 140.602 |
| 87.323 | 86.897 | 87.136 | 86.898 | 145.011 |

Table 11: Angle in degrees between wave vector K and magnetic field B for data collected from 05:15:30 - 05:35:30 UT on 18 02 2002. The mean and standard error on the it is 87.585 ± 0.100 for C1; 87.658 ± 0.109 for C2; 87.567 ± 0.104 for C3; 87.647 ± 0.112 for C4. The fifth column shows angle in degrees between normal n and wave vector k for data collected from 05:15:30 - 05:35:30 UT on 18 02 2002. The mean and standard error on the it is 114.824 ± 9.756

## Angle in degrees between normal n and magnetic field B

| $\phi_{Bn}C1$ | $\phi_{Bn}C2$ | $\phi_{Bn}C3$ | $\phi_{Bn}C4$ |
|---|---|---|---|
| 56.567 | 66.469 | 58.396 | 66.701 |
| 65.167 | 58.636 | 73.922 | 59.097 |
| 73.981 | 125.861 | 60.758 | 126.997 |
| 58.459 | 40.719 | 57.976 | 47.724 |
| 65.157 | 65.162 | 77.209 | 64.936 |
| 56.019 | 62.988 | 64.423 | 66.967 |
| 66.074 | 42.387 | 51.141 | 40.814 |
| 54.237 | 52.564 | 58.479 | 54.054 |
| 28.653 | 59.195 | 50.352 | 57.744 |
| 62.485 | 65.205 | 64.215 | 63.260 |
| 103.416 | 45.723 | 46.967 | 45.315 |
| 127.858 | 141.632 | 132.036 | 139.944 |
| 63.586 | 69.658 | 56.595 | 109.230 |
| 116.138 | 49.570 | 126.464 | 130.412 |
| 104.688 | 104.295 | 102.762 | 106.554 |
| 122.786 | 152.260 | 143.956 | 144.552 |
| 35.460 | 34.382 | 45.043 | 33.510 |
| 40.782 | 64.348 | 68.141 | 65.655 |
| 38.440 | 28.519 | 41.669 | 24.778 |
| 24.095 | 57.720 | 50.836 | 56.001 |

Table 12: Angle in degrees between normal n and magnetic field B for data collected from 05:15:30 - 05:35:30 UT on 18 02 2002. The mean and standard error on the it is 68.202 ± 6.942 for C1; 69.365 ± 7.719 for C2; 71.567 ± 6.768 for C3; 75.212 ± 8.247 for C4.

# Part B

## Brief description of THEMIS mission

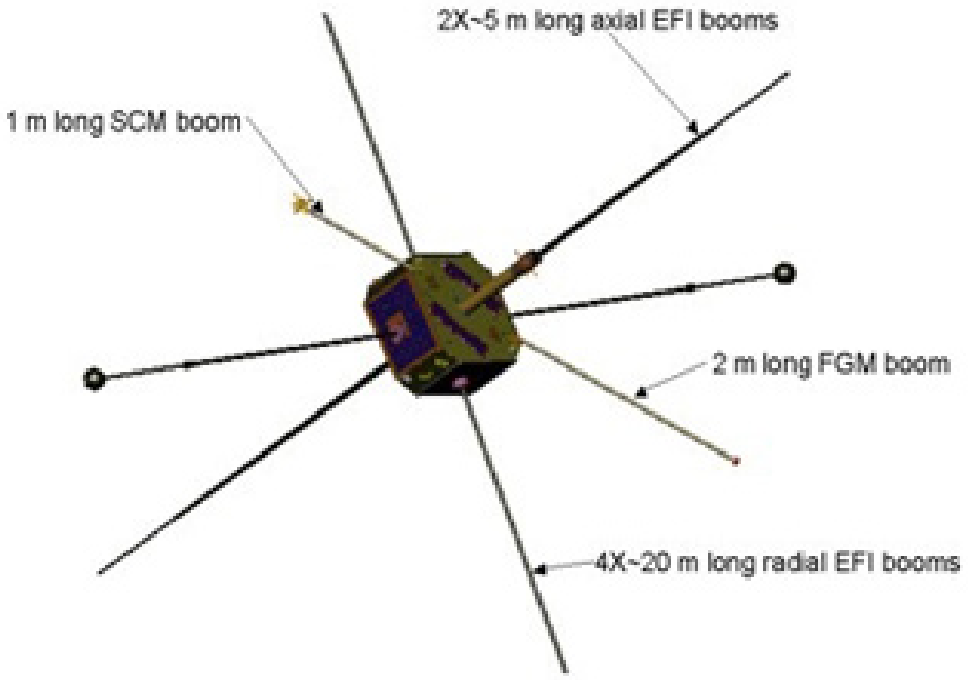


Figure 5: A picture of one the five THEMIS probes [Themis webpage]

.

The THEMIS mission [Angelopoulos, 2002.] is designed to help understand the substorm instabilities that abruptly and explosively release solar wind energy stored within the Earth magnetotail. THEMIS was launched on February 17, 2007. THEMIS consists of five identical spacecraft in carefully chosen orbit whose apogees line up once every four days over a dedicated array of ground observations located in Canada and northern America. THEMIS is an acronym for Time History of Events and Macroscale Interactions during Substorms. Three inner probes spacecraft ∼10 Earth radii ($Re$) from Earth monitor current disruption onset, while two outer probes spacecraft at 20 and 30RE remotely monitor plasma acceleration due to lobe flux dissipation. The array of spacecraft and ground observations will enable researchers to pinpoint when

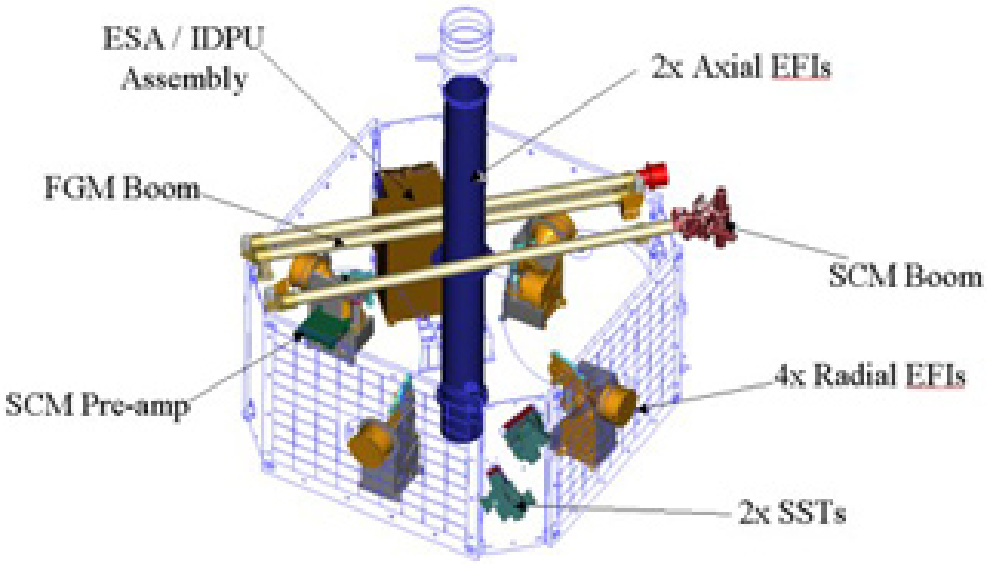


Figure 6: A diagram of the inside of one the THEMIS probes with five instruments [Themis webpage]

.

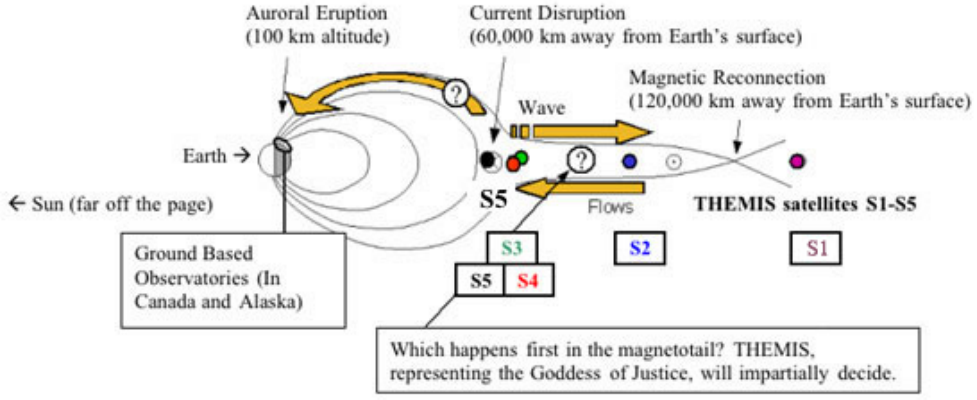


Figure 7: A diagram of the array of THEMIS probes [Themis webpage]

.

and where substorms begin, thereby distinguishing between models that begin with current disruption in the near-Earth magnetotail and those that begins with magnetic reconnection in the distant magnetotail. The same array of spacecraft and ground

Figure 8: This visualization shows the 20 THEMIS ASI ground station locations. These ground stations will assist the THEMIS satellite constellation in measuring the Aurora Borealis over North America. Each ground station has an all-sky imaging white-light auroral camera and a magnetometer. The ground stations' radial coverage is rendered at 540km [Nasa webpage]

.

observatories permits researchers to link phenomena observed in the magnetotail to those observed in the ionosphere. The inner probes are easily monitored by the ground instruments. It is therefore possible to investigate the correlation and coherency of the magnetic field observed by space instrument and those on the ground.

- Electric field instruments (EFI)
- Fluxgate magnetometers (FGM)

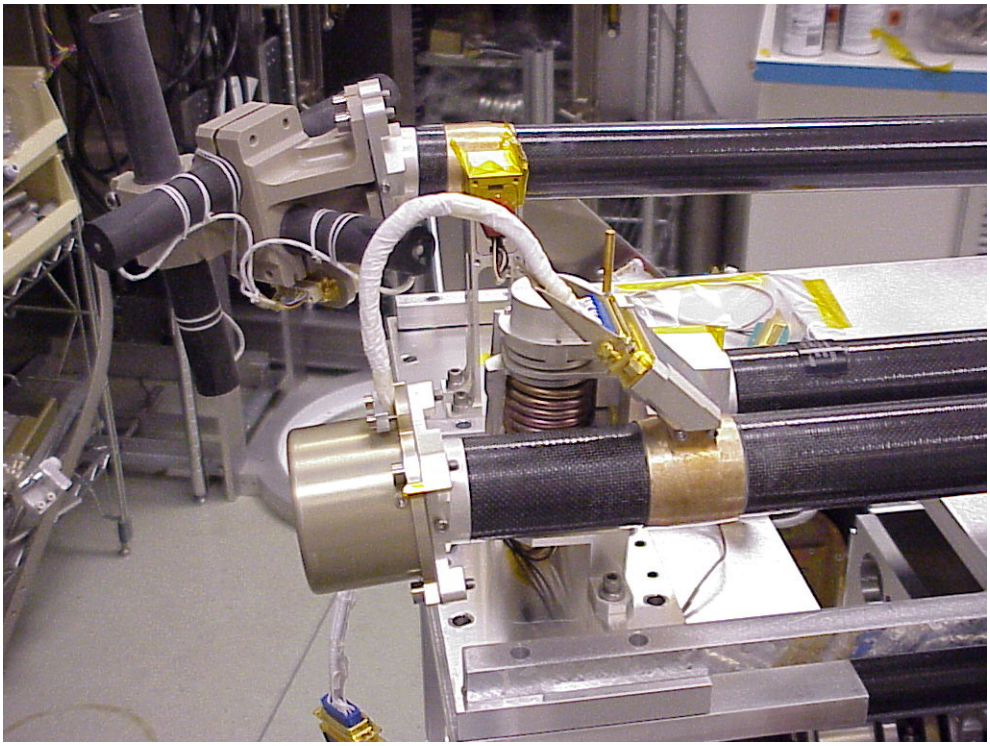

Figure 9: FGM THEMIS probes [Themis webpage]

.

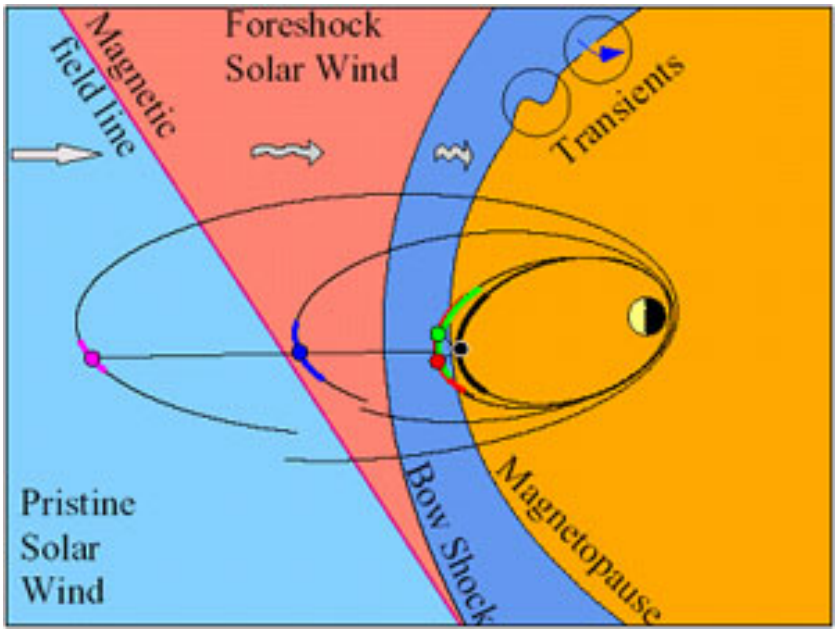


Figure 10: FGM THEMIS probes on dayside of the solar-terrestrial formation [Themis webpage]

.

- Search coil magnetometers (SCM)
- Electrostatic analyzers (ESA)
- and Solid state telescopes (SST)

The THEMIS ground observatories comprise 20 all-sky imagers and 21 ground magnetometers covers North America from Eastern Canada to Alaska, providing the information needed to place THEMIS probe observations within their global context.